Ion acceleration from laser-plasma interaction in underdense to near-critical regime: wakefield effects and associated plasma structures

François Sylla

▶ **To cite this version:**

Thèse présentée pour obtenir le grade de

DOCTEUR DE L'ECOLE POLYTECHNIQUE

Spécialité : Lasers et matière

par

François SYLLA

Ion Acceleration from Laser-Plasma Interaction in Underdense to Near-Critical Regime : Wakefield Effects and Associated Plasma Structures

Soutenue publiquement le 05 Décembre 2011 devant le jury composé de :

Prof. Dimitri BATANI	CELIA, Bordeaux	
Prof. Claude DEUTSCH	LPGP, Orsay	Rapporteur
Prof. Julien FUCHS	LULI, Palaiseau	Président
Prof. Karl KRUSHELNICK	CUOS, Ann Arbor	Rapporteur
Prof. Victor MALKA	LOA, Palaiseau	Directeur de thèse
Dr. Philippe MARTIN	CEA, Saclay	
Prof. Vladimir TIKHONCHUK	CELIA, Bordeaux	

Contents

Acknowledgements

Les toutes premières pages de ce document se doivent de rendre hommage à toutes les personnes ayant contribué à la constitution de son contenu. Bien que le reste du document soit écrit en anglais, je tenais ici à ce que mes remerciements soient adressés dans la langue de la plupart de mes collaborateurs et amis.

Tout naturellement et sans emphase, Victor Malka est la personne déterminante de ce travail de thèse pour lui avoir apporté trois choses essentielles: un cadre, des moyens et une présence. Le cadre est ce sujet exploratoire ambitieux, à la frontière des connaissances de la physique de l'interaction laser-plasma, qui mérite que l'on s'y consacre pleinement pendant trois ans et plus encore. Je le remercie de la confiance dont il a fait preuve envers moi en m'accordant le privilège de me frotter à ce thème passionant, au sein de son équipe de qualités scientifiques et humaines exceptionnelles. Les moyens correspondent surtout à la très grande autonomie d'exploration qui m'a été donnée et qui, je le crois, est des meilleures écoles de formation à la recherche expérimentale, voire même à tout type de recherche. Enfin, la présence fait référence à une disponibilité et une implication tout à fait remarquables, qui s'apprécient d'autant plus que ses hautes responsabilités au sein de projets scientifiques nationaux et internationaux sont des plus accaparantes. Je lui suis particulièrement reconnaissant pour ce dernier point d'engagement fort tenu de bout en bout et en toute circonstance.

Ce travail expérimental reste un fait collectif qui tient aussi de l'abnégation de mes partenaires d'expérience, Alessandro Flacco, Subhendu Kahaly et Mina Veltcheva. Ces trois-là ont joué lors de nos aventures en Salle Jaune une partition formidable avec beaucoup de constance, de maîtrise et d'intuition. J'ai été très heureux de me retrouver dans cet orchestre panaché qui a fait vivre avec courage l'accélération d'ions par laser sous toutes ses formes.

L'interprétation des fruits des travaux expérimentaux effectués au cours de ma thèse a grandement été rendue possible par le concours inestimable d'Agustin Lifschitz, véritable virtuose de la simulation numérique, qui fait émerger les réalités physiques *ex silico*. Je le remercie de sa patience et de son engouement à théoriser des faits expérimentaux parfois très abscons.

Un merci appuyé à Jean-Marcel Rax de m'avoir fait partager son érudition tous azimuts, ainsi que pour son aide dans la rédaction de certains passages analytiques de mon travail de thèse, qui m'ont initié aux saveurs de la modélisation simple des situations expérimentales.

Ich danke besonders meiner traumhaften Franziska für ihre jahrelange Liebe und Geduld. Ich habe wirklich die Förderung und den Rückhalt von dir geschätzt. So eine wertvolle und dienliche Rolle in meiner alltäglichen Arbeit und Laune hat sonst niemand gespielt.

Chapter 1

Laser-plasma interaction for ion acceleration

1.1 Scientific context

Laser-plasma interaction is an exciting discipline requiring understanding of many diverse physical processes. It can only be embraced through an encyclopaedic approach in the etymological sense (*encyclopaedia*: Ethymol.: εγκυκλιος: circular, παιδεια : walk, learning. Metaph.: what enfolds all sciences). This remark emphasizes the recursive nature of the field-plasma description along with the necessity to build up a body of knowledge composed of contributions from several scientific fields (statistical physics, electromagnetism, fluid mechanics, relativity...). The description of the interaction takes the form of a self-consistent cycle linking the fields, the particles of the medium, and their induced properties. Figure 1.1 illustrates schematically the cyclic integrating process of the interaction.
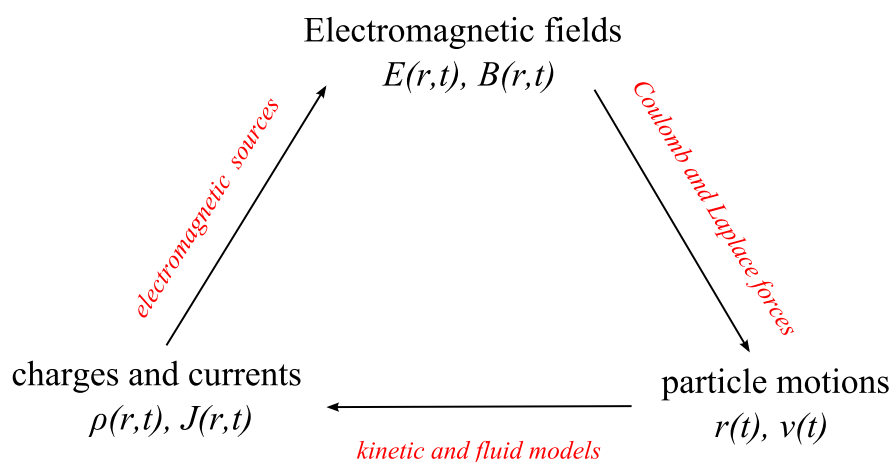
Figure 1.1: Field-plasma interaction

The analysis of such self-consistent phenomena always requires to cut the loop at a given point and to unfold the process in a causal way. This is indeed the approach

of plasma theoreticians and experimentalists starting from a laser source to trigger the interaction with the plasma. Afterwards, the complexity, in the sense of the multiple interplays and interdependences, of the laser-plasma interaction makes every experimental effort aiming at controlling this interaction for subsequent purposes (coupling, heating, resonance) dependent upon the *simultaneous* measurements of each of the quantities involved in the cycle. The experimental work reported in this document rests on the use of not-less than seven diagnostics, most of them optical, to access and resolve this interdependence in time and space.

1.1.1   Intense laser

The electromagnetic laser pulse we used for our studies can be reasonably modelled in the paraxial wave approximation by a transverse gaussian beam in vacuum [1], provided that the beam is not too tightly focussed to introduce non-negligible axial field components [2]. Then, the paraxial vector potential near the propagation axis z is given by (usual notations):

$$\mathbf{A}(r,z,t) = \underbrace{A_0 \frac{w_0}{w(z)} \exp\left[-\frac{r^2}{w(z)^2} - 2\ \ln(2)\left(\frac{z-ct}{c\tau}\right)^2\right]}_{\hat{A}(r,z,t)} \mathcal{R}\left(e^{i(\omega t - kz)e^{i\phi(z)}} e^{-i\frac{kr^2}{2R(z)}}\right) \mathbf{e}$$

(1.1)

where τ is the laser duration (FWHM in intensity), w_0 is the laser waist and $w(z)$ is the transverse beam sizes at 0 and z ($1/e^2$ in intensity), $\mathbf{e}$ the complex unit polarization vector (e.g. $\mathbf{e} = \mathbf{e_x}$ for a linear polarization along x, $\mathbf{e} = 1/\sqrt{2}(\mathbf{e_x} \pm i\mathbf{e_y})$ for a circular polarization). The electric field is then given by: $\mathbf{E_L} = -\partial \mathbf{A}/\partial t$

In vacuum, the laser transverse size evolves as:

$$w(z) = w_0\sqrt{1 + \frac{z^2}{z_R^2}}$$

(1.2)

where $z_R = \pi w_0^2/\lambda$ is the Rayleigh length and represents in practice the range over which the beam is collimated. For our laser wavelength $\lambda_L = 820$ nm, and a typical focal spot of $w_0 \sim 10\ \mu$m, the Rayleigh length yields 400 μm. This range can be quite limiting when long-range and intensity-dependent phenomena are targeted (typically particle acceleration). However in a plasma medium, when the vector potential amplitude A_0 is strong enough to drive relativistically the electrons, a relativistic laser self-focusing induces a channelling which maintains a sizeable intensity over several Rayleigh lengths [3, 4]. This non-relativistic/relativistic limit, which positions the interaction regime, is set by the normalized parameter a_0 (usual notations).

$$a_0 = \frac{eA_0}{m_e c}$$

(1.3)

(and also $\hat{a}(r,z,t) = e\hat{A}(r,z,t)/(m_e c)$ is the normalized envelop of the pulse). Hence, for $a_0 > 1$, the interaction becomes relativistic. The corresponding laser

electric field amplitude can be deduced through the equation:

$$E_L = a_0 \frac{m_e c \omega_0 c}{e} \tag{1.4}$$

$$\rightarrow \quad E_L \ [10^{12} \ \mathrm{Vm}^{-1}] \simeq 3.2 \ a_0/\lambda \ [\mu m] \tag{1.5}$$

Experimentally, the parameter a_0 is obtained via the laser power P_0 and intensity I_0 in the waist plane.

$$P_0 = 2\sqrt{\frac{\ln(2)}{\pi}} \frac{E_0}{\tau} \sim \frac{E_0}{\tau} \tag{1.6}$$

$$I_0 = \frac{2P_0}{\pi w_0^2} \tag{1.7}$$

with E_0 the pulse energy. Thus, for a linear polarization[1]:

$$a_0 = \left(\frac{I_0 \lambda^2 e^2}{2\pi^2 \varepsilon_0 m_e^2 c^5} \right)^{1/2} \tag{1.8}$$

$$\rightarrow \quad a_0 \simeq 0.86\lambda \ [\mu m] \sqrt{I_0 \ [10^{18} \ \mathrm{Wcm}^{-2}]} \tag{1.9}$$

I conclude this section by mentioning that the type of ultrashort and intense lasers we used ($\tau = 30$ fs, $I > 10^{18}$ Wcm^{-2} and $a_0 > 1$) produces fields on the order of several TVs/m capable of field-ionizing atoms [5] hundreds of femtoseconds prior to the pulse peak. The minimum intensity I_{sb} required to suppress the ionization potential barrier E_i of an atom is given by (with usual notations):

$$I_{sb} = \frac{\pi^2 \epsilon_0^3 c E_i^4}{2e^6 Z^2} \tag{1.10}$$

$$\rightarrow \quad I_{sb} \ [\mathrm{Wcm}^{-2}] \simeq 4 \times 10^9 \frac{E_i^4 [\mathrm{eV}]}{Z^2} \tag{1.11}$$

The table 1.1 shows the theoretical ionization intensity thresholds for the gaseous targets I employed in my study, justifying the plasma formalism developed throughout the present work.

Atom	Ionization degree	Intensity [Wcm^{-2}]
H	1+	1.4×10^{14}
He	1+	1.4×10^{15}
	2+	8.8×10^{15}

Table 1.1: Field-ionization intensity threshold for the gases used in this work

---

[1]for a circular polarisation, $a_0^{circ} = a_0^{lin}/\sqrt{2}$

1.1.2 Plasma

Though only recently identified and named by Irving Langmuir in 1928 [6], a plasma is a state of the matter that represents 99.9% of the visible matter in the universe. Apart from our atmosphere, a neutral gaseous boundary layer about the earth, it dominates the interstellar space from the terrestrial ionosphere up to the end of the universe. This state can be defined as following:

" an *organised* collection of *free* particles in *interaction*"

The words in italic emphasize what makes the particularity of a plasma, in comparison with a hot gas for instance, as a system in which a collective behaviour of the charged elements (electrons, ions) emerges through their self-organization or rearrangement [7] when a perturbation (mechanical, thermal, electromagnetic...), frequently associated with instabilities (Brillouin [8], Raman [9], Weibel [10]...), is present. The systemic nature of the plasma prompts the adoption of a formalism capable of describing collective phenomena along with the definition of state parameters that pilot the internal interactions.

Statistical ordering

The description of such a macroscopic object, that can comprise a number of indistinguishable particles close to the Avogadro number ($\mathcal{N}_{\mathcal{A}} = 6.02 \times 10^{23}$), can only be addressed statistically to avoid an unsolvable system of $\mathcal{N}_{\mathcal{A}} = 10^{23}$ equations of the four unknown quantities: particle position r and velocity v, electric $\mathbf{E}$ and magnetic $\mathbf{B}$ fields. This approach is termed the plasma kinetic theory. For that, each type of particles j is associated a single-particle distribution function $F_j(\mathbf{r}, \mathbf{v}, t)$ in the phase space $(\mathbf{r}, \mathbf{v})$[2], which corresponds to the number of particles of that type present in a volume $d^3r \; d^3v$, centred on (r, v) at the instant t. With that definition, when the total number of particle of each type is conserved, the distribution function is constant in time along each particle trajectory (Liouville's theorem).

$$\frac{d}{dt} F_j[r(t), v(t), t] = 0 \tag{1.12}$$

To expand the left-hand side of (1.12), it is convenient to consider the electromagnetic fields averaged over the volume $d^3r \; d^3v$, and neglect the microscopic field fluctuations occurring when particle collide (pre-kinetic timescale). This simplification is named the Vlasov approximation and yields, for a j-type particle of mass m_j and charge q_j:

$$\frac{\partial F_j}{\partial t} + \mathbf{v} \cdot \frac{\partial F_j}{\partial \mathbf{r}} + \frac{q_j}{m_j}(\mathbf{E} + \mathbf{v} \times \mathbf{B}) \cdot \frac{\partial F_j}{\partial \mathbf{v}} = 0 \tag{1.13}$$

---

[2]a multiple-particle distribution function is the general description level, still, only mandatory when pre-kinetic timescale behaviours, like short-distance Coulomb collisions, are under study.

This approximation is very reasonable in hot plasmas, where the mean kinetic energy per particle is larger than the mean interaction potential energy per particle, so that the thermal velocities and, a fortiori, the velocities gained in the intense laser field, determine the whole plasma dynamics.

Though reducing the complex plasma description to that of a space with seven dimensions, the Vlasov approximation does not give a direct access to the laboratory observables, that correspond to fluid quantities like the density, mean velocity and pressure (or temperature). However, they can be retrieved from the kinetic description considered over a longer timescale (hydrodynamic timescale) by calculating the moments of the distribution functions (product of the distribution function by a given polynomial function of the velocity $\mathbf{v}$):

$$0^{th}\text{-order: density,} \quad n_j(\mathbf{r}, t) = \int F_j(\mathbf{r}, \mathbf{v}, t)d\mathbf{v} \quad (1.14)$$

$$1^{st}\text{-order: velocity,} \quad \mathbf{V}_j(\mathbf{r}, t) = \int \mathbf{v}F_j(\mathbf{r}, \mathbf{v}, t)d\mathbf{v}/n_j(\mathbf{v}, t) \quad (1.15)$$

$$2^{nd}\text{-order: pressure,} \quad \mathbf{P}_j(\mathbf{r}, t) = m_j \int \|\mathbf{v} - \mathbf{v_j}\|^2 F_j(\mathbf{r}, \mathbf{v}, t)d\mathbf{v} \quad (1.16)$$

On this timescale, when the system is at the local thermodynamic equilibrium (LTE) at a given temperature T, then the distribution function has the usual Maxwell-Boltzmann dependence:

$$F_j(\mathbf{r}, \mathbf{v}) = n_j(r)f_j(\mathbf{v}) = \underbrace{n_{0j} \exp\left(\frac{-q_j\phi(\mathbf{r})}{kT}\right)}_{\text{Boltzmann distribution}} \underbrace{\left(\frac{m_j}{2\pi kT}\right)^{\frac{3}{2}} \exp\left(\frac{-m_j\mathbf{v}^2}{2kT}\right)}_{\text{Maxwell distribution}}$$

$$(1.17)$$

with n_{0j} the equilibrium density, k the Boltzmann constant and $\phi(\mathbf{r})$ the Poisson potential. As the moments of the kinetic distribution function reveal the hydrodynamic quantities, the moments of the kinetic Vlasov equation (1.13) give access to the corresponding hydrodynamic equations depicting the particle number and momentum conservation:

$$0^{th}\text{-order:} \quad \frac{\partial n_j}{\partial t} + \nabla \cdot (n_j\mathbf{v}_j) = 0 \quad (1.18)$$

$$1^{st}\text{-order:} \quad \frac{\partial \mathbf{V}_j}{\partial t} + (\mathbf{V}_j \cdot \nabla)\mathbf{V}_j = -\frac{\nabla \cdot \mathbf{P}}{n_j m_j} + \frac{q_j}{m_j}(\mathbf{E} + \mathbf{V}_j \times \mathbf{B}) \quad (1.19)$$

The unfolding to higher orders (pressure at second order, heat flux tensors at third order etc...) is commonly truncated at the second order to close the system by means of a model on the pressure tensor $\mathbf{P}_j$, that can only be justified with a kinetic analysis of the problem. However, from (1.19), the pressure term can have little impact on the particle dynamics when the field term become significant. This is exactly what happens within the excitation and the relaxation timescales due to intense lasers.

The positioning of the analysis in the previous temporal ordering, called the Bogoliubov hierarchy, which is bound by pre-kinetic fluctuations on the one side and global thermodynamic equilibrium on the other side, is determined by the required precision. The kinetic degree allows the unravelling of all the interesting physical phenomena relative to plasma physics (this is the degree adopted by the most sophisticated simulation algorithms); nonetheless, being developed in the phase space, the results are not directly tangible. Though inferior, the more intuitive hydrodynamic description is the one used for the description of the common plasma characteristics and behaviours. Within the limitations of that degree, the most complete framework of description in the near-Thermal Local Equilibrium, for which the plasma represents a mix of charged fluids flowing in a *quasi-neutral* state in presence of fields , is the magnetohydrodynamics (MHD), and was pioneered by Hannes Alfvén in 1942 [11].

Collective parameters

Characteristic of the plasma behaviour, the non-linear coupling between current of charges and self-consistent electromagnetic fields manifests by the collective shielding of any electromagnetic perturbation by the particles and thus the existence of waves of charges. The charged particle responses to a field perturbation have temporal and spatial scales characterizable by some collective parameters, and they differ significantly from one type of particle to the other one owing to the inertia. This multi-scale founds the dichotomy in the analysis between the electronic and ionic fluids, a convenient operation for building simplified models of the fast electronic responses, of the order of a laser optical cycle (2.3 fs) for an electronic density of 10^{19} cm^{-3}, prior to ion motions (and the development of instabilities on an ion timescale). However, all the derivable parameters have the same form for both type of particles so in the following, I shall use an $_e/_i$ subscript to refer to electronic/ionic quantities.

The electric and magnetic shieldings by charges develop when (external) scalar or vector potentials appear in a plasma. In presence of a scalar potential, the electrons assume a Boltzmann distribution and cancel out the resulting electric field over the Debye length.

$$\lambda_{De} = \sqrt{\frac{\varepsilon_0 k T_e}{n_e e^2}} \tag{1.20}$$

$$\rightarrow \quad \lambda_{De}\ [\mu\mathrm{m}] \simeq 7.44 \cdot 10^6 \cdot \sqrt{\frac{T_e\ [\mathrm{eV}]}{n_e\ [\mathrm{cm}^{-3}]}}$$

with n_e the electron density and e the elementary charge.
In presence of a vector potential varying in time, the induced electron currents flow and create an opposite magnetic field over the London length, also called

plasma skin depth.

$$\lambda_{Le} = c\sqrt{\frac{\varepsilon_0 m_e}{n_e e^2}} \tag{1.21}$$

$$\rightarrow \quad \lambda_{Le} \; [\mu\text{m}] \simeq \frac{5.29 \cdot 10^9}{\sqrt{n_e \; [\text{cm}^{-3}]}}$$

Thus, the Debye and London lengths represent the penetration scale lengths of respectively static electric and time-varying magnetic fields in the plasma.

These lengths also appear as the ratio of the velocity of sound in the electronic fluid (Debye)[3] and the velocity of light (London) to the frequency ω_{pe}, called the electron plasma or Langmuir frequency[4].

$$\omega_{pe} = \sqrt{\frac{n_e e^2}{\varepsilon_0 m_e}} \tag{1.22}$$

$$\rightarrow \quad \omega_{pe} \; [\text{Hz}] \simeq 5.64 \cdot 10^4 \sqrt{n_e \; [\text{cm}^{-3}]}$$

$$\tag{1.23}$$

For the following, one can also express the ion plasma frequency for a doubly-ionized helium plasma in practical units:

$$\rightarrow \quad \omega_{pi} \; [\text{Hz}] \simeq 1255.2\sqrt{n_i \; [\text{cm}^{-3}]}$$

Physically, the inverse plasma frequency represents the timescale over which the electronic fluid trys to restore the neutrality of the plasma. However in Ref. [6], ω_{pe} is also depicted as the oscillation frequency of an electron layer about its rest position. This transition towards a wave vocabulary stems from the fact the layer cannot come back to rest in absence of energy dissipative terms and therefore, launch a wave in the whole plasma by perturbing resonantly the neighbouring layers. The wavelength corresponding to that wave, called the Langmuir wave, is proportional to the London length (considering that the wave phase velocity is c).

$$\lambda_{pe} = 2\pi c\sqrt{\frac{\varepsilon_0 m_e}{n_e e^2}} = 2\pi \lambda_{Le} \tag{1.24}$$

$$\rightarrow \quad \lambda_{pe} \; [\mu\text{m}] \simeq \frac{3.33 \cdot 10^{10}}{\sqrt{n_e \; [\text{cm}^{-3}]}}$$

Thus, when an intense laser pulse is sent onto a plasma, a Langmuir and a transverse electromagnetic (ω, k) waves coexist and interact according to the dispersion relationship (1.25):

$$\omega^2 = \omega_{pe}^2 + k^2 c^2 \tag{1.25}$$

---

[3]using a general form of the velocity of sound $c_{se} = \sqrt{\frac{kT_e}{m_e}} = \sqrt{3}v_{eth}$, with v_{eth} the electron thermal velocity from the gas kinetic theory

[4]for the ion plasma frequency, $\omega_{pi} = \sqrt{Zm_e/m_i}\,\omega_{pe}$, with Z the ionization degree

and the corresponding group velocity:

$$v_g = \frac{\partial \omega}{\partial k} = c \underbrace{\left(1 - \frac{\omega_{pe}^2}{\omega^2}\right)^{1/2}}_{\eta(\omega)} \tag{1.26}$$

with $\eta(\omega)$ the plasma optical index.

Since the propagation of the laser is only possible for a non-evanescent wave, i.e. for a wave vector **k** which is real, this condition results for the frequencies into: $\omega > \omega_{pe}$. The limit $\omega = \omega_{pe}$ is referred to as the "critical" limit and is reached at the critical electron plasma density n_c for a given laser $\lambda = 2\pi c/\omega$ wavelength.

$$n_c \quad = \frac{\omega^2 \varepsilon_0 m_e}{e^2} \tag{1.27}$$

$$\rightarrow \quad n_c \; [\text{cm}^{-3}] \quad \simeq \frac{1.1 \times 10^{21}}{\lambda^2 [\mu m]}$$

Two regimes of importance for the laser-plasma interaction are then defined [5]:

- the "under-critical/under-dense" regime given by $n_e < n_c$ in which the laser can propagate.

- the "over-critical/over-dense" regime given by $n_e > n_c$ in which the electrons shield out the laser fields.

Similarly to the Langmuir wave resulting from the coupling between an electrostatic perturbation and the electronic Coulomb force, an MHD Alfvén wave can also propagate in an initially magnetized plasma from the interplay between a magnetic perturbation and the electronic Laplace force. The propagation equation of a weak perturbation δB, perpendicularly to the direction of a uniform magnetic field B_0, takes the form ($\delta B \ll B_0$):

$$\left(\frac{\partial^2}{\partial t^2} - V_A^2 \Delta\right) \delta B = 0 \tag{1.28}$$

with V_A the Alfvén velocity:

$$V_A \quad = \frac{B_0}{\sqrt{\mu_0 n_i m_i}} \tag{1.29}$$

$$\rightarrow \quad \frac{V_A}{c} \quad \simeq 6.94 \times 10^4 \cdot \frac{B_0 \; [\text{T}]}{\sqrt{n_i \; [\text{cm}^{-3}]}} \tag{1.30}$$

The quasi-neutrality hypothesized by the (ideal) MHD imposes a common motion of the electrons and ions on a timescale longer than ω_{pe}^{-1} (ambipolar coupling and

---

[5]when the laser fields are large enough to drive relativistically the electrons, the critical limit between transparency and opacity is shift from n_c to γn_c, with γ the electron relativistic factor [12]

no displacement currents). Therefore, the magnetic perturbation sets the whole plasma in convection, what explains the form of the Alfvén velocity in (1.30) that only depends on the ionic fluid carrying the plasma inertia. For an initially non-magnetized plasma, this velocity would describe the recoil velocity of the ionic fluid over the distance λ_{pe} due to an external magnetic pressure $B_0^2/2\mu_0$ applied at the plasma boundaries.

1.2 Brief review of the experimental study of the ion acceleration

1.2.1 Early efforts

Experiments on laser ion acceleration are as old as the laser invention in the 60's (cutoff at 1 keV/nucleon in Ref. [13]). Later, efforts in standardizing the interaction [14] made it possible with picosecond-carbon-dioxide lasers to increase the maximal ion energy to 300 keV/nucleon and to renew, with an enhanced interaction control, the parametric investigations of the acceleration [15]. The advent of the Chirped Pulse Amplification (CPA) technology in the mid-80's [16] gave access to high-field physics to a large number of academic users and set the kick-off of systematic experimental investigations of ion acceleration with sub-picosecond solid-state lasers. At the end of the 90's, accelerated ions having cutoff energies ranging from 0.02 to few MeV/nucleon could be routinely detected and studied with Ti:Sapphire short lasers interacting with gas jets [17], clusters [18] or solid thin foils [19, 20].

1.2.2 Performances and limitations

Beside a vast fundamental interest spanning from the understanding of interstellar ices [21] to the laboratory study of Warm Dense Matter [22,23], the laser-plasma ion acceleration bears the promise of potential societal application [24], the most exciting one being the hadrontherapy [25, 26], at lower costs (one can also mention the fast ignition scheme [27]). However, this revolutionary potential will become realistic merely when stable high ion beams with clinically suitable spectra (preferably monoenergetic but not necessarily) of cutoff up to 200 MeV/nucleon (to reach for instance a body-depth of 25 cm), with a suitably controllable energy distribution will be obtained reliably. This has oriented the early efforts towards record energies (58 MeV/nucleon with a PetaWatt-class laser in [28, 29]) and record laser-ion conversion efficiencies (12% reported in [29]), and stimulate an astounding number of experimental studies within only five years [28–37].

Even if the ion beams produced nowadays can exhibit outstanding and robust properties like high beam brightness and current (10^{13} ions/shot and kA-range currents within 1 picosecond) [31, 34], or excellent laminarity (ultralow emittance

measured in [34]), already suitable for proton radiography [38] and isochoric heating [22], scaling laws extracted from half a decade of intensive experimentations [39] have drawn a rather pessimistic prospect as for the upcoming generation of beams in accordance with energy and spectral application requirements (quasi-monoenergetic beams could be obtained in Ref. [40] but at ~ 1 MeV/nucleon). Experiments carried out in Ref. [32] in 2002 showing an ion energy increase by almost a factor four when reducing by 30 the thickness of the targets could have raised hope to reach rapidly 100's of MeV/nucleon with nanometer-thick targets, but the work done in Ref. [36] demonstrated that the target should have a minimal thickness at the risk of suppressing the acceleration due to a target pre-expansion effect triggered by the limited laser temporal contrast (ratio of the pulse pedestal to the peak intensities). This intrinsic saturation was confirmed by the use of a state-of-the-art double plasma mirror [41] to enhance the laser contrast (better than 1:10 at 200 hundred picoseconds) in Ref. [42], where it is reported on an increase in the ion cutoff energy by a factor of 10 when the target thickness is reduced by 1000, down to 80 nm (and further decrease making the signal vanish).

1.2.3   Characterization and mechanisms

Since 2001, the proton energy gain has only changed by little amount, from 10 MeV [33] to about 17 MeV [43] with few-Joule energy lasers for instance, contrary to predictions from numerical calculations that predicted in ideal cases much higher gains. This prompted the experimental research to dive into the understanding of the parametric interplay between the laser and the plasma characteristics. The experimental reports caused the flowering of sophisticated theoretical models, alas based on *ad hoc* parameters (laser absorption, duration of the acceleration, plasma gradients). The validation of any of them required in consequence the development of *in situ* complementary diagnostics, forming a complex apparatus around the interaction location. This is indeed the approach adopted in Refs. [44–46] for laser interactions with a thin foil, and also more modestly in the experimental investigations of the present work for laser interactions with a gas jet. With the available laser intensities $I \leq 10^{21}$ Wcm^{-2}, orders of magnitude below the intensities to drive directly and relativistically the ions $I \geq 10^{24}$ Wcm^{-2}, two limit-mechanisms of ion acceleration, one adiabatic and one (dia)thermal, both mediated by the electrons, have been retained so far for their agreements with the experimental data.

Adiabatic "Coulomb Explosion" (CE)

It is mainly invoked for explaining underdense acceleration [17] and small cluster explosion [18], and was theoretically revisited in Refs. [47–51]. Within the laser-underdense plasma interaction framework, it depicts the expansion of the ion population due to the space-charge field created when the laser pulse breaks the plasma quasi-neutrality and expels the electrons piling up in a step-like profile. Here, the adiabaticity comes from the fact that no resonance between the

laser field and the plasma electronic population exists: (i) the laser frequency ω_L and duration τ_L are considered to be much larger than, respectively, the plasma frequency ω_{pe} and the inverse plasma frequency ω_{pe}^{-1} and (ii) the spatial plasma (essentially radial for underdense plasmas) and the intensity scale lengths are considered to be much larger than the laser wavelength λ_L. Then, only matters the secular drift of the electronic fluid in the slowly-varying-vector-potential envelop due to the action of the laser ponderomotive force $\mathbf{F}_p$[6], given by (for a linearly polarized pulse):

$$\mathbf{F}_p = -m_e c^2 \nabla \gamma_{\perp e} = -m_e c^2 \nabla \left(\sqrt{1 + \frac{a_0^2}{2}} \right) \tag{1.31}$$

with $\gamma_{\perp e}$ the transverse relativistic factor of the electrons.

The adiabatic response of the electrons results in the creation of an electric field $\mathbf{E}$, balancing the ponderomotive force $e\mathbf{E} = \mathbf{F}_p$ and accelerating the ions. This simple modelling was assumed in Ref. [17] and used to assess the laser on-axis intensity from the detected cutoff energies. However, it was suggested [50] that this approach has a clear limitation since the evacuation time needed by an ion to gain the maximum energy (this ion is located near the laser axis) is likely to exceed the laser duration that maintains the charge separation. Also, the existence of a plasma Debye sheath between the fully-ionized plasma and the neutral gas at a given radius can provide an additional electrostatic potential, due to hot electrons from the focal volume streaming radially, that modifies the momentum of ion projectiles streaming outwards (though tackled a long time ago in astrophysics [52,53], this aspect has never been studied in the laser-underdense plasma context). The latter fact is proposed in the experimental part of the present document for explaining certain observations we did on the ion cutoff energies (see chapter 3, subsection 3.4.3) .

Strictly speaking, the denomination "Coulomb explosion" is not fully correct for the ponderomotive mechanism briefly presented. CE is in fact related to the expansion of ions due to their own repulsive electric field, *in absence* of any electron, on a timescale on the order of ω_{pi}^{-1}, the inverse ion plasma frequency [7]. The transition from the ponderomotive mechanism to a state of electronic depletion for pure CE can be formalized following Tripathi *et al.* [54] and Macchi *et al.* [50]. Depletion happens when the laser ponderomotive force exceeds the local Coulomb electric field that retains the electrons near ions. This translates into the relationship along the radial direction (see equation (1.31)):

$$F_p(r) > eE(r) \Leftrightarrow -m_e c^2 \nabla \gamma_{\perp e}(r) > \frac{n_{e0} e^2 r}{n_{2,3} \epsilon_0} \tag{1.32}$$

where n_{e0} is the initial electron density, $\gamma_{\perp e}(r) = (1 + a(r)^2/2)^{1/2}$ for a linearly polarized pulse and $n_{2,3} \in [2,3]$ the dimension of the problem.

---

[6]this force is $Z m_e / m_i$ times weaker on ions than on electrons

[7]characteristic time to double the radius of an exploding uniformly-charged ion cylinder

For a gaussian envelop of radius r_0, $a(r) = a_0 \exp(-r^2/r_0^2)$ and:

$$\nabla\gamma_{\perp e}(r) = \frac{a'(r)a}{2\left(1+\dfrac{a^2}{2}\right)^{1/2}} \tag{1.33}$$

The ponderomotive force is expected to be stronger near the laser propagation axis, so that the condition (1.32) can be examined for $r \approx 0$. Hence:

$$\nabla\gamma_{\perp e}(r) \quad \xrightarrow[r\approx0]{} \quad -\frac{a_0^2 r}{r_0^2\left(1+\dfrac{a_0^2}{2}\right)^{1/2}} \tag{1.34}$$

$$\text{so:} \quad F_p(r) > eE(r) \iff \frac{a_0^2}{\left(1+\dfrac{a_0^2}{2}\right)^{1/2}} > \underbrace{\frac{n_{e0}e^2 r_0^2}{n_{2,3}\epsilon_0 m_e c^2}}_{\beta} \tag{1.35}$$

Finally, the condition (1.32) takes the form:

$$a_0^4 - \frac{\beta^2 a_0^2}{2} - \beta^2 > 0 \tag{1.36}$$

The resolution of (1.36) leads to the following condition:

$$a_0 > \left[\frac{\beta^2}{4} + \left(\frac{\beta^4}{16} + \beta^2\right)\right]^{\frac{1}{2}} \tag{1.37}$$

In spherical geometry $n_{2,3} = 3$, for $n_e = 1 \times 10^{19}$ cm^{-3} and $r_0 = 10\ \mu$m, $\beta = 11.7$, so that $a_0 > 8.3$. This simple criterion shows that reaching a pure CE case in a wide channel explosion configuration is not simple with usual TeraWatt-class laser systems. It requires usually to benefit from a significant pulse self-focusing in the plasma to enhance the field. The reader can also refer for a complementary approach to the study of Sun *et al.* [55], where relativistic self-focusing was first understood as a reason that can induce electron cavitation i.e. complete electron expulsion from the focal volume.

Because CE provides moderate acceleration and energy conversion efficiencies (respectively ≤ 1 MeV/nucleon and ~ 0.2 %), experimental investigations of that mechanism were deserted over the past ten years. Part of the present work is dedicated to revisiting that mechanism, analytically (chapter 2) as well as experimentally (chapter 3).

Thermal Target Normal Sheath Acceleration (TNSA) [28, 29]

Contrary to CE, the TNSA, with acceleration gains of 10s of MeV/nucleon and average conversion efficiency of about 1% has been massively tested experimentally, analytically and numerically. It refers quasi-exclusively to the interaction of a laser pulse with a solid target, but has been also once proposed to explain ion acceleration directly from a gas jet [56].

The thermal (non-adiabatic) aspect stems from the fact that it starts as a superposition of several resonances (between the laser and the electrons, between the plasma fields and the electrons) causing randomness and important cycle-to-cycle momentum transfer fluctuations [57] and leading eventually to the dispersion in the phase space of the electronic distribution function (usually referred to as heating). This general stochastic process corresponds in other words to the laser absorption by the plasma (with different variations depending on the plasma gradient [58, 59], laser incident direction and polarization [60] and intensity [61]) and this step solely determines the acceleration mechanism. For the usual TNSA [29, 31], the most energetic electrons (the so-called hot/fast electrons) of density of the order of 10^{21} cm^{-3} and energy close to the laser ponderomotive potential [62], thermally expand and travel within an angle of tens of degrees [63] at a relativistic speed through the target [64, 65], creating at the target rear surface a plasma sheath (see further for a detailed reference on that complex object), which hosts a strong electric field of amplitude on the order of few TVs/m, that accelerates the ions along the direction normal to the surface.

The onset of the acceleration can be simply pictured using the particle diffusion in a quasi-neutral plasma in non-local thermal equilibrium. Very basically, without any external field, the electron diffusion, much more efficient than the ion diffusion because of the large mass ratio, leads to a charge separation that generates an ambipolar electric field, which sets the ions in motion to regulate the particle flux and to maintain the quasi-neutrality.
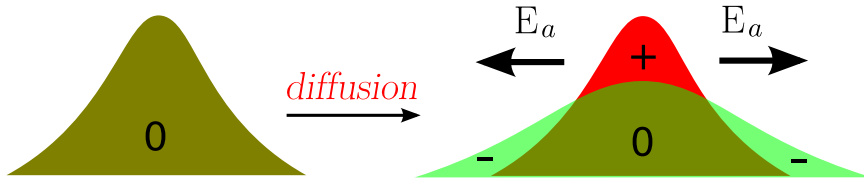
Figure 1.2: Diffusion of charged species (+ and -) in a quasi-neutral plasma and ambipolar field $\mathbf{E}_a$ creation (adapted from [66])

To grasp the experimental parameters piloting the acceleration, I briefly present the sheath *fluid* behaviour as developed in Ref. [67], for a timespan much larger than the inverse electron-ion collision frequency ν_{ei} (hydrodynamic timescale).

$$\nu_{ei}(v) \quad = \frac{n_i Z^2 e^4 \Lambda}{4\pi\varepsilon_0^2 m_e^2 v^3} \tag{1.38}$$

$$\rightarrow \quad \langle\nu_{ei}\rangle_v [\text{Hz}] \quad \simeq 5 \times 10^{-6} \Lambda \cdot n_e \ [\text{cm}^{-3}] \cdot (T_e \ [\text{eV}])^{-\frac{3}{2}} \tag{1.39}$$

with v the electron velocity before collision and Λ the coulomb logarithm, the large values of which denote a preponderance of low-angle upon large-angle collisions [68] ($10 < \Lambda < 20$ in usual plasma conditions). The numerical average

value is computed for a maxwellian distribution of temperature T_e [67].
Let us start by expressing the mobility and diffusion coefficients for an electron/ion of charge q:

$$\mu_{e,i} = \frac{q}{m_{e,i}\nu_{ei}} \quad \text{and} \quad D_{e,i} = \frac{kT_{e,i}}{m_{e,i}\nu_{ei}} \tag{1.40}$$

(in agreement with the fluctuation-dissipation theorem: $qD = \mu kT$).
If the quasi-neutrality is assumed, then it is reasonable to pose for a spatial scale larger than the Debye length: $n_e \approx Zn_i$. Without a loss of generality, I set $Z = 1$ out of simplicity. Then: $n_e = n_i = n$. So the particle fluxes yield:

$$\text{electronic flux,} \qquad \mathbf{\Gamma}_e \;=\; -n\mu_e\mathbf{E} - D_e\nabla n \tag{1.41}$$

$$\text{ionic flux,} \qquad \mathbf{\Gamma}_i \;=\; n\mu_i\mathbf{E} - D_i\nabla n \tag{1.42}$$

with $\mathbf{E}$ being the self-consistent electric field solution of the Maxwell-Gauss equation.
Without a regulating electric field $\mathbf{E} \approx 0$, $\Gamma_e \gg \Gamma_i$, which leads to the diffusive charge separation. The fluxes balance between the species is made through the creation of an ambipolar field $\mathbf{E}_a$.

$$\mathbf{\Gamma}_e(\mathbf{E}_a) = \mathbf{\Gamma}_i(\mathbf{E}_a) \Rightarrow \mathbf{E}_a = \frac{D_i - D_e}{\mu_i + \mu_e}\frac{\nabla n}{n} \tag{1.43}$$

or equivalently by using the explicit forms from (1.40)(with $q = e$):

$$\mathbf{E}_a \;=\; \frac{kT_e}{e}\left[\frac{\dfrac{T_i m_e}{T_e m_i} - 1}{\dfrac{m_e}{m_i} + 1}\right]\frac{\nabla n}{n} \tag{1.44}$$

$$\rightarrow \; E_a \;=\; \frac{kT_e}{eL} \qquad \text{for} \qquad T_e \geq T_i \tag{1.45}$$

where the characteristic plasma scale length $|\nabla n/n|^{-1}$ is noted L[8].

In consequence, the ambipolar field couples the two fluids entailing the motion of the whole plasma. However, the description of the acceleration in laser-plasma experiments cannot be reasonably limited to that of the relaxation of an ambipolar quasi-neutral plasma (all the more since the previous description was made in the hydrodynamic timescale). The plasma-vacuum interface implies in fact the existence of a complex non-quasi-neutral transition region, the so-called the sheath [69, 70] (hence the name of the mechanism), with a structure identified in experiments [71, 72], that modifies the ion flow and acceleration (e.g. from density singularities [73], multi-species interplay [74]) in a non-elucidated manner [75]. Interestingly, proposed TNSA models [76–82] and affiliated experiments [30,34,39,83–85] in the collisionless regime have confirmed the ambipolar collisional scaling law in (1.45) as governing the global acceleration scheme.

---

[8]usually taken as the local Debye length

CE & TNSA

These mechanisms are not mutually exclusive for the description of the acceleration in real cases as I explain in the following. The hole boring effect [86] at the target front face leads to laser absorption into hot electrons by the oscillating part of the $e\mathbf{V} \times \mathbf{B}$ force (for a linear laser polarization [61]) and to the stripping of an ionic layer of thickness $\sim c/\omega_{pe}$, that subsequently Coulomb explodes. The hot electrons produce from their side a TNSA acceleration as described previously. The superposition of the two effects is well depicted in the figure 3.7 in Ref. [87], where two accelerated branches can be identified in the phase space $p_x - x$, the TNSA branch being more quantitative. Likewise, the laser pulse propagating in a gas jet bores a channel of typically 20 μm diameter and induces a cylindrical sheath at the plasma-gas interface at about 100 μm from the channel. After CE of the channel, or acceleration by the wakefield as observed in our experiments, the ejected ions will cross this sheath where momentum transfer can happen (this point is addressed in the following chapters).

A more involved discussion of what happens in the sheath itself shows the simultaneity of the two mechanisms. For $|\nabla n/n|^{-1} \ll \lambda_{De}$ at the target rear face, a dense positive layer of ions is accelerated by the ambipolar field as an all and moves at high speed away from the target. Without neutralization by the co-moving hot electrons, this layer Coulomb explodes and spreads out the ion spectrum[9] [88]. For $|\nabla n/n|^{-1} \geq \lambda_{De}$, experiments of controlled density rear ramp [85, 89] ascribed the acceleration to the ion wavebreaking in the sheath [81], whereby the formed shock experiences CE and transfers additional momentum to the ions firstly accelerated via TNSA. Finally, in Refs. [90, 91], an azimuthal magnetic field, created in the sheath by the hot electrons currents outbreaking at the rear side of an underdense plasma (in practice a gas jet), pinches the accelerated ions into a central filament, which Coulomb explode asymmetrically in the forward direction.

In conclusion, a convenient and practical way to distinguish the acceleration regimes is in fact the laser absorption process at the beginning of the interaction (thermal/adiabatic). Nevertheless, the previous brief explanation underlines that they are in fact very entangled to each other. This remark enables the realization of the richness that could exist between the two limit-mechanisms, and also the possibility that it could underlie when it comes to the interpretation of the experimental observations [56, 91].

1.2.4   Alternative schemes

The review article by Fuchs *et al.* in 2005 [39] somehow made the community aware of the quite unfavourable TNSA scaling of the ion cutoff energies with the

---

[9]this is indeed what happens in regular cases since $\lambda_{De} \gg \lambda_{Di}$

laser intensities. Energies of 100s MeV/nucleon, onset of any effort for broadband applications, would only be attained for intensities above 10^{22} Wcm^{-2} with a pulse of tens of femtoseconds (corresponding to the french LUIRE (10 J) and ILE (100 J) laser projects at the horizon 2015). Moreover, the feasibility of ion acceleration using such cutting-edge systems supposes a laser contrast in intensity at the nanosecond scale better than 10^{11} at 10 J of energy[10], what has not been demonstrated yet (Chvykov *et al.* [92] demonstrated a contrast level of 10^{11} with a 30fs-1.5 J laser system). Finally and importantly, the TNSA does only produce spectra with 100 % energy spread, imposing the selection of a spectral window for societal applications, and necessarily, consequent radio-protective facilities to cut out secondary radiation.

For intensity ranges above 10^{21} Wcm^{-2}, numerous theoretical alternatives have been proposed from 2003 [93–100], but none has been conclusively demonstrated yet, due to multiple experimental obstacles underlaid by their implementations.

- collisionless electrostatic shock acceleration [95, 96] is produced when an intense pulse bores a hole over the target skin depth and steepens the electrons [96] or directly the ions [95] like a piston. This entails the formation of an ion shock within the target skin depth. As the skin-depth-ion shock propagates in the target, the ions from the target bounce off it at the velocity $2v_{shock}$[11] [101]. Up to hundreds of MeV/nucleon can be obtained with that scenario. However, it requires ultrasmall plasma scale lengths (and thus ultrahigh laser contrast) to be effective. Experimental works claiming this mechanism only reported on few MeV/nucleon (with underdense plasma in Ref. [102] for transverse ion acceleration and with mass-limited targets in Ref. [103]).

- break-out afterburner (BOA) acceleration [97] occurs when a laser pulse of about 1 picosecond heats volumetrically and sustainably the electrons from a target of the thickness of the order of the skin depth (until tens of nanometers thanks to relativistically-induced transparency [12]). This induces an enhanced charge separation compared to the TNSA, with the particularity, as the last phase of a three-phase mechanism, of accelerating quasi-monoenergetically [104] high-Z component up to 100s of MeV/nucleon. Here the experimental difficulty is the ability to prevent the significant pre-decompression of a nanometric target, irradiated at 10^9 J/cm^{-2} peak fluence, entailing a plasma gradient detrimental for efficient charge separation. Related recent experiments report on C^{6+}-acceleration at 40 MeV/nucleon with a maxwellian spectrum and at 3 MeV/nucleon with monoenergetic features [105].

---

[10]considering that the ns ASE pedestal contains 1 % of the total energy and that the ionization threshold fluence is 10 nJ/μm^{-2}

[11]with $v_{shock} \propto \sqrt{I/n_e}$ in [96] and $\propto \sqrt{I/n_i}$ in [95]

- the radiation pressure acceleration (RPA) [98] is dominant when the laser pulse with I above 10^{21} Wcm^{-2} is circularly-polarized to suppress the electron heating and ultrathin targets of nanometer scale are used. The main difference of this regime with that of Ref. [96] comes from the fact that the whole thin target is accelerated by total expulsion of the electrons by the ponderomotive push. The very favourable energy scaling of RPA[12], capable of delivering monoenergetic ions up to 500 MeV/nucleon, have boosted the interest for that scheme since 2008. However, besides the laser contrast issue, common to all scenarios using ultrathin foils, the laser polarization is another stringent constraint in that case. As mentioned in Ref. [98], a deviation from a perfect circular polarization switches the process to a TNSA-dominated mechanism and below a limit ellipticity[13], Ref. [106] predicted a total flat spectrum. In practice, this condition is all the more troublesome since a tight focusing at high intensity modifies the polarization [107]. Experimentally, with diamond-like carbon ultrathin foils of 5.3 nm, Ref. [108] attributed the observed peaks in C^{6+}-spectra to RPA, but without (*i*) presenting the spectra of the carbons from the contaminant layer of about the same thickness nor (*ii*) discussing the spectral implications of the complex interplay between light and heavy ions forming the non-neutral bunch of accelerated ions [88]. With a carbon dioxide laser delivering a train of pulses and a millimetric hydrogen jet at an overdense density for that laser[14], Ref. [109] reports on monoenergetic proton spectra at 1 MeV/nucleon, but without discussing the influence of the multiple pulses nor the laser depolarization effect likely to occur in the long plasma.

Thus, with all the experimental reports nowadays available, it is quite difficult to assert that alternative approaches to CE and TNSA have been validated in practice. It is all the more delicate to conclude since peak structures in ion spectra, the main targeted signature of the new mechanisms, can be observed in experiments involving the traditional ones [40, 110] and since any alternative is highly sensitive to parameters which are *not* under control. Therefore, it would be reasonable to conclude saying that the upcoming experimental progress in ion acceleration mostly hung on that of the laser technology as in the near-past (contrast enhancers (XPW [111], plasma mirrors [112]), absolute spectral and spatial phase controllers (Dazzler [113], deformable mirrors [114]), crystal thermal regulator (cryostats [115])).

1.3   Content

The present work reports on the material collected over the 54 days of laser "Salle Jaune" access I enjoyed during this research (14 days for proton acceleration

---

[12]the energy varies as $(I\tau/\sigma)^\alpha$, with τ the laser duration, σ the target areal density and $\alpha \approx 1-2$ at $I \sim 10^{21}$ Wcm^{-2}

[13]$\epsilon \leq 0.7$

[14]$\lambda_L \approx 10$ μm and $n_c \approx 10^{19}$ cm^{-3}

from thin foils and 40 days for alpha acceleration from gas jets). The switch from a study of a very overdense to an underdense interaction regime was encouraged by (*i*) temporal contrast issues affecting the laser system in 2009, and above all, (*ii*) with the development of very dense and thin gas jets, the perspective of an unprecedented experimental exploration of the interaction physics in an intermediate range of densities from few percent of n_c to n_c. In this range, not optimal for electron acceleration in usual schemes [116–118], ion acceleration from gas jets could be accessible with our laser equipments and exploited to unravel new exciting physics [90, 119]. In a wider perspective, this work represents, to my knowledge, the very first experimental attempt of simultaneous cross-description with numerous diagnostics of phenomena related to the physics of the relativistic interaction in a near-critical regime.

1.3.1   Pre-studies

From a theoretical viewpoint, pioneering numerical studies by Emmanuel D'Humières [120] with the particle-in-cell (PIC) code CALDER [121] in 2D geometry predicted the possibility of accelerating proton beams in the laser propagation direction to tens of MeV/nucleon, by using a laser pulse with $I_0 = 10^{20}$ Wcm^{-2} impinging onto a plasma slab of thickness $5-120$ μm and density $n_e = 0.1-1$ n_c. Though not identical to these numerical inputs, our experimental parameters lay in the vicinity, and called for more custom-tailored simulations to test this promising path. This investigation was carried out by Gonzalo Sanchez-Arriaga using the 3D version of the same PIC code and demonstrated in theory an ion acceleration to hundreds of keV/nucleon in the radial direction with regards to the laser axis, and to few keV/nucleon in the longitudinal direction. The differences in gain and acceleration geometry between the two investigations originate from (*i*) different plasma profiles used in the simulations (slab in the first case and real jet shape in the latter one) and (*ii*) a different geometry assumed in calculations entailing a different pulse propagation[15]. The 3D simulations revealed the formation of an annular channel in the laser wakefield formed of an central filament and a dense shell around it, both structures playing a role in radial ion acceleration. These facts, the richness of the underlaid physics and potential new source developments, called for further experimental investigations.

1.3.2   Aims

The very first goal of the experiments I carried out was to demonstrate ion acceleration from gas jets by using an ultrashort laser pulse, i.e. with a pulse duration shorter than the inverse ion plasma frequency. All previous investigations were indeed carried out with pulses longer than the ion response timescale ($\omega_{pi}^{-1} \simeq$

---

[15]in particular, the pulse self-focusing is underestimated in the 2D version and therefore, intensity-dependent effects on the pulse (like the filamentation instability) do not manifest with an equal strength as in the 3D version

503 fs for $n_i = 10^{19}$ cm^{-3}), so that no wakefield effect was suggested as playing possibly a role in that acceleration [17, 102]. On the contrary, our experimental conditions would make it possible to create in the laser wake a sustainable wakefield through laser-plasma resonance, with possible implications on the ion acceleration as predicted in Ref. [119].

Within this context, the geometry of the acceleration was to be clarified, with a special examination of the possibility of generating ion beams in the laser propagation direction. The theoretical work reported in Ref. [90] showed that electrons accelerated by a strong wakefield can mediate sizeable ion acceleration in the laser propagation direction when the hot electronic cloud reaches the plasma-vacuum interface. If longitudinal ion acceleration and a related discussion on the geometry were already reported in the experimental work by Willingale *et al.* using a PetaWatt-class laser [56] (with a different physical interpretation as in [90], hence an on-going debate with Bulanov *et al.* [91, 122]), the eventuality of similar achievements with a TeraWatt-class laser with higher repetition rate would make a statistic/parametric study of the phenomenon accessible and thus, could propose elements to settle the debate. Beyond academic concerns, such beams would make feasible, for instance, debris-free ion radiography at high repetition rate and, in a more general perspective, the implementation of cost-effective ion accelerators of fundamental and societal interests, with less laser contrast constraints than any equivalent based on laser-thin foil interaction.

Jointly to the ion acceleration demonstration, the description of the plasma structures associated to the acceleration was a clear objective. Taking benefit of a transparent gaseous medium, optically probable as opposed to thin foils, the development of fine diagnostics with enhanced resolutions was targeted to access to time- and space-resolved measurements of azimuthal and quasi-static magnetic fields in the Mega-Gauss range. Not only these data can unveil qualitatively the amplitude of plasma waves in the laser wake, invisible by transverse probing in our conditions[16] or hot electron injection in the wakefield [123], but also they allow to assess quantitatively the "current pinching" power of such fields suitable for plasma lensing. Additionally, this type of measurements, when carried out at the plasma-vacuum interface, could allow an experimental verification of the magnetic-vortex-assisted mechanism of ion acceleration proposed in Refs. [90] and [91].

Finally, in the numerical studies that Gonzalo Sanchez-Arriga carried out in the pre-study phase, plasma structures like an ion central filament and electromagnetic solitons appeared in the laser wake. These structures were well-known from previous numerical studies [119, 124], and established in theory as potential ion accelerating structures (about a decade ago for solitons [125], and recently for the central filament [51]). As precursors of ion acceleration *in silico* in our conditions,

---

[16]at $n_e = 10^{19}$ cm^{-3}, the temporal period of these waves ω_{pe}^{-1} is shorter than the duration of the probing laser light τ_{pr} in our conditions, so that the oscillations appear blurred. At lower densities, $\omega_{pe}^{-1} > \tau_{pr}$, but their contrast is insufficient to be detectable by standard shadowgraphy

the evidence of such structures in experiments was identified as an important step
to check the models and to propose first feedbacks from the laboratory on this
fundamental topic.

1.3.3   Thesis structure

The rest of manuscript is organized as following:

- the chapter 2 proposes extensive analytical developments from an electro-
  static model in various geometries (cylindrical and spherical) that I did on
  the Coulomb explosion taken in its usual form, i.e. in *simple cases* with
  total channel depletion and without wakefield action. I derived in particular
  the energy cutoff and ion spectrum that can be confronted to the experimen-
  tal observables when the laser pulse is longer than the inverse ion plasma
  frequency. *Non-simple cases* are then introduced with results of numerical
  simulations to emphasize the physical effects that are due to the wakefield
  action when the laser pulse is shorter than the inverse ion plasma frequency.

- the chapter 3 reports on the experimental apparatus that I implemented for
  the study and discusses the results which are relevant to the first objective
  concerning the ion acceleration demonstration and related parametric studies.

- the chapter 4 reports and discusses results relevant to the second objective
  concerning the plasma structures associated to the laser propagation and
  ion acceleration.

- appendix A presents in detail the very dense and thin gas jets that I
  developed and used for all experimental investigations reported in the
  present manuscript.

- appendix B recalls the derivations that are necessary to reconstruct the ion
  spectrum from a Thomson Parabola device which is commonly used as a
  specific particle spectrometer.

- appendix C proposes additional derivations on Coulomb explosion that
  complement the theoretical considerations in chapter 2.

- appendix D is a lists of the papers written during the Ph.D. period and
  gives a selection of some of articles.

Chapter 2

Collective ion response in under-critical plasmas

The intuitive response of the ion population from a plasma submitted to the action of an intense laser pulse, that expels ponderomotively the electrons, is an expansion due to the positive space charge field, which could be isotropic in cluster case [18], radial in underdense plasmas [17] or semi-isotropic with solid targets [126]. This response is named the Coulomb explosion (CE) and constitutes a general phenomenon of particular importance for plasma physics, be it under- or over-critical, due to its fundamental character. In chapter 1 subsection 1.2.3, a more precise description of the term "Coulomb explosion" was made, and for the following, I assume out of simplicity the term in its general sense (with or without electron depletion). In laser-plasma interactions, CE has been investigated in numerous theoretical studies [47, 50, 54] and invoked in experimental works as it occurs in laser ablation [127], laser micromachining [128] or laser particle acceleration [17,18,102]. In underdense plasmas, the relevance of CE is of particular interest for unveiling in *simple cases* the conditions of acceleration by spectra analyses (geometry, efficiency, limiting parameters), since this task requires only a classical electrostatic formalism. However, the literature does not propose any extensive spectral study of ions accelerated by CE. The main requirement for *simple cases* to be applicable is the absence of electrons and significant laser wakefield effects that can modify the ion energy (and spatial) distribution during the explosion [51, 129, 130]. In practice, such cases are met when the intense laser pulse has a duration exceeding the ion explosion time ω_{pi}^{-1} [17]. Inversely, the *non-simple cases* occur when (i) electrons are present, (ii) the laser pulse is intense enough to create strong nonlinear plasma oscillations in its wake and (ii) the pulse duration is shorter than the inverse ion plasma frequency $\tau\omega_{pi} < 1$, so that the wakefield can act on the ion dynamics independently from the pulse. In practice, the non-simple cases can be easily met with an ultrashort relativistic pulse from the LOA *Salle Jaune* laser focussed in a He^{2+} plasma of $n_e \sim 1 \times 10^{19}$ cm^{-3} density. In this chapter, I calculate analytically ion spectra $\frac{\mathrm{d}N_i}{\mathrm{d}E}$ in simple conditions valid

when $\tau\omega_{pi} > 1$ and I discuss the reverse case and its original features mainly with numerical tools.

2.1 Coulomb explosion in simple cases

I will first consider the cylindrical and spherical symmetries and then specially the planar one. Let us consider the general case at the initial state of a positive charged core surrounded by a negative shell of arbitrary thickness in a given dimension n (see figure C.1)[1]. This situation would correspond to the initial state of an under-critical plasma in presence of the laser field expelling ponderomotively outwards the electrons without heating (secular motion of electrons in the laser field without dephasing). After a transition regime (negligible with regard to the laser duration, when neglecting the electron mass), the electrons are schematically piled up at a radius r where the recoil force due to the ion core is assumed to be equal to the laser ponderomotive force (this position of equilibrium defines the so-called laser radius). This situation is a simplified limit considering the fact that the pulse in our conditions is *unlikely* to deplete the channel from all electrons.
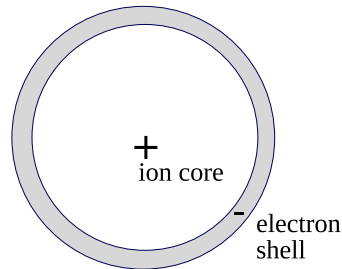
Figure 2.1: Positive ion core surrounded by a negative electron shell in the initial state

2.1.1 Fixed radius r for cylindrical and spherical symmetries

The electron shell is assumed to be fixed at r.

Uniformly charged core

The ion core is assumed to be uniformly charged. The ions moves in agreement to the space charge field (SCF) until r where the SCF is shielded by the electron shell. Then, the ions drift ballistically. This case is in practice equivalent to a laser pulse duration longer than the evacuation time of the channel it has created ($\tau\omega_{pi} > 1$ i.e. $\tau > 250$ fs for an He^{2+} plasma at 1×10^{19} cm^{-3}).

---

[1]the thickness of the shell is related in practice to the core size for particle number conservation, but this consideration is of no interest for the present derivations

To calculate the ion energy distribution $\frac{\mathrm{d}\,N_i}{\mathrm{d}\,E}$ when all ions have passed the shell, we will derive the equations of motion in each geometry. But prior to derivations, one can notice that the problem is qualitatively equivalent to the motions of fluid particles in a self-similar expansion, so long that the ion trajectories *do not* cross each other. This non-crossing hydrodynamic assumption (NCHA) is rigorously satisfied for ions, initially at rest, located beneath r (an inner layer pushes out an outer one) but ceases a priori to be valid beyond. This analogy prompts to the use of the lagrangian description of the ion dynamics and the adoption of the lagragian variable $\xi(t)$. The figure 2.2 depicts that dynamics in the (r,t) plane. The position of an ion at the time t is referenced to its initial position r_0: $r_{r_0}(t) = r_0 + \xi(t)$. Thus, the validity condition for the NCHA is $\frac{\partial r}{\partial r_0} \neq 0$.
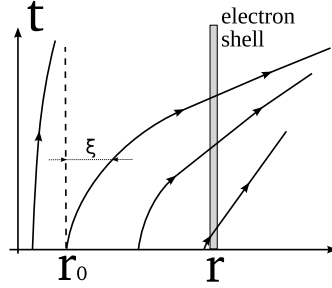
Figure 2.2: Ion trajectories $r_{r_0}(t) = r_0 + \xi(t)$ in Lagrangian description. The electron shell shields out the charge to an ion beyond r

From the Maxwell-Gauss relationship in $n \in \{2;3\}$ dimensions, one can write:

$$E(r_0 + \xi, t)(r_0 + \xi)^{n-1} = \frac{n_{i0}Ze}{\epsilon_0}\frac{r_0^n}{n} \qquad (2.1)$$

where $E(r_0 + \xi, t)$, n_{i0}, Ze and ϵ_0 are respectively the electric field at $r_{r_0}(t)$, the initial ion density and charge (in elementary charge e unit) and the vacuum permittivity. Thus, the NCHA assures that the electric field flux through the sphere of radius $r_{r_0}(t)$ depends only upon the initial condition r_0. The equation of motion is given by:

$$m_i\frac{\partial^2\xi}{\partial t^2} = m_i\frac{\omega_{pi}^2}{n}\frac{r_0^n}{(r_0 + \xi)^n} \qquad (2.2)$$

The integration of equation (2.2) is done by multiplying either side by $\frac{\partial\xi}{\partial t}$.

$$\text{for } n = 2, \quad \frac{m_i}{2}\left(\frac{\partial\xi}{\partial t}\right)^2 = m_i\frac{\omega_{pi}^2}{n}\left[r_0^n\ln\left(\frac{r_0 + \xi}{r_0}\right)\right] \qquad (2.3a)$$

$$\text{for } n = 3, \quad \frac{m_i}{2}\left(\frac{\partial\xi}{\partial t}\right)^2 = m_i\frac{\omega_{pi}^2}{n}\left[r_0^{n-1} - \frac{r_0^n}{r_0 + \xi}\right] \qquad (2.3b)$$

Equations (2.3) gives immediately the ion kinetic energy $E_c(r_0, \xi) = \frac{m_i}{2} \left(\frac{\partial \xi}{\partial t} \right)^2$ in both geometries. One can notice:

$$\lim_{\xi \to +\infty} E_c(r_0, \xi) = \begin{cases} +\infty & \text{for } n = 2 \\ \dfrac{m_i \omega_{pi}^2}{n} r_0^2 & \text{for } n = 3 \end{cases}$$

The non-physical divergence for $n = 2$ comes from the fact that charges extend to the infinity in that geometry (this is also the case in planar geometry). At finite distances conserving the cylindrical symmetry, the derivations stay valid. For a fixed radius $r_0 + \xi = r$, the energy derivative and maximum are given by equations (2.4) and (2.5)

$$\frac{\mathrm{d}\, E_c}{\mathrm{d}\, r_0}(r_0) = \frac{m_i \omega_{pi}^2}{n} \begin{cases} r_0^{n-1} \left[n \ln \left(\dfrac{r}{r_0} \right) - 1 \right] & \text{for } n = 2 \\ (n-1) r_0^{n-2} - \dfrac{r_0^{n-1}}{r} & \text{for } n = 3 \end{cases} \tag{2.4}$$

and

$$E_{c,\max} = \frac{m_i \omega_{pi}^2}{n} \begin{cases} \dfrac{r^2 e^{-1}}{2} & \text{for } n = 2 \\ \dfrac{4}{27} r^2 & \text{for } n = 3 \end{cases} \tag{2.5}$$

where $e^{-1} = 1/e^1 = 1/\exp(1)$.

For a He gas jet ionized into He^{2+} with $n_i = 10^{19}$ cm^{-3}, a laser radius of $r = 10 \ \mu$m and an infinite pulse duration:

$$\omega_{pi} = 3.97 \times 10^{12} \text{ Hz} \tag{2.6}$$

$$E_{c,\max} = \begin{cases} 7 \text{ MeV} & \text{for } n = 2 \\ 4.64 \text{ MeV} & \text{for } n = 3 \end{cases} \tag{2.7}$$

These values are obtained considering that the laser pulse does not evolve during CE in a gas jet for example. This hypothesis is rather bold at moderate a_0 and would contradict numerical and experimental observations. A more reasonable position would be to consider that $r = \lambda_{pe}$, with λ_{pe} the plasma period (see (1.25)), as the plasma electrons organise to shield the laser fields while the pulse propagates in depth. Moreover, this viewpoint leads to the fact that the field will increase from self-focusing and then enhance the probability of clean electron depletion. On that assumption, the maximum energy depends only upon the ionization degree Z. For a doubly ionized helium plasma:

$$\frac{m_i \omega_{pi}^2 \lambda_{pe}^2}{n} = \frac{4\pi^2 c^2 m_e}{n} \left(\frac{n_i}{n_e} \cdot Z^2 \right) = \frac{4\pi^2 c^2 m_e}{n} \cdot Z \tag{2.8}$$

$$\to \quad E_{c,\max} = \begin{cases} 4.08 \text{ MeV} & \text{for } n = 2 \\ 2.19 \text{ MeV} & \text{for } n = 3 \end{cases} \tag{2.9}$$

In other words, one could expect from this assumption to observe a plateau in the energy for some interval of plasma densities where its validity could be probable (e.g. for a smooth laser propagation without dramatic instabilities and for clean electron channel depletion).

It is interesting to confront quantitatively the previous modelling against the experimental data on radial ion acceleration from a gas jet reported by Krushelnick *et al.* in [17], where precisely, moderate initial a_0 was used. In their conditions, $\tau = 900$ fs and $\tau_L \omega_{pi} \simeq 5.6$, thus the channel should evacuate before the laser field vanishes, what is favourable for the *simple cases*-criterion to apply[2]. In this article, the authors reported on the radial acceleration of He^{2+} at $n_e = 5 \times 10^{19}$ cm^{-3} from a helium jet ($Z = 2$) to a cutoff level of 3.6 MeV. Interestingly this value lies between the values obtained with the spherical (2.2 MeV) and cylindrical (4.1 MeV) geometries, what would correspond to an ellipsoidal cavity. This shape is in agreement with the experimental laser pulse in fact. With deuterium ($Z = 1$) and Neon ($Z = 8$) jets, energies on the order 1 MeV and greater than 6 MeV were reported. Equations (2.9) predicts 1.1 MeV for deuterium and 8 MeV for Neon, also in agreement with the experimental data.

In Wei *et al.* [102], the authors reports also on ions accelerated from a helium jet in the radial direction with a similar laser pulse but carrying more than three times the energy (~ 180 J). In this case, the ion cutoff energy is seen to vary almost linearly with the plasma density ($\propto n_e^{0.7}$), and reaches up to 13 MeV at $n_e = 3 \times 10^{20}$ cm^{-3}. This is in contradiction with deductions from equations (2.9). In fact, in that case, it is probable that the high value in vacuum of the normalized vector potential $a_0 \sim 15$ almost directly depletes seriously the plasma channel over the vacuum focal spot of 5 μm. Thus, the set of equations (2.5) could be used instead of (2.9) where self-focusing is wished to expel sufficiently the electrons. For that case, the cutoff energy should indeed increase with the plasma density. For helium, with, a spot radius of $r = 5$ μm, $n_i = 1.5 \times 10^{20}$ cm^{-3}, in cylindrical geometry I get a cutoff energy of 23 MeV and in the spherical geometry, 12 MeV. These values are again in decent agreement with the reported value.

One can reduce the equations (2.3) by noting $\varepsilon = E_c/E_{c,\text{max}}$ and $X = r_0/r$ (ε and $X \in [0, 1]$).

$$\varepsilon = \begin{cases} 2e^{-1}X^2 \ln\left(\dfrac{1}{X}\right) & \text{for } n = 2 \\ \dfrac{27}{4}(X^2 - X^3) & \text{for } n = 3 \end{cases} \tag{2.10}$$

The figure 2.3 depicts the functions $\varepsilon(X)$ in the interval $[0, 1]$ for both symmetries. The reader can thus notice that the inverse functions $X(\varepsilon)$ are bivalued in this interval (solutions X_- and X_+), except for the position giving the maximum kinetic energy.

I now calculate the corresponding spectra $\frac{dN_i}{dE}$. Let us write the following formal

---

[2]also the same experimental case was assessed numerically in Ref. [50] and the authors concluded that the channel is depleted
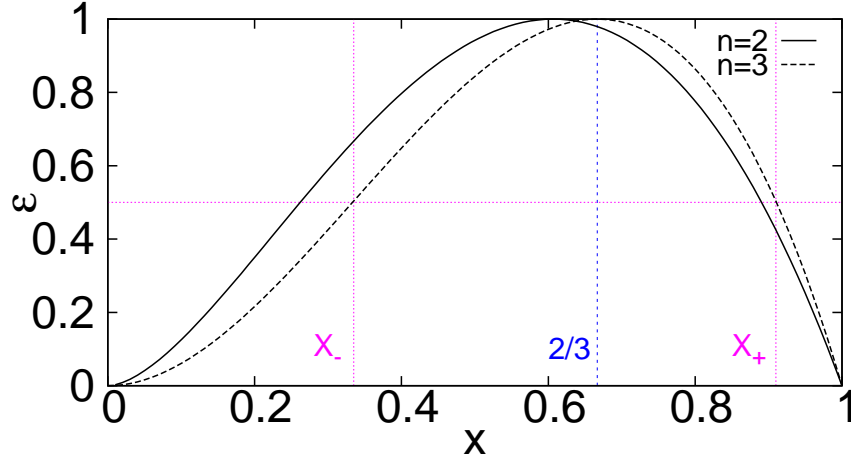
Figure 2.3: kinetic energy from CE in cylindrical ($n = 2$) and spherical ($n = 3$) symmetries. The maximum is taken for $X = e^{1/2}$ ($n = 2$) and $X = 2/3$ ($n = 3$). For a given ε, there exist two roots X_- and X_+

discrete equation:

$$\mathrm{P}(E) = \sum_{r_0} \mathrm{P}(r)\mathrm{P}(r_0 \to E) \tag{2.11}$$

where $\mathrm{P}(E)$ is the probability to get a particle at r with energy E, $\mathrm{P}(r_0)$, the probability for a particle to start from r_0 and $\mathrm{P}(r_0 \to E)$, the conditional probability for a particle starting at r_0 to gain the energy E when reaching the shell at r. The passage from a discrete to a continuous description is formally done by:

$$\begin{aligned}
\mathrm{P}(E) &\to \frac{\mathrm{d}\,N_i}{\mathrm{d}\,E} \\
\sum_{r_0} &\to \int_0^r \mathrm{d}\,r_0 \\
\mathrm{P}(r_0) &\to \frac{\mathrm{d}\,N_i}{\mathrm{d}\,r_0} \\
\mathrm{P}(r_0 \to E) &\to \delta\left[E - E_c(r_0)\right]
\end{aligned}$$

with δ being the Dirac function. Hence, after simple manipulations:

for $n = 2$,

$$\frac{\mathrm{d}\,N_i}{\mathrm{d}\,E} = \underbrace{\frac{2\pi n_{i0} r^2}{E_{c,\max}}}_{\dfrac{2N_i}{E_{c,\max}}} \underbrace{\int_0^1 \mathrm{d}X X \delta\left[\tilde{\varepsilon} - 2e^1 X^2 \ln\left(\frac{1}{X}\right)\right]}_{\mathcal{F}_2(\tilde{\varepsilon})}$$

for $n = 3$,

$$\frac{\mathrm{d}\,N_i}{\mathrm{d}\,E} = \underbrace{\frac{4\pi n_{i0} r^3}{E_{c,\max}}}_{\dfrac{3N_i}{E_{c,\max}}} \underbrace{\int_0^1 \mathrm{d}X X^2 \delta\left[\tilde{\varepsilon} - \frac{27}{4}(X^2 - X^3)\right]}_{\mathcal{F}_3(\tilde{\varepsilon})}$$

where $\tilde{\varepsilon} \in [0, 1]$ is the reduction $E/E_{c,\max}$.

The functions $\mathcal{F}_2$ and $\mathcal{F}_3$, representing the normalized ion distribution, can be calculated analytically via the roots of the function argument of δ, i.e. via the functions $X(\tilde{\varepsilon})$[3]. From the aforesaid remark about the bivaluation of $X(\varepsilon)$ in the interval $[0, 1]$, I note X_- and X_+, the two roots either side of the position $X(1)$ (see figure 2.3). These roots can be exhibited (I drop the tilde sign since no confusion is now possible):

$$\text{for } n = 2 \quad \begin{cases} X_-(\varepsilon) & = & e^{\dfrac{\mathrm{W}_0\left(-\dfrac{\varepsilon}{e^1}\right)}{2}} \\[2em] X_+(\varepsilon) & = & e^{\dfrac{\mathrm{W}_{-1}\left(-\dfrac{\varepsilon}{e^1}\right)}{2}} \end{cases} \tag{2.12}$$

where W_0 and W_{-1} are respectively the upper (principal) and lower branches of the Lambert W function.

Similarly, by posing the parameter θ so that $\cos \theta = 1 - 2\varepsilon$, the solutions can be simply expressed as:

$$\text{for } n = 3 \quad \begin{cases} X_-(\varepsilon) & = & \dfrac{1}{3} - \dfrac{2}{3}\cos\dfrac{\theta + \pi}{3} \\[1.2em] X_+(\varepsilon) & = & \dfrac{1}{3} + \dfrac{2}{3}\cos\dfrac{\theta}{3} \end{cases} \tag{2.13}$$

Thus, the final calculations for the distributions can be achieved for both dimensions:

$$\begin{aligned} \mathcal{F}_2(\varepsilon) & = & \int_0^1 \mathrm{d}X X \frac{\delta\left[X - X_-(\varepsilon)\right]}{2e^1\left|2X\ln\left(\dfrac{1}{X}\right) - 1\right|_{X_-}} + \int_0^1 \mathrm{d}X X \frac{\delta\left[X - X_+(\varepsilon)\right]}{2e^1\left|2X\ln\left(\dfrac{1}{X}\right) - 1\right|_{X_+}} \\[1.5em] & = & \frac{1}{2e^1\left|2\ln\left(\dfrac{1}{X_-}\right) - 1\right|} + \frac{1}{2e^1\left|2\ln\left(\dfrac{1}{X_+}\right) - 1\right|} \\[1.5em] & = & \frac{1}{2e^1\left|\mathrm{W}_0\left(-\dfrac{\varepsilon}{e^1}\right) + 1\right|} + \frac{1}{2e^1\left|\mathrm{W}_{-1}\left(-\dfrac{\varepsilon}{e^1}\right) + 1\right|} \end{aligned} \tag{2.14}$$

---

[3]using: for $x \mapsto f(x)$ and $i \in \mathbb{N}$; $f(x_i) = 0$, $\delta\left[f\right](x) = \sum_i \frac{\delta(x - x_i)}{|f'(x)|_{x_i}}$

and,

$$
\begin{aligned}
\mathcal{F}_3(\varepsilon) &= \int_0^1 \mathrm{d}X\, X^2 \frac{\delta\left[X - X_-(\varepsilon)\right]}{\frac{27}{4}\left|2X - 3X^2\right|_{X_-}} + \int_0^1 \mathrm{d}X\, X^2 \frac{\delta\left[X - X_+(\varepsilon)\right]}{\frac{27}{4}\left|2X - 3X^2\right|_{X_+}} \\[2mm]
&= \frac{|X_-|}{\frac{27}{4}\left|2 - 3X_-\right|} + \frac{|X_+|}{\frac{27}{4}\left|2 - 3X_+\right|} \\[2mm]
&= \frac{\left|1 - 2\cos\dfrac{\theta + \pi}{3}\right|}{\frac{27}{4}\left|1 + 2\cos\dfrac{\theta + \pi}{3}\right|} + \frac{\left|1 + 2\cos\dfrac{\theta}{3}\right|}{\frac{27}{4}\left|1 - 2\cos\dfrac{\theta}{3}\right|}
\end{aligned}
\tag{2.15}
$$

$$
\tag{2.16}
$$

Figure 2.4 shows the distribution profiles with typical increasing convex trendlines.
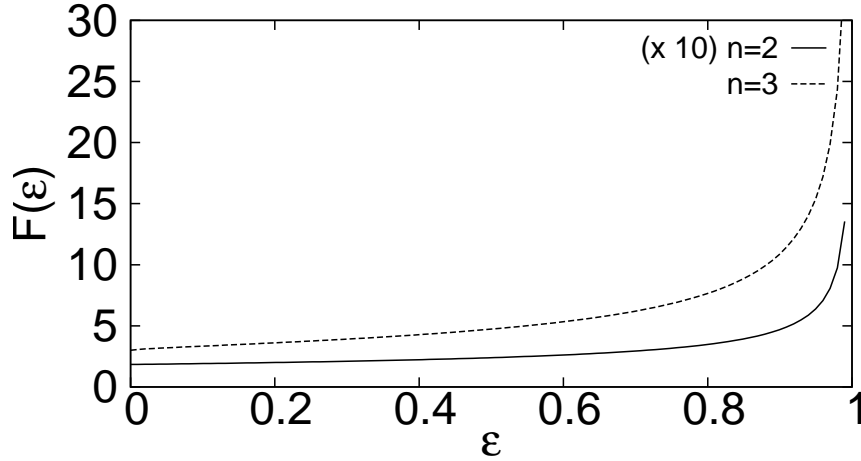
Figure 2.4: Distribution functions $\mathcal{F}(\varepsilon)$ from CE of a uniformly charged core in presence of a neutralizing shell at a fixed radius in cylindrical ($n = 2$) and spherical ($n = 3$) symmetries

For further developments on the shell slowing down effect and that of a neutral core at fixed radius r, the reader can refer to section C.1 in the appendix C. I now consider the complementary time-dependent case.

2.1.2 Fixed time τ for cylindrical and spherical symmetries

The electron shell is assumed to be absent until the time τ when the structure is suddenly neutralized. This situation models the CE when the electrons have been

expelled by the laser pulse far from the plasma region under study and flow back without inertia when the pulse is over. A self-consistent treatment of the explosion would require indeed a dynamic resolution of that problem with a neutralization instant depending on the initial ion position $\tau(r_0)$, but this is beyond the scope of simple formulation I targeted. The same lagrangian description as in previous section is used and figure 2.5 illustrates the situation. Prior to computing the ion
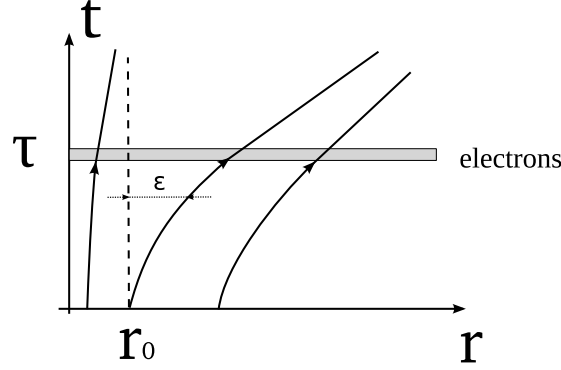
Figure 2.5: Ion trajectories $r_{r_0}(t) = r_0 + \xi(t)$ in Lagrangian description. The electron shell shields out the charge to any ion after time τ

spectra obtained from time τ, I proceed first to the derivations of the trajectories $r_{r_0}(\xi(t))$ within the NCHA. For that, a general formulation of the CE , valid for plasma laser-induced channel as well as for cluster problems, can be used.

General analytical formulation of CE

Let us come back to the Maxwell-Gauss equation (2.1) and introduce $Q_n(r_0)$, the charge enveloped by the cylinder ($n = 2$) and sphere ($n = 3$) of radius r_0.

$$\text{for } n = 2, \quad E(r_0 + \xi) = \frac{Q_n(r_0 + \xi)}{2\pi\epsilon_0(r_0 + \xi)^{n-1}} \tag{2.17}$$

$$\text{for } n = 3, \quad E(r_0 + \xi) = \frac{Q_n(r_0 + \xi)}{4\pi\epsilon_0(r_0 + \xi)^{n-1}} \tag{2.18}$$

If the particles do not cross each other (NCHA):

$$Q_n(r_0 + \xi) = Q_n(r_0) \tag{2.19}$$

Then for one ion, with the same notations as in (2.1),

$$m_i \frac{\partial^2(r_0 + \xi)}{\partial t^2} = \frac{ZeQ_n(r_0)}{4\pi\epsilon(r_0 + \xi)^{n-1}} \tag{2.20}$$

By introducing a characteristic radius R in the problem (this can be e.g. the laser radius or that of an ion cluster), the following reduced notations can be used

without a generality loss:

$$X_0 = \frac{r_0}{R}$$

$$\text{for } n = 2, \quad Q_2(X_0) = \frac{Q_2(r_0)}{\pi n_{i0} Z e R^2}$$

$$\rho_2(X_0) = \frac{1}{2\pi X_0} \frac{d\, Q_2}{d\, X_0}$$

$$\text{for } n = 3, \quad Q_3(X_0) = \frac{3 Q_3(r_0)}{4\pi n_{i0} Z e R^3}$$

$$\rho_3(X_0) = \frac{1}{4\pi X_0^2} \frac{d\, Q_3}{d\, X_0}$$

(note the difference between Q and Q)

$Q_{2,3}(X_0)$ represents the fraction of the total charge within the cylinder/sphere of radius r_0 and $\rho_n(X_0)$ the corresponding reduced density. For a uniform distribution, $Q_n(X_0) = X_0^n$ and $\rho_2(X_0) = 1/\pi$ and $\rho_3(X_0) = 3/(4\pi)$. In general, $Q_n(\infty)=1$. Consequently,

$$\frac{\partial^2 (r_0 + \xi)}{\partial t^2} = \underbrace{\frac{n_{i0} Z e^2}{m_i \epsilon}}_{= \omega_{pi}^2} R^n \frac{Q_n(X_0)}{(r_0 + \xi)^{n-1}} \tag{2.21}$$

Finally, with the additional reduced notations $\mathrm{T} = t\omega_{pi}$ and $X = \frac{r_0+\xi}{R}$:

$$\frac{\partial^2 X}{\partial \mathrm{T}^2} = \frac{Q_n(X_0)}{X^{n-1}} \tag{2.22}$$

Equation (2.22) is a general analytical formulation for CE of channel and cluster in cylindrical and spherical symmetries. I solve now this equation.

Solutions

Like equation (2.2), (2.22) can be integrated by multiplying by $\frac{\partial X}{\partial \mathrm{T}}$

$$\text{for } n = 2,$$
$$\frac{\partial X}{\partial \mathrm{T}} = \sqrt{2 Q_2(X_0) \ln\left(\frac{X}{X_0}\right)} \tag{2.23}$$
$$\text{for } n = 3,$$
$$\frac{\partial X}{\partial \mathrm{T}} = \sqrt{3 Q_3(X_0)\left[\frac{1}{X_0} - \frac{1}{X}\right]} \tag{2.24}$$

After a double integration by parts, and posing $Z = \frac{X}{X_0}$ (expansion factor), the implicit trajectory of an ion starting at X_0 can be deduced:

for $n = 2$,

$$2Z\mathfrak{F}\left[\sqrt{\ln(Z)}\right] - \mathrm{T}\sqrt{\frac{2Q_2(X_0)}{X_0^2}} = 0 \qquad (2.25)$$

for $n = 3$,

$$\sqrt{Z(Z-1)} + \ln(\sqrt{Z} + \sqrt{Z-1}) - \mathrm{T}\sqrt{\frac{2Q_3(X_0)}{X_0^3}} = 0 \qquad (2.26)$$

with $Z\mathfrak{F}\left[\sqrt{\ln(Z)}\right] = \displaystyle\int_0^{\sqrt{\ln(Z)}} \mathrm{d}U\, e^{U^2}$ being the Dawson integral.

It is remarkable that, for a uniformly charged core, the coefficient $\frac{Q_n}{X_0^n} = 1$ so that the expansion Z is *independent* upon the initial condition X_0 and $Z(X_0, \mathrm{T}) = Z(\mathrm{T})$. This is due to the self-similar nature of CE in that case for which the NCHA is never violated. The function $Z(X_0, \mathrm{T})$ can be numerically calculated for both a uniform and non uniform initial ion distribution. As an example of the non uniform distribution in spherical symmetry, I choose the following model for the charge distribution $Q_3(X_0)$:

$$Q_3(X_0) = \frac{X_0^3}{1 + X_0^3} \qquad (2.27)$$

The figure 2.6 plots the numerical resolution for both type of distribution.
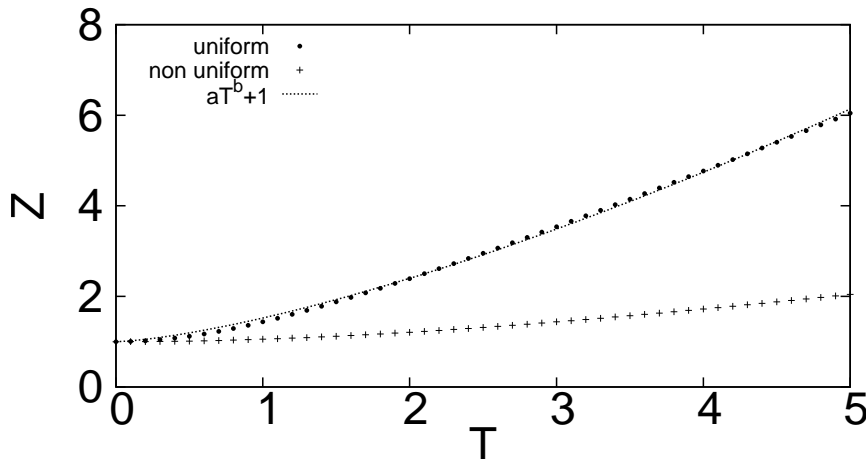

Figure 2.6: Expansion factor Z versus reduced time T for CE in spherical symmetry with uniform and non uniform charge distributions (model from equation (2.27) with $X_0 = 2$). A simple function of the form $f_3(\mathrm{T}) = a\mathrm{T}^b + 1$, with $a = 0.79$ and $b = 1.58$ fits satisfactorily $Z(\mathrm{T})$ in the uniform case

(note that, in the uniform case for $n = 2$ and $n = 3$, the function $Z(X_0, \mathrm{T}) = Z(\mathrm{T})$ is bijective, translating the fact that it depicts an explosion)
I now come back to the derivation of the ion spectrum $\frac{\mathrm{d} N_i}{\mathrm{d} E}$.

Spectra

Let us rewrite the equation (2.3b) with the expansion parameter $Z(X_0, \mathrm{T}) = \frac{X}{X_0} = \frac{r_0 + \xi}{r_0}$ previously introduced:

$$\text{for } n = 2, \quad \frac{m_i}{2} \left(\frac{\partial \xi}{\partial t} \right)^2 = m_i \frac{\omega_{pi}^2}{2} r_0^2 \left[\ln(Z) \right] \tag{2.28a}$$

$$\text{for } n = 3, \quad \frac{m_i}{2} \left(\frac{\partial \xi}{\partial t} \right)^2 = m_i \frac{\omega_{pi}^2}{3} r_0^2 \left[1 - \frac{1}{Z} \right] \tag{2.28b}$$

Likewise, introducing the characteristic radius R, I do the following reduction of the kinetic energy:

$$\varepsilon = \frac{\dfrac{m_i}{2} \left(\dfrac{\partial \xi}{\partial t} \right)^2}{\dfrac{m_i \omega_{pi}^2 R^2}{n}}$$

For a He gas jet ionized into He^{2+} with $n_i = 10^{19}$ cm^{-3} and a characteristic radius R being the laser radius of $r \sim 10$ μm, the energy normalization factor yields:

$$\omega_{pi} = 3.97 \times 10^{12} \text{ Hz} \tag{2.29}$$

$$E_{c,\max} = \begin{cases} 36 \text{ MeV} & \text{for } n = 2 \\ 24 \text{ MeV} & \text{for } n = 3 \end{cases} \tag{2.30}$$

If now the same approach as in subsection 2.1.1 is followed, then $R = \lambda_{pe}$ (λ_{pe} is the plasma wavelength) and:

$$E_{c,\max} = \begin{cases} 22 \text{ MeV} & \text{for } n = 2 \\ 14.8 \text{ MeV} & \text{for } n = 3 \end{cases} \tag{2.31}$$

Thus, equations (2.28) can be reduced into equations (2.32):

$$\text{for } n = 2, \quad \varepsilon(X_0, \mathrm{T}) = X_0^2 \cdot \left[\ln(Z(\mathrm{T})) \right] \tag{2.32a}$$

$$\text{for } n = 3, \quad \varepsilon(X_0, \mathrm{T}) = X_0^2 \cdot \left(1 - \frac{1}{Z(\mathrm{T})} \right) \tag{2.32b}$$

The figure 2.7 plots the reduced energy ε in spherical symmetry:
Then, the inverse function $X_0(\varepsilon)$, which gives the initial position of an ion for a given energy ε at time T, is:
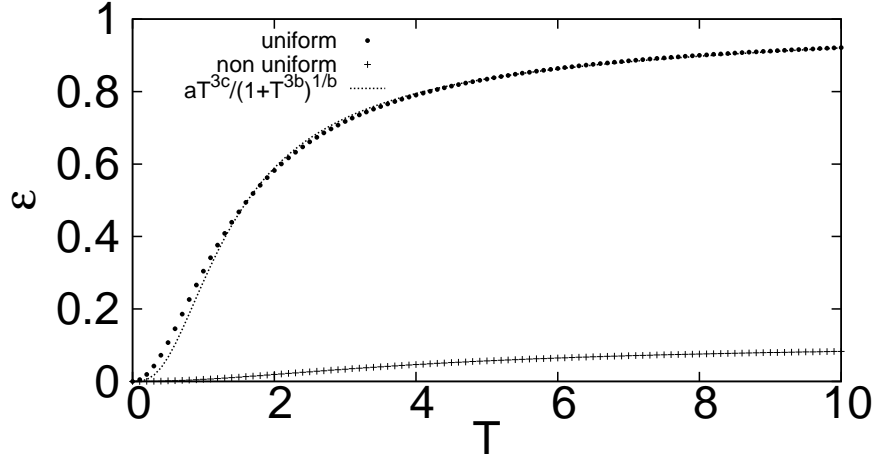
Figure 2.7: Kinetic energy ε versus reduced time T for CE in spherical symmetry with uniform and non uniform charge distributions (model from equation (2.27) with $X_0 = 2$). A simple function of the form $g_3(\mathrm{T}) = a\mathrm{T}^{3c}/(1 + \mathrm{T}^{3b})^{1/b}$, with $a = 0.79, b = 0.66$ and $c = 1.025$ fits satisfactorily $\varepsilon(\mathrm{T})$ in the uniform case

for $n = 2$,

$$X_{s,2} = X_0(\varepsilon, \mathrm{T}) = \sqrt{\frac{\varepsilon}{\ln(Z(\mathrm{T}))}} \sim \sqrt{\frac{\varepsilon}{\ln(f_2(\mathrm{T}))}} \qquad (2.33a)$$

for $n = 3$,

$$X_{s,3} = X_0(\varepsilon, \mathrm{T}) = \sqrt{\frac{\varepsilon}{1 - \dfrac{1}{Z(\mathrm{T})}}} \sim \sqrt{\frac{\varepsilon}{1 - \dfrac{1}{f_3(\mathrm{T})}}} \qquad (2.33b)$$

Finally, the time-dependent ion spectrum can be expressed as:

for $n = 2$,

$$\frac{\mathrm{d}\,N_i}{\mathrm{d}\,E} = \frac{\pi n_{i0} R^2}{\dfrac{m_i \omega_{pi}^2 R^2}{2}} \underbrace{\int_0^1 \mathrm{d}\,X_0 X_0^2 \delta\left[\tilde{\varepsilon} - \varepsilon(X_0, \mathrm{T})\right]}_{\mathcal{F}_2(\tilde{\varepsilon}, \mathrm{T})}$$

$$\sim \frac{\pi n_{i0} R^2}{\dfrac{m_i \omega_{pi}^2 R^2}{2}} \underbrace{\int_0^1 \mathrm{d}\,X_0 X_0^2 \delta\left[\tilde{\varepsilon} - X_0^2 \cdot (\ln(f_2(\mathrm{T}))\right]}_{\tilde{\mathcal{F}}_2(\tilde{\varepsilon}, \mathrm{T})}$$

and,

for $n = 3$,

$$\frac{\mathrm{d}\, N_i}{\mathrm{d}\, E} \;=\; \frac{4\pi n_{i0} R^3}{\dfrac{m_i \omega_{pi}^2 R^2}{3}} \underbrace{\int\limits_0^1 \mathrm{d}\, X_0 X_0^2 \delta\left[\tilde{\varepsilon} - \varepsilon(X_0, \mathrm{T})\right]}_{\mathcal{F}_3(\tilde{\varepsilon}, \mathrm{T})}$$

$$\sim\; \frac{4\pi n_{i0} R^3}{\dfrac{m_i \omega_{pi}^2 R^2}{3}} \underbrace{\int\limits_0^1 \mathrm{d}\, X_0 X_0^2 \delta\left[\tilde{\varepsilon} - X_0^2 \cdot \left(1 - \frac{1}{f_3(\mathrm{T})}\right)\right]}_{\tilde{\mathcal{F}}_3(\tilde{\varepsilon}, \mathrm{T})}$$

Similarly to (2.16), the distribution function can be made explicit using X_s from (2.33) (I drop the tilde sign again for the energy):

$$\mathcal{F}_2(\varepsilon, \mathrm{T}) \sim \tilde{\mathcal{F}}_3(\varepsilon, \mathrm{T}) \;=\; \frac{X_{s,2}}{2\left(\ln(f_2(\mathrm{T}))\right)}$$

$$= \frac{\sqrt{\varepsilon}}{2\ln(f_2(\mathrm{T}))\sqrt{\ln(f_2(\mathrm{T}))}} \tag{2.34a}$$

$$\mathcal{F}_3(\varepsilon, \mathrm{T}) \sim \tilde{\mathcal{F}}_3(\varepsilon, \mathrm{T}) \;=\; \frac{X_{s,3}}{2\left(1 - \dfrac{1}{f(\mathrm{T})}\right)}$$

$$= \frac{\sqrt{\varepsilon}}{2\left(1 - \dfrac{1}{f(\mathrm{T})}\right)\sqrt{\left(1 - \dfrac{1}{f(\mathrm{T})}\right)}} \tag{2.34b}$$

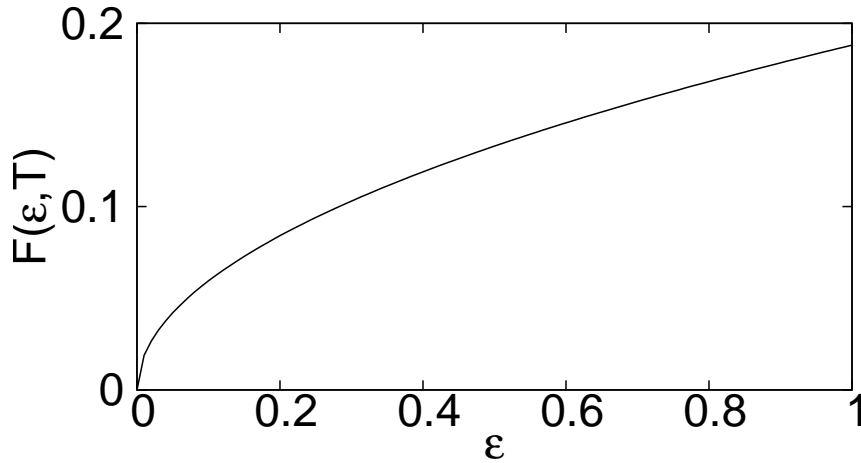The figure 2.8 shows the corresponding ion distribution function.

Figure 2.8: Distribution function $\tilde{\mathcal{F}}_{3,T}$ for $f(1) \approx 1.523$

(note that in cylindrical symmetry, the distribution function $\tilde{\mathcal{F}}_2(\varepsilon, \mathrm{T}) \propto \sqrt{\varepsilon}$ has the same profile).

Consequently, the reader can notice that the ion distribution functions $\mathcal{F}_n$, and thus the ion spectra $\frac{\mathrm{d}N_i}{\mathrm{d}E}$, have in both cylindrical and spherical symmetries an increasing trendline for each studied case. By fixing the radius or the time for spectrum calculations, one changes only the concavity of the profile. I should mention that this remark is not valid in planar symmetry as demonstrated in section C.2 in the appendix C.

In what has just been examined heretofore, I alternatively address the case under study either with a fixed radius defining the electron shell position or with a fixed time typical of the sudden restoring of the quasineutrality. A general statement would be to consider for the spectrum calculations a dependence in time *and* space, but this is beyond the scope of this manuscript.
As announced in the introduction of this chapter, the previous section results are mainly applicable when the ion explosion takes place while the laser pulse is still present, i.e. in absence of electrons. Moreover, it assumes a total electron depletion of the channel (sort of channel cavitation [55]). The next section deals with not-so-simple cases, for which the electron effects modify the ion dynamics and spectrum.

2.2   Ion response in non-simple cases

The non-simple cases denotes significant electronic effects on the ion energy distribution, so that both populations must be included in the treatment. Obviously, this cases occur when the ion evacuation time is longer than the pulse duration and when the laser pulse can drive sizeable plasma oscillations in its wake, resulting in strong wakefield influence. Less obvious, non-simple cases happen also when the laser ponderomotive force is not strong enough to expel completely the electrons from the plasma channel. In general, the study of the response in this regime requires the use of numerical particle codes in multiple dimensions. When neglecting the wakefield effects,i.e. with long laser pulses, these cases can be treated numerically by adopting a fast-running 1D-cylindrical ponderomotive model [50], or even analytically with use of model including thermal effects that modify the electronic distribution function (for instance an ergodic-kinetic model for analogue cluster explosions in Ref. [131]).

2.2.1   Laser wakefield effect

Laser wakefield excitation

It is well-known that an intense laser pulse can excite a plasma wave in its wake as the result of an interplay between on the one hand, the laser ponderomotive

force which separates the charges and creates a local space charge field, and on the other hand, the recoil force proportional the space charge which tends to restore the neutrality. That plasma wave consists in periodic density modulations of wavelength λ_{pe}. The associated electric field is termed the laser wakefield. The wakefield amplitude can grow non-linearly as the ponderomotive force increases into the relativistic regime [132] and become as a matter of fact an excellent candidate to accelerate electrons to high energies within few millimeters [133, 134].

However, the amplitude of such wave is limited by wavebreaking [135, 136] depicting the fact that the electrons trapped in the wave can be accelerated to the wave phase velocity and thus destroy its structures and eventually cause damping of the associated electric field. In the linear regime ($a_0 < 1$), the maximum amplitude E_p that the electric field can reach is obtained when all electrons oscillate at the plasma wave frequency [137]:

$$E_p \qquad = \frac{m_e c \omega_{pe}}{e} \qquad (2.35)$$

$$\rightarrow \quad E_p \, [\mathrm{GVm}^{-1}] \quad \simeq 96\sqrt{n_e \, [10^{18} \ \mathrm{cm}^{-3}]} \qquad (2.36)$$

In the nonlinear regime ($a_0 > 1$), the maximum amplitude of the field in a plasma wave can overshoot E_p. In one dimension, the wavebreaking field in a cold plasma is given by [138]:

$$E_W = E_0 \sqrt{2(\gamma_p - 1)} \qquad (2.37)$$

with γ_p the Lorentz factor of the plasma wave.
An analytical treatment of the wakefield excitation in the nonlinear regime is only possible in one dimension, usually satisfactory to tackle longitudinal electron wakefield acceleration [139]. For multidimensional studies, numerical tools (e.g. the codes WAKE [132, 140] or CALDER [121]) are required for quantitative predictions. In particular, their use can reveal 2D features of the wakefield (curvature [141], transverse wavebreaking [142]) of interest as far ion dynamics is concerned.

Resonance and wakefield structure

To be relevant for ion dynamics considerations, the wakefield should last for a sufficiently long time compared to the ion response timescale ω_{pi}^{-1} when it is of moderate potential compared to the repulsive Coulomb potential between ions [119], or can be shorter than ω_{pi}^{-1} provided it is intense enough. The general case with an ultrashort 35-fs laser pulse at relativistic intensities impinging on a plasma with $n_e \sim 10^{19}$ cm^{-3} lies between these two limit aspects. The first aspect concerns the resonance of the wakefield and the second one, its nonlinearity.

In the linear regime, the resonance can be seen by combining the electron fluid equations of conservation and the Poisson equation. For a small density

perturbation $\delta n = n - n_0 \ll 1$ and a given laser envelop $\hat{a}(r, z, t)$ (see (1.1)), the linearized and laser-cycle-averaged fluid equations lead to [139]

$$\left(\frac{\partial^2}{\partial t^2} + \omega_{pe}^2\right)\left(\frac{\delta n}{n_0}\right) = c^2 \frac{\nabla^2 \hat{a}^2}{4} \tag{2.38}$$

Clearly, the relationship (2.38) depicts a harmonic oscillator of eigenfrequency ω_{pe} driven by the term $c^2 \nabla^2 \hat{a}^2/4$ which is the laser ponderomotive force introduced in equation (1.31). The resonance of the plasma perturbation is thus produced by a ponderomotive force acting on a timescale close to $2\pi/\omega_{pe}$. This condition is easily fulfilled in theory with the ultrashort laser I used for the experiments with a plasma density close to $n_e \sim 1 \times 10^{19}$ cm^{-3}. This can be quantitatively demonstrated for instance within the quasistatic assumption in the laser frame coordinate, whereby all physical quantities are considered to vary slowly with time. First the term $\delta n/n_0$ can be replaced in (2.38) by the normalized electrostatic potential $\phi = e\Phi/(m_e c^2)$ using the Poisson equation.

$$\left(\frac{\partial^2}{\partial t^2} + \omega_{pe}^2\right)\phi = \omega_{pe}^2 \frac{\hat{a}^2}{4} \tag{2.39}$$

Then, with the variable changes $(z, t) \to (\xi = z - v_g t, \tau = t)$, the first and second derivative $\delta/\delta\tau$ and $\delta^2/\delta\tau^2$ are neglected with regard to $\delta/\delta\xi$ in the equation of the potential. One obtains afterwards the usual equation describing the excitation of plasma wave by a laser envelop:

$$\left(\frac{\partial^2}{\partial \xi^2} + k_{pe}^2\right)\phi = k_{pe}^2 \frac{\hat{a}^2(\xi)}{4} \tag{2.40}$$

To understand how a resonant wakefield can impact the ion dynamics, equation (2.40) must be solved to extract the longitudinal and radial fields. For a gaussian envelop (see $\hat{a}(z, r, t)$ in (1.1)) , a solution for the normalized potential vanishing ahead of the pulse ($\xi \to \infty$) was extracted in Ref. [143]:

$$\phi = -\sqrt{\pi}a_0^2 \frac{k_{pe}L}{4} e^{-k_{pe}^2 L^2} e^{-2r^2/w_0^2} \sin(k_{pe}\xi) \tag{2.41}$$

with $L = c\tau/(2\sqrt{\ln(2)})$. Then, the longitudinal and radial electric fields take the form:

$$E_z = -\frac{\partial \Phi}{\partial \xi} = E_p \sqrt{\pi}a_0^2 \frac{k_{pe}L}{4} e^{-k_{pe}^2 L^2/4} e^{-2r^2/w_0^2} \cos(k_{pe}\xi) \tag{2.42}$$

$$E_r = -\frac{\partial \Phi}{\partial r} = -E_p \sqrt{\pi}a_0^2 \frac{Lr}{w_0^2} e^{-k_{pe}^2 L^2/4} e^{-2r^2/w_0^2} \sin(k_{pe}\xi) \tag{2.43}$$

At a given r position, one can note that the mean electric field is null, so that a planar wakefield does not affect the net particle motions. This goes otherwise when a gradient exist, as in real cases with a finite gaussian-like pulse profile, since

a ponderomotive wakefield force proportional to ∇E^2 and non-null in average can operate. In particular, at a given ξ position, the radial field is zero on axis and take its maximum at the radius $r = w_0/\sqrt{2}$. Therefore, the ponderomotive radial action of the wakefield proportional to ∇E_r^2 and *independent* upon the charge, will expel the particles from the cylinder of radius $w_0/\sqrt{2}$, thus forming an annular wake channel. Moreover, one can notice that E_r is dependent upon the pulse duration via L and the pulse radius via w_0. In this respect, following Andreev *et al.* [129], Gorbunov *et al.* showed analytically in the linear regime [119] that a laser pulse of both durations and radius as narrow as λ_{pe} can excite a strong wakefield of the same radial extent, that, when resonant and sustained over several plasma periods, can significantly kick ions radially and pinch in particular some of them into a central filament.

Thus, if the plasma is underdense, with $\omega_{pe} \ll \omega_L$, the particle code WAKE can be used to visualize the wakefield structure in an axisymmetry geometry. The figure 2.9 illustrates a resonant wakefield in the wake of a 35-fs ultrashort pulse (the code calculates the pseudo potential $\Psi = \phi - a_z$, more convenient for the extraction of the longitudinal electric field $E_z = \frac{\partial \Psi}{\partial \xi}$). The use of the code instead of readily plotting the equations (2.42) enables to appreciate a linear effect due to the transverse plasma inhomogeneity causing dephasing and the progressive wake-front curvature (see at $z - ct = 160$ μm) [129].
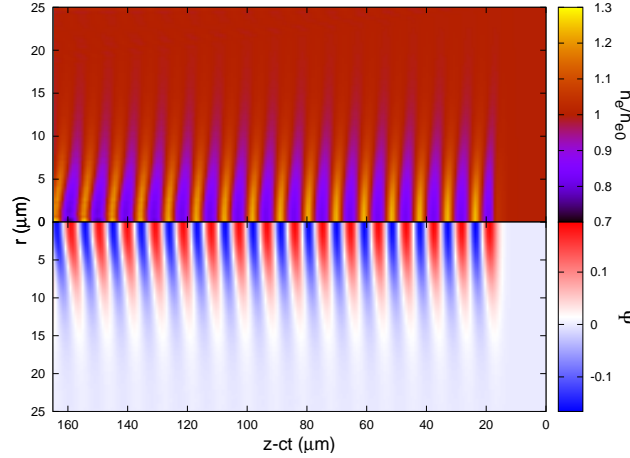
Figure 2.9: WAKE simulations illustrating a resonant plasma oscillations and wakefield in the wake of an ultrashort relativistic pulse after 200 fs of propagation ($n_e = 1.3 \times 10^{19}$ cm^{-3} ($2\pi/\omega_{pe} \sim 31$ fs), $\tau_L = 34$ fs, $a_0 = 0.7$). The laser is pulse is at $z - ct = 10$ μm. The top panel shows the electron density normalized to the the initial density. The bottom panel plots the wakefield potential. The bending of the wavefront is a precursor of the wavebreaking [141]

In the nonlinear regime which applies to the experiments I carried out, similar qualitative conclusions can be drawn, though an early wavebreaking can hinder

the development of a long resonant train of plasma modulations. In that case, ion pushing arises from the fact that the wake-wave becomes highly nonlinear and can support strong fields before wave-breaking (see (2.37)). In the very following, I propose to illustrate numerically the effects of a_0 and laser radius on the ion dynamics in the 2D axisymmetrical geometry using the code WAKE.

The figure 2.10 plots the wakefield excited by an ultrashort gaussian pulse for different a_0 parameters. As a_0 is increased from 0.8 to 2, i.e. from the linear to
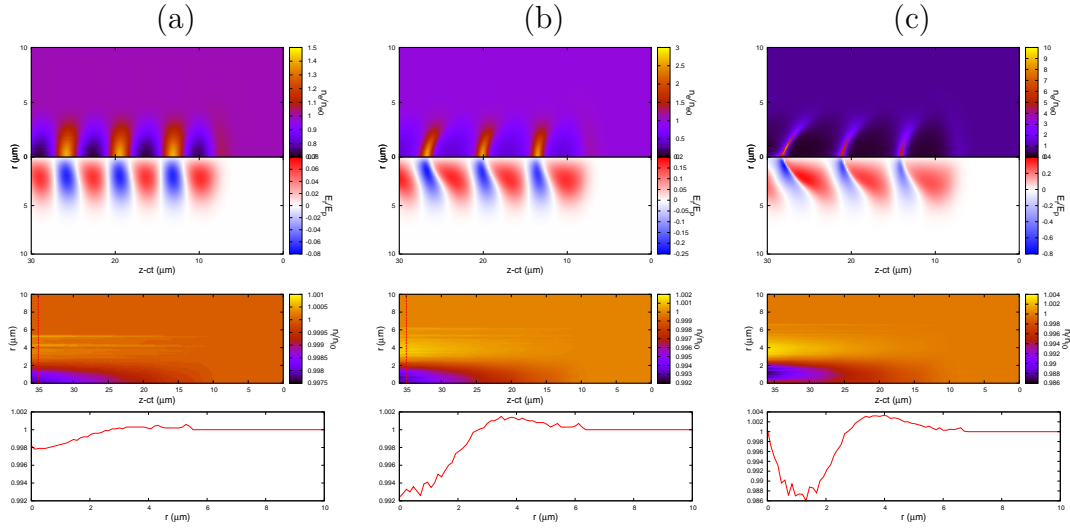

Figure 2.10: (Up) normalized electron density and radial electric field, and (bottom) normalized ion density in the wake of a 35-fs pulse of radius $r/\lambda_{pe} = 0.64$ ($r = 7$ μm) with $n_e = 1 \times 10^{19}$ cm^{-3} and (a) a_0=0.8,(b) $a_0 = 1.4$, (c) $a_0 = 2$. In the bottom row, lineouts are taken along dashed lines

moderately nonlinear regime, the plasma modulations and the electric field start to bend in space as a result of a longer (nonlinear) plasma wavelength near the axis $\lambda_{Npe}(r)$, where the laser field is the strongest, than far from the axis (at that position $\lambda_{Npe}(r) \approx \lambda_{pe}$, the linear plasma wavelength[4]) [141, 144]. For $a_0 = 2$ on the top panel (c), the curvature is seen to increase deeper in the wake because of the increase of the dephasing between the centre and the edge of the wave. When that curvature reaches a critical value, transverse wavebreaking results from electron trajectory crossing in the transverse direction. Figure 2.11 illustrates that point on the basis of a 1D-nonlinear picture proposed by Bulanov et al. [142]. When the electrons start to oscillate over several wavefronts in the transverse direction, transverse wavebreaking occurs as a consequence of the destruction of the wave structure (dephasing is then equal to $2\pi c/\lambda_{pe}$).

---

[4]in the linear regime, the presence of transverse plasma inhomogeneity is enough to bend the wakefield phase front [129]
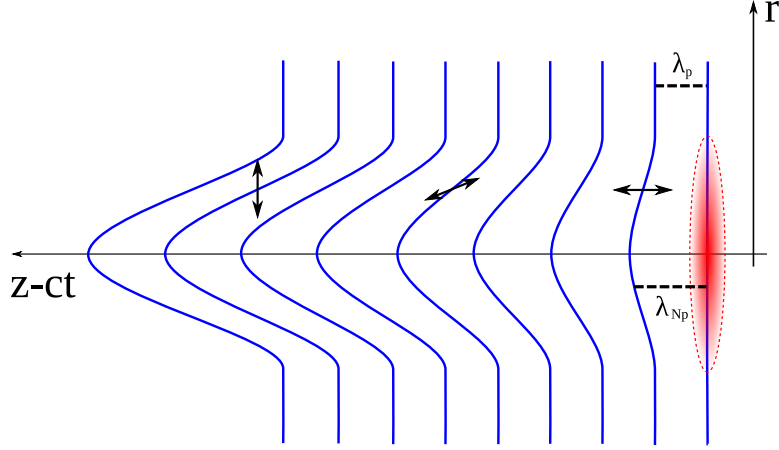
Figure 2.11: 1D picture of the transverse wavebreaking in the nonlinear regime. The red dotted line mimics the gaussian pulse propagating towards the right, the blue lines represent the plasma wavefronts in the laser wake. λ_p and λ_{Np} are respectively the linear and nonlinear wavelengths. The black arrows indicate the electrons oscillation direction in the wave

In this quasistatic approximation, for a square pulse depending only on the comoving variable $\xi = z - ct$, the nonlinear wavelength can be analytically calculated behind the pulse [144–146]. In the limit of a quasi-relativistic plasma wave, the normalized wake potential ϕ is found to be within the range $\phi_{\min} \leq \phi \leq \phi_{\max}$, so that:

$$\frac{\lambda_{Npe}}{\lambda_{pe}} = \frac{2}{\pi}\sqrt{1 + \phi_{\max}} \cdot E_2(k) \tag{2.44}$$

$$\text{with} \quad E_2(k) = \int_0^{\pi/2} d\theta \sqrt{1 - k^2 \sin^2 \theta} \tag{2.45}$$

$$\text{and} \quad k = \sqrt{1 - \frac{1}{(1 + \phi_{\max})^2}} \tag{2.46}$$

Figure 2.12 plots the dependence of the wavelength against the maximum potential.

In particular, for $\phi_{\max} \geq 9$, the nonlinear wavelength becomes twice as big as the linear one. This can be taken as a useful criterion for the transverse wavebreaking threshold right after the first wake period (see also subsection 3.4.3 in chapter 3 for a discussion about this point).

Beneath the wavebreaking threshold, the increase of the curvature of the electron modulation is associated to the accumulation of electrons near the axis and to a growth of the radial electric field. Interestingly, that field is quasi-sinusoidal at $a_0 = 0.8$ and its mean value over a plasma oscillations is close to zero (see please the color map and the corresponding colorscale). On the contrary for $a_0 = 2$, the radial electric field has a "sawtooth"-shape and its mean value is negative. For that case, the consequence on the ion dynamics can be appreciated in the bottom
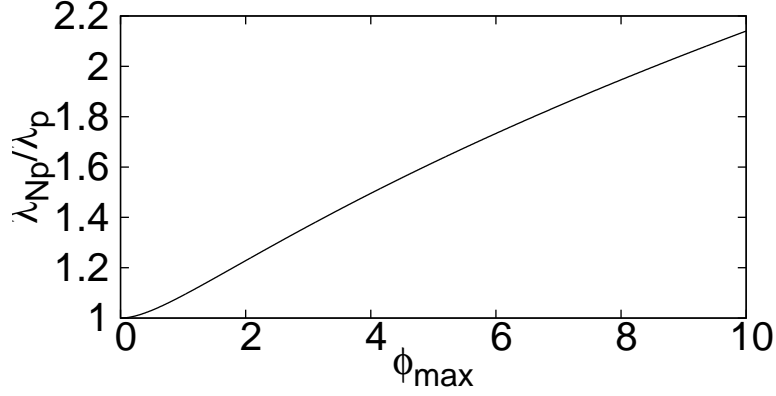
Figure 2.12: Nonlinear plasma wavelength versus the normalized maximum wake-field potential in the quasistatic approximation

panel (c) where an annular channel with an on-axis filament has been formed only after three plasma period, what is not observed at lower a_0. One can add that in the nonlinear case, since the cycle-averaged radial electric field is no more null, the wakefield force acting on the ions is not of ponderomotive nature strictly speaking. Thus, the particle drift is not secular and the acceleration is more efficient.

Inversely, a_0 can be fixed and the laser radius varied to show the importance of that parameter for exciting a sizeable wakefield. This point is illustrated in figure 2.13. For a radius greater than λ_{pe}, the wavefront curvature is observed from
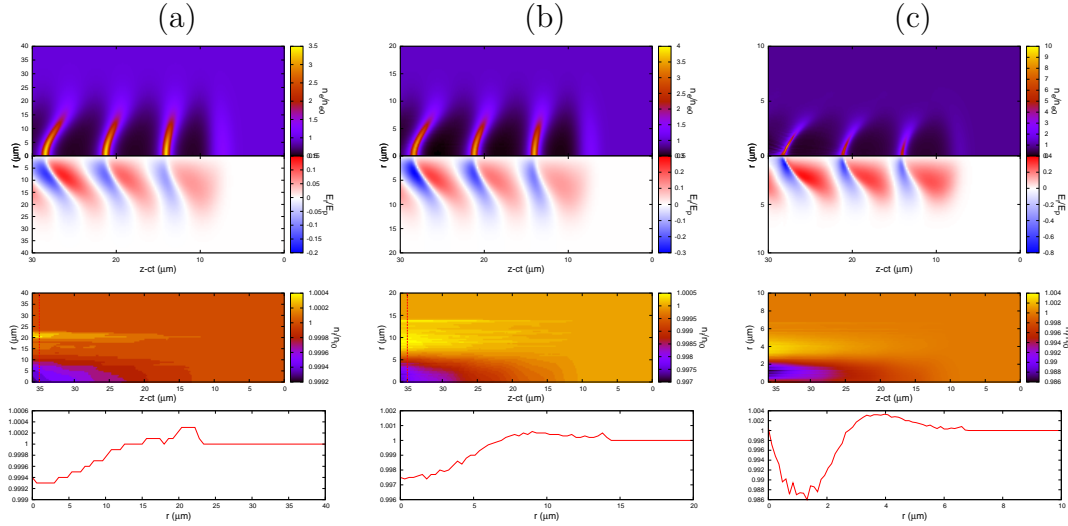

Figure 2.13:   (Up) normalized electron density and radial electric field, and (bottom) normalized ion density in the wake of a 35-fs pulse with $a_0 = 2$, $n_e = 1 \times 10^{19}$ cm^{-3} and (a)$r/\lambda_{pe} = 16$ ($r = 34$ μm)
, (b) $r/\lambda_{pe} = 1.6$ ($r = 17$ μm), (c) $r/\lambda_{pe} = 0.64$ ($r = 7$ μm). In the bottom row, lineouts are taken along dashed lines

top panels (a) and (b) to increase as $z - ct$ increases, but the resulting gradients in density and field remain smaller than for radius smaller than λ_{pe} in top panel (c). Consequently, for large radii, the ion dynamic is not dramatic and in particular no ion central filament is formed within the window of observation (see bottom panels (a),(b) as compared to (c)). This fact is of experimental interest as the efficient coupling of a laser gaussian pulse with a gas jet imposes to have smooth focusing with a Rayleigh range greater than the jet gradient scale length. This determines a minimum focal spot radius to be used safely. In practice, $r/\lambda_{pe} \simeq 1$. As a matter of fact, the excitation of a wakefield relevant for ion dynamics studies needs to benefit from at least moderate self-focusing of a pulse at relativistic intensities ($a_0 > 1$) in the plasma gradient [147].

Finally, it is interesting to examine the energy that ions gain in the nonlinear regime when they move radially within the same small temporal window used for the WAKE runs. The following figure 2.14 addresses this point. As said just before,
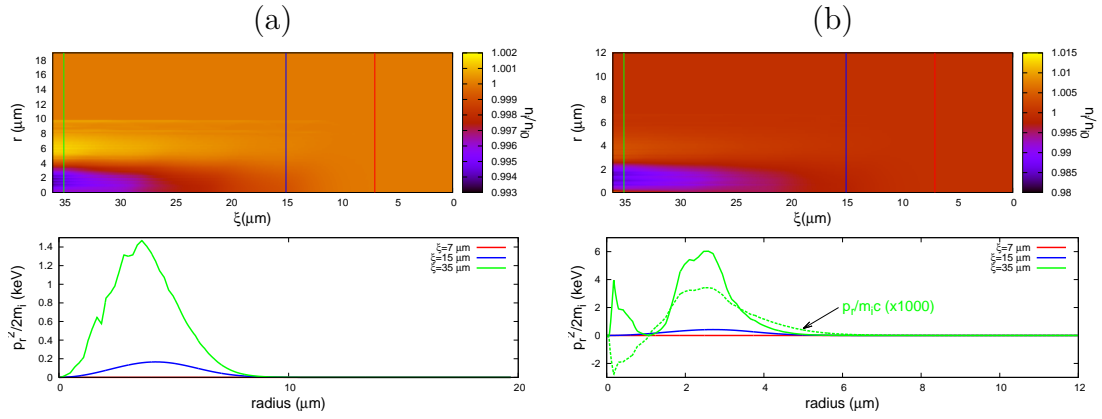
Figure 2.14: Ion radial kinetic energy obtained with $n_e = 1 \times 10^{19}$ cm^{-3} and a 35-fs laser pulse with $a_0 = 2$ for different laser pulse radii (a) $r/\lambda_{pe} = 1$ ($r = 11$ μm) , (b) $r/\lambda_{pe} = 0.64$ ($r = 7$ μm). (Up) normalized ion density in the laser wake. (Bottom) Ion radial kinetic energy in the planes indicated by the color lineouts in the upper panel.

within that small temporal window, only the laser pulse tightly focused below λ_{pe} excites a wakefield of sufficient strength to pinch ion centrally (see top panel (a) as opposed to top panel (b)). In bottom panel (b), the momentum in dashed green line exhibits negative values indicative of that pinching. The maximum kinetic energy is obtained in the green plane, at about three plasma periods from the laser pulse. This energy is modest, on the order of few keV (peak at 6 keV). This shows that an ultrashort pulse similar to that used in our experiments (see section 3.3 in the experimental chapter 3) does not transfer significant momentum to ions, as the product $\tau_L \omega_{pi}$ is quite small for that plasma density. Furthermore, one can calculate the radial energy that would be gained by ions when the ultrashort

laser creates a positively charged cavity depleted from electrons (very nonlinear case with $a_0 \gg 1$). When assuming a 35-fs pulse of radius $r = 10~\mu$m, the ion cavity looks rather spherical in the moving window coordinates. Thus, I can apply the equation (2.32b) to obtain the maximum energy from Coulomb explosion of the cavity at $\mathrm{T} = t\omega_{pi} \sim 0.1$, i.e after about 50 fs of expansion. I get an energy of 4 keV, on the same order as WAKE results (from this model, the maximum energy is about 6 MeV and reachable after few tens of ω_{pi}^{-1}). Finally, the radial distribution of the kinetic energy exhibits a bell shape which is forewarning of the formation of a shock at later time. This particular aspect will be addressed right after in the case of the central filament, but the conclusion are more general and applicable to whole channel.

The striking signature of the wakefield effect on the ion dynamics is the formation of an ion central filament. In a recent paper, Popov *et al.* evidenced in the blow-out regime the formation of a central ion filament due to the electrostatic effect of trapped electrons [51]. In this case, the filament is compressed by a factor of 40 above the unperturbed initial ion density and eventually Coulomb explodes as the electrons cannot shield the positive charge density out. Such compression of the central filament by the radial electric field of the wakefield leading to CE was also observed in our numerical pre-studies (see subsection 1.3.1). As it is expected to happen in experiments, I now investigate this explosion with an electrostatic model and calculate the spectrum that can subsequently be obtained.

2.2.2   CE of the central filament

Time-limited spectrum

The spectrum calculation for the CE of the filament could be formally obtained by taking the case of section 2.1.1 with $r \to \infty$. This assumption is indeed not unreasonable, since the filament has in practice, before explosion, a dimension much smaller than the laser radius. However, as mentioned hereinbefore, this limit is non-physical in the cylindrical symmetry. Thus, for the unity of the analysis, I shall then consider the spectrum formation is time-limited in both symmetries. Then, by considering the characteristic R_0 of the filament, the distribution functions can be obtained with the equations (2.34) (with the same reduced notations):

$$\text{for } n = 2, \quad \mathcal{F}_2(\varepsilon, \mathrm{T}) \;=\; \frac{\sqrt{\varepsilon}}{2\left[(\ln(Z(\mathrm{T})))\right]^{\frac{3}{2}}} \tag{2.47a}$$

$$\text{for } n = 3, \quad \mathcal{F}_3(\varepsilon, \mathrm{T}) \;=\; \frac{\sqrt{\varepsilon}}{2\left[\left(1 - \dfrac{1}{Z(\mathrm{T})}\right)\right]^{\frac{3}{2}}} \tag{2.47b}$$

For the spherical symmetry, one can notice:

$$\mathcal{F}_{3,\infty} = \lim_{T \to \infty} \mathcal{F}_{3,T} = \frac{\sqrt{\varepsilon}}{2} \tag{2.48}$$

The same limit distribution is obtained by doing $r \to \infty$ in (2.3b) for the case with the neutralizing electron shell (section 2.1.1). Physically, this means that the ions can reach their final kinetic energies before arriving at the shell (in practice, the energy varies little from $T \sim 10$, see figure 2.7).

Non uniform distribution: shock formation

All precedent developments were made mainly with uniform ion density profiles. I previously said that this assumption ensures that the particles never intersect each other during the explosion (NCHA). This point was demonstrated by Kaplan *et al.* [148] in spherical symmetry for cluster CE. The following illustrates in details this point starting from equation (2.26). I adopt the model proposed by Kaplan *et al.* in [148] for the charge distribution Q_3:

$$Q_3(X_0) = \frac{X_0^3}{(1 + X_0^{3\mu})^{\frac{1}{\mu}}} \tag{2.49}$$

where μ is a numerical variable in $[1/3, \infty]$. For a uniform (steep) profile, $\mu = \infty$. In (2.27), I took for example $\mu = 1$ to show how the expansion factor Z can be affected by a non uniform profile. The numerical resolution of (2.26) give access to the time-resolved ion positions in both cases. From figure 2.15, one can notice the
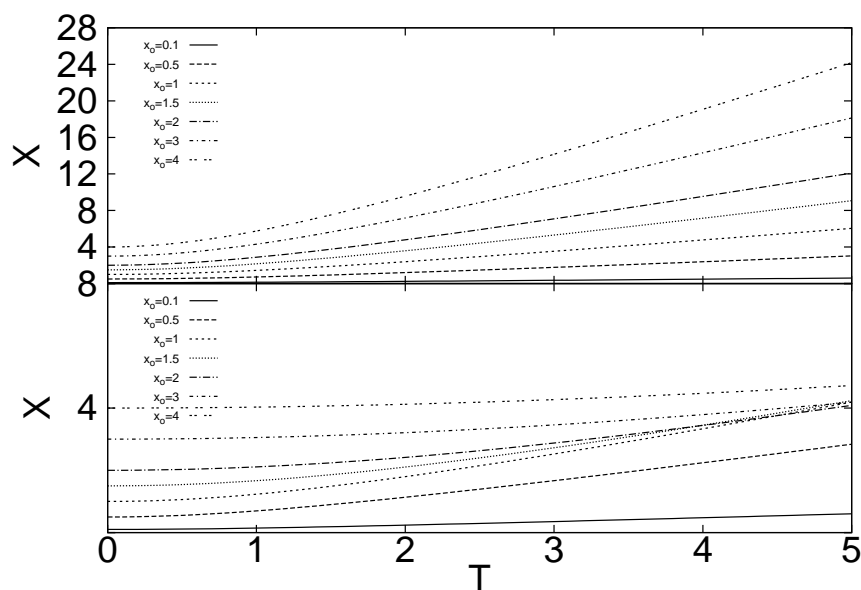

Figure 2.15: Ion positions versus time for different initial position. (Top) Uniform density distribution $\mu = \infty$. (Bottom) Non uniform density distribution ($\mu = 1$)

ion crossing in the non uniform case occurring at T $\sim$ 3.8. For that case, this time corresponds to the formation of an ion shock, the amplitude of which depends upon the initial gradient profile. Mathematically, this amplitude is tuned by the μ coefficient (stiffness coefficient) and its effects can be appreciated in figure 2.16.
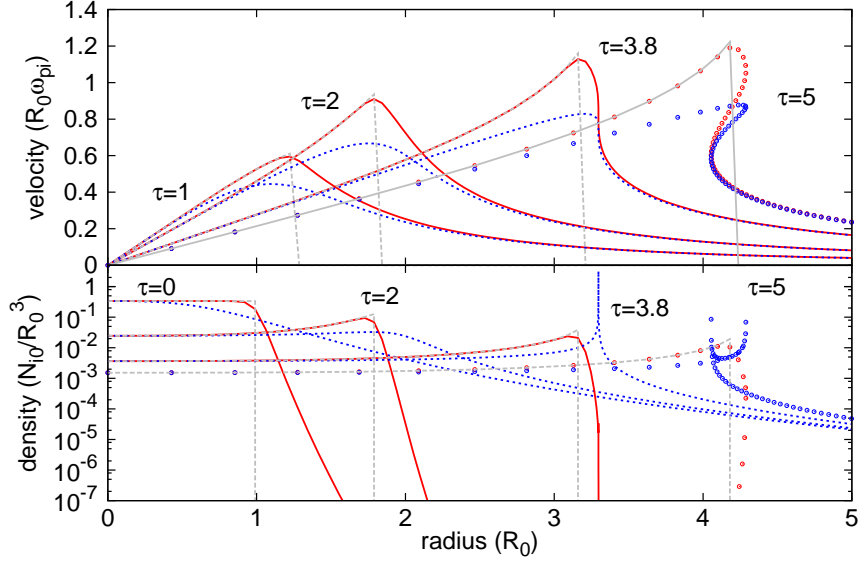

Figure 2.16: Ion velocity and density versus position during the CE for different reduced time τ in the NCHA. The colors stand for: dashed blue line: $\mu = 1$, solid red line : $\mu = 10$, dashed grey line: $\mu = \infty$. Empty-dotted lines are used when the ions have crossed each other (for $\tau \geq 3.8$)

As discussed by Kaplan *et al.*, the role of the non uniformity is independent upon the chosen model. It suffices that a gradient exists to generate such a shock. The same conclusion has been drawn afterwards by other authors in the context of laser ion acceleration from solid target and the shock due an initial gradient is termed there ion wavebreaking [81, 89]. Also in [96], the same type of shock is formed in the skin depth of a thin foil bored by an intense laser pulse and it accelerates bulk ions bouncing off the surface. After the shock time, the equation (2.19) is invalid and the implicit formulation (2.26) incorrect. One should then have recourse to a basic particle code to study late expansions.

Simple particle model

I wrote a simple particle code for spherical cases solving the issue of particle crossing by following the recommendations of Kaplan *et al.*. Basically, it numerically solves the equation (2.26) by recalculating at each time step the distribution $Q_3(X) \neq Q_3(X_0)$ corresponding to the total number of charges within the sphere

of radius X[5]. In this condition, even if the crossing occurs, the particle beyond
the shock will continue to be pushed by the correct cumulated charge. Figure
2.17 presents the results of the same calculation as in figure 2.16 and brought
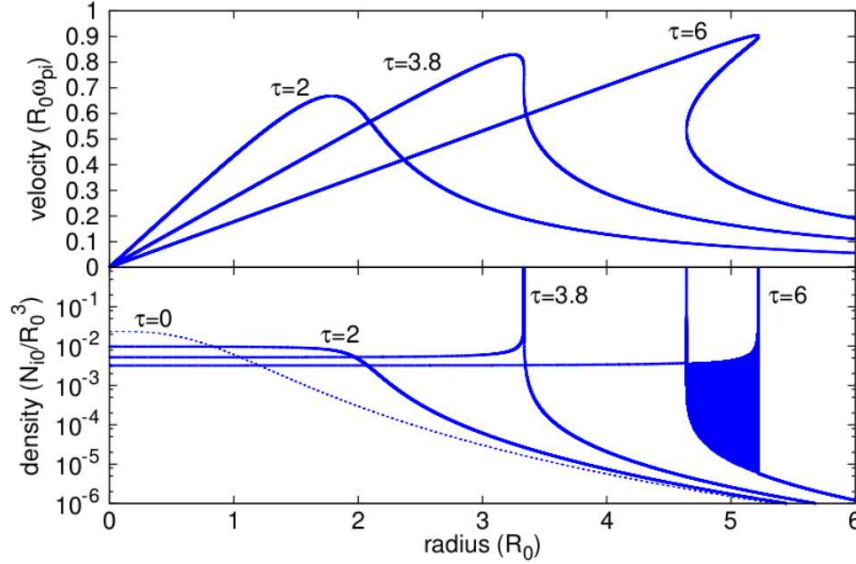further in time. The overtaking happens at the same moment as in the previous

Figure 2.17: Ion velocity and density versus position during the CE for different
reduced time τ with $\mu = 1$. After the crossing of the ions (ion wavebreaking at
$\tau \approx 3.8$), the density profile presents a shock shell (blue region) between two
peaks moving at different velocities (caustics)

section, which is normal since the hydrodynamic approach stays valid until that
moment. Afterwards, two distinct ion peaks (called caustics in [149]) moving at
different velocities appear at positions where the velocity exhibits vertical tangents
in the phase space (top panel). This is due to the complex ion distribution in
the region between the peaks (blue region), called the shock shell, where the
velocity is trivalued. Because of the horizontal tangent in the phase space (see top
panel in figure 2.17), the ion spectrum presents a singularity located at the cutoff
and the global spectrum is like plots in figure 2.4. In [48, 148], special attention
is paid to this extending shell within the context of large-cluster CE, as it can
host energetic ion-ion collisions from the mix of velocities over the cluster size.
Therefore, high-yield nuclear fusion reactions were predicted [148] and methods
for their implementing using ultrashort lasers proposed [48, 131].

The previous conclusions were obtained in the linear or slightly nonlinear regime
assuming cold fluid behaviour of the plasma in a quasistatic approximation and

---

[5]I did it by rearranging the particles according to their positions at the considered time step
and then summing the charge until radius X

the electrostatic evolution of the central filament compressed by the wakefield. The reported phenomena can in fact be generalized by using Particle-In-Cell (PIC) codes for a kinetic treatment in a multiple dimensions. The radial ion expansion in the wake of a short laser pulse is now quantitatively investigated.

2.2.3 Radial ion expansion by the wakefield from PIC code

Several simulation runs were carried out by Agustin Lifshitz by using the quasi-axisymmetrical geometry code CALDER CIRC [150] in order to predict the ion spectrum at late instants of the interaction. In particular, this tool enables to consider kinetic effects due to the particle crossing (contrary to the electrostatic developments in section 2.1), to the wavebreaking (contrary to the code WAKE) and also to the sheath existing at the interface between the plasma and the neutral gas, capable of accelerating particles. Figure 2.18 presents the most general sketch of the entities relevant for ion acceleration in our conditions. The channel is typically of 10 μm radius while the overall plasma at our working intensity is about 100 μm.
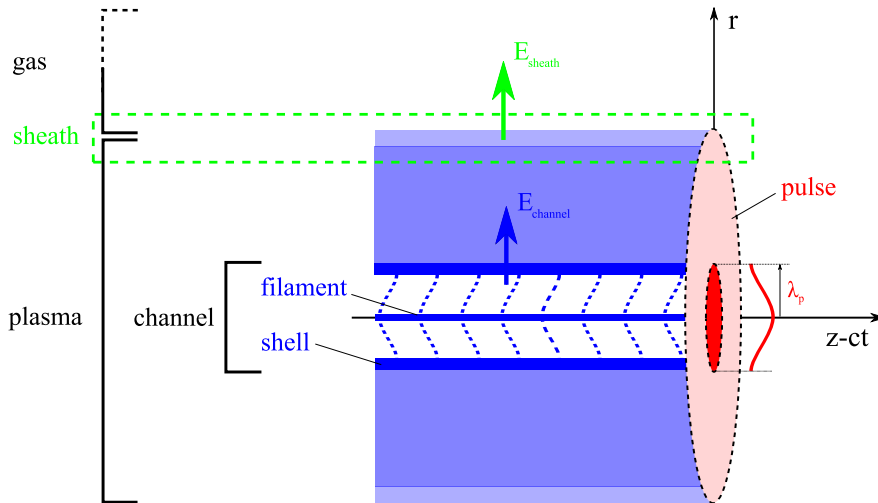
Figure 2.18: Schematic of the two main accelerating plasma structures in the laser wake: the plasma channel at low radius, the sheath at large radius. The dashed lines map out the density modulations at early moments due to the wakefield

Plasma channel formation in time

To understand the phenomena and to fasten the calculations, a small plasma slab of 50 μm thickness and 0.005% n_c density was first used for the interaction with a gaussian ultrashort relativistic pulse similar to the one produced in "Salle Jaune" (see section 3.4). Relevant density maps depicting the plasma evolution in the vicinity of the channel are presented in figure 2.19, the pulse being incident

from the left of the pictures. In panel (a), the intense pulse excites at early

(a)   (b)

(c)   (d)

Figure 2.19: Temporal evolution of plasma electron and ion density map near the laser propagation axis. The laser pulse propagates towards the right. (a) and (b): electron density at t=300 fs and t=800 fs. (c) and (d) ion density at t=800 fs and t=4 ps

moments a nonlinear plasma wave in its wake, creating a train of bubble-like and positively-charged cavities where electrons are almost absent. The electron depletion indicates 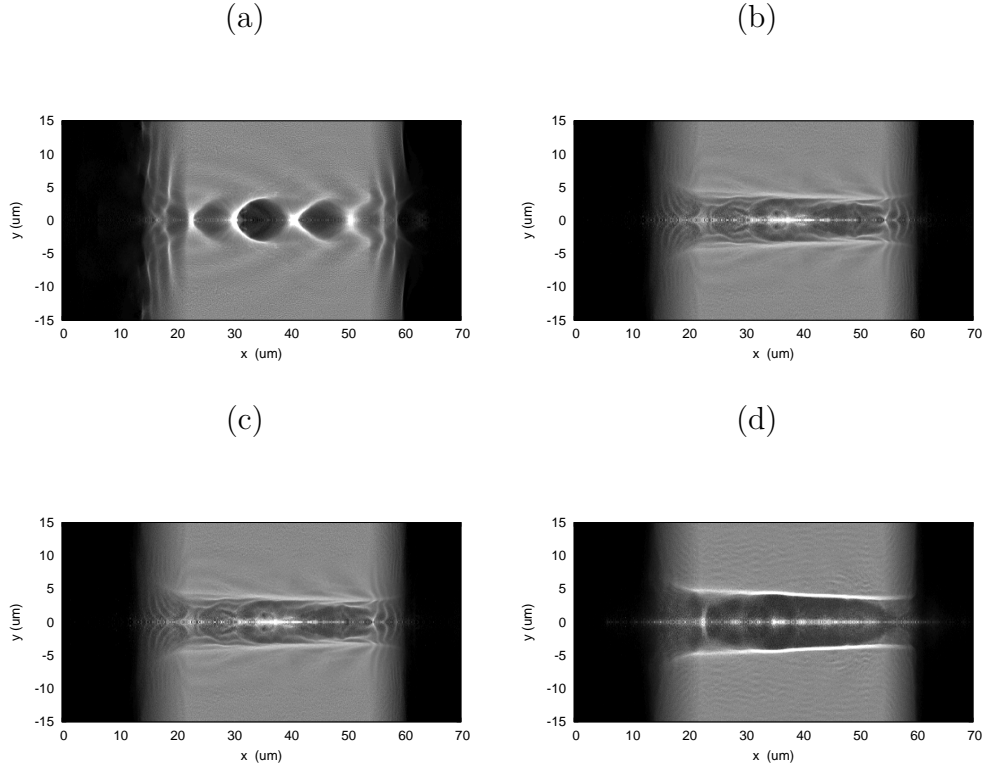the presence of a strong wakefield (see also similar WAKE maps in figures 2.10 and 2.13). After 800 fs, the plasma has started to reorganise in a channel composed of a shell and filament (panel (b)). At that time, electron and ion maps are very similar (confront panel (b) and (c)), as light electrons flow around the heavy ions to restore the quasineutrality when the wakefield decays. At a later time ~ 4 ps, a clear annular channel can be seen in the ion map in panel (d), with a strongly pinched central filament and a dense shell. One can notice in panel (d) that the channel has a longitudinal density modulation (clearly see for the filament). This is at the origin of the modulations that can be observed in the ion spectrum in the transverse direction. This point will be addressed later on. The channel structures results essentially from the effect of the wakefield on the ions as presented in the following.

Spatio-temporal dependence of the wakefield

The following figures show the evolution of the radial electric field at early moments felt by the ions initially located at different transverse position in a given longitudinal plane where the filament and the shell are well defined.
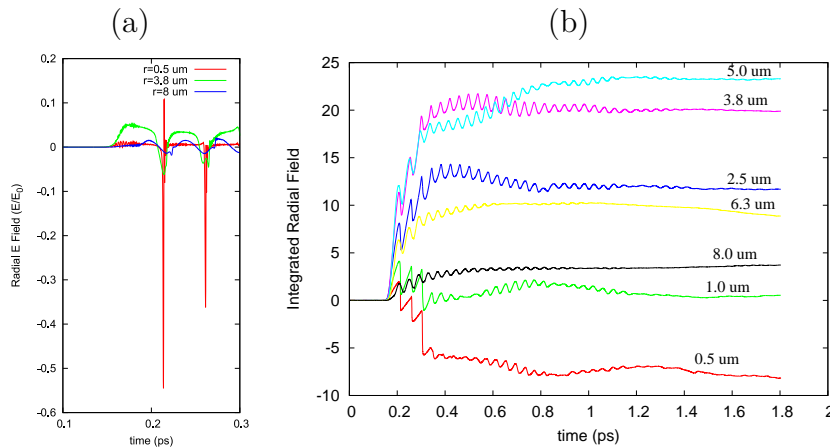

Figure 2.20: Temporal evolution of radial electric field and its integrated value at different radii about the laser propagation axis.

The laser enters that plane about 160 fs after the beginning of the simulation. Figure 2.20, panel (a) plots the radial field for the first 150 fs of the interaction for three different radii (r=0.5 (red), 3.8 (green) and 8 (blue) μm). Close to the axis (red line), the radial field is quite weak over the first 60 fs and presents strong negative peaks afterwards. The instants of these peaks corresponds to the time that the back of a bucket of the wakefield crosses the plane under study. This wakefield is negative in average over several cycles, as shown in panel (b) for a longer timespan and is responsible for the formation of the central filament. At r=3.8 μm (green line in panel (a) and pink in panel (b)), the wakefield is positive in average and radially expels ions contributing to the formation of the dense shell. At a larger radius r=8 μm, the radial wakefield is the weakest and has a quasi-null average value, without a significant effect on the charge populations. As said in the previous section, it is apparent from this figure, that the nonlinear wakefield exerts on charges an accelerating force which is not of ponderomotive nature when the near-axis positions are considered.

Spectral modulations

The ion acceleration is diagnosed in the simulation by examination of the distribution in the phase space. The figure 2.21 shows the output of that diagnostics when two different angle filters are applied in that space (a wide filter collecting all angles in fact and a filter selecting ions at $90° \pm 10$ mrad from the laser axis). The filter plays a role in our case in selecting the direction of acceleration. For

a transverse acceleration, a 90°-filter is then applied, with additionally a small angular tolerance of 10 mrad to mimic the aperture of a detector that would be along the normal to the laser propagation direction in the laboratory (in our experiments, the solid angle of the detector was 1.2×10^{-8} sr). Comparisons
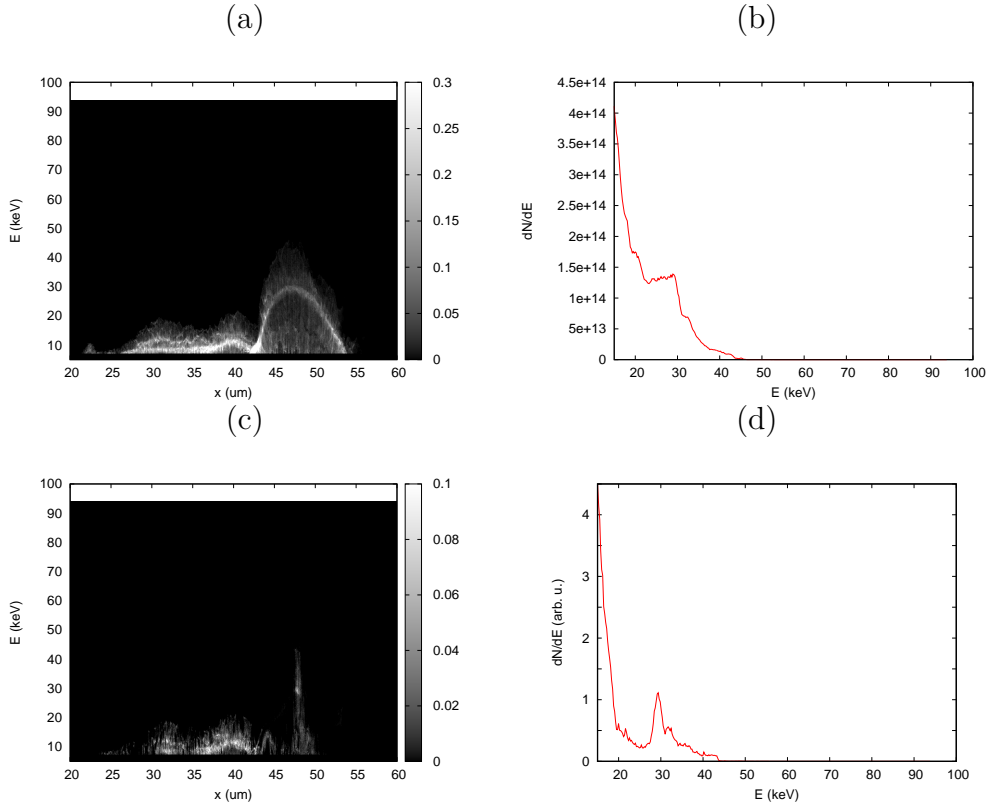
Figure 2.21: Ion spectrum detection depending on the angle of collection. All angles collected: (a) phase space (energy versus longitudinal position) and (b) spectrum. 90° collection: (c) phase space (energy versus longitudinal position) and (d) spectrum

between the case with all angles and that with only a tiny pencil beam around the normal shows clear differences in terms of spectrum. First, in both panels (a) and (c), the maximum energy varies longitudinally, because the propagating laser field and thus, the wakefield amplitude vary along that direction. Moreover, bright and dark small regions in the maps can be observed. This indicates an inhomogeneity of the phase space (more pronounced when the 90°-filter is applied), meaning that ion acceleration originates in fact from discrete foci of variable efficiency. The consequence of the presence of singularities instead of a continuum becomes obvious when spectra are considered with and without the filter. When all angles are collected, the singularities in the phase space overlap, so that irregularities in the spectrum wash out into a maxwellian-like shape with a kind of short plateau between 20 and 30 keV in panel (b). This plateau corresponds to the

lobe observable in panel (a) for $x = 45 - 50$ μm. When the 90°-filter is applied, a sharp peak appears at 30 keV in panel (d), and is related to the peak in panel (c) at $x \simeq 48$ μm. In fact, in that case, the filter is thin enough to resolve a single acceleration focus and interestingly, the spectral distribution from that focus resembles that calculated in section 2.1.1 for a pure CE (see figure 2.4). Qualitatively, this type of peaked spectrum were obtained in our experiments (see subsection 3.4.4). I will address later in the experimental part a case with a higher plasma density where, even when applying the same filter, the overlapping cannot be avoided, so that the spectra appear maxwellian. I now present the late evolution of the ions as observed in a more complete view with a larger simulation revealing in particular an accelerating sheath effect.

Long run: shock and sheath effects

The previous description was using a small plasma to quickly confirm the dominant accelerating effect of the wakefield on the ions. However, one can expect that the accelerated ion bunches will experience other effects, notably because shocks could happen when inner ions overtake outer ones in presence of a density gradient as explained in the subsection 2.2.2 for the case of the central filament. Moreover, for quantitative comparisons with experimental data, the laser propagation should be well described. Therefore, one long run was carried out in the experimental conditions over tens of picoseconds and with a plasma of 700 μm FWHM similar to jets I used. Figure 2.22 shows the density map at about 4 ps after the onset of the interaction. As in the small plasma case, the channel
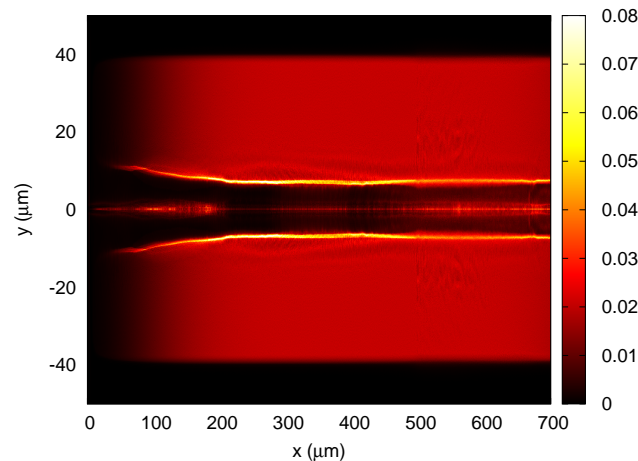

Figure 2.22: Ion density map in unit of n_c at about 4 ps after the laser entered the plasma on the left side of the box

exhibits a central filament and a shell. In this case, the wakefield amplitude varies more significantly from laser self-focuses and longitudinal channel modulations can be cleanly appreciated. Similarly, the acceleration evolution can be monitored

in time for ions at given channel plane initially localized at different positions in the transverse direction. Figure 2.23 represents the radial trajectories and the energy gained by these ions.
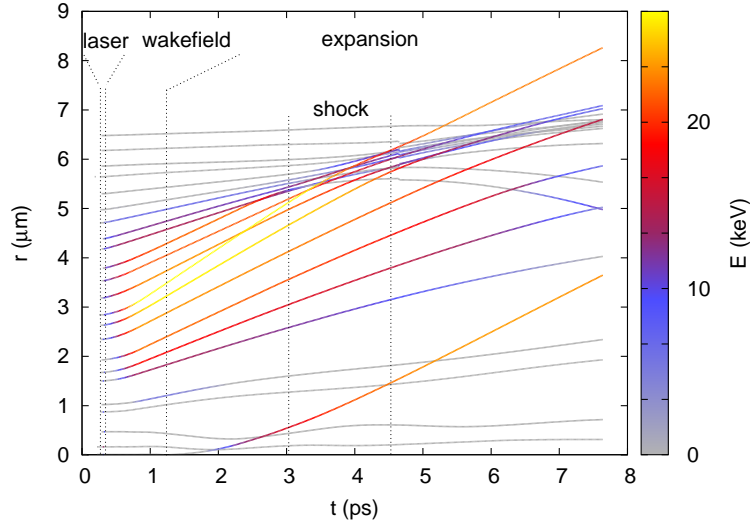

Figure 2.23: Time-resolved radial trajectories of ions from the channel at different initial positions in the transverse direction. Each trajectory has a color scaling with the energy gained in time. Ions from the filament Coulomb explode at 1.5 ps. A shock with the ions from the shell develops around 4 ps

In that figure, one can again notice that ions, irrespective of their initial positions, gain their momenta during the wakefield lifetime, until about 1.2 ps, and then expand differently. Ions from the central filament are first compressed by the wakefield (here, the dominant contribution with regard to that of injected electrons) and then explodes when it has significantly decayed at 1.5 ps. Ions from the shell (initially at r=$2.5 - 4.5$ μm) are accelerated outwardly by the wakefield until 1.2 ps and are quasi-ballistic until 3 ps when the shock starts to form. The shock slows down all ions but some of them with high incident momenta are re-accelerated outwards, while others with lower incident momenta reflect off the shock and back to the laser axis. The effect of the shock on the overall spectrum can be appreciated in figure 2.24. The spectrum is obtained by filtering the phase space at 90° in the same tight manner as previously for the small runs. The shock is seen to shift the peak down to lower energies. A small fraction of ions are accelerated by the shock to a higher energy than before the shock and they form at 5 ps when the spectrum stabilizes a long trail extending up to 35 keV. Also, the peak is affected by the shock, as it increases the energy spread. Consequently, the effect of the shock is to contribute to the slowing down and the explosion of the ion bunch constituting the main peak. Note that the radial size of the mesh used in the simulations ($\Delta r = 0.19$ μm) is in fact too large to resolve the shock front close to the explosion, and therefore post shock spectra could not be very realistic.
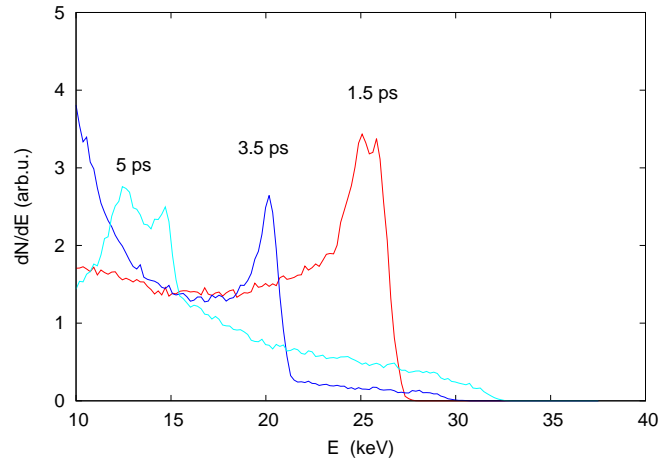
Figure 2.24: Modification of the ion spectrum by the shock formation at 3 ps

Anyway, the post-shock ion distribution can finally experience the additional effect due to an ambipolar field at the plasma-gas interface at r∼ 100 μm (see figure 2.18).

I have shown qualitatively that the plasma-gas interface, called the sheath, can host an ambipolar electric field resulting from a differential diffusivity between ions and electrons (see figure 1.2). In the present case, it is due to hot electrons coming from the centre of the channel and heated directly by the laser pulse. This field can accelerate the ions at the interface and those coming from the channel if it has not decayed significantly when the bunches arrive. This acceleration resembles then the TNSA mechanism characteristic of laser-thin foil interaction experiments that I carried out at the beginning of my thesis (see subsection 3.1.2 in the experimental part). In the present case (sort of "transverse TNSA"), the accelerated ions are not merely the ions at rest from the interface as in the thin foil case, but also the ions with higher momenta coming from the channel and injected in the sheath. The figure 2.25 presents the ion spectrum with (total - red line) and without (green line) considering the sheath effect .
The sheath significantly increases the ion cutoff energy, by a factor 4 in this case. It should be noted that the energy gain in the sheath depends in fact strongly on the laser pulse radial profile when it self-focuses in the plasma, as observed in smaller simulations. If the pulse is tight with a sharp gradient, very large sheath field can be obtained and ions streaming radially can be injected before the field vanishes and gain significant energy. Thus, depending on the initial pulse shape, a great variability in the cutoff is obtained.
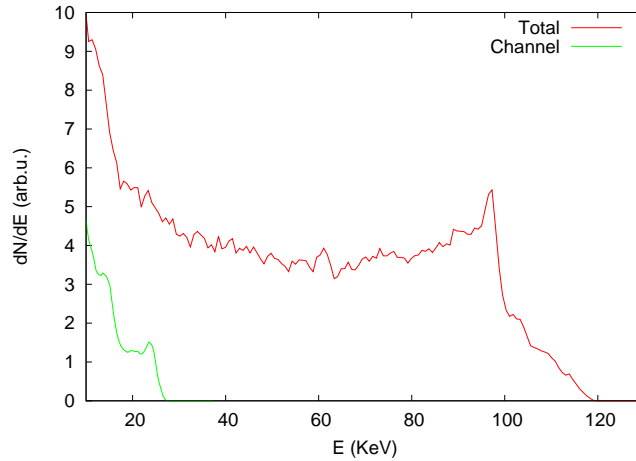
Figure 2.25: Ion spectrum without (green) and with (red) the sheath taken at the same instant (around 4 ps)

2.3   Conclusion

In this chapter, I considered from a theoretical viewpoint the ion response to a laser excitation in the under-critical regime. For a long pulse, I derived several analytical formulae for the ion distribution that can be applied in cases when pure Coulomb explosion with total electron depletion happens. These correspond to the view of the ion acceleration along the transverse direction as obtained experimentally in the past. For an ultrashort pulse, situations where the electron dynamics plays a major role in governing the ion acceleration have been presented and numerically discussed. These correspond to the new regime of experiments that I carried out within my Ph.D. The main effect on the ion population is then due to the laser wakefield that reshapes within 1 ps the channel in the pulse wake into an annular structure. A more involved description of the acceleration at later moments and of the final ion distribution must include occurrence of a shock and an re-acceleration by the sheath at the plasma-gas interface.

It will now be possible to tackle the experimental part with the intention to confront and discuss the previous theoretical elements that I presented with regard to the data that we collected.

Chapter 3

Experimental studies of ion responses to an ultrashort laser in plasmas

This chapter reports on the experimental observations on ion acceleration from underdense plasmas that I made during my thesis work. They are the first ones of this kind, using an ultrashort and intense laser pulse of 35-fs duration at minimum, and in particular, cover a regime for which the laser pulse duration is shorter than the inverse ion plasma frequency and where wakefield effects play the main role. To draw an overall view of this type of acceleration, a large amount of data were collected to carry out some parametric studies (different laser pulse duration and polarization, plasma densities and profiles). For accessing a wide range of parameters, and track the processes in time and space, new apparatus and setup were developed and implemented successfully. In the following, I present in detail the experimental tools I used and discuss the physical aspects emerging from the ion cutoff energy scans.

3.1   Laser and contrast

3.1.1   Laser "Salle Jaune"

The major part of the experimental campaigns I did took place at the Laboratoire d'Optique Appliquée in France[1], with the Titane:Sapphire (Ti:Sa) laser from "Salle Jaune" (λ=820 nm, 10 Hz of repetition rate and 2 J of energy). It uses the chirped pulse amplification (CPA) technique [16] (in fact, it is a double CPA system) to deliver after compression between 0.5 and 0.8 J on target within 30 femtoseconds ($\sim$ 30 TeraWatt of peak power) (see figure 3.1.1). Part of the laser energy can be derived before the compression into a secondary beam line to carry out some pump-

---

[1]a five-week period of experiments was also spent in November 2010 at the Brookhaven National Laboratory (USA) for CO_2-laser-highly overdense plasma interaction with gas jets, but I will not report on results from these studies in the present manuscript

probe experiments (see the section 3.3). This system has the particularity to be the first one to have implemented the cross-polarized wave (XPW)[2] technique [111] to enhance the front end contrast (experimentally by two orders of magnitude) so as to make the interaction of the intense pulses with thin foils more controllable.
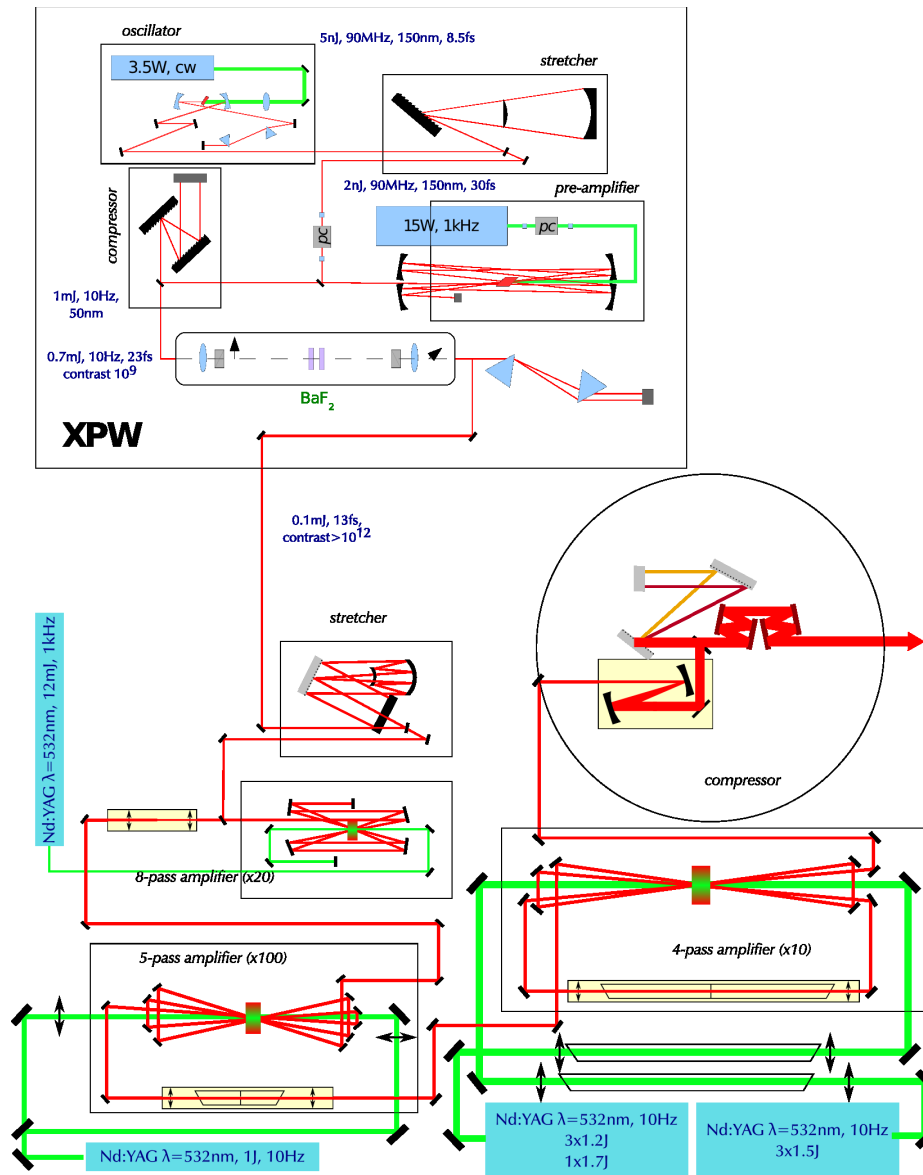

Figure 3.1: Block scheme of the "Salle Jaune" laser system (30 TeraWatt, 30 fs)

---

[2]using two BaF$_2$ crystals with high third-order non-diagonal coefficients inducing a pulse polarization rotation which is intensity-dependent

3.1.2   Contrast

The laser temporal contrast is the ratio of the peak intensity to the ASE level[3]. When I started the studies of ion acceleration for the present Ph.D. thesis at the beginning of the year 2008, we managed, with Alessandro Flacco, to carry out series of parametric investigations of the interaction using aluminium foils as thin as 400 nanometers [151], which was indeed the evidence of a satisfactory laser temporal contrast as compared to the state-of-the art active plasma mirrors technique [152]. Later, in 2009, the same type of experiments with micrometric foils could not be experimentally reproduced (see figure 3.2). For thicknesses
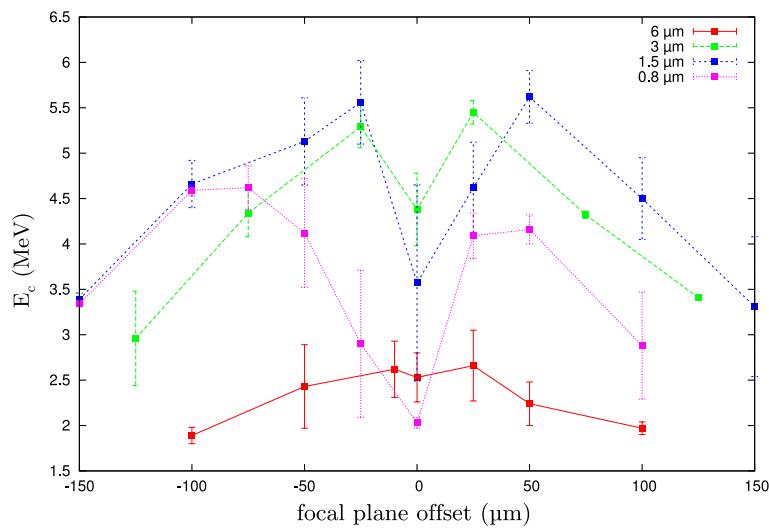
Figure 3.2: Proton cutoff energy versus the laser focal plane offset for different Al foil thicknesses in 2009

below 3 μm, at the best laser focus, a minimum proton cutoff energy is obtained. This is an experimental signature of a contrast issue, resulting in a diminishing of the acceleration efficiency when the intensity is too high (see for instance [36, 151] for a discussion on that signature).

To clarify that conclusion, we used a fast diode diagnostic to rule out any detrimental effect of prepulses on a nanosecond timescale. Finally, we carried out with Pascal Monot from the CEA Saclay comparative assessments of the temporal contrast using two independent 3ω-autocorrelators (devices 1 and 2 in the following). The result of that comparative study is shown in figure 3.3.

Both devices 1 and 2 revealed a contrast degradation in 2009 by an order of magnitude within tens of picoseconds as compared to the level in 2007. I used the lagrangian and multiphase 1D hydrodynamic code ESTHER [153] to quantify that

---

[3]rigorously, one should speak of the laser fluence in Jcm^{-2} and not of the intensity in Wcm^{-2}
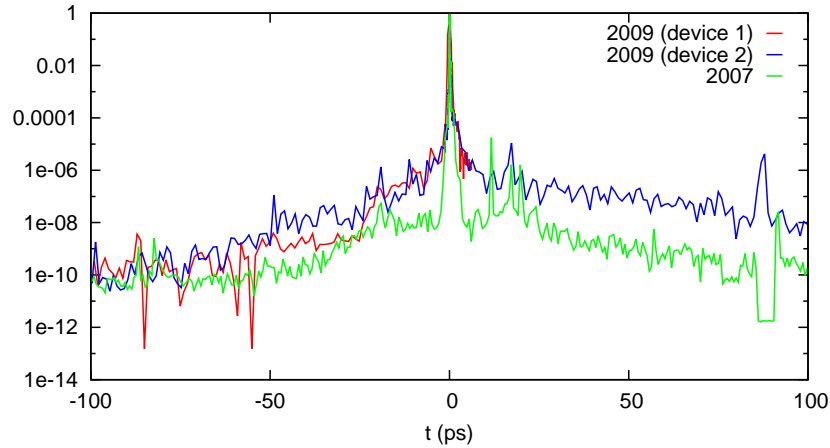
Figure 3.3: Laser "Salle Jaune" temporal contrast in 2007 and 2009. Two independent 3ω-autocorellators (devices 1 and 2) were used for comparative measurements in 2009

loss in contrast in terms of foil expansion before the arrival of the femtosecond pulse. The temporal profiles I put in the code were those of the Salle Jaune laser in 2007 and 2009 (green and red lines respectively in figure 3.3) and the peak intensity taken to be $I = 10^{19}$ Wcm^{-2}. The laser pulse is P-polarized and incident at 45° on an Al foil of 1 μm thickness. The result is shown in figure 3.4.
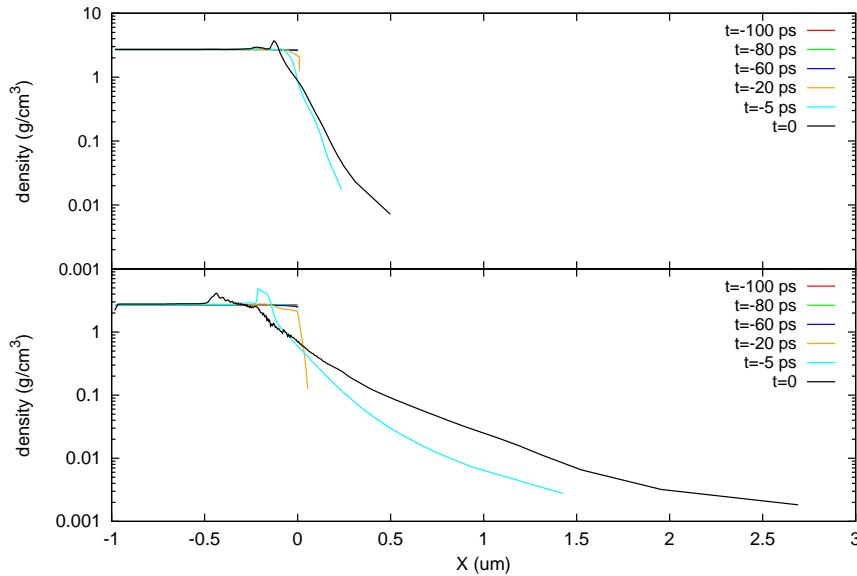
Figure 3.4: Time-solved 1D hydrodynamic expansion of a 1-μm-thick aluminium foil interacting with the exact pedestal corresponding to the laser conditions of our experiments with peak intensity $I = 10^{19}$ Wcm^{-2}, using the code ESTHER [153]. (Top) With the pulse profile in 2007 (see green line in figure 3.3). (Bottom) With the pulse profile in 2009 (see red line in figure 3.3)

When the femtosecond pulse arrives at $t = 0$, the shock wave, launched by the laser from the front surface at $x = 0$, propagated over less than 250 nm with the 2007-profile and almost over 500 nm with the 2009-one. Also, for the latter case, the foil rear surface has started to expand slowly. The exponential fit of the front gradient about the critical density (10 mg/cm^3) gives a plasma scale length $L/\lambda = 0.1$ in 2007 and $L/\lambda = 0.5$ in 2009, where λ is the laser wavelength. Thus, if an increase of the plasma scale length can be favourable for the laser-plasma coupling by a more efficient resonance absorption [154], the compressional wave, created at the critical surface, is powerful enough in the 2009-case[4] to heat mechanically half a micron of the target and alter radiatively the rear surface where the ion acceleration is supposed to take place.

The experimental and numerical conclusions prompted us to switch, for the ion acceleration study, to gaseous targets for which the ionization threshold is higher, at around 10^{14} Wcm^{-2} (see table 1.1). This switch offered also the possibility of studying the ion acceleration from underdense plasmas in enhanced temporal contrast conditions (in [17, 102], low contrast laser system are used). Experimentally, the control of this parameter might improve the control of the laser propagation along with shot-to-shot reproducibility. Recently, it proved to be beneficial for the stability and gain in electron acceleration and TeraHertz emissions based on Laser Wakefield Acceleration (LWFA) schemes [155].

3.2   Gas jet

Gas jets have been extensively used over the past fifteen years for laser plasma wakefield acceleration of electrons in a single stage [134, 156–158][5]. The plasma is easily formed when the intense laser pedestal interacts with the gas (see also section 3.4.2). For ion acceleration, predecessors used millimetric supersonic He jets delivering typically up to 10 % of the critical density of a Ti:Sapphire laser equal to $n_c = 1.68 \times 10^{21}$ cm^{-3} [17, 102]. For the experimental investigations reported in the present work, I developed a gamut of innovative gas jets delivering atomic densities up to $n_a = 2 \times 10^{21}$ cm^{-3}, i.e several times the critical density n_c when the gas is ionized by the laser pulse, over a submillimetric distance (typically 400 μm, see the appendix A for details on the benefits of those high-density jets), as shown in figure 3.5. In the following, I note $n_{ca} = 1.68 \times 10^{21}$ atoms·cm^{-3} to refer to the atomic density equal to the critical electron density n_c.

---

[4]due to an enhanced plasma heating

[5]for multi-stage acceleration to high energies, gas cells tend to establish themselves [159, 160] because of the great stability of the flow over several millimeters [161]
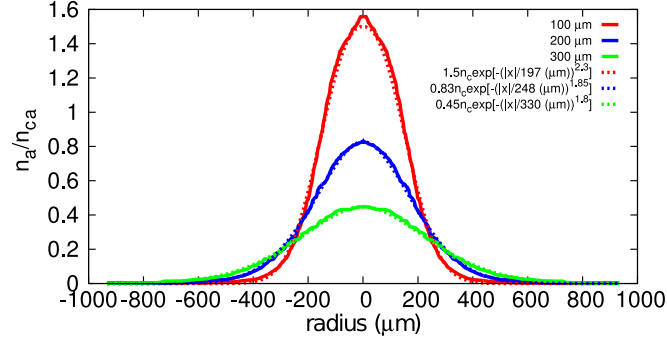
Figure 3.5: Neutral He profiles normalized to n_{ca} at 100 (red line), 200 (blue line) and 300 μm above a 400 μm sonic nozzle. The dotted lines indicate the best exponential fits

Flows outside the nozzle

The jets were characterized in space and time by interferometry [162]. Spatially, the geometry of the nozzle plays a crucial role in the interaction with a propagating laser beam, as it determines the vertical and radial gradients of the plasma to be formed. Sonic, transonic and supersonic flows were characterized (see figure 3.6). For the sonic flow, the Mach number M at the nozzle exit is in theory equal to the unity, whereas for the transonic and the supersonic ones, M is larger than the unity ($M_{\text{transonic}}$ is close to the unity, $M_{\text{supersonic}}$ equals several units and $M_{\text{hypersonic}} \gg 1$). Temporally, for a given nozzle geometry, a wide range of
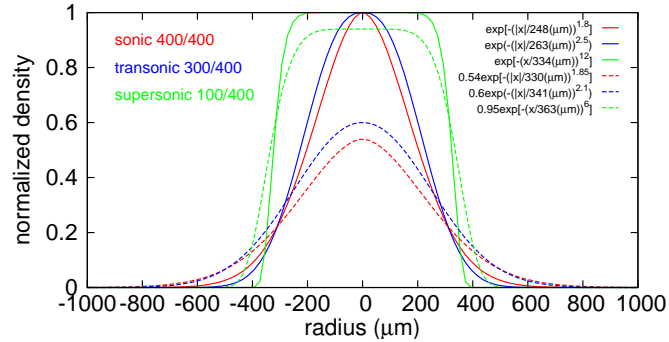
Figure 3.6: Sonic (red), transonic (blue) and supersonic (green) flows (best fits) for three nozzles of throat diameters 400, 300 and 100 μm respectively (same exit diameters of 400 μm). The density are normalized to the peak densities at 200 μm. The solid and dashed lines correspond to profiles at 200 and 300 μm from the exit respectively. Both vertical and radial gradients become larger as the Mach number decreases towards one

peak densities within $[10^{18}, 10^{21}]$ cm^{-3}, i.e. from very underdense to overdense plasmas, can be explored by setting the interaction at a certain instant of the flow
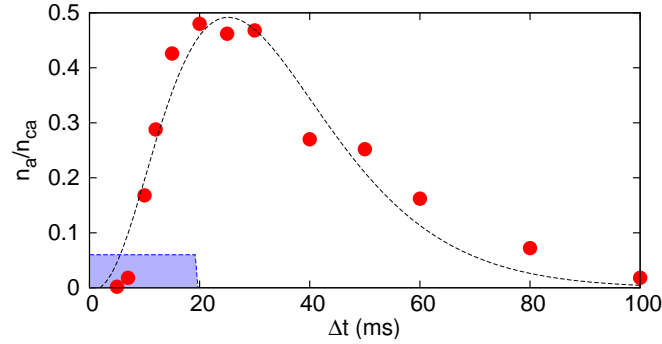
Figure 3.7: Time-resolved neutral peak density n_a normalized to n_{ca} at 200 μm from the exit of a slightly supersonic nozzle (300 μm throat diameter, 400 μm exit diameter). The blue region indicates the opening time of the valve. The interpolated dashed line is an indication to guide the reader

evolution (see figure 3.7).

Operating mode

The method adopted in the following studies to vary the density differs from the one usually employed in laser-plasma interaction (like for instance for electron acceleration from a gas jet). Here, the gas pressure feeding the valve is kept constant at $p = 300$ bar out of technical and practical constraints (I used a pneumatic pressure booster, see appendix A), and delays Δt between the gas and the laser pulse are varied. Equivalently, Δt can be fixed and the opening time of the valve varied. Thus, the interest of this method rests on the fact that the interaction regime is determined with a time, which can be set experimentally much more conveniently than a pressure[6]. However, it can be implemented in practice only at the cost of an extensive pre-characterization of the output flows to be used.

Jet=peak density+gradient

The instant of the interaction between the laser and the jet is in fact chosen to match a peak density *and* a plasma gradient (hence, a gradient scale length), defining the initial conditions. The operating mode coupled with those jets enables one to change *independently* either of these parameters over a large range of values, and simply access different regimes of the interaction. For instance, in figure 3.8, the delays Δt equal to 10 and 80 ms give similar peak densities (see red lines in figure 3.7 top panel) but larger radial gradients at 80 ms (see red dots in the bottom panel). This consideration makes sense when structures like nonlinear coherent structures (soliton/vortex) are targeted in the laser-plasma interaction

---

[6]at the precision of the jitter of a simple time-delay pulse generator

(see chapter 4 about this topic). The appendix A shows the corollary example where the gradient can be kept fixed and the peak density varied.
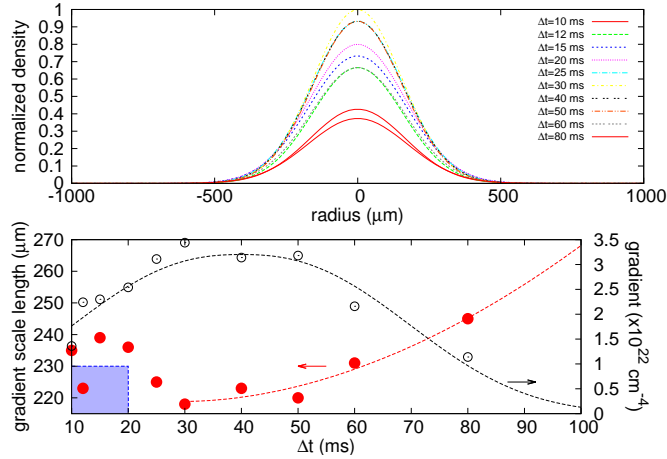
Figure 3.8: Profile evolution for different laser-jet delays Δt using the same nozzle as in figure 3.7. (Top) radial profiles. (Bottom) gradient calculated as the peak density over the gradient scale length (black empty dots), and gradient scale lengths from gaussian fits of the profiles (red dots). The blue region indicates the opening time of the valve. The interpolated dashed line is an indication to guide the reader

Implementation of high density jets

To fulfil (i) a high peak density, (ii) a small radial extension and (iii) a moderate exhaust mass flow rate compatible with a secondary vacuum pump system[7], a fast-switching bid valve[8] associated with nozzles having throat diameters of hundreds of microns, was employed with inlet gas at $p \leq 300$ bar.
Usually, the laser focal spot in vacuum is located at the edge of the nozzle, at about $200 - 300$ μm above the exit. This avoids nozzle ablation by the hot plasma and ensures a decent coupling with the plasma, a steep plasma scale length of 200 μm (avoiding laser defocusing) and access to near-critical plasma densities.

The jets that I developed were part of the experimental setup which I now present in details.

3.3   Experimental setup

The typical experimental setup implemented for the investigations is presented in figure 3.9. It receives the beam lines from the laser system and encompasses

---

[7]using turbo-molecular pumps requiring not more than tenths of millibar at the risk of fatal damages

[8]rise and fall time within 3 ms

several (seven) diagnostics for the ion detection and the monitoring in time and space of the plasma structures. Photographs of (*i*) the interior of the interaction
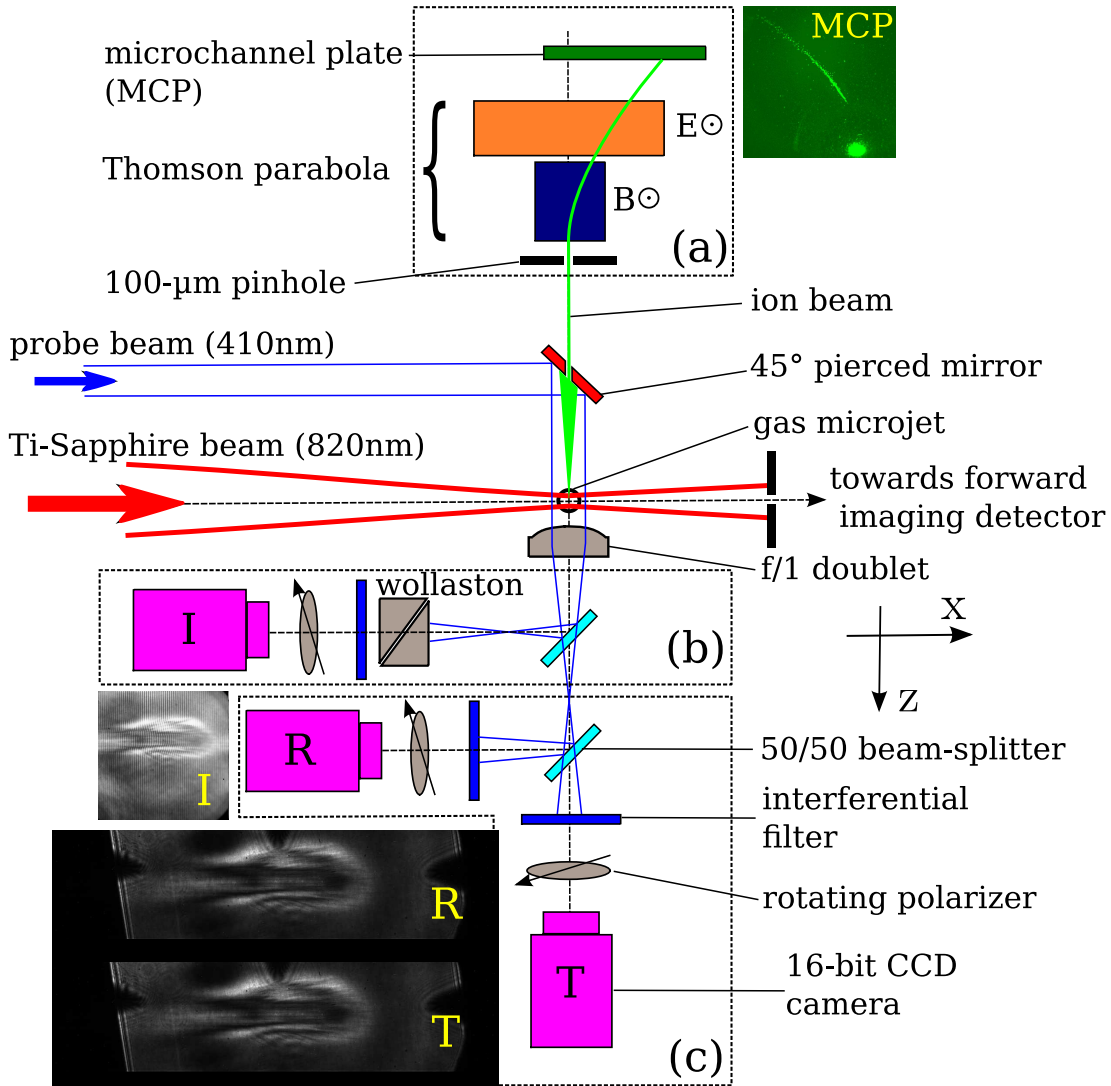
Figure 3.9: Experimental setup for the interaction of a microjet and a short Ti-Sapphire pulse, illuminated by a linearly-polarized-frequency-doubled probe pulse. (a) Imaging Ion spectrometer at the normal of the main beam with Thomson parabola and chevron microchannel plate (MCP). A second ion spectrometer is also set on the laser axis. (b) Nomarski interferometer. (c) Polarimeter using Faraday rotation effect

chamber, with the Ti:Sa and probe beam tracing, (*ii*) the ion detector (part (a) in figure 3.9) and (*iii*) the interferometer (part (b)) and polarimeter (part (c)) are shown respectively in figures 3.10, 3.11 and 3.12.
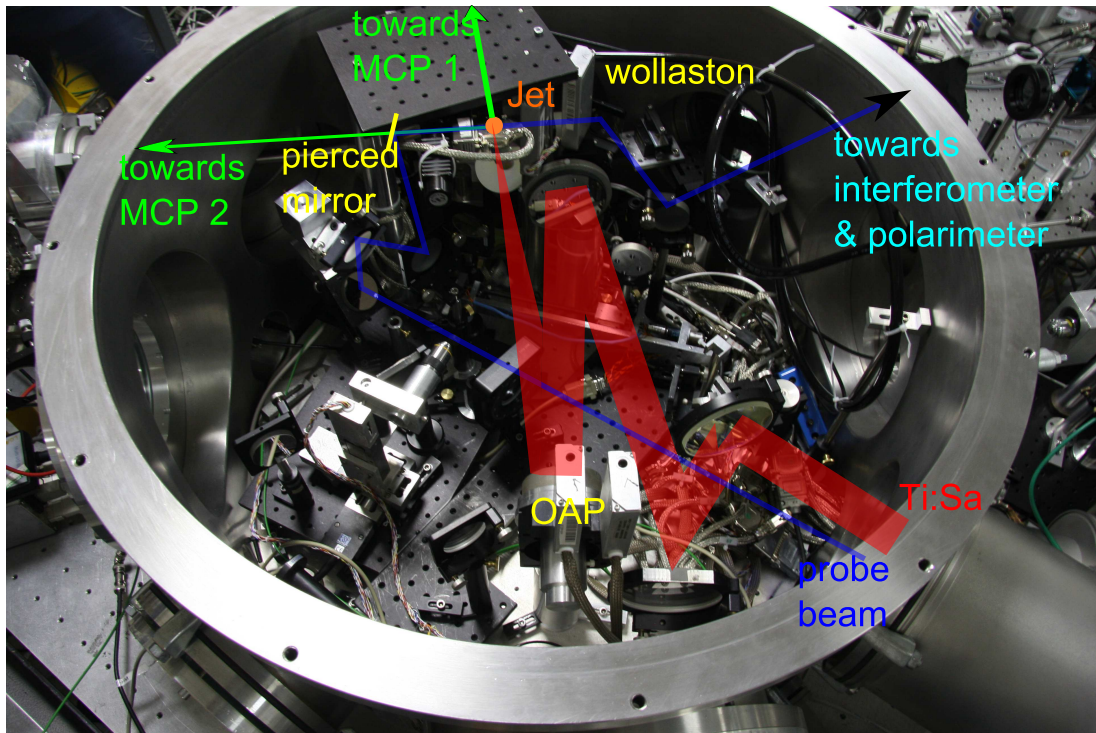
Figure 3.10: Beam tracings and main components set up during the experiments
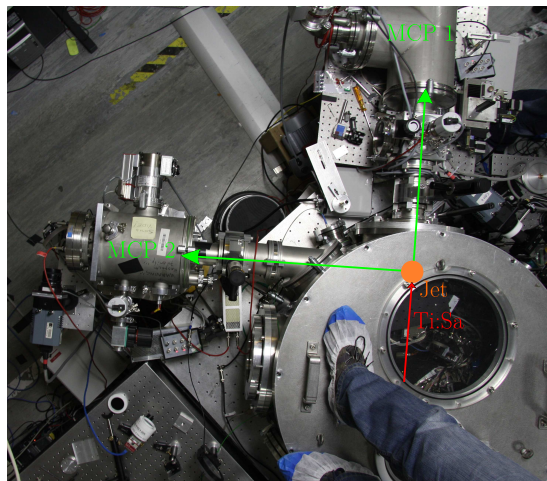
Figure 3.11: Pair of identical ion detectors (Thomson parabola (see the appendix B) and MCPs) along and transverse to the laser propagation direction
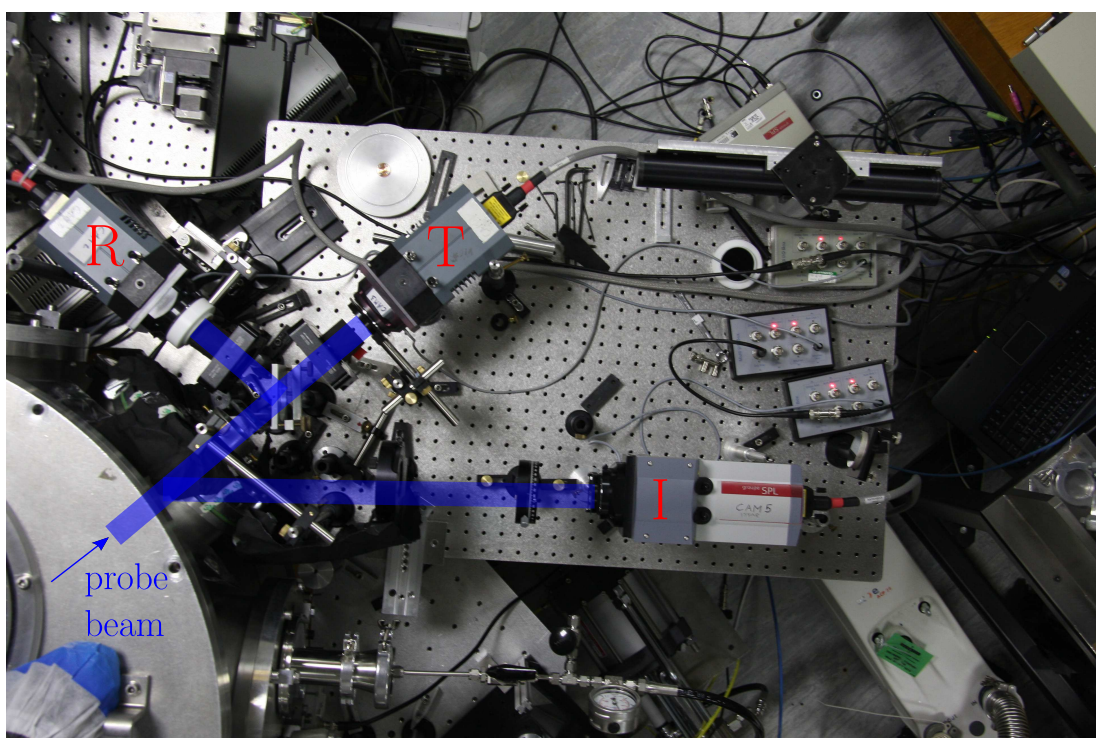
Figure 3.12: Optical diagnostics with $2\omega_L$ probe beam implemented in the experiments: interferograms are recorded by the camera I, polarigrams are recorded by cameras R and T

3.3.1   Beam lines

The ultrashort main laser pulse of duration $\tau = 35$ fs is linearly-polarized (along z see figure 3.9) and carries towards the target an energy of about $E_0 = 810$ mJ. This energy is assessed (i) by measuring the energy before and after compression at low laser flux to measure the average grating transmission (58%) and then (ii) by measuring the energy before and after the mirror transport line (including the final focusing off-axis parabola (OAP)) to assess the loss due to mirror reflections and scatterings (74%). This pulse is focused with an $f/10$ OAP mirror to a 14-μm ($1/e^2$) focal spot onto the He microjet. The focal spot is shown in figure 3.13.
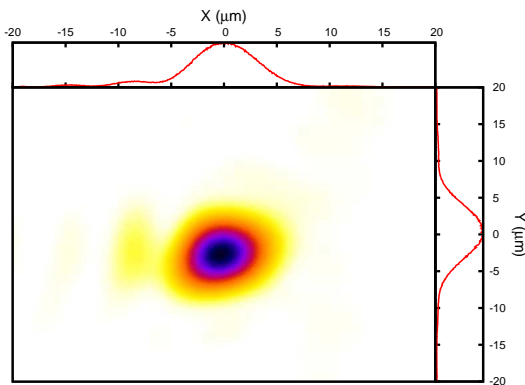
Figure 3.13: Focal spot during ion acceleration experiments (recorded with a 12-bit CCD camera with absolute calibration)

The quality of the spot was systematically optimized at the beginning of each series of experiment by means of a deformable mirror (32 actuators) to correct the optical aberrations [9]. This optimization enables one to obtain a spatial contrast (ratio of the peak intensity to that of the first lobes observable in figure 3.13) better than 7 and near 63% of the total energy encompassed in the iso-intensity circle at $1/e^2$ of the peak intensity.
With this focal spot, the typical vacuum laser intensity reaches $I_0 \sim$ few times 10^{19} Wcm^{-2} (calculated with the equation (1.7)). These values ensure a relativistic driving of the plasma electrons, along with a peak power enabling the relativistic self-focusing of the pulse [55, 163][10]. This latter point is crucial to reach sizeable amplitudes of the laser vector potential a_0 that condition the acceleration scenario.

In order to monitor optically in time and space the interaction, a "pump-probe" configuration is adopted and thus, a second ultrashort beam with less energy and independent beam path is installed. In practice, the main beam is split before focusing and 10% of the energy sent onto a BBO-crystal for second harmonic

---

[9]In our conditions, the preponderant aberrations are astigmatism, first order coma and trefoil, from slight misalignment and parabola structural defects

[10]$1 < P_L/P_c < 1000$ for $0.1 < n_e < 100$ % n_c, with P_L the laser peak power, and $P_c = 16.2$ n_c/n_e [GW], the critical power limit for relativistic self-focusing

generation. This frequency-doubling allows probing a plasma with a density until four times the opacity limit without doubling. The intensity and spatial quality of the collimated frequency-doubled beam is improved by passing through a 50-μm-pinhole-filtered beam reducer. It is finally incident on the jet at normal to the main laser axis for illuminating and probing the interaction transversely (see figure 3.9).

3.3.2 Diagnostics and methods

The laser positioning with regard to the nozzle output is done via Top-View (plasma self-emission) and Side-View (plasma transverse illumination) optical imaging. The ion detection is done along and at normal to the main laser axis of propagation. Measurements of ion emission and plasma probing at 90° from the main laser propagation axis, are simultaneously done by means of a 45°-pierced mirror reflecting the probe beam onto the microjet without blocking the ion beams.

Beam positioning

The gross positioning of the laser above the nozzle is done in air with an CW HeNe laser that mimics the Ti:Sa pulse path. The precision of this alignment is of the order of 500 μm. The fine lateral and vertical positionings are done under vacuum with two on-line plasma diagnostics.

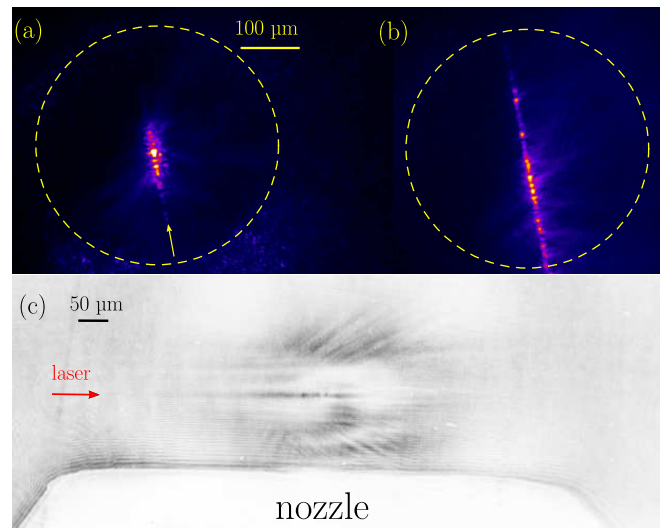Figure 3.14: Laser alignment diagnostics. Top-View (plasma self-emission): (a) with a 30-fs long pulse (the laser direction is along the yellow arrow), (b) with a 300-fs long pulse. The yellow dashed circle indicates the nozzle exit position. Side-View: (c) shadowgraphy of the plasma structures with the laser channel in the centre

Laterally: the self-emission of the plasma excited by the laser is collected by

a lens in the direction normal to the plane of the laser polarization (upward Thompson emission) and imaged on a 12-bit CCD camera (see figures 3.14(a-b)). To make a fine alignment of the laser axis along the nozzle diameter with a precision of ~ 10 μm, the pulse can be stretched from 30 to 300 fs to produce a long thin bright line covering the whole diameter (panel (a) and (b) in figure 3.14). **Vertically**: the probe beam illuminates transversally the interaction and maps out the plasma density gradients with a measured resolution of 2 μm. The thin horizontal dark line in the center of figure 3.14(c) is due to the sharp edges of the channel bored as the pulse propagates. The oblique dark lines could be due to the laser filaments directly, stimulated Raman side scattering [164] or hot electrons ejected from the focal volume.

Real-time and specific ion detector

The ion detector is composed of a 100-μm spatial filter (solid acceptance is 1.2×10^{-8} sr) with a Thomson parabola spectrometer (collinear magnetic and electric fields, see figure 3.9(a) and also the appendix B) coupled to 40-mm imaging microchannel plate chevron assembly. A linearized 16-bit CCD camera (1024×1024 px) enables single-shot recordings of scintillating traces and thus shot-to-shot statistical analyses of ion spectra.

The direction of the field deflections with regard to the laser axis and, in particular the magnetic deflection, have important implications for the spatial resolution of the ion sources along the laser axis. If the magnetic deflection is parallel to the laser axis, ions originating from different point sources along the laser path will produce in general overlapping traces on the MCP (see figure 3.15(a)). This means, that the ion emissions are not resolved but integrated in the direction of the laser axis. Inversely, if the magnetic deflection is perpendicular to the laser axis, the laser-plasma coupling can be resolved spatially in the laser direction, with a resolution of few pixels[11] (see figures 3.15(b-c)). In practice, if the ion sources are located within this resolution, the deflection configurations are equivalent and the source can be considered as point-like. For all the spectra analyses presented in the following, this condition is fulfilled.

I now present on figure 3.16 how the ion spectra are extracted in an automated routine.

First, the routine solves the equations of motion of a helium ion of a given energy E entering the Thomson parabola (TP) along the source-pinhole axis and drifting towards the MCP plane. The input values of the magnetic and electric fields comes from direct measurements on the TP[12]. For a specified input energy range,

---

[11]typically 200 μm with our imaging system

[12]for the magnetic field, with a Hall effect probing device
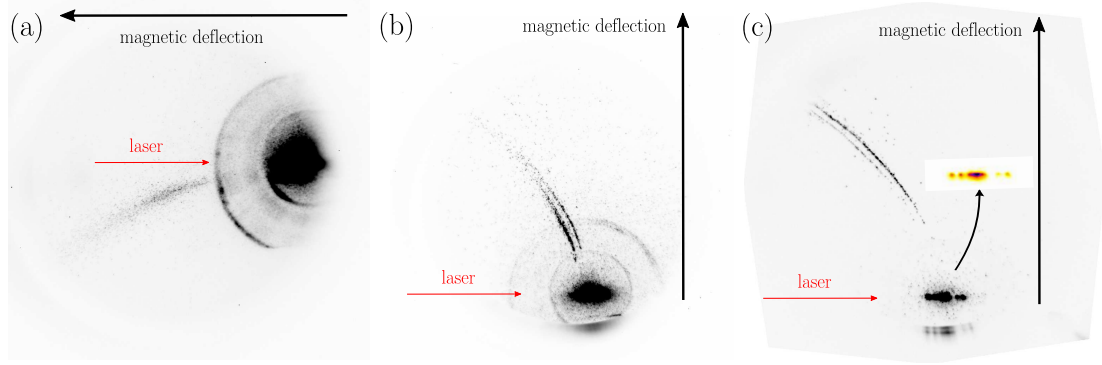
Figure 3.15: Different TP magnetic deflection configuration (same electric field). (a) magnetic deflection parallel to the laser axis. In this configuration, only single traces per species are observed. (b) magnetic deflection perpendicular to the laser axis (similar conditions as in (a)). Several parallel traces (here He$^+$) are obtained. (c) With lower gas density than in (b). Inset: (colors) multiple bright spots at the origin of the traces can be resolved

a trace specific to each ion species is obtained (approximated branch of parabola originating from the point in the MCP plane aligned with the source and the pinhole, see also the appendix B for precisions).

The energy bins are calculated by reference to the magnetic field dispersion (horizontal dispersion on figure 3.16(a)). For a fixed energy bin width (typically $dE = 1$ keV), the spatial size along the trace is computed to match the dispersion law $\propto E^{-\frac{1}{2}}$ (see appendix B). The transverse spatial size of a bin is fixed so as to collect all the counts from a trace without overlapping over the neighbouring trace (typically 10 pixels wide).

In theory, errors due to possible shot-to-shot fluctuations of the source position, masked in practice by a thick blocker to observe low level signals, could affect the results of an automated extraction with a given mapping trace configuration. I assess formerly this error by detuning the origin of the mapping trace by +/- 5 pixels along the magnetic dispersion axis. Given the magnification of the whole imaging system (pinhole imaging + MCP lens imaging), this detuning would correspond to a 500 μm shift of the source position in the jet plasma, i.e. almost the FWHM of the density profile which is typically of 700 μm. The results of this operation on the He^{2+} spectrum from the figure 3.16 is shown in figure 3.17.

One can notice that the error due to this formal (important) fluctuation does not affect qualitatively the spectrum and the features remain clearly identifiable. The deviation from the reference is more pronounced in region where the bin size is comparable to the amplitude of the detuning (around 170 keV). It results in an
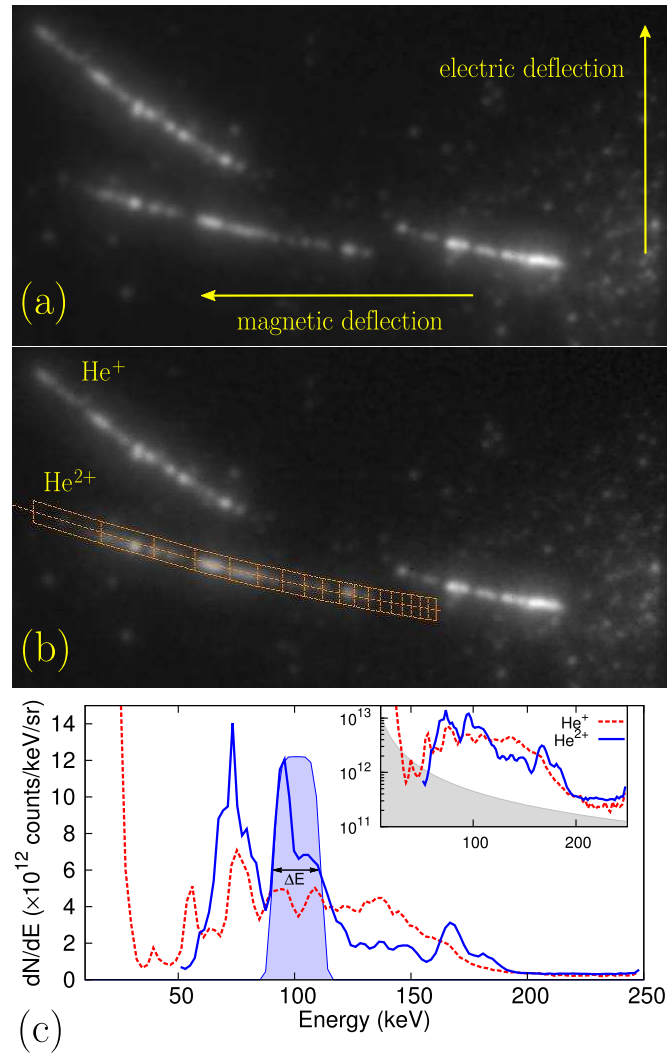
Figure 3.16: Spectrum extraction routine: (a) Recording of raw MCP picture after the Thomson parabola with the magnetic deflection parallel to the laser axis, (b) mapping of He ion traces and binning of the counts, (c) plotting of the calibrated spectra for each species. The picture corresponds to a single-shot recording

energy-shift error (1.6 % RMS for the peak around 150 keV) and a count-shift error (25 % RMS for the peak around 150 keV).

Thus, I conclude that in the worst case of detuning, unlikely to happen, the routine is robust enough to render the quality of the spectrum over the entire ion energy range over which the spectra features have been experimentally investigated.

Optical plasma probing: interferometer & polarimeter

An $f/1$ achromatic doublet coupled with a 50/50 beam splitter enables to record at the same time with a measured spatial resolution of 2 μm, interferograms
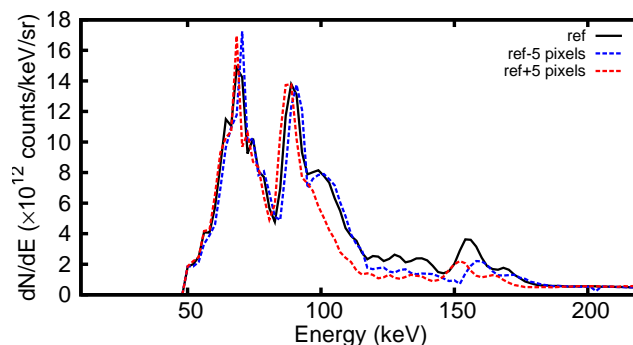
Figure 3.17: Extracted He^{2+}-spectra obtained for three different origins of the mapping trace. Solid line: reference origin position. Dashed line: Origin position detuned by - 5 pixels (blue) and + 5 pixels (red)

encoding the plasma density variations using a Nomarski interferometer [165] (see figure 3.9(b)), and polarigrams revealing the component of the plasma magnetic fields collinear to the probe beam direction (see figure 3.9(c)).

The interferometer contains a Wollaston biprism of 10×10 mm^2 with a 410-nm interferential filter to improve the temporal coherence of the interferences. The advantages of this system as compared to the usual Michelson or Mach-Zehnder interferometers are the compacity, stability and a direct temporal coherence of the ordinary and extraordinary rays (by design)[13]. Its inconvenient is the stringent coupling between the interference and imaging systems[14], which imposes to design the biprism for specific conditions of use. Figure 3.18 shows an example of the type of interferograms obtained at relatively low densities in clean conditions where fringes can be continuously mapped out and the plasma has an axisymmetric geometry enabling to Abel-invert the extracted and unwrapped dephasing.

At higher densities, strong shocks and multiple filaments appear, making the fringes discontinuous and blurred, with additionally, a loss of the axisymmetric geometry of the plasma from laser channel bending and anisotropic radial expansion. In these conditions, only partial density extraction within localized regions of the map could be done on the basis of strong geometrical assumptions. For these extreme conditions, to circumvent at least the issue of the non-axisymmetry, an interesting but heavier solution to be tested to retrieve the density would be a tomography at multiple angles [167].

The polarimeter is composed of two identical assemblies, each comprising in particular a Glan-Taylor polarizer (extinction ratio better than 10^{-4}) and a 16-bit CCD camera (see figure 3.9(c)). For each assembly, a scan of the rotating polarizer

---

[13]which is significant when considering ultrashort pulses
[14]linking the interfringe, the image separation and the magnification
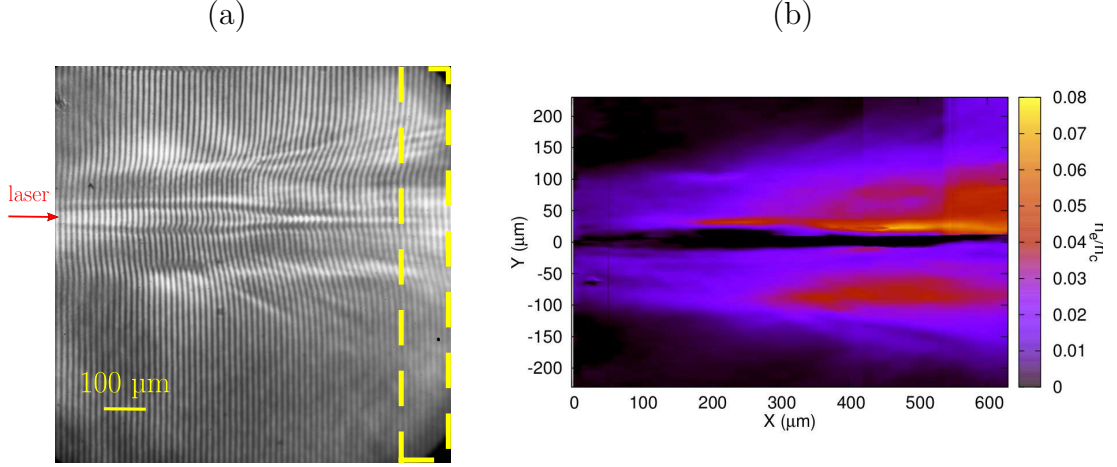
Figure 3.18: (a) Interferogram obtained with a Nomarski interferometer (at about 100 ps after passage of the pulse). The dashed-yellow region indicates the overlapping zone between the images produced by the biprism (rejected for the analysis). The experimental spatial resolution is $2-3~\mu$m (b) Plasma density map extracted from the interferogram in (a) with a generalized Abel-inversion [166]

is carried out for probe beam transmission calibration (every five degrees over the entire rotation). For the measurements, the polarizers are detuned by a common angle from each minimum of transmission (typical detunings $\theta_R = +10$ and $\theta_T = -10°$ for respectively the transmitted and reflected images from the beam splitter). In the laboratory frame, because of the reflection of the beam splitter, both polarizers are rotated in the *same* direction by the same amount.

The magnetic field detection rests on the measurement of the rotation, due to Faraday effect, of the incident linear polarization of the probe beam electric field when it crosses the magnetized plasma [123, 168]. The total rotation angle along a path l_z is given by:

$$\phi_{rot}(x,y) = \frac{e}{2m_e c n_c} \int_{l_z} n_e(x,y,z) B_z dz \tag{3.1}$$

Here B_z is the magnetic field component collinear to the probe beam direction, n_c the plasma critical density for the probe beam. Thus, knowing ϕ_{rot}, n_e and l_z gives access to B_z. Precisely, n_e can be obtained by interferometry (as we did) or on-axis holography [169] and ϕ_{rot} is encoded by the ratio of the intensities recorded in each arm of the polarimeter. With the notations of figure 3.19, the Malus' law gives the explicit form of this ratio depending on the Faraday rotation.

$$R(x,y) = \frac{I_1}{I_2} = \left(\frac{I_{10}}{I_{20}}\right) \frac{1 - \beta_1 \sin^2\left(\pi/2 + \theta_1 - \phi_{rot}^{\pm}(x,y)\right)}{1 - \beta_2 \sin^2\left(\pi/2 + \theta_2 - \phi_{rot}^{\pm}(x,y)\right)} \tag{3.2}$$
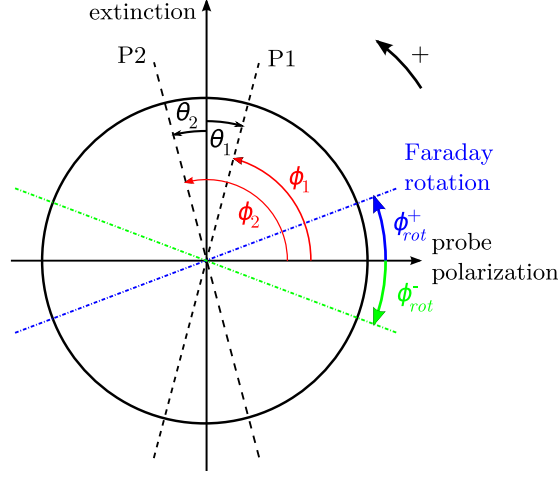
Figure 3.19: Faraday rotation configuration. The two polarizers P1 and P2 are detuned from the extinction by θ_1 and θ_2 respectively. The Faraday effect due to the magnetized plasma induces locally a positive or negative rotation $\phi_{rot}^{\pm}$ of the initial probe polarization

with $I_{1,20}$ the incident intensities and $\beta_{1,2}$ the extinction coefficient of the polarizers P1,2. By posing $\psi_i = \pi/2 + \theta_i - \phi_{rot}^{\pm}$, and $\Delta\psi = \psi_1 - \psi_2$, the equation (3.2) is equivalent to the following equation:

$$a + b\sin(2\psi_2) + c\cos(2\psi_2) = 0 \tag{3.3}$$

with:

$$
\begin{cases}
a &= RI_{20} - I_{10} + I_{10}\beta_1\sin^2(\Delta\psi) + \dfrac{I_{10}\beta_1\cos(2\Delta\psi) - \beta_2 RI_{20}}{2} \\[2mm]
b &= \dfrac{I_{10}\beta_1\sin(2\Delta\psi)}{2} \\[2mm]
c &= \dfrac{\beta_2 RI_{20} - I_{10}\beta_1\cos(2\Delta\psi)}{2}
\end{cases}
\tag{3.4}
$$

For general values of a, b and c, the solution of (3.3) reads[15]:

$$\psi_2 = \tan^{-1}\left(\frac{\pm\sqrt{b^2 + c^2 - a^2} - b}{a - c}\right) \quad (\text{mod } \pi) \tag{3.5}$$

with the sign indetermination lift when practical values are used. The optimal detuning angles $\theta_{1,2}$ that maximizes the ratio R in equation (3.2) depends upon the Faraday rotation angle to be produced (so that the optimum can only be chosen a posteriori), and is maximum when equal to ϕ_{rot}. In practice, the expected magnetic field magnitude on the basis of numerical simulations done in the pre-study should little Faraday-rotate the electric field, so that we worked with small angles, in agreement with the experimental literature reporting on small angles of less than ten degrees [123, 170].

---

[15]for $\Delta\psi = 0$ (so $b = 0$), the solution keeps the same form. In fact, the detuning $\Delta\psi \neq 0$ is of experimental importance only

Taking the intensity ratio from the two shadowgrams R and T obtained with opposite detuning angles (see figure 3.9(c)) prevents the extracted ϕ_{rot} map to be corrupted by probe beam shot-to-shot fluctuations in intensity, and image shift from plasma refraction or vibrations. However, this requires a pixel-to-pixel correspondence of the pictures. A sub-pixel-accurate matching of the two pictures was achieved by tagging the field of view at three reference-areas prior to the beam-splitting, and by running a numerical pattern matching routine. An example of the type of symmetrized maps of $n_e|B|$ obtained when the pulse travels through the plasma can be seen in figures 3.20 (b).

(a)

(b)

Figure 3.20: Maps extracted from the automated routine 1.3 ps after the beginning of the interaction. The laser propagates in the right direction. Parameter: $\tau_L = 35$ fs. (a) Electron density map (peak density $n_e \sim 2\% \ n_c$). (b) After inversion to obtain the product $n_e|B|$

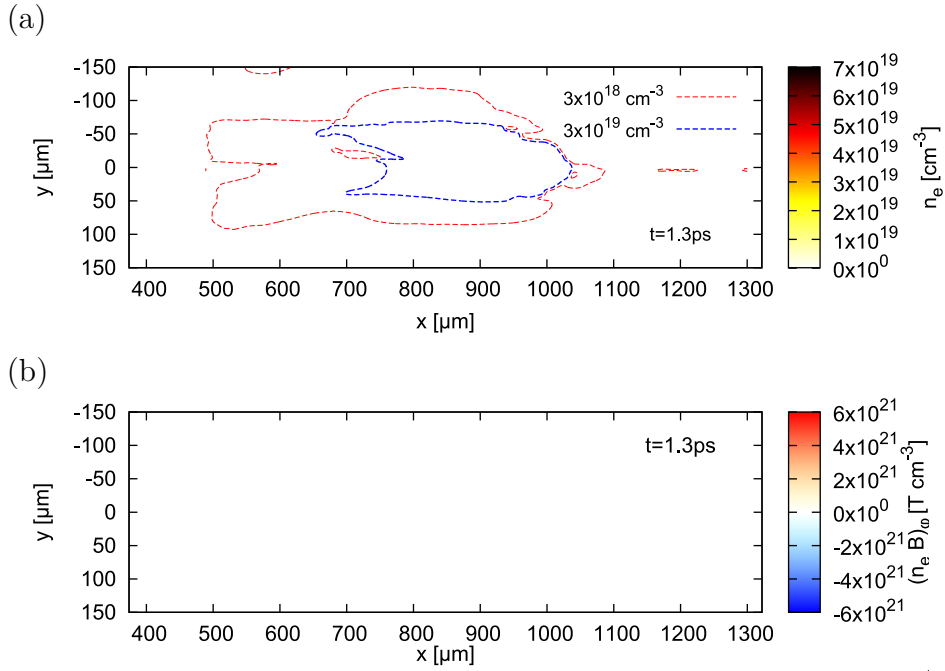The apparatus that I depicted previously was then used to carry out the study of the ion acceleration from laser-gas jet interaction.

3.4   Ion acceleration: experiments

After describing the numerous tools that were developed/implemented for the investigations of the acceleration, I now proceed to the presentation of the experimental data collected during the campaigns and related to the demonstration of ion acceleration from gas jets by means of an ultrashort laser pulse.

3.4.1   Preamble

During my Ph.D. work, the main objective of demonstrating the ion acceleration from underdense plasma with an ultrashort laser pulse was fulfilled. For the first time, direct measurements of suprathermal ions from gas jets with an ultrashort laser pulse were reported. Among the aims presented in subsection 1.3.2, the clarification of the geometry of the acceleration was also targeted. This motivated the installation of a pair of ion detectors along the longitudinal and radial direction with regards to the laser propagation axis, as presented in section 3.3. This setup up allowed us to conclude that in our experimental conditions, ions are accelerated to a detectable level and reproducibly only along the radial direction, whatever the flow, density or even gas[16] that we used. These strong observations are in agreement with 3D PIC simulations carried out in preparation of the experimental campaigns (see subsection 1.3.1). I should mention that longitudinal ion acceleration was observed only one day using a thin sonic jet at near-critical neutral density. This observation was done with a brass nozzle, whose internal duct was ablated after a sequence of thirty consecutive shots, thus producing a flow of unknown density and gradient, so that an experimental investigation of this very interesting fact could not be carried out in a controlled way. It was decided to focus on the transverse acceleration, the conditions of which were perfectly controllable and reproducible. However, a discussion on this point is done as a perspective in the last part of the present document (see chapter 5, section 5.2).

The main accelerating mechanism under study looks analogue to the usual Coulomb explosion from laser-underdense plasma interaction [17]. However, in our case the ultrashort laser pulse can excite a strong wakefield, the ponderomotive effect of which [119] can exceed that of the laser pulse. It is this mechanism of radial acceleration, a sort of wakefield-assisted Coulomb explosion which is here reported and parametrically studied.

For this work, I studied the dependences of the ion acceleration with the experimental parameters, namely the laser pulse duration and polarization on the one hand and the plasma density and profile on the other hand. I propose for each case under study some physical interpretations/explanations, when possible, supported by PIC simulations.

---

[16]Helium and argon were tested at LOA. It can also be noticed that hydrogen was used at the Brookhaven National Laboratory ($C0_2$ laser system, $\lambda_L = 10 \ \mu$m), but no ion was detected in the laser propagation direction

3.4.2 Laser dependences

The laser energy is always kept constant at about 800 mJ on target. If not stated otherwise, the pulse duration is 35 fs and linearly polarized along the horizontal direction (perpendicular to the jet flow direction).

Pulse duration effect on the cutoff energy

The pulse duration is varied by adjusting the chirp[17]. In practice, the chirp means that the different spectral components of the ultrashort pulse of bandwidth ~ 150 nm about 800 nm arrive with delays onto the target, increasing the total duration of the irradiation. The sign of this chirp defines whether the frequencies seen by the plasma during the interaction increase (positive) or decrease (negative).

It is interesting to compare the behaviour of the acceleration with the laser duration for two different flows with similar peak densities but very different gradient scale lengths, as the propagation of the intense pulse in a tenuous plasma can nonlinearly modify the longitudinal (and also radial) pulse shape [171–173], leading to a more intense pulse, with expected consequences on the ponderomotive force and the wakefield. I used sonic and supersonic thin jets from nozzles with identical output diameters 400 μm, giving gradients scale lengths of respectively ~ 250 and ~ 150 μm (see figure 3.6). Thus, the dependence of the cutoff energy of ions accelerated along the laser radial direction upon the pulse duration, for the same plasma peak density, was recorded and is summarized in figure 3.21. The cutoff energy is defined as the coordinates along the MCP ion traces when the signal reaches the noise level. Within the same parametric scans, the noise level was observed to be unchanged. The top and bottom panels in figure 3.21 refer to positive and negative pulse chirp respectively.

As expected for each flow, the cutoff energy drops as the pulse duration is increased. In fact and intuitively, increasing the pulse duration reduces the pulse peak intensity and then the intensity radial gradient and finally, the pulse ponderomotive force proportional to that intensity gradient. For that point, CE in its usual picture without wakefield effect seems to be sufficient to render the observations. No particular effect of the pulse chirp can be noticed.

However and interestingly, for durations shorter than 150 fs, the supersonic flow gives significantly higher cutoff energies for the same plasma peak density $n_e = 1.3 \times 10^{19}$ cm^{-3}, and shows a higher sensitivity to the pulse duration, as the acceleration efficiency drops faster when the duration is increased. This can be understood with a small PIC run (using CALDER-CIRC 3D quasi-axisymmetric code), by comparing the evolution of the vector potential a_0 of an 35-fs laser pulse in a short and a long plasma ramp simulating the supersonic and sonic gradient
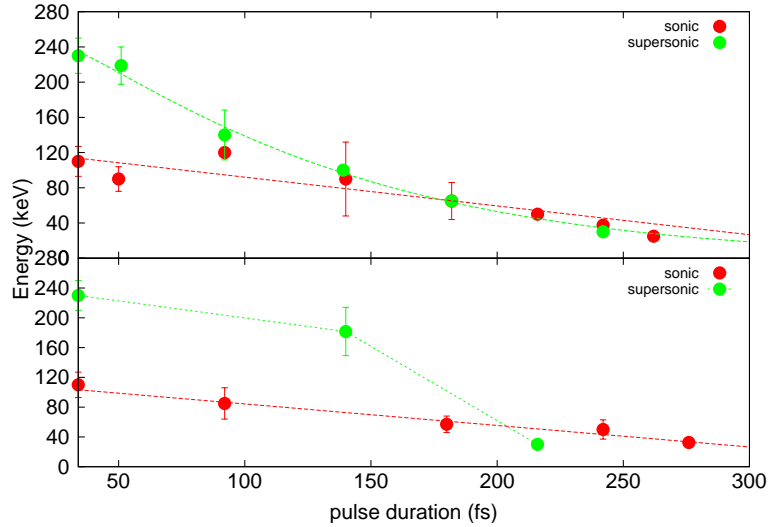
Figure 3.21: Cutoff energy dependences upon the laser pulse duration (chirp adjustment) for two different flows (see figure 3.6 for nozzle correspondence). (Top) positive chirp and (bottom) negative chirp. The peak densities for this scan is 1.3×10^{19} cm^{-3} for both type of flows
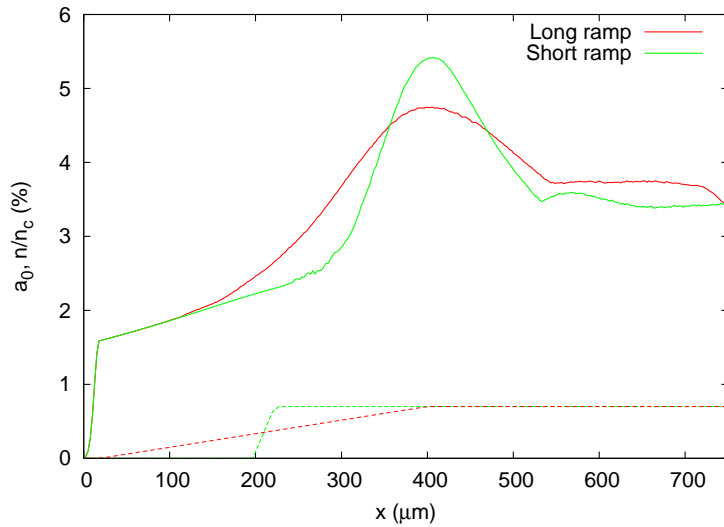
Figure 3.22: CALDER-CIRC simulations of the laser normalized vector potential evolution in short (~ 50 μm, green solid line) and long plasma ramps (~ 300 μm, red solid line). Initial $a_0 \sim 1.7$. The dotted color lines indicate the plasma profiles with $n_e = 1 \times 10^{19}$ cm^{-3} peak density

scale lengths. Figure 3.4.2 presents the results of the calculations.
One can notice, that the vector potential is 22% greater in the short ramp case than in the long one. This entails an increase of about only 20% of the laser ponderomotive force amplitude (see equation (1.31)) in the supersonic case

---

[17]second order in the spectral phase noted $\phi^{(2)}(\omega)$

compared to the sonic jet, and cannot explain the significant difference in energy cutoff of about 100% at $\tau = 35$ fs. The simple CE picture based on the laser ponderomotive push merely does not fit and the effect of the wakefield must be invoked.

As the density parameter is expected to control the amplitude (and duration) of the wakefield created by a given ultrashort pulse (see equations (2.36) and (2.37)), it is then interesting to test the previous conclusion and compare the behaviour of the ion cutoff energy versus the pulse duration as in figure 3.21, but for the same flow (same gradient scale length) taken at two different peak densities. However, if the plasma density is increased significantly, for instance by a factor of ten to reach $n_e = 1.4 \times 10^{20}$ cm^{-3}, the supersonic flow does not produce any detectable radial acceleration, while the sonic jet allows to accelerate ions at even higher energies than in $n_e = 1.3 \times 10^{19}$ cm^{-3} (this point will be presented in details in the following, see figure 3.32 in subsection 3.4.3). Therefore, I present in figure 3.23 this dependence only for the sonic flow. The top and bottom panels refer to positive and negative pulse chirp respectively.
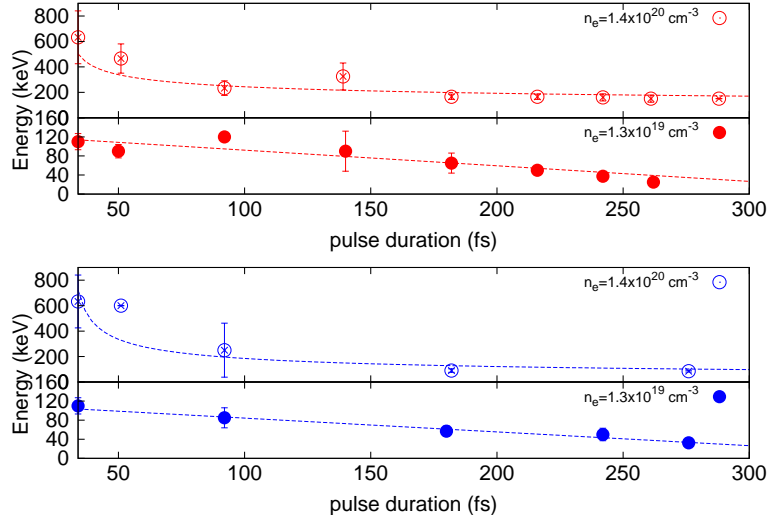
Figure 3.23: Cutoff energy dependences upon the laser pulse duration (chirp adjustment) for the sonic flow. (Red) positive chirp and (blue) negative chirp. The empty dots refer to a scan at peak densities ten times higher (1.4×10^{20} cm^{-3}) than for full dots (1.3×10^{19} cm^{-3})

For $n_e = 1.4 \times 10^{20}$ cm^{-3} (high density), the cutoff energy is higher than for $n_e = 1.3 \times 10^{19}$ cm^{-3} (low density) at any pulse duration (up to 5 times for a 35-fs pulse). At both densities, the cutoff decreases when the pulse duration increases to about 250-300 fs. Within the range 35-100 fs, a clear difference in trendline can be noticed between $n_e = 1.3 \times 10^{19}$ and 1.4×10^{20} cm^{-3}. For the higher density, the cutoff energy is quickly reduced when increasing the durations. Beyond 100

fs, a similar linear trendline is followed at a both densities. No particular effect of the laser pulse can be noticed at high density.

I propose to discuss first the case with a long pulse ~ 250 fs and $n_e = 1.3 \times 10^{19}$ cm^{-3}. For these parameters, $a_0 = 0.7$ and $\omega_{pe}/\omega_L \ll 1$, so that the portable code WAKE stays valid and can be used to describe the laser propagation through the plasma. Moreover, $\tau_L \omega_{pi} \sim 1$, which is a rather suitable condition to test the model in chapter 2. I present in figure 3.24 the WAKE results of the pulse propagation through 1.4 mm of He^{2+}-plasma (about four times the Rayleigh range) with an upward longitudinal gradient close that of the real jet over 300 μm and a plateau at $n_e = 1.3 \times 10^{19}$ cm^{-3} afterwards. The real jet terminates at about twice the beam Rayleigh range. The downward gradient of the real jet is not simulated so that the plasma effects on the pulse are exaggerated.
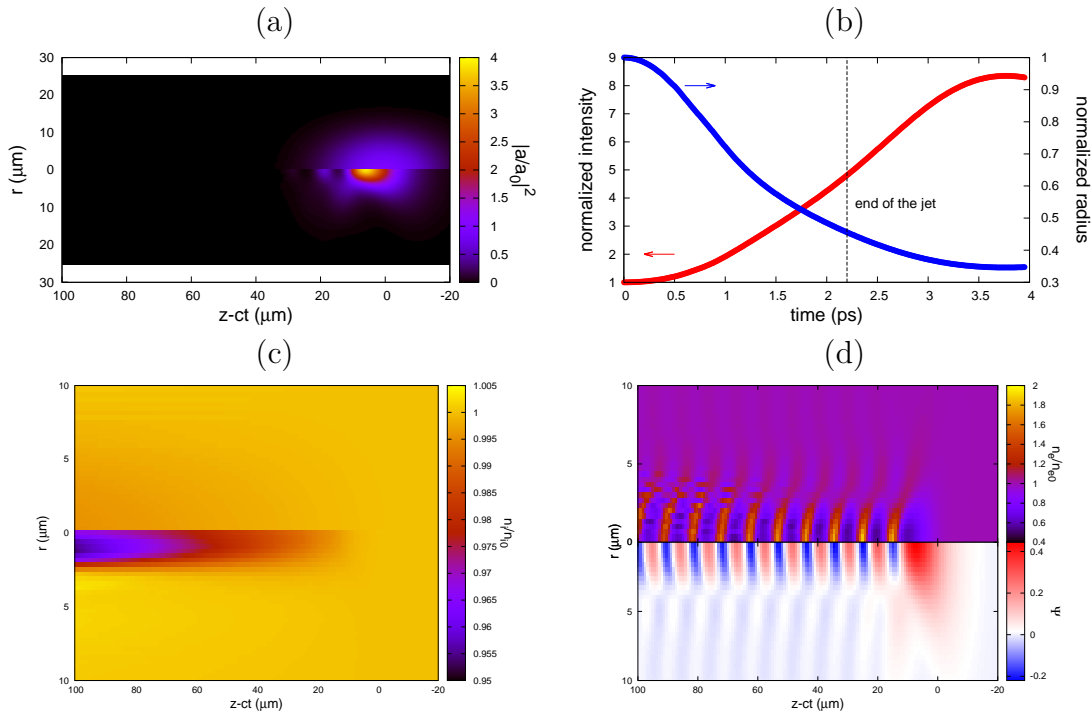
Figure 3.24: WAKE simulations of a long pulse propagation in a plasma ($\tau_L = 250$ fs $a_0 = 0.7$ $r/\lambda_{pe} = 1.2$ $n_e = 1.3 \times 10^{19}$ cm^{-3} ($2\pi/\omega_{pe}^{-1}$=31 fs). (a) Laser vector potential normalized to its initial value at different instant of the propagation: (top panel) at t=0, (bottom panel) at t=2.2 ps (700 μm propagation in the plasma). (b) Time-resolved laser peak intensity and radius. The dashed line indicates the end of the jet in experiment. (c) Ion density in the laser wake at t=0 (top panel) and t=2.2 ps (bottom panel). (d) Electron density modulations (top panel) and wakefield potential Ψ (bottom panel) at t=2.2 ps

One can notice in figure 3.24 panel (a) that the pulse is only slightly modulated

and longitudinally compressed, and essentially keeps its initial gaussian shape. Nonetheless, it is visible in panel (b) that it has self-focused, so that, at the end of the experimental jet, the peak intensity is five times higher than the initial value and a_0 is close to 1.8. In top panel (c), the ions do not react quickly enough within the temporal window when the pulse intensity is not relativistic, whereas in bottom panel (c) with a relativistic intensity, ion boring is observable far from the pulse (100 μm) and the radial kinetic energy is of few keVs. Correspondingly, in panel (d), moderate plasma modulations and wakefield potentials develop in the pulse wake, even at a relativistic intensity level. These results are in line with the discussion in subsection 2.2.1, where it was illustrated that a pulse initially of radius $r/\lambda_{pe} > 1$ and $a_0 < 1$ needs to propagate long enough to "intensify" and "adapt" to the plasma via self-focusing, in order to excite a sizeable wakefield acting efficiently on the ions. Thus, we can consider that the pulse, in this condition, is not much affected by the propagation while reaching a relativistic intensity level. I can a priori reasonably test the CE model exposed in chapter 2.

Since in these conditions $\tau_L \omega_{pi} \sim 1$, both approaches considering a fixed radius (see 2.1.1) and a fixed time (see 2.1.2) can be examined.

fixed radius: for $n_i = n_e/2 = 0.65 \times 10^{19}$ cm^{-3}, equation (2.7) reads a maximum kinetic energy in spherical geometry of ~ 3 MeV, two orders of magnitude higher than the recorded energy. Likewise, if I consider, that the radius is $r = \lambda_{pe}$, equation 2.9 gives 2.19 MeV (higher cutoffs are obtained in cylindrical geometry). Thus, the model with a fixed radius is not adapted in that case.

fixed time: for $\tau_L \omega_{pi} = 0.8$, equation (2.32) and figure 2.7 give in spherical geometry $\varepsilon = 0.19$, i.e. 2.9 MeV and 2.3 MeV if the radius is taken to be respectively 10 μm and λ_{pe} (higher cutoffs are obtained in the cylindrical geometry). Again, the model is not satisfying to explain the experiments.

A posteriori, both models fail in predicting the cutoff energy whereas the pulse duration is quite comparable to the ion evacuation time. This means that the total channel depletion assumption in particular must be severely wrong. In subsection 1.2.3, a criterion of electron depletion (1.37) depending on the normalized vector potential a_0 was derived. For the parameters of the experiment, total depletion is met when:

$$\text{for } n_{2,3} = 2, \quad \beta = 23 \ \Rightarrow \ a_0 > 16 \tag{3.6a}$$

$$\text{for } n_{2,3} = 3, \quad \beta = 15 \ \Rightarrow \ a_0 > 10 \tag{3.6b}$$

As matter of fact, total depletion of the channel can be ruled out when assuming that calculation. In Ref. [50], Macchi *et al.* carried out particle simulations in 1D cylindrical symmetry that confirm the unfavourable conditions of our experiments with long pulses to induce channel depletion.

Consequently, the cutoff energy should be significantly reduced compared to what the CE models predict. The experimental situation with the long pulse is in fact the analogue to the case of the neutral core I treated in 2.1.1, where the cutoff energy, proportional to the coefficient C_a, drops with the size of the neutralized region. Similarly, this situation could be equivalent to that of an effective radius much smaller than the laser spot of size λ_{pe}. With the fixed-time model in spherical geometry, the cutoff energy of ~ 40 keV for $\tau = 250$ fs would correspond to an effective radius of 1.5 μm.

In fact, considering the high values of a_0 required to deplete the channel, it is well probable that none of the points in figure 3.23 fulfils the criterion (1.37), all the more since a thin plasma inducing moderate self-focusing was used. Thus, a quantitative discussion on the other points in the figure, for shorter durations where wakefield effects are expected to take place, cannot be reliably carried out on the basis of either the *simple-case* models or the code WAKE (in particular at $n_e = 1.4 \times 10^{20}$ cm^{-3} where the code is invalid). However, some qualitative considerations can be proposed.
The difference of behaviours at high and low densities in the region $\tau_L = 35 - 100$ fs where the pulse is relativistic, can be due to the fact that self-focusing and filamentation are nonlinear and more effective at high density and high intensity [144, 174, 175]. It is therefore reasonable to expect clear difference in the laser ponderomotive and wakefield actions when the duration is varied by a factor of 3 at high density and to observe in that condition sharper dependence of the ion cutoff energy on the duration than at low density.

Thus, when using an ultrashort pulse in our conditions, high cutoff energies can be obtained (up to 800 keV) with ultrashort pulses and sonic jets. Interestingly, the sensitivity of that acceleration to the pulse duration increases with the density and steepness of the plasma, mainly for duration of tens of femtoseconds, consistently with effects expected from laser propagation (self-focusing, filamentation) and subsequent wakefield excitation in such conditions. I can add that no particular influence of the sign of the chirp can be emphasized in this scan. This important fact tends to confirm that the onset of the acceleration rests mainly on ponderomotive mechanism (with or without channel depletion). I now present some effects on the acceleration of the laser polarization for fixed pulse duration of 35 fs.

Laser polarization effects on the cutoff energy and spectrum

The dependence of the ion acceleration upon the laser polarization has been investigated using a thin supersonic jet (100/400, see figure 3.6). Linear and elliptical (in particular circular) polarizations were tested.

linear: In [176], by using 3D PIC simualtions with a P-polarized semi-infinite laser pulse propagating in underdense plasma, Naumova *et al.* predicted a 3D

pulse anisotropy with preferential pulse filamentation in the S-plane. In this work, ion compression into a thin axial layer was observed in the laser wake and was more efficient in the S-plane than in the P-plane. Similarly, in the numerical pre-studies we carried out by using 3D-PIC code with a 35-fs (see 1.3.1), an annular channel with a central ion filament was formed because of the strong wakefield, with enhanced filament compression along the direction perpendicular to the polarization. As a result, the explosion of that filament accelerates ions by CE to higher energies in S-plane than in the P-plane. These facts were tested experimentally during my PhD time. A large half-wave plate [18] was inserted just before the focusing off-axis parabola and rotated incrementally over more 90° to change the direction of the linear incident laser polarization from P to S, i.e the electric field being horizontal or vertical respectively. No particularity can be underlined from this scan done with more than 50 laser shots. The S and P polarizations give the similar energy cutoffs and spectral profiles for both ion species He^+ and He^{2+} as presented in figure 3.25.
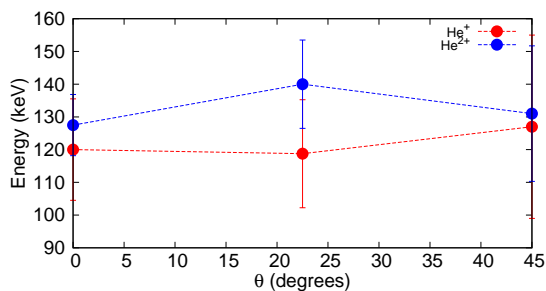
Figure 3.25: Energy cutoff for different incident laser linear polarization. Only three angles of rotation are plotted. Peak density $n_e \sim 5 - 7 \times 10^{18}$ cm^{-3}. $\theta = 0$: P-polarization. $\theta = 45°$: S-polarization

Our experimental results show an axisymmetric ion acceleration, independent of the linear polarization, on the contrary to predictions of Naumova *et al.* along with those of our pre-studies. This difference could be due to the fact that ions in the anisotropic layer/filament are not in sufficient number to be detected above the threshold level of the ion detector. Thus, the detected ions may be originating from the outer layer of the annular channel that presents an axisymmetric density distribution. In line with this study, we wanted to test the dependence of the acceleration upon the pulse ellipticity and in particular in case of circular polarization.

circular: A quarter-wave plate was inserted and rotated over 90° to change the ellipticity ε of the laser polarization. The ellipticity is defined in the following as:

$$\varepsilon = \tan(\theta + \frac{\pi}{4}) = \frac{a}{b} \tag{3.7}$$

---

[18]low-order, 810-nm-AR coated and thickness=200 μm

where θ is the angle by which the plate is rotated, a and b, the axes of the ellipse mapped out by the laser electric field. The offset angle in the tangent argument is due to calibration of the plate I used. The dependence of the cutoff energy upon θ is plotted in figure 3.26.
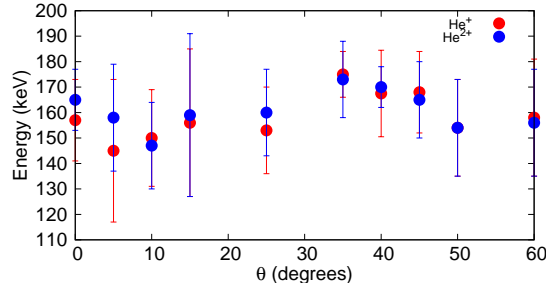
Figure 3.26: Energy cutoff versus the $\lambda/4$-plate angle of rotation. Peak density $n_e \sim 1 - 2 \times 10^{19}$ cm^{-3}. $\theta = 0$: circular polarization. $\theta = 45°$: linear polarization

As in the linear polarization case, no remarkable behaviour of that cutoff energy can be observed. However, here, the spectra show interesting features when shifting from linear to circular polarization. Figure 3.27 presents the spectra of three consecutive shots with the same ellipticity at peak density $n_e \sim 1 - 2 \times 10^{19}$ cm^{-3}. The circular polarization produces spectra with a conspicuous lobe towards 100-150
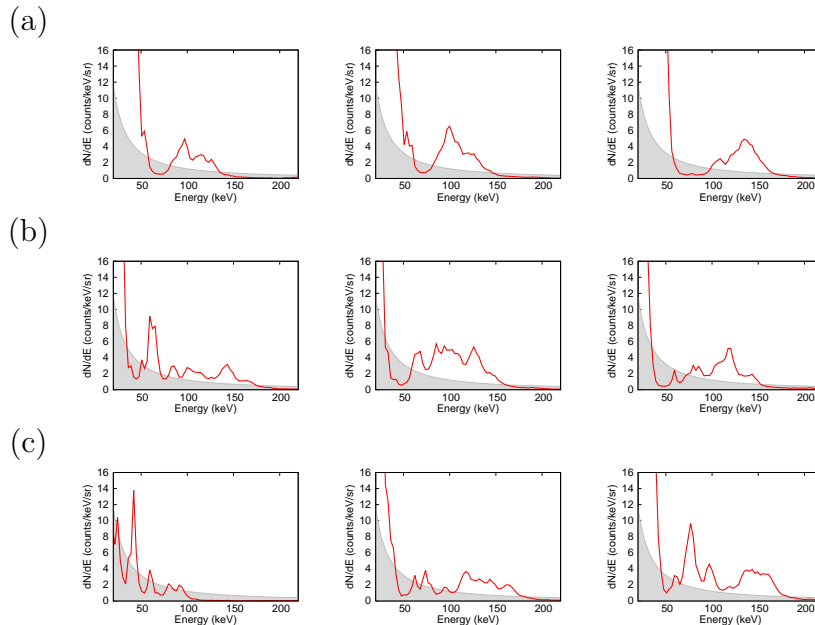
Figure 3.27: Ion spectra for different laser ellipticity for three consecutive shots in each row. (a) $\varepsilon = 1$ ($\theta = 0$, circular polarization). (b) $\varepsilon = \sqrt{3}$ ($\theta = 15°$, elliptical polarization). (c) $\varepsilon =$undef ($\theta = 45°$, linear polarization)

keV. In the elliptical and linear cases, multiple unstable peaks are observed. This dependence can be qualitatively tackled by considering the laser ponderomotive force for a linearly and circularly polarized pulse. Instead of using the transverse electron relativistic factor $\gamma_{\perp e}$ as in (1.31), this force can be directly related to the laser electric field via (with the notations of subsection 3.4.2 in the focal plane):

$$\mathbf{F}_p = -\frac{e^2}{4m_e\omega_L^2}\nabla[E_L(r,z,t)\mathbf{e}]^2 \tag{3.8a}$$

$$\text{for linear polarization,} \quad \mathbf{F}_p = -\frac{e^2}{4m_e\omega_L^2}\nabla E_L^2(r,z)\cos^2(\omega_L t - ct) \tag{3.8b}$$

$$\text{for circular polarization,} \quad \mathbf{F}_p = -\frac{e^2}{4m_e\omega_L^2}\frac{\nabla E_L^2(r,z)}{2} \tag{3.8c}$$

Note that averaging the force over the laser cycles gives the same expression for both polarizations $\propto \nabla E_L^2/2$. The $\cos^2$ dependence in (3.8b) introduces only for the linear polarization an oscillatory component of the force that will drive the electrons at a frequency $2\omega_L$. This might have some consequences on the electron temperature as qualitatively argued in the following. In the nonlinear regime, for a linearly polarized plane wave, Meyer-ter-Vehn *et al.* [177] showed that the introduction of a stochastic field representing the perturbed background plasma leads to a net energy transfer and electron heating in the focal volume. It proceeds from the dephasing of the electron oscillations due the random perturbation, so that the power transferred to the electrons is no more purely reactive but becomes active. The small stochastic perturbation the authors introduced may arise from the fluctuations of the electromagnetic field in the plasma, from the Raman instabilities for instance [178]. The use of a linearly-polarized field that drives the electron at a different frequency from that of the laser might favour the oscillation dephasing as compared to the circularly-polarized case. This polarization effect was numerically evidenced by Macchi *et al.* [96] in the overdense regime using 1D simulations where a linear polarization was observed to heat electrons much more efficiently than a circular polarization for similar initial plasma conditions.

The link between the electron temperature in the focal volume and the experimental shape of the ion spectra is now qualitatively discussed. Suppose that ions are accelerated in bunches and exhibit a spectrum of the kind presented in chapter 2 for *simple cases* with a prominent sharp peak located at the cutoff level. In absence of any electron, these bunches will explode significantly while travelling at non-relativistic velocities towards the detector (about 1 m away), because of the repulsive self-field they create (the Coulomb repulsion is stronger than current attraction at velocity $v \ll c$). Consequently, a large spectrum should be obtained. If well-localized lobes are observed, efficient neutralization must have taken place. This neutralization is due to electrons that accompany the drifting bunches and set a Maxwell-Boltzmann equilibrium around the positive charge (see the "collective parameters" part in 3.4.3). But we know that the characteristic scale length of the potential created by the electron is the electron Debye length λ_{De}. Equation

1.21 shows that $\lambda_{De} \propto \sqrt{T_e/n_e}$, with T_e the electrons temperature as meant in the previous discussion. Thus, for a given electron density, the neutralization is expected to become less effective for increasing electron heating, resulting in ion bunch spread. According to that qualitative reasoning, spectra with better-defined lobes should be obtained for a circular polarization.

The dependences of the ion cutoff energy on the laser duration and polarization was experimentally investigated and showed statistically relevant and interesting features that I discussed quantitatively when possible, if not qualitatively. Numerical simulations (PIC) in 2D or 3D should now be carried out to quantitatively confirm especially (*i*) the non-depletion of the channel, (*ii*) the sharper decrease of the energy for ultrashort pulses at high plasma density, (*iii*) the effect of a given elliptical laser polarization on the electron temperature and indirectly, on the neutralization of the ions bunches. I present now the experimental dependences of the ion cutoff energy on the plasma parameters.

3.4.3   Plasma dependences

The plasma density and gradient are varied to record their respective influence on the ion cutoff energy when the laser pulse at a relativistic intensity has a fixed duration ~ 35 fs. The relevance of such study rests on the fact that the wakefield amplitude and sustainability depend upon the the laser propagation conditions as a matter of fact, on plasma density and gradient. To vary parametrically the plasma density and the gradient should impact the pulse propagation and focusing, and thus the duration and amplitude of the laser wakefield. For the whole following study, the pressure and the laser-jet delay are fixed and the valve opening time varied to increase the peak density seen by the laser pulse (see the gas jet operating mode in section 3.2).

Peak density effect on the cutoff energy

For this scan, the pulse is sent onto a helium supersonic jet only. This jet presents a sharp gradient scale length of about ~ 150 μm and a plateau of 400 μm (see supersonic 100/400 in figure 3.6). As already mentioned in 3.4.2, the interaction of the laser with that jet did not produce any detectable ion signal above 8×10^{19} cm^{-3}. It was therefore very suitable for investigating the interaction at low densities, i.e. within a range where the pulse and the plasma free oscillations are quasi-resonant. The figure 3.28 shows the dependence of the He$^+$ and He^{2+} cutoff energies to the peak density. It is interesting to notice that for both ions species, the cutoff reaches an optimum, which is an observation qualitatively different from the continuous increase up to maximal reachable density $n_e = 3 \times 10^{20}$ cm^{-3} reported in Ref. [102]. As mentioned in chapter 2, subsection 2.1.1, our experiments is carried out with $\tau\omega_{pi} < 1$, where electronic and wakefield effects should be dominant, contrary to long-pulse conditions in
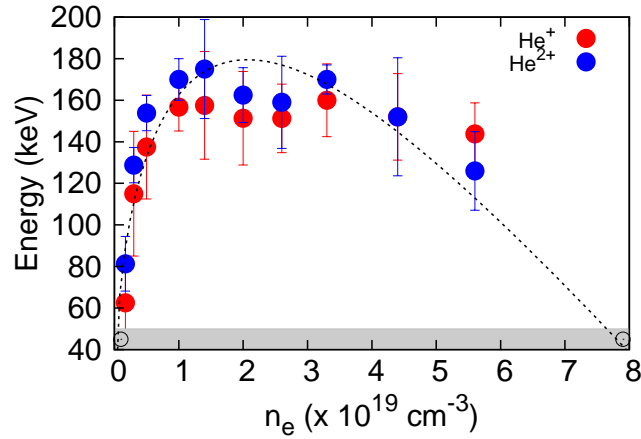
Figure 3.28: Energy cutoff versus plasma density for He ions at the normal to the laser axis using a supersonic flow. Empty dots refer to shots with no observable trace (gray shaded region out of the detector scope). The dashed line is a trendline indication

that reference. Thus, this optimum seems to indicate the quite different regime of the observed acceleration. Furthermore, the species follow the same trendline and present similar energy cutoffs, though the charge-to-mass ratio is twice as big for He^{2+}. Moreover, a closer look shows that the He^+-line lies generally below the He^{2+} ones, by about 10-15 keV in average, and up to 40 keV for some shots. These points can be interpreted as signature of charge exchange in the plasma, with additional energy gain in the sheath at the plasma-gas interface along the transverse direction (see figure 2.18) and will be addressed in details in the next subsection.

In figure 3.28, the ion cutoff energy increases sharply until about $n_e = 1 \times 10^{19}$ cm^{-3}. Then, a plateau is observed until about 4×10^{19} cm^{-3}. The trendline is then slowly decreasing until a peak density where no ions could be detected at around 8×10^{19} cm^{-3}. When testing the criterion of total depletion (1.37), high values of $a_0 = 15 - 30$ are obtained, unlikely to happen during the pulse propagation in the submillimetric plasma. This argument, coupled to a regime where strong wakefield effects are expected makes here the basic relationships for CE derived in chapter 2 irrelevant. The bell shape of the trendline can in fact be interpreted as a competition between two antagonist effects related to the laser wakefield.

If one considers the acceleration from the wakefield viewpoint as discussed in section 2.2 with numerical arguments, the rising part of the curve at low density is expected. In the linear regime, the amplitude of the radial electric field of the wakefield increases with $\sqrt{n_e}$ (see equation (2.42)). In the moderately nonlinear regime, numerical calculations that I did with WAKE confirm that point, until the moment the plasma wave would break. With the pulse duration of $\tau_L = 35$

fs used in the experiment, the quasi-resonance where $\tau_L = \pi/\omega_{pe}$ would occur in theory for $n_e = 3 \times 10^{18}$ cm^{-3}. If one considers the fact that pulse self-compression operates at our intensity level [173], the matching pulse duration for a plasma with $n_e = 1 \times 10^{19}$ cm^{-3} should be on the order of 18 fs, what is in agreement with simulations where a plasma matching the experimental jet was used (see 2.2.3 for the long run case). So this situation would create a sustainable wakefield of high amplitude. As shown in subsection 2.2.3 and figure 2.23, the ions from the channel gain their momenta in the strong wakefield. Thus, the longer the wakefield, the higher the energy gain.

On the other hand, I explained in section 2.2 that the wakefield lifetime is limited in 2D geometry by the transverse wavebreaking in particular [142]. This phenomenon should lead to the decay of the acceleration efficiency even if the wakefield amplitude can be quite high just before wavebreaking, since the accelerating field will vanish too early (with regard to ω_{pi}^{-1}), hindering a significant energy gain by the ions. I thus propose to discuss here qualitatively the falling part of the curve by considering as the limiting mechanism the transverse wavebreaking as pictured in figure 2.11 in subsection 2.2.1. I consider the fact that transverse wavebreaking arises after N_W periods, when the dephasing between the central part of the wake (nonlinear) and the periphery (linear) is equal to λ_{pe}, i.e. $N_W(\lambda_{Npe} - \lambda_{pe}) = \lambda_{pe}$. Recalling the equation (2.44), the ratio of the wavelengths can be written to show the dependence upon the plasma density when the quasi-resonance is met, i.e. when the wakefield amplitude is maximum. With $\sqrt{\gamma_{\perp e}} = \tau_L \omega_{pe}/\pi$ in the nonlinear regime and the same notations as in equation (2.44)):

$$\gamma_{\perp e} = 1 + \phi_{\max} \tag{3.9}$$

$$\frac{\lambda_{Npe}}{\lambda_{pe}} = \frac{2}{\pi}\sqrt{\frac{n_e e^2}{m_e \varepsilon_0}} \frac{\tau_L}{\pi} \cdot E_2(n_e) \tag{3.10}$$

Hence, the condition on the number of oscillations reads:

$$N_W = \frac{1}{\frac{2}{\pi}\sqrt{\frac{n_e e^2}{m_e \varepsilon_0}} \frac{\tau_L}{\pi} \cdot E_2(n_e) - 1} \tag{3.11}$$

The figure 3.29 plots the number of wake periods obtained by this model.

The model is relevant only when $\lambda_{Npe}/\lambda_{pe} \geq 1$. Therefore, the rising part of the function $N_W(n_e)$ has no physical meaning within the framework of the model (red region in figure 3.29 for $\tau = 35$ fs). Within the interval of validity, the transverse wavebreaking is seen to be favoured when the density increases. Moreover, the interval of validity shift towards higher densities if the pulse duration shortens from self-compression. Interestingly, with that qualitative model, within the range $n_e = 1 - 3 \times 10^{19}$ cm^{-3}, a large number of oscillations are expected for pulse durations within 18 and 35 fs.

From the interplay of the two effects acting oppositely when the plasma density is increased, it is consistent that an optimum in ion energy cutoff be reached for
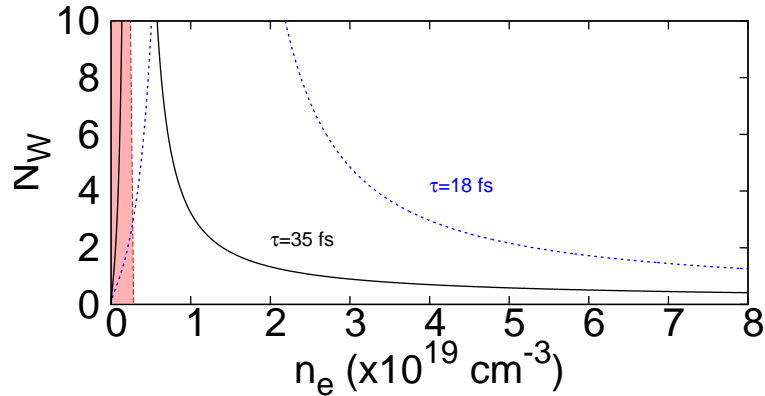
Figure 3.29: Number of plasma oscillation before transverse wavebreaking versus the plasma peak density for two laser pulse durations. The rising part of the curves have no physical meaning with regard to the model (red region for $\tau = 35$ fs)

certain range of density. For the density range corresponding to the increasing part, the wakefield excitation would dominate, while beyond the plateau at higher densities in the falling part, the transverse wavebreaking would be dominant. A more quantitative study of this dependence should be done with PIC codes in our conditions to confirm that analysis and in particular to assess the validity of the criterion I used for the occurrence of the transverse wavebreaking. I now proceed to the analysis of the ion number at the optimum of acceleration.

Ion number and long-term evolution from charge-exchange

Over the cutoff plateau, it is interesting to notice that in fact, though the cutoff energy stagnates, the number of accelerated ions (in total and for each species) increases by a factor of two (and then decreases as the cutoff energy decreases). The figure 3.30 presents that result. The shape of the curve in figure 3.30 might
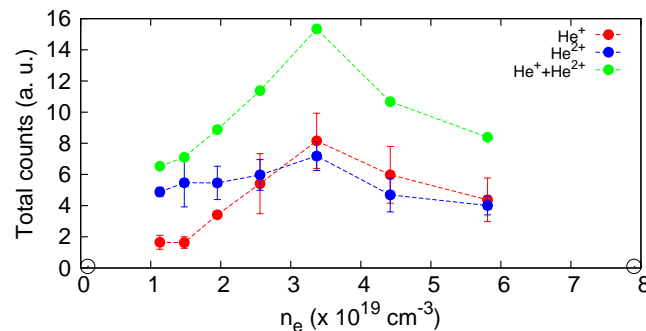
Figure 3.30: Integrated count number versus density over the energy range $[50, 250]$ keV. Empty dots refer to shots with no observable trace

be revealing two opposing effects depending on the density, that operate during

the laser propagation. On the one hand, the laser radiative energy concentration in a small focal volume, due to self-focusing enhancement as the ratio of the laser power P_0 to the critical power P_c for self-focusing increases with n_e[19] [55,174,179]. On the other hand, the laser energy dilution in the plasma due to diffraction and plasma defocusing as steep and dense electron gradients arise at the front of the pulse[20] [4]. This effect can also be associated to the laser filamentation instability, which depletes in energy the main laser channel into side filaments, and the growth rate of which becomes larger when the density grows [107,175]. Competition between these two limit cases might be a suitable qualitative explanation for (i) a constant level of cutoff energy, since the plasma radius reduces from laser self-focusing while the density grows, with the excitation of an increasingly strong wakefield and correspondingly, the increasing number of accelerated ions, and (ii) a decrease in the cutoff energy along with that in ion numbers when the laser starts scattering in the plasma and losing its energy in heating filaments, accompanied with a weaker wakefield and early wavebreaking. Quantitative conclusions would require some numerical modellings.

Besides, the fact that both species reach the same energies, with a small difference though, and follow the same trendlines is not insignificant. These facts are remarkable owing on two main points:

- the ratio $I_0/I_{sb}(\text{He}^{2+}) \sim 1000$ in our conditions ensures full ionization of helium in the focal volume, where I_0 is the laser incident intensity and $I_{sb}(\text{He}^{2+})$ is the threshold intensity for suppression of the potential barrier (see values in 1.1). He^+ should only be present at large radius, far from the laser[21], and not be accelerated to suprathermal energies.

- for a given acceleration time and electric field, He^{2+} ions should exhibit twice as large final velocities and four times higher kinetic energy than He^+ ions, when starting from a mixture where both populations are present and at rest.

Thus, the previous observations cannot be explained without invoking very probable charge-exchange that transform He^{2+} into He^+ without momentum transfer. Indeed, within the energy range $[20, 500]$ keV, elastic collisions of He^{2+} projectiles with He atoms are largely dominated by a one-electron capture process with a typical capture cross section $\sigma = 10^{-16}$ cm^2 (see figure 3.31). Charge-exchange also affects He^+, but with a lower probability. Afterwards, for the small offset in energy, I can propose the following explanation: in simulations with CALDER-CIRC,

---

[19] $P_c = 16.2 n_c/n_e$ [GW] in 2D geometry

[20] the plasma refractive index in the relativistic case yields $\eta_r = \sqrt{1 - n_e/(\gamma_{\perp e} n_c)}$, with $\gamma_{\perp e}$ the transverse relativistic factor of the electrons, so that the phase velocity increases as the density increases entailing the divergence of the wavefront

[21] numerical simulations by Rachel Nuter from the CEA/DAM with $I_0/I_{sb}(He^{2+}) \sim 1000$, in our interaction conditions, exhibit a He^+-corona at 100 μm from the laser axis of propagation
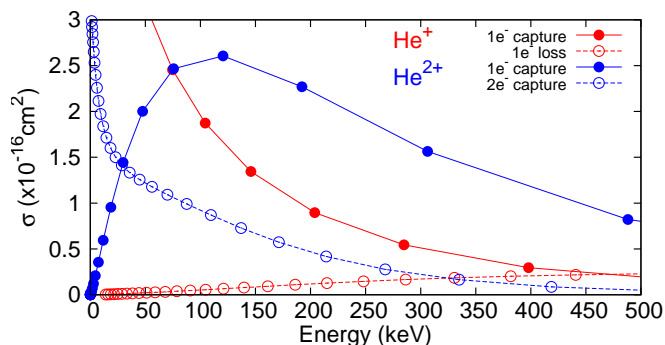
Figure 3.31: Cross-sections for different channels of interaction with the neutral gas He versus incident kinetic energy of helium ions projectiles (He^+ in red and He^{2+} in blue), taken from [180]. Single electron capture (red full dots) and loss (red empty dots) by He^+. Single (blue full dots) and double (blue empty dots) electron capture by He^{2+}

we observed that a sheath is formed at the plasma-interface in the transverse direction. It corresponds to the radial limit of field-ionization of the gas by the intense pulse (see figure 2.18). Therefore, the position of that interface depends upon the initial pulse transverse shape and the condition of focusing in the plasma. As explained in chapter 1 subsection 1.2.3 for TNSA, the sheath can support an electric field that slowly decay with time. In our case, that electric field is transverse ("transverse TNSA"), and would transfer differently some momenta to the ionic species (see the discussion of that point in the PIC part in subsection 2.2.3).

It is difficult to provide a conclusive experimental argument to back up this all-theoretical discussion about charge exchange, all the more since He atoms were not collected to assess the relative fractions of each species. However, one can notice in figure 3.30, that below $n_e = 3.5 \times 10^{19}$ cm^{-3} (plateau cutoff at 160 keV in 3.28), the rate of increase of He^+ is larger than that of He^{2+}. This can be due to more probable electron charge-transfer, as the free-mean-path of He^{2+} projectiles decreases when density increases at constant cross section[22]. Additionally, we have clearly observed experimentally that *only* He^+ ions are detected to comparable cutoff energies when sonic and transonic jets with larger gradient scale lengths are employed with the same laser parameters (this point is addressed with further details in the following part). Qualitatively, in these cases, the longer gradients scale lengths (*i*) thicken the neutral gas corona and (2) contribute to the pulse self-focusing to sizes smaller than in the supersonic case. Consequently, it well probable that charge-exchange during He^{2+} outward streaming occur more efficiently in these latter cases. Once again, quantitative conclusions need numerical contributions.

---

[22]the average free-mean-path $\mathcal{L}$ is given by $\mathcal{L} = 1/(n_e \sigma)$

As the laser propagation determines the structure of the wakefield, it is important to compare the resulting acceleration for a given density level but different gradient scale length.

Gradient effect on the cutoff energy

As mentioned in the previous section, when sonic and transonic flows are used with our laser parameters, only He^+ ions are being detected. However, the aforesaid discussion also shows arguments in favour of charge-exchange relating directly the detected He^+ ions to the initially accelerated He^{2+}. Therefore, a comparative study of different plasma profiles based merely on He^+ detection is fully valid to unravel feature of the acceleration specific to each type of flow. The figure 3.32 presents the results of this comparative study of the acceleration with sonic, transonic and supersonic nozzles (see figure 3.6 for the corresponding profiles). Two main observations can be emphasized:
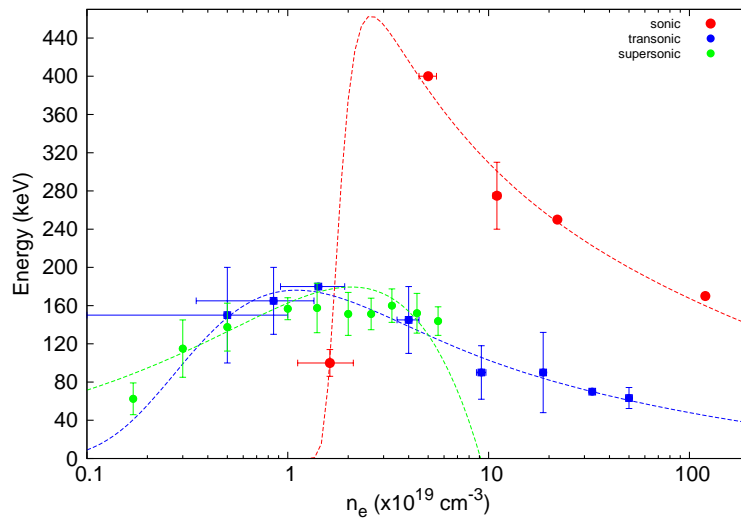
Figure 3.32: Cutoff energy dependences upon the peak density (semi-log scale) for three different flows (see figure 3.6 for nozzle correspondence) at 200 μm from nozzle exits. The fit functions are trendline indications

- for peak densities from $\sim 5 \times 10^{19}$ cm^{-3} to near-critical densities, the sonic flow provides a much more efficient acceleration with a cutoff energy almost three times higher than other flows at 5×10^{19} cm^{-3}

- within the same density range, the large gradient scale length nozzles exhibit a smooth cutoff energy decrease (red and blue lines in figure 3.32), whereas the cutoff energy sharply decays for a steep gradient scale length (green line in figure 3.32)

It is interesting to note that a transonic jet, that exhibits peak density and gradient values intermediate between sonic and supersonic jets (see figure 3.6 and appendix

A), has a behaviour which is a somehow hybrid of the two other limit flows as far as ion acceleration is concerned.

Within the low density range $n_e < 10^{20}$ cm^{-3}, the figure 3.4.2 showed that in our conditions, a sharp gradient scale length from a supersonic nozzle will improve the laser self-focusing compared to a smooth gradient from a sonic nozzle. Thus, a stronger wakefield should be excited in the first case and the ion acceleration should be more favourable. Inversely, one can expect the sharper gradient to be more detrimental at higher density, $n_e \geq 10^{20}$ cm^{-3}, as multiple instabilities and energy depletion [107, 174, 175] will affect significantly a tightly focussed pulse, leading to its destruction before it has efficiently excited the plasma. For that density range, the interest of the adaptive-like sonic gradient appears clearly in order to reach MeV-range cutoff energies with that interaction configuration, where a longer interaction length would enable higher intensity via self-focusing. I can scarcely comment further with regard to theses preliminary observations, as no simple model or accessible numerical tool like WAKE can be used in our conditions to reliably and quantitatively analyse the effect of the gradient on transverse ion acceleration. The study of this dependence is PIC-pending. These numerical investigations are all the more delicate since a long and well-resolved simulation box must be employed to take into account properly the laser self-focusing in the various gradients and also to be able to describe the ion bunch evolution through, shocks and sheath, along the transverse direction over at least ten picoseconds (see 2.2.3 for an example of this type of long run). I let now the considerations on the cutoff energy and start commenting on the overall ion spectral distribution that we obtained in the experiments.

3.4.4   Ion spectral properties

So far, no quantitative discussion has been initiated yet about the spectra that are obtained in the experiments I carried out for transverse acceleration investigations. This section deals with that topic in particular, on account of the fact that, for first time, striking modulations were experimentally obtained in the spectra of ions accelerated from laser-underdense plasma interaction. Besides this observation, the dependence of the spectrum to the plasma density reveals some fundamental aspects of the accelerating mechanism, along with important implications of the instruments used to detect the ions.

Modulations of the spectrum

The spectral structures are studied with a supersonic flow allowing in our conditions the observations of both ion species (jet 100/400, see figure 3.5). The gas density is so that typically $n_e = 1 - 3 \times 10^{19}$ cm^{-3} (plateau region in 3.28). The figure 3.33 shows the type of recorded spectra with thin multi-humps, which are extracted according to the method exposed in subsection 3.3.2.
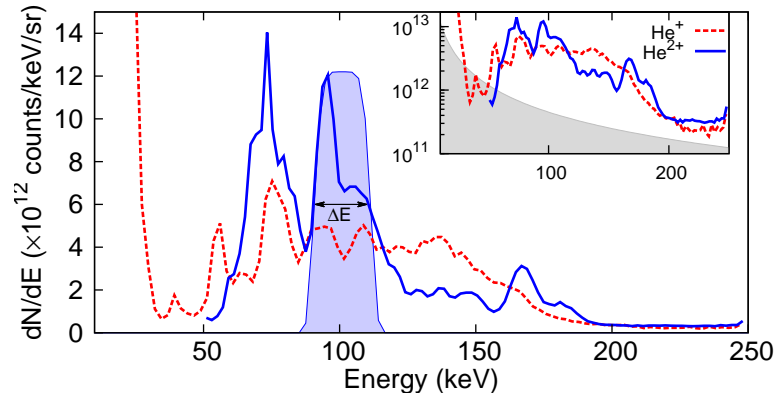
Figure 3.33: Extracted ion spectra (relative counting, bin width $dE = 2$ keV). $\Delta E < 20$ keV for He^{2+}. Inset (logscale): cutoff ~ 200 keV, signal-to-noise ratio $50 : 1$ (shaded below dark noise level)

As discussed in the previous section 3.4.3 and illustrated in figure 3.31, charge-transfers without momentum transfer are likely to occur when the He^{2+} projectile travels through the neutral gas towards the detector. This is in our case the probable origin of the presence of He^+ within the same energy range $[60 - 200]$ keV. However, the He^+-trace follows the same trendline but does not exactly reproduce the He^{2+}-trace. This could stem from the fact that (i) the trace extraction configuration for one species might be slightly offset with regards to the other species[23], (ii) the charge exchange is only probabilistic, and thus features in He^{2+}-spectrum might be absent in He^+-spectrum, (iii) transverse sheath effects as explained in the previous section might play a role in shifting the traces with regard to each other and (iv) the electric environments of He^+ and He^{2+} bunches might be variable and inducing different behaviours (for instance a bunch-CE) while propagating radially outwards.
For both species, there exists an energy gap at low energies. A lower energy branch is visible for He^+, ending at ~ 25 keV, but not for He^{2+}, because of the limit of the MCP detector at ~ 48 keV for that species.

Even though the positions of the humps along with their amplitudes can fluctuate from shot to shot, these modulations are a robust spectral feature appearing whenever the same interaction conditions are satisfied. The following figure 3.34 presents three consecutive shots to illustrate that point.

The same hereinbefore mentioned spectral properties are applicable for each of the first three panels and emerge as average features in the fourth one(thin multi-humps, separated spectral branches, correspondences between the species). More precisely, from the table 3.1, the position of the peaks around 100 keV in

---

[23]in the worst case, by few CCD pixels, making no difference at low energy and about 2% RMS error at 150 keV, see 3.3.2
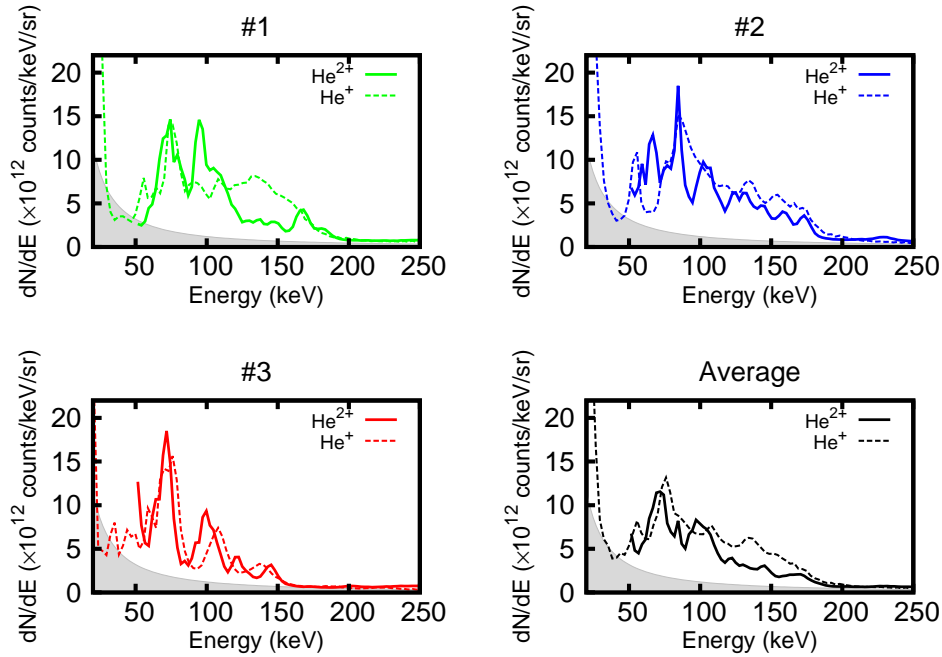
Figure 3.34: Spectra from three consecutive shots for both He species. Same extraction parameter as for figure 3.33. The shaded regions lie below the noise level. The average spectrum is the arithmetic mean of the three subsequent spectra

the He^{2+}-spectrum varies relatively by only few percent, with an average energy spread of about 20%.

shot (#)	peaks	FWHM	$\Delta E/E$
1	74 - 101	20.5 - 20.6	27.7 - 20.4
2	84 - 105	7.6 - 18.8	9 - 17.9
3	72 - 102	17 - 22.6	23.6 - 22.3

Table 3.1: Peak positions and corresponding energy spreads relative to He^{2+}-spectra for three consecutive shots in similar conditions as in figure 3.33

As established in chapter 2 for 2D and 3D geometries in simple conditions[24], and also in studies [17, 47], the pure CE of an ion population will end up into a spectrum with a peak located at the energy cutoff. However, neither a direct ion energy measurements in [17] nor an indirect ion velocity assessment in [47]

---

[24]and also in 1D for a stationary problem

did produce that signature. The explanation given by the authors rests on the theoretical fact that, during the laser-plasma interaction, multiple CE happen along the laser propagation axis, and each of which having a different amplitude, as the laser intensity varies (focusing/defocusing, absorption, instabilities etc...). The figure 3.35 illustrates the multiple Coulomb explosions at different different cross-sections.
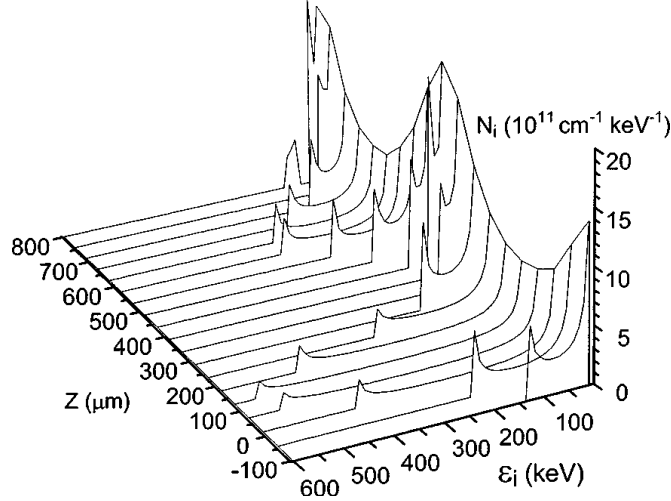
Figure 3.35: Energy distribution of fast ions at different cross sections for parameters of the experiment reported in Ref. [47]. The laser propagates towards positive Z (extracted from [47])

Consequently, there will be on the ion detector, that integrates all the radial emissions, an overlapping of several energy-shifted peaked spectra resulting in a broad maxwellian-like energy profile. The figure 3.36 shows the overlapping effect on the calculated spectrum which becomes maxwellian.

In the present case, the same remarks could apply but with different implications due to the following points:

- the ratio P_L/P_c for plasma densities within $1 - 3 \times 10^{19}$ cm^{-3} yields $8 - 25$, which is enough for self-focusing to be operative even for an ultrashort pulse as that from Salle Jaune [25], but modest compared to the same ratio $P_L/P_c = 173$ in [17]. As a result, one can expect that the pulse will focus in the plasma more slowly in our case (see the envelop evolution equation in [179]).

- the size of the plasma at the shooting height ~ 700 μm is about twice the laser vacuum Rayleigh range z_R (see equation (1.2)) in our case, whereas it

---

[25]in [181], the product $\omega\tau/\gamma^{1/2}$ is proposed instead of P_L/P_c as a criterion of laser self-focusing
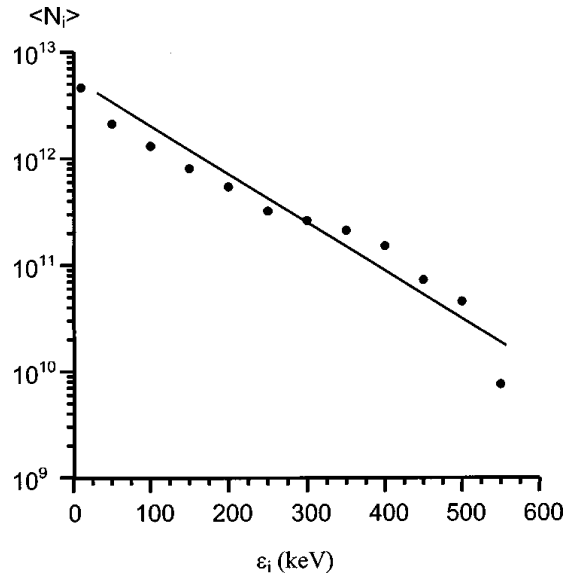
Figure 3.36: Total number of fast ions with energies exceeding ε_i integrated over the laser channel length for parameters of the experiment reported in [47]. The solid line is the Maxwellian function with a temperature of 80 keV (extracted from [47])

> is about 10 z_R in [17]. As laser self-channelling happens in reference [17], a long-range laser-plasma interaction inducing important CE throughout the plasma is reported by the authors.

The conjunction of both previous points should lead in the experiments I carried out to sizeable laser vector potential a_0, leading to a strong nonlinear wakefield responsible of the transverse acceleration, but also to a limited number of foci of acceleration, as the wakefield amplitude should follow that of the laser before wavebreaking, and so do the density modulations in the channel created by the wakefield (see the modulations in 2.22). In this respect, the overlapping of spectra should be of lesser impact when integrating the ion emissions. Thus, observation of isolated peak spectra, similar to the ones predicted by CE theory in the long-pulse case and with electron depletion should be highly favoured (see also the peaked spectra from PIC code in 2.2.3).

This explanation can be completed by a geometrical argument about the detector, and was already tackled in subsection 2.2.3 in chapter 2. Indeed, the detector entrance selects a pencil of vector momenta originating from the source. In other other words, the detection filters in a small volume around 90° in the ion polar phase space. The entrance is made of a pinhole of 100 μm diameter located at 80 cm from the jet (see also figure B.1 for a general outlook of the detector). Thus, the solid angle angle is 1.2×10^{-8} sr, i.e. 20 times smaller than that reported in [17], and susceptible of collecting only ion emissions at the laser-axis normal. I presented in figure 2.21 simplified PIC simulations of transverse acceleration that

proved the effect of a sharp momentum selection into revealing inhomogeneities in the phase space and peak structures in ion spectra.

In these conditions, the short interaction length *and* fine detection configuration used for our experiments are very likely to explain the experimental modulations and peaks. I now present an additional set of data corroborating this interpretation.

Density effect on the spectrum

I come back to the set of data used to plot figure 3.28 and consider now the whole spectrum profile and not only the cutoff level. Figure 3.37 shows the spectral modifications when the plasma density is varied. The panels on each row correspond to two consecutive shots in the same conditions (shot 1 and 2). The couple of columns on the left refer to He^+'s traces and that on the right to He^{2+}'s.

I focus first on the He^{2+} columns. If one only consider the trendline and not the peaks, a clear tendency can be observed as the density increases. To summarize, at low densities $n_e \sim 1 \times 10^{19}$ cm^{-3} and below (panels (a) and (b)), the spectra have a profile matching a square-root-like trendline. Recalling spectral shape from (2.34) and from figure 2.8, the observed spectra seem to be in agreement with CE theoretical calculations from the "transient" model in simple cases I developed in chapter 2. However, in our conditions, the criterion for having a pure CE are not fulfilled, so that this low-density case is in fact a *non-simple* regime of acceleration (see 2.2). At intermediate densities $n_e \sim 2 - 3 \times 10^{19}$ cm^{-3}(panels (c) and (d)), large spikes arise in the spectra. This corresponds to the density window that was highlighted in the previous part (plateau in cutoff energy for growing density) as propitious for spectral modulations and their stability was also discussed. As for the trendline, the decreasing amplitudes of consecutive peaks tell it is reversed compared to low density cases. Finally, at high densities $n_e > 4 \times 10^{19}$ cm^{-3}, the spectrum is readily of maxwellian-shape and vanishes at around 6×10^{19} due to electron-ion charge exchange (see figure 3.31 and the associated discussion).
In parallel, by considering the He^+-spectra on the left of figure 3.37, it would have been difficult to draw some conclusions as clear as in the other case. The reason comes from the complex statistical charge-exchange happening at large radius that is responsible for the presence of that species. Therefore, I would recommend for the analysis of such spectra to focus primarily on the He^{2+} traces[26].

The same qualitative conclusions are obtained with PIC simulations using CALDER CIRC. The parameters are the same as in subsection 2.2.1 and mimic the experiment except for the plasma length which is here ten times smaller to

---

[26]a similar method is commonly used when only proton features are considered for diagnosing the laser-thin foil interaction

reduce runtime. A tight filter is used in the phase space to simulate the effect of the pinhole aperture, which affects the spectral profile as previously discussed (see subsection 2.2.3). Two limit densities are tested, one in the low density regime $n_e = 1 \times 10^{19}$ cm^{-3} (same as in figure 2.21) and the other in the high density regime $n_e = 5 \times 10^{19}$ cm^{-3}. The figure 3.38 presents the conclusions.

From these simulations, a basic physical explanation would be the fact that at low density, only a limited number of powerful accelerating foci occurs in the channel, whereas at high density, a continuum of explosions is created all along the channel. In the latter case, the aperture of the pinhole is insufficiently small
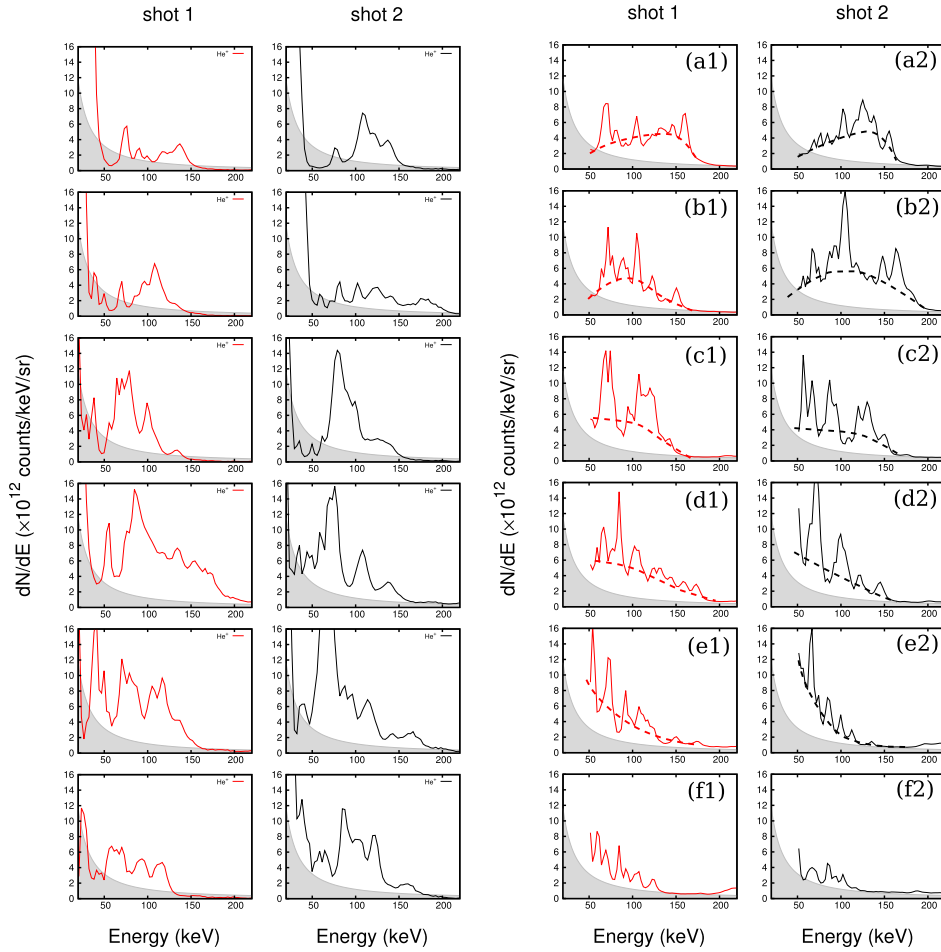
Figure 3.37: Helium species spectra obtained from CE with $n_e \in [1,6] \times 10^{19}$ cm-3 for two consecutive shots (shot 1 and 2) in the same conditions as in 3.28 (relative counting, energy bin $dE = 2$ keV). The scales are common to all panels. (Left) He$^+$-energy distribution. (Right) He^{2+}-energy distribution. The electron density n_e is (a) 1, (b) 1.4, (c) 2, (d) 3.3, (e) 4.4 and (f) 5.6$\times 10^{19}$ cm^{-3}. The shaded region lies below the noise level. The dashed line is a trendline indication

(a)   (b)

(c)   (d)
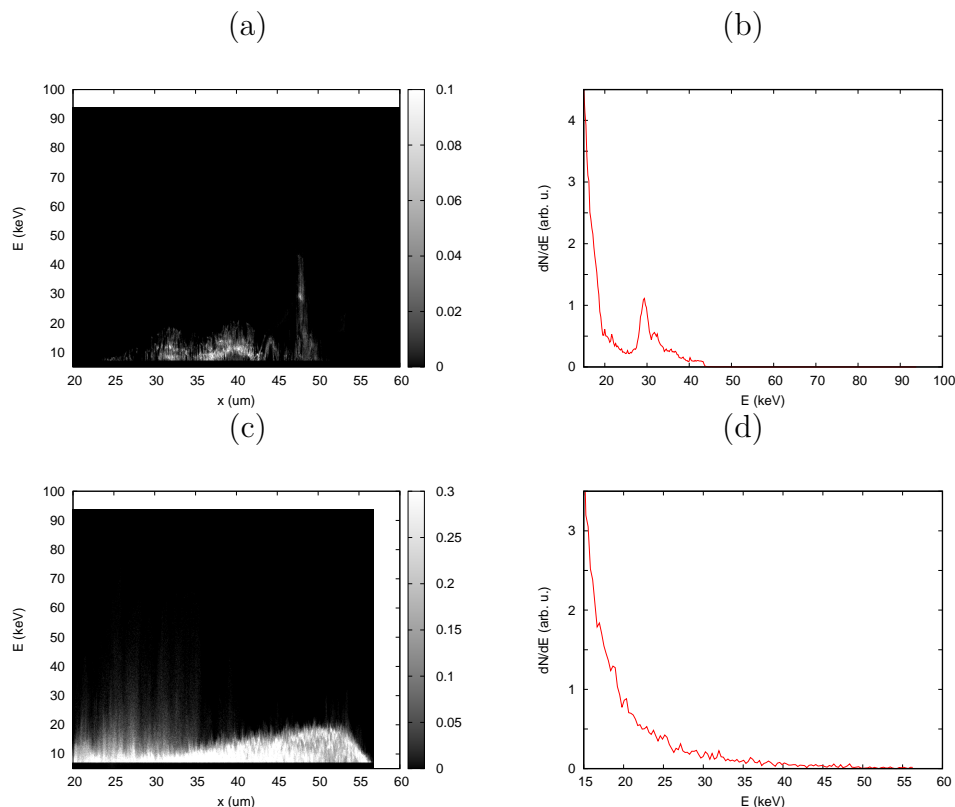
Figure 3.38: Spectral dependence with the plasma density: (a) phase space and (b) spectrum for $n_e = 1 \times 10^{19}$ cm^{-3}. (c) phase space and (d) spectrum for $n_e = 5 \times 10^{19}$ cm^{-3}

to resolve the peaks efficiently. Therefore, to a given plasma density corresponds a solid acceptance threshold above which single peaks cannot be obtained. This is in fact the same argument as given in [47] and [17], but this time in a different regime of acceleration implying the laser wakefield and in a more refined version linking the density parameter and the detector aperture.

It can be also interesting to add that the number of accelerated ions varies significantly within a given energy bin. Thus, these experimental and numerical studies (re)demonstrate that the increase in density does not simply increase the number of "explosions" along the channel until the gaps between peaks are filled, but reshapes the energy distribution, because the laser pulse does not propagate equivalently in all the cases.

3.5   Conclusion

In this part, a detailed description of the experimental setup (including the new gas jets and the seven diagnostics) implemented in "Salle Jaune" was presented. Stable ion acceleration *only* along the direction transverse to the laser propagation axis was demonstrated. Although its geometry is similar to previous experimental

reports on Coulomb explosion, the acceleration has some dependences upon the laser and plasma parameters indicating that the electrons play a major role in the ion acceleration and that it is produced by the strong wakefield the ultrashort pulse can excite in its wake. The use of a thin jet and a spatially selective ion detector made it possible to well isolate within a certain density range singularities in the phase space resulting in single peaks in the ion spectrum. The data analysis should be prolonged by series of resource-demanding PIC runs to assess quantitatively the role of each parameter at stake.

After considering the ion acceleration from the viewpoint of the resulting gain, I will deal with the acceleration from the viewpoint of some plasma structures at the origin.

Chapter 4

Structures in underdense to near-overdense plasmas

The previous chapter was dedicated to the acceleration of ions from transverse push of the laser wakefield. The particles, distributed in modulated spectra, are in fact detected after a chain of nonlinear and probabilistic phenomena arising in cascade, from the ionization and laser self-focusing to charge-exchange and re-acceleration in a sheath. These effects can be associated with interesting plasma structures. To study these structures can definitely reveal clues on the real conditions of the acceleration. We were not able to observe directly any wakefield in our experiments, primarily because it is a dynamic object with a typical timescale of tens of femtoseconds or less for the density range we tested. Therefore, with the duration of our illuminating probe beam ($\sim$ 35 fs), no snapshot with clear modulations can be taken in the temporal domain (snapshots have been taken in the frequency domain [182]). However, other structures linked to the acceleration and remnant in the plasma can be observed in our conditions. In particular, the figure 4.1 is the shadowgraphic illustration of the scheme in figure 2.18 presented in the theoretical part. The main components playing a role in the acceleration in underdense regime (channel and sheath) are identifiable, apart from the wakefield for the reasons I just mentioned.

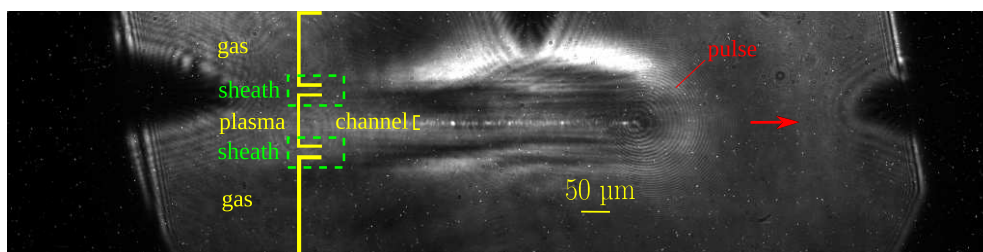

Figure 4.1: Ultrashort laser pulse and plasma channel and sheath in the wake ($n_e \sim 5 - 6 \times 10^{19}$ cm^{-3}). For this shot, ions were accelerated to about 200 keV

This section deals with some of the experimental observations of remarkable plasma structures that develop on a picosecond timescale or more. The experimental

setup is naturally that in figure 3.9 and the transonic jet (300/400, see figure 3.6) was mostly used for conducting these experiments. When the highest density was targeted close to and above n_c, the sonic jet was implemented.

4.1 Channel & filament

The shadowgraphic diagnostic enables one to take snapshots of the plasma. It gives a qualitative information of the spatial distribution of the electron density gradients. In our experimental case, this type of map can be monitored from the moment the laser enters the jet, denoted t_0, and creates the plasma, until 300 ps afterwards. Within that timespan, all the interesting phenomena related to ion acceleration due to the interaction with the pulse can take place. The final step of a cascade is the hydrodynamical-like expansion of the hot plasma.

4.1.1 Channel evolution: early Taylor-Sedov blast wave

The figure 4.2 illustrates the evolution of the plasma channel bored by the laser from a moment where the pulse already passed (the pulse breaks out of the plasma at about $t_0 + 2.2$ ps). The sequence is associated with the acceleration of He ions up to energy cutoff on the order of 200 keV. In this case, only single trace of He^+-ions were recorded. This could be due to efficient charge exchange affecting He^{2+}-ions when they travel through the corona, as proposed in chapter 3 subsection 3.4.3. One can see, already from $t_0 + 6$ ps in panel (a), that the channel has sharp and thin edges. These are the shadowgraphic signatures of a shock formed in the plasma when the electron fluid accumulates in the shell and the channel empties. From panels (b) to (e), the shock is seen to propagate transversally, as does the entire plasma corona.

It is interesting to consider the rate at which that shock actually expands. For each shadowgram, I selected two given cross-sections on the left side (entrance of the jet) where the channel expansion starts earlier and monitored in time the radial position of the first dark line (local minimum of intensity). The figure 4.3 reports the results for one cross-section (similar for the other cross-section).
The shock position does not change much until $t_0 + 44$ ps ($r \sim 13.4$ μm). This timespan would fairly correspond to the time needed for the shock to peak in amplitude. Afterwards the position increases nonlinearly. In Ref. [183], it was suggested that the deposition of energy by femstosecond laser pulses in gases could produce cylindrically symmetric blast waves in the collisional regime, under the form of a radially expanding channel (called plasma filament in the text). In their case, cluster jet were used to increase the laser absorption and facilitate the formation of dense shocks. In our case, the use of helium at a higher density prevents the formation of clusters (see appendix A, section A.3), while clear shocks
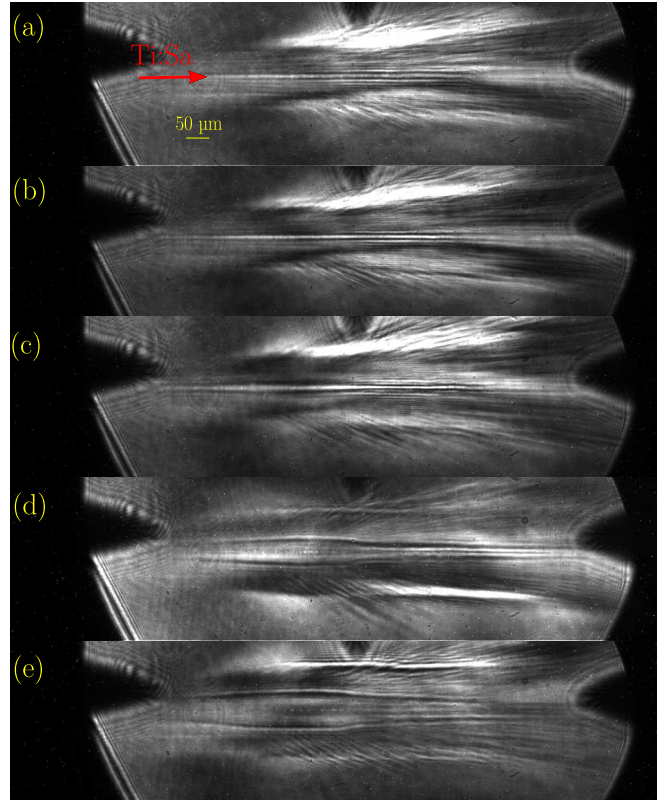
Figure 4.2: Shadowgrams showing the time-resolved evolution of the channel bored by the intense pulse entering the plasma from the left side at t_0. Plasma density: $n_e \sim 5 \times 10^{19}$ cm^{-3}. (a) $t_0 + 5.8$ ps, (b) $t_0 + 10.7$ ps, (c) $t_0 + 30.7$ ps, (d) $t_0 + 144$ ps and (e) $t_0 + 277$ ps
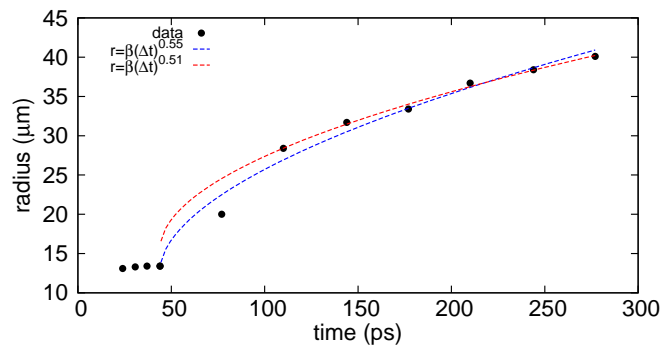
Figure 4.3: Shock position versus time from $t_0 + 24$ ps. The dashed coloured lines are least squares fits of the data with functions of the form $r = \beta \Delta t^\alpha$ over different range of time. Blue: from 44 ps. Red: from 110 ps

can still be observed and tracked. A historically important solution to collisional blast waves [1] belongs to the Taylor-Sedov analytical class of solutions, whereby a shock wave cruises undisturbed without radiating (energy-conserving shock) in a

---

[1] used by G. I. Taylor to infer from photographs the energy released during the test-explosion of the first atomic bomb in Alamagro (USA) in July 1945

non-resistant medium. This solution is self-similar of characteristic radius $R(\Delta t)$ given by a dimensional analysis [184]:

$$R(E, \gamma, t) = \beta(E, \gamma, t)(\Delta t)^{\alpha} \qquad (4.1)$$

with E the total driving energy, γ the adiabaticity coefficient of the gas ($\gamma_{He} = 1.67$), Δt the time elapsed from the moment the expansion can be considered to be self-similar and α the deceleration parameter. By analogy to the collisional regime, I thus did the least squares fits of our data in the collisionless regime by functions of the form of (4.1) and the best fits are plotted in figure 4.3 for two different range of time. The blue fit starts from 44 ps where significant increase of the shock position is observed and α reads 0.55. If the fit starts from a moment where the radius is twice the initial value, i.e from 110 ps, then α reads 0.51. This latter criterion for relevant timespan was also used in Ref. [183] to ensure that the expansion be self-similar, i.e. quasi-independent of the initial conditions. The values experimentally obtained for α are both very close to that of a cylindrical self-similar blast wave, where $\alpha = 1/2$. In the experimental works reported in Refs. [183, 185], the important departure of the deceleration parameter from the Taylor-Sedov value is attributed to the radiation of the shock and the development of surface instabilities. In our case where α is very close to $1/2$, with channel walls being straight and smooth. It is thus likely that the channel expands, after about 40 ps in the collisional regime, like a quasi-adiabatic (non-radiative) cylindrical self-similar blast wave. Also, it is interesting to notice that in Ref. [183], by using a 35-fs pulse with 100 mJ (>800 mJ in our case), such a self-similar expansion solution could be identified only after 7 ns.

This fact is also interesting to briefly emphasize another point concerning the hydrodynamic (collisional) regime. In fact, if the plasma can be considered to be set in this regime from tens of picosecond after the beginning of the interaction, it is not possible in consequence to assess the cutoff energies of the suprathermal ions that we detected on the basis of the expansion of the blast wave as presented in figure 4.2. This indeed gives only access to the velocity of the infrathermal particles of the hot plasma heated by the laser [47]. A simple linear fit of the data points in figure 4.3 gives the average velocity (thus overestimating the asymptotic velocity value) of the electron shock front of 1.1×10^5 m/s i.e., if the plasma is considered to be quasi-neutral, an ion kinetic energy close to 300 eV[2], three orders of magnitude below the energies we measured.

4.1.2 First indication of the formation of the central filament

The results discussed in the present subsection concerning the central filament are preliminary because observations as direct as a shadowgraphic trace for

---

[2]then the electron-ion collision rate ν_{ei} ($T_e = 300$ eV) $\simeq 2 \times 10^{12}$ Hz, close to $\omega_{pi} \simeq 3 \times 10^{12}$ Hz, so that the ion expansion is collisional

the channel in the previous part were not made, but should be targeted for a final experimental demonstration. However, evidences from the analysis of the experimental phase maps, reproducible over several laser shots give a good indication of an on-axis density hump that can be attributed to the presence of a filament. To avoid axial artefacts appearing when Abel-inversion is implemented, I reason directly at the unwrapped phase level. The figure 4.4 represents the phase extracted from a small region around the channel in the shot of panel (b) in figure 4.2 at $t_0 + 10.7$ ps (relative dephasing). The plasma induces here a
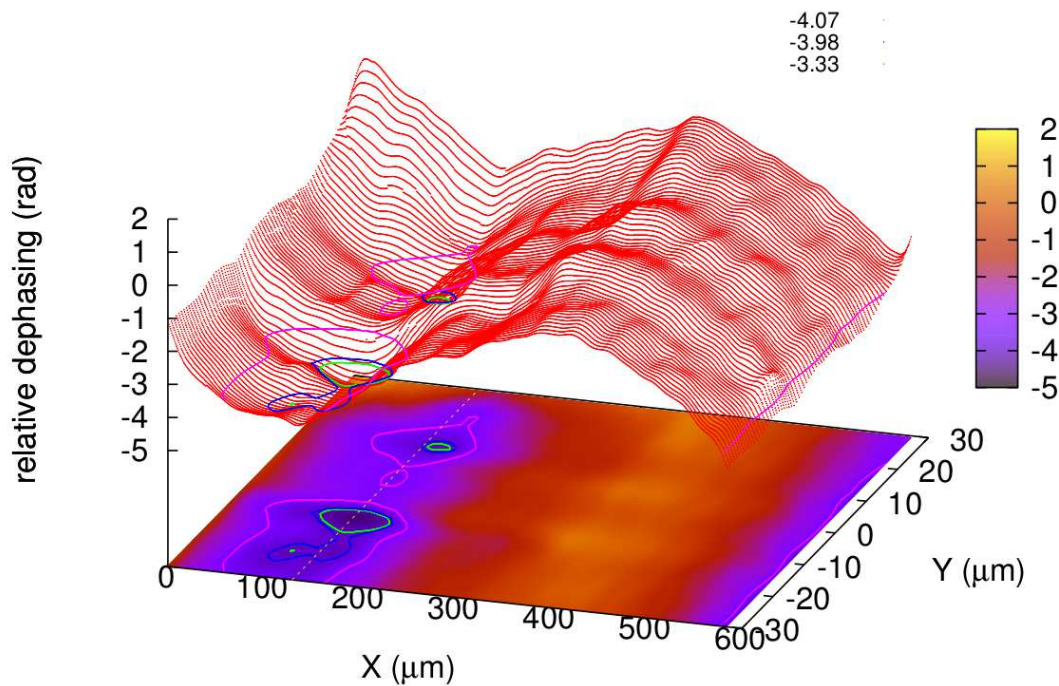
Figure 4.4: Experimental phase map extracted from an interferogram taken 11 ps after the laser enters the plasma. The laser propagates along the X-axis and is centred at $Y = 0$. A long modulation can be observed along the laser propagation axis. A short modulation can be measured transversally, with an on-axis density as indicated by the pink contour plots at relative dephasing -3.33 rad

negative dephasing, so that lower values implies higher plasma densities. A long sinusoid-like modulation of about 600 μm is formed along the laser propagation direction (X-axis). At $X = 130$ μm, a short transverse modulation is apparent from the contour plot at -3.33 rad. The cross-section at this X-position along the dashed yellow line is shown in figure 4.5. The plot shows the edges of the channel presented in the previous part, at ± 13 μm from the centre and also a small phase dip that could be a density hump exactly on the laser axis. Note that the background line is not flat because of a shift between the reference-image and
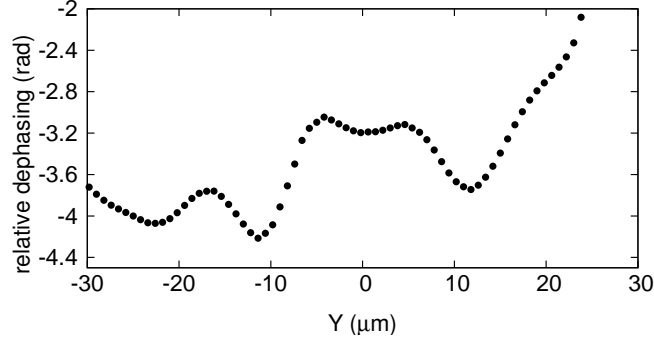
Figure 4.5: Lineout along the transverse dashed line at $X = 130$ μm in figure 4.4

the measurement [3], but this does not corrupt the qualitative identification of the humps. The following set of graphs shows the evolution in time of that profile at the same cross-section. On that sequence spanning until $t_0 + 77$ ps, the channel is
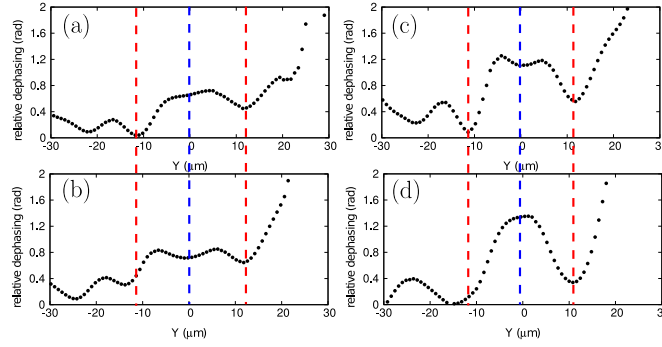
Figure 4.6: Time-resolved transverse modulations (relative dephasing). Lineouts are taken along the abscisse $X = 130$ μm at different instants after the pulse enters the jet at t_0 (see figure 4.4). The red dashed lines indicate the initial position of the channel walls in shadowgrams (see figure 4.2). The blue dashed line could be due to an electron density humps in the center of the channel. (a) $t_0 + 5.4$ ps, (b) $t_0 + 5.8$ ps, (c) $t_0 + 10.7$ ps, (d) $t_0 + 77$ ps

seen to deepen until panel (c) at $t_0 + 11$ ps, and then to expand slightly. This is in agreement with the fact that the radial shock forms by emptying the channel in the pre-blast wave phase, as mentioned in the previous part. At $t_0 + 77$ ps, no phase dip is observable anymore and this could be attributed to the expansion of the central density hump.

All these observations are in-line with the possible presence of a central filament and its expected explosion, as predicted by the numerical investigations (see 2.2). Future investigations with a greater magnification and a better contrast could provide a definitive demonstration of that important wakefield structure and its

---

[3]from different illumination in both cases, causing a phase drift

evolution. I present now clear evidence of some other fundamental structures appearing in the laser wake along with their original link to ion acceleration.

4.2 Nonlinear coherent structures

As the intense laser pulse propagates in an underdense plasma, it can excite different nonlinear coherent structures and modes in its wake. This appears due to the efficient electromagnetic energy transfer from the pulse to the plasma mostly under the form of plasma Langmuir waves and accelerated electrons [186]. Two other interesting modes of energy conversion can as well arise during the pulse propagation in an underdense plasma:

- when the main frequency component of the pulse spectrum is red-shifted[4] and becomes lower than the local plasma frequency, so that the electromagnetic field can be trapped. Thus, the ponderomotive effect of that field tends to push outwards the electrons and to form a cavity, called electromagnetic soliton [124, 186, 187]. These type of structures where experimentally demonstrated with pulse energies of 10s of Joule in Refs. [188, 189] using the proton radiography technique mapping out the electric field distribution in a plasma [38].

- when fast electrons accelerated in the laser propagation direction after the nonlinear Langmuir wake wave of large amplitude breaks [134] and creates a central current inducing a quasistatic azimuthal magnetic field [190]. By repulsion from the neutralizing currents flowing at the periphery of the channel, the magnetic field can grow with help of the Weibel instability [10]. In Ref. [191], the double-current layer is seen to bend from a "bending" instability, analogue to the fluid Kelvin-Helmholtz instability [192] and to distribute the electron streamlines into a zig-zag-ordered row of vortices.

The two modes are observed in numerical simulations to lead to the formation of circular structures of the size of the collisionless skin depth $\sim c/\omega_{pe}$. In the soliton case, the creation of a long-lasting electron cavity by the trapped electromagnetic field allows the CE of the ion core [124, 125, 187], causing the expansion of the soliton into a so-called post-soliton, which is in fact the form that was experimentally demonstrated [188, 189, 193]. In Ref. [125], the explosion is shown to accelerate the ions to several 10s of keV, a nonthermal level that should be detectable experimentally if sufficiently high number of ions are accelerated.

Solitons and vortices correspond to unstable modes (the appearance of which is dependent upon the fluctuating background noise) and are not mutually exclusive.

---

[4]the dispersion relation for a relativistic pulse is $\omega_L^2 = c^2 k_0^2 + \omega_{pe}^2/\gamma_{\perp e}$, $\gamma_{\perp e}$ being the electron transverse relativistic factor. As the plasma electrons gain momentum, the laser is red-shift. Another argument is the conservation of the number of incident photons when the pulse energy is absorbed

In fact, numerical along with experimental findings suggest that they appear simultaneously as hybrid-structures [189, 194]. Within the context of my thesis work, we have observed either of these fundamental structures and noticed that their presences hinder the acceleration of ions in the transverse direction.

4.2.1 Anticorrelation ion/coherent structures

Figure 4.7 shows the MCP recordings at 90° from the laser axis for two plasma gradient conditions.
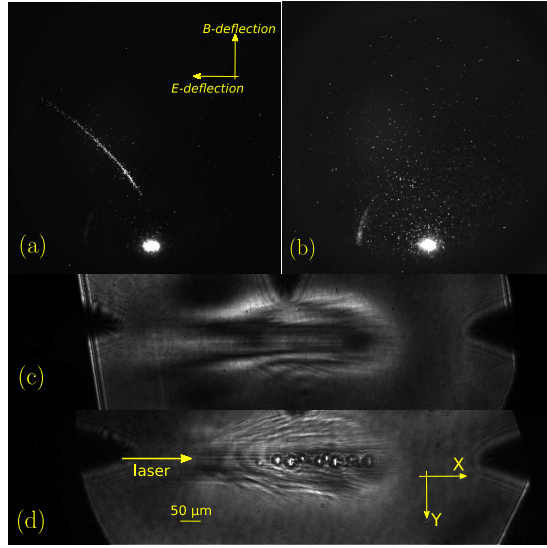
Figure 4.7: (a) and (b): MCP recordings at laser axis normal direction for $n_e \sim 10^{20}$ cm^{-3}. (a) short plasma gradient ~ 150 μm. He$^+$ trace with energy cutoff ~ 250 keV. (b) long plasma gradient ~ 250 μm. (c) and (d): Shadowgram after 1 ps after the pulse enters the jet (resolution ~ 1 μm, magnification 8.2). (c) short plasma gradient. (d) long plasma gradient. The shadowgram shows a clear train of bubble-like structures in the laser wake. The laser polarization is normal to the picture (S-polarized)

In (a), the laser is shot on the gas jet at an early stage of its expansion in the vacuum chamber so that the plasma gradient is steep ~ 150 μm (with a gaussian fit). In (b), the interaction occurs at a late time of the expansion (80 ms after the closing of the valve), and the gradient is smooth ~ 250 μm. For both conditions, the peak density in the jet has the same value $n_e \sim 10^{20}$ cm^{-3}. We observe *systematically* transverse ion acceleration in case (a) and no trace in case (b). In both cases, no ion was detected in the forward direction (see figure 3.9 for the geometry). The absence of He^{2+} is ascribed to electron capture by the ions from charge-exchange in the neutral gas corona (see the related discussion 3.4.3 in chapter 3). In panel (d), one can see the typical shadowgram obtained in case (b). A train of zig-zag ordered and well-separated bubble structures with an average size of about 30 μm ($\gg \lambda_p = c/\omega_{pe}$, the plasma wavelength) can be clearly seen

in the wake of the laser pulse. The bubbles have a bright spot in their centres that is not observable when the probe beam is turned off. This means that the emission is not of self-emission nature and results from refractive effects of the probe light by these structures behaving like microlenses. An interesting point is the quasi-circular shape of these structures, meaning that, during the transverse illumination of 30 fs, their centres are quasi-static in the picture plane.

To understand this inverse correlation, we investigated in time the interaction in the long gradient case. Figure 4.8 presents a sequence of five shadowgrams taken at different delays after the pulse enters the jet at t_0.
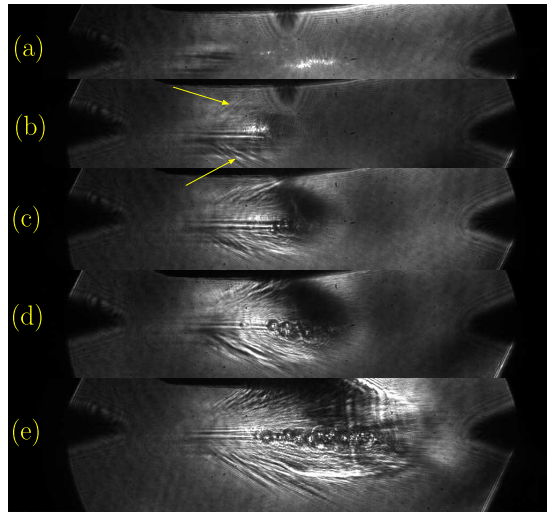
Figure 4.8: Time-resolved pulse penetration in the plasma gradient. (a) reference instant t_0, (b) $t_0 + 540$ fs, (c) $t_0 + 940$ fs, (d) $t_0 + 1.54$ ps, (e) $t_0 + 2.84$ ps. Arrows indicate the growth of prominent laser filaments

Very early in the interaction ($t_0 + 540$ fs), sizeable filaments develop next to the main laser channel [174] (see arrows in panel (b) in figure 4.8). As the pulse propagates along, the filamentation becomes stronger and multiple circular structures appear about the laser channel, near the center of the jet. In this time-resolved scan, we observe that the structures appear randomly in the laser path and no correspondence could be drawn between the pulse and bubble positions. Moreover, even if this shadowgram diagnostic is not intrinsically time-resolved, contrary to the proton radiography technique [38], the stability of the interaction was satisfactory to assess statistically the average size of the structure until the moment when the shadowgrams become blurred and unexploitable, at about 7 ps after the onset of the interaction, probably due to severe probe beam plasma refraction. Over that timespan, we observed that the structures have fairly the same size, irrespective of their positions to the laser front and measured an average increase of less than 10 μm in size.

Besides being copiously generated by the interaction, the nonlinear structures distribute spatially into two remarkable patterns, identifiable by following the bright central blobs, which arose randomly for the same experimental conditions. Figure 4.9 illustrates both antisymmetric (zig-zag about the laser axis) (panel (a)) and axial (panel (b)) distributions of the bubbles.
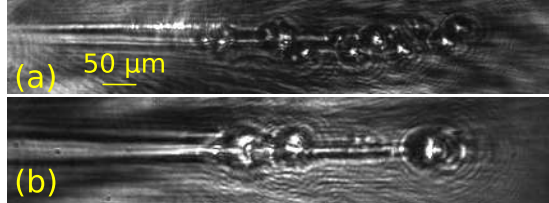
Figure 4.9: Spatial distribution of the bubbles for two shots in the same conditions at $t_0 + 1.54$ ps showing (a) antisymmetric (zig-zag) and (b) symmetric axial patterns about the main plasma channel

In Ref. [195], the authors carried out 2D particle-in-cell simulation with $a_0 = 3$, $\tau = 30$ fs and about 1 mm of plasma at $n_e = 10^{19}$ cm^{-3}. They obtained for initially P- and S-polarized light (i.e. an electric field collinear and normal to the observation plane), respectively antisymmetric and axial density map patterns resembling our experimental results (see figures 3 and 4 in Ref. [195]). In particular, the antisymmetric modulation is ascribed to the hosing instability (see also Ref. [187]). Although in our experiment the incident laser polarization is normal to the observation plane, corresponding to the S-polarization in simulations [187, 195], hosing instabilities have also been observed experimentally in similar conditions [196]. Therefore, following [187, 195, 196], we proposed to ascribe our observations to the laser excitation of the hosing instability inducing the development of von Karmàn row of electron vortices (a) and to shadowgraphic traces left by post-solitons (b).

Thus, it is clear that the interaction in this operating regime ($n_e \sim 10^{20}$ cm^{-3}, long gradient ~ 250 μm) produces numerous instabilities (filamentation, hosing, vortex/soliton), known to seriously deplete the pulse energy [124, 125, 187], that avoid an efficient plasma channel charging for subsequent transverse ion acceleration. Moreover, despite their expansions by ion core Coulomb explosion [187, 188], the bubbles do not provide a detectable acceleration, possibly because of a number of accelerated ions below the detector noise level. Therefore, we were unable to verify the post-soliton acceleration scenario predicted in Ref. [125].

4.2.2   Single structure isolation

To confirm the electromagnetic nature of the coherent structures, we carried out some polarimetric measurements. To simplify these measurements, we have identified a regime where few structures are generated at each laser shot, near

the center of the jet (statistically close to one). For that, we used a stretched laser pulse $\tau = 250$ fs carrying the same energy ($a_0 = 0.8$) and a small sonic nozzle of 200 μm diameter delivering a jet of peak density of few 10^{19} cm^{-3} which we let expand in vacuum to increase the gradient before the interaction. This apparatus enables (i) a well-localized interaction, (ii) smoother interferograms and polarigrams without filaments and bubble overlapping but still (iii) efficient energy transfer to the structures [187].
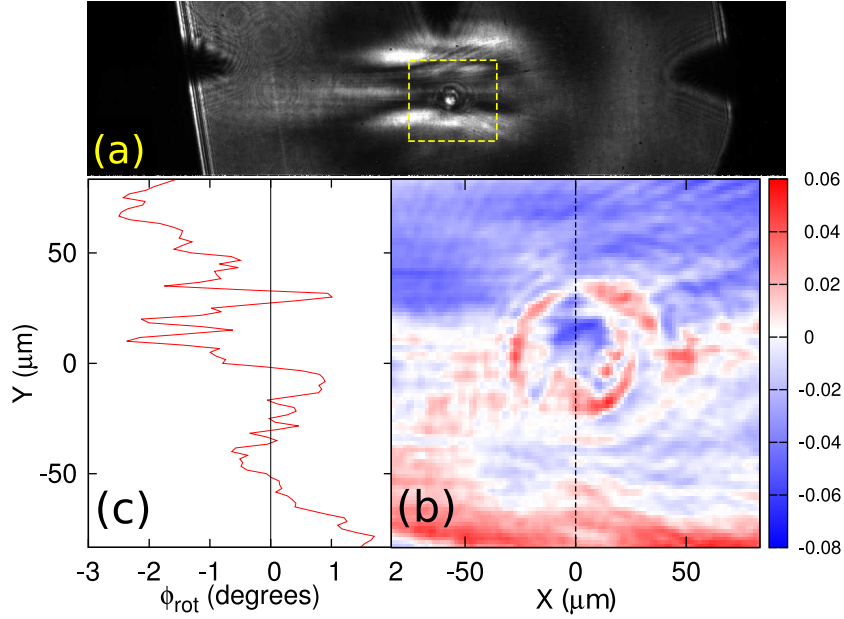
Figure 4.10: (a) Shadowgram with one isolated structure in the laser wake at $t_0 + 940$ fs ($\tau = 350$ fs, 10^{19} cm^{-3}). (b) ϕ_{rot} map (in radians) of the yellow square dotted zone in (a). Detuning angle of the polarisers: $\pm 10°$. (c) Line-out along the black dotted line in (b)

Figure 4.10(a) shows a shadowgram with one single spherical structure of 57 μm diameter in a clean area. In that simplified case, we were able to extract a ϕ_{rot} map around the structure (panel (b)). From panel (b) and (c), we can deduce that the structure in this condition have an almost axisymmetric polarimetric imprint about the laser polarization direction. The density in the bubble shell is found to be $\sim 7 \times 10^{19}$ cm^{-3}, five times that of the surrounding plasma. This density would correspond to a wavelength of about 4 μm, implying quite an important redshift assuming a laser field trapping in the plasma. Though the polarimetric information is the convolution of B_z by the density along the integrated probe beam path in the plasma, we will assume for the remaining that the main contribution comes from the structure and not from the surrounding plasma, as the major part of the bubble seems to be lying in a weakly magnetized structure (white region). Doing so, we thus calculate the maximum magnetic field extractable from our data. For $n_e = 7 \times 10^{19}$ cm^{-3}, an average path l_z in the shell of 25 μm (from

panel (c)), $n_c = 4 \times 1.67 \times 10^{21}$ cm^{-3} and a Faraday rotation of 0.04 radians, we find $B_z \leq \phi_{rot} \cdot \frac{2m_e c n_c}{n_e l_z e} = 570$ T. Though lower, this value is on the same order of magnitude as in the numerical computations in similar conditions [124, 125] and is consistent with the fact that the fields dissipate as the structure expands.

4.2.3 Dependence on the depletion length

I have studied the dependence of the excitation of the nonlinear coherent structures on the experimental parameters like plasma density and laser pulse duration. The results of these scans are presented on figures 4.11 and 4.12.
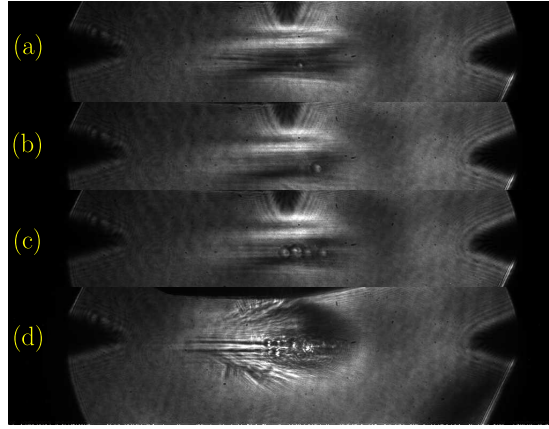
Figure 4.11: Density dependence of nonlinear coherent sturctures excitation for the same instant of the interaction ($\sim t_0 + 1.6$ ps). n_e is equal to (a) 7×10^{18} cm^{-3}, (b) and (c) 3×10^{19} cm^{-3}, (d) above 10^{20} cm^{-3}

The figure 4.11 illustrates the fact that the number of excited coherent structures fluctuate from shot to shot for the same laser and plasma conditions (see panels (b) and (c) in particular) and also that the average size of the bubbles at a given instant seems to decrease with the density, which could be related to an initial size, of the order of c/ω_{pe}, inversely proportional to $\sqrt{n_e}$. Clearly, at higher density more structures are excited for a given pulse duration. In figure 4.12, the density is fixed at about $n_e = 10^{19}$ cm^{-3} and the pulse duration is varied.

As such, no significant difference can be noticed in that pulse duration scan. However, the combined results of the density and pulse duration scans can be interpreted considering the depletion length of a laser pulse in an underdense plasma. It was suggested in Ref. [186] that the laser pulse in such conditions loses the total of its energy to the benefit of the plasma over a propagation length l_{dep}. For a pulse duration verifying $\tau_L \omega_{pe} \gg 2\sqrt{2}/a_0$, the depletion length can be approximated by (see also Ref. [188]):

$$l_{dep} \approx l_{pulse} \left(\frac{\omega_L}{\omega_{pe}} \right)^2 \tag{4.2}$$
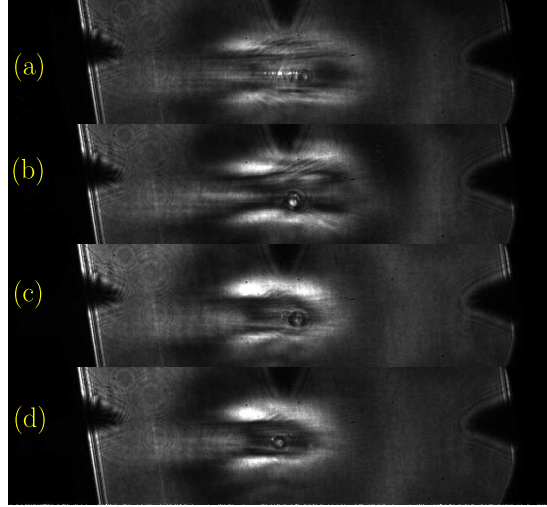
Figure 4.12: Laser pulse duration dependence of nonlinear coherent structures excitation for the same instant of the interaction. τ is equal to (a) 35 fs, (b) 250 fs, (c) and (d) 350 fs

where $l_{pulse} = c\tau_L$ and ω_L is the laser central frequency. The formula assumes that the pulse energy is transferred to Langmuir waves of moderate amplitudes (no wavebreaking) in absence of high-frequency parametric instabilities like Raman backward scattering (envelope approximation) [186]. Though these conditions are not necessarily fulfilled in our case (especially the non-wavebreaking assumptions), it is interesting to consider qualitatively the data with regard to equation (4.2).

As the pulse duration increases or the density decreases, the pulse will be less depleted for a given plasma extension. Thus, the excitation of coherent structures will become less probable and their number should drop in consequence. Very recently, it was experimentally demonstrated in Ref. [197] that solitons are copiously excited only after a laser propagating distance in the plasma of the order of l_{dep} and when the energy transfer is comprised within 30 and 40 %. In our case, the use of microjet at $n_e \sim 10^{19}$ cm^{-3} makes the entire plasma region be well within $l_{dep} \geq 1$ mm, even with an ultrashort pulse at 35 fs. This explains well the insensitivity of the observations to the pulse duration. Inversely, for a fixed pulse duration, when the density is increased to few 10^{20} cm^{-3}, the depletion length becomes comparable to the plasma extension and copious coherent structure excitation can be observed.

Thus, to conclude this section, I emphasize the fact that the experimental procedure proposed to study optically an isolated coherent structure, by tailoring *in situ* the plasma gradient scale length, increases in fact the pulse depletion length to rarefy the generation of the coherent structures. The conjunction of a small plasma extension of less than a millimeter, a wide range of densities and

adjustable pulse duration gives a reliable control of the onset of these interesting instabilities for future fundamental studies directly in the laboratory.

4.3 Laser collapse at near-critical density

One of the goals of the experiments I carried out was to study the ion acceleration at near-critical plasma density. At this density level, we were able to measure a transverse acceleration of up to 100s of keV. However, as suggested by E. D'Humières in its Ph.D. thesis work and more recently in Ref. [100], the interaction of an ultrashort intense pulse of the kind of the "Salle Jaune's" could produce highly energetic ions in the longitudinal direction mainly. If no ions could be detected reproducibly along that direction for these conditions, a large-scale structure was observed to expand asymmetrically at a quasi-relativistic velocity in the plasma.

4.3.1 Time dependence

I first present in figure 4.13 the temporal evolution of the plasma with a series of interferograms (showing plasma gradients and encoding the electron density) acquired at different laser-probe delays for the same plasma conditions. Out of convenience, we define that the laser propagates along y and is linearly polarized along x (thus, all panels in figure 4.13 are in the $y-z$ plane, see figure 3.9). On the left side of panel (a), 200 fs after the onset of the interaction, the plasma channel radius has dramatically reduced due pulse self-focusing as the laser penetrates the plasma [174]. The laser beam penetration terminates with a collapse well before the beam reach the critical density. Several filaments have developed next to the main channel. The on-axis bright spots, from plasma self-emission integrated with the CCD camera, are likely to indicate the longitudinal position where the laser pulse collapses. At this location, the laser breaks up into several filaments as can be seen later in panel (b), at 1.2 ps delay

In panel (b), a striking circular plasma structure with sharp edges has grown asymmetrically about the laser axis, with its center located on the left side of the middle of the jet, where the plasma density is around $n_e \sim 1 \times 10^{21}$ cm^{-3}. The structure appears opaque (dark regions below the background level), probably due to the strong absorption and refraction of the probe beam caused by large density gradients. Formation of such a structure may result from the ionization of the dense gas by the expanding cloud of hot electrons [64, 198, 199], efficiently heated in the small volume where the pulse has collapsed. Note that the interferograms are extremely noisy in these conditions, with loss of the fringes in some regions and a strong asymmetry of the plasma expansion, and therefore require for density extraction a lower probe wavelength and a mandatory multi-angle tomography as already mentioned in 3.3.2. Also, in panel (b), multiple thin bright filaments can
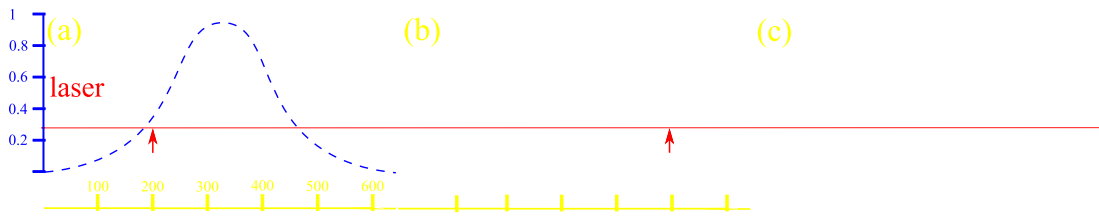
Figure 4.13: Electron density interferograms for the peak density $n_e \approx 0.95 n_c$ at the probe delays at: (a) $t_0 + 0.2$ ps, (b) $t_0 + 1.2$ ps and (c) $t_0 + 3.3$ ps, where t_0 corresponds to our reference time. The blue dotted line in (a) maps out the eletron density profile at the laser axis height (blue scale in unit of n_c). The yellow scale is in microns. The small red arrows indicate the position of the laser pulse assuming the laser group velocity equal to c. From $\sim t_0 + 0.4$ ps, the spherical structure is opaque to the probe beam.

be seen at the basis of the opaque structure and these filaments seem longer in the upper part of picture (lower density) than in the lower part (higher density close to the nozzle exit) because of the light refraction on the vertical density gradient.

In panel (c), at 3.3 ps delay, the walls of the channel have started to expand transversally. The lower edge of the structure have reached the limit of the field of view, at the nozzle exit, emphasizing an asymmetric expansion either side of the laser axis (red line). The structure appears now elliptical and elongated along the laser propagation direction, with a forward burgeoning bubble developing ahead of the structure and separated from the main structure by a vertical bright edge. This secondary structure might be analogous to the dense plasma blocks ("light bullets") observed in the collisional regime near the critical density and moving along a decreasing density gradient [200], but I did not investigate further this unclear point to be addressed in a future study.

Until the collapse point in the ramp of the jet, the laser pulse propagates straight in the plasma, although the gas jet presents an important gradient in the vertical direction[5] (see also figure 3.6 in section 3.2). This makes sense since the ponderomotive push of the pulse with $a_0 = 2.2$, is able to expel radially most of the electrons, so that the propagation is only subject to small-scale pointing-instabilities (e.g. the hosing instability) and not to plasma refraction effects. However, the peripheral part of the pulse with a much lesser ponderomotive potential should be sensitive to an inhomogeneous plasma refraction index. A priori, in a homogeneous plasma, the upper part with a smoother gradient should have expanded faster than the lower part. Such a behaviour seems to be followed by the thin bright filaments oriented towards the top of the picture (see panels (b) and (c)). Thus, it is probable that these filamentary structures are directly scattered parts of the laser light with a moderate intensity or fast electrons heated by this scattering.

---

[5]this gradient should normally have directed the pulse upwards

However, this is not what is observed for the large opaque structure and the asymmetry is in fact reversed. Therefore, either the ionization must be inhomogeneous with a characteristic scale length larger than the typical size of the filaments but smaller than that of the sphere, or probe beam refraction effects play a major role in the detection. As for the nature of this sphere, it could be a giant solitary magnetic vortex produced in laser-plasma resonance conditions when the laser is depleted [201], that pushes radially the plasma due to the magnetic pressure and the density gradient [100]. This point has not been elucidated yet and I cannot provide the reader with a conclusive interpretation for that observation. However, as discussed in Ref. [100], this type of vortex could be of utmost importance for the generation of multi-MeV-range beams of ions in the laser propagation direction.

4.3.2   Asymmetrical expansion at quasi-relativistic speed

Irrespective of the nature of the structure, the axial and radial expansion velocities of this structure within the first picosecond of the interaction can be investigated. I present in details the method used in the radial expansion case. I chose a given axial coordinate for which filaments do not significantly perturb the identification of the structure outer edges (vertical yellow line at $x = 465$ μm from the left border on panel (a) in figure 4.14). At various laser-probe delays, the cross-section along the yellow line is recorded to plot figure 4.14 panel (b). Each cross-section maps out the transverse plasma density gradients, so that a peak in intensity reveals here a sharp density edge (the intensity is arbitrary and thus can be normalized to the unity). Each column in the map 4.14 represents an average cross-section obtained from at least three shots in the same conditions. A total of 30 shots were necessary to plot this map.

The structure expands asymmetrically around the laser axis ($r = 0$ in panel (b)), as can be observed from the inset in panel (a) and the contours in panel (b), the expansion being faster towards the nozzle (negative coordinates and increasing densities). The opaque structure is clearly visible from about $t_0 + 400$ fs and we measured, over a timespan of one picosecond, average quasi-relativistic radial velocities in both downward and upward directions, respectively $c/2$ and $c/3$ (see oblique red lines in figure 4.14 panel (b)). The measurements in the upper part in panel (b) are affected by some noise due to a copious filamentation producing multiple parasitic peaks. However, by testing other axial positions free of filaments for the cross-sectioning, the same qualitative results have been obtained. This radial expansion rate of electron fronts in plasma is higher by an order of magnitude than other reported measurements in similar laser-plasma experiments [202]. In the axial direction, the same method is used and the results are graphed in figure 4.15. The bright white band in the upper part is due to the presence of filaments and self-emission along the laser axis. In the longitudinal
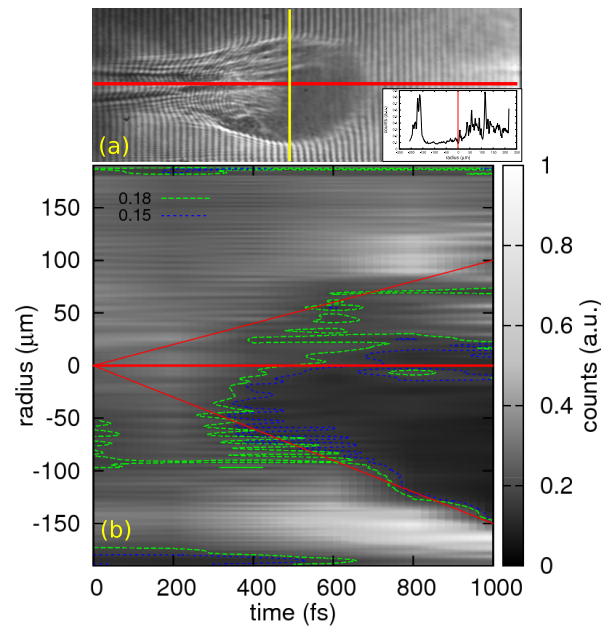
Figure 4.14: Asymmetric ultrafast radial expansion. (a) Interferogram at $t_0 + 1$ ps. Inset: cross-section along the yellow line. (b) Cross-sections along the yellow line in panel (a) versus time. Each cross-section is averaged over at least two shots. Horizontal solid red line: laser axis. Isolines at levels 0.15 (dashed blue) and 0.18 (dashed green) show the opaque structure formation. Oblique solid red lines indicate the slope of the expansion. Upper part in panel (b) (positive coordinates): $v_+ = c/3$. Lower part in panel (b) (negative coordinates): $v_- = c/2$

direction, the front expands at a velocity $c/2$. This front velocity is the same as the one measured in the lower part of panel (b).
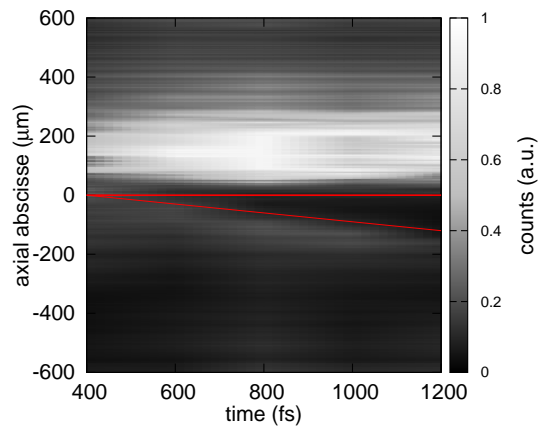
Figure 4.15: Longitudinal ultrafast expansion. The oblique red line indicates the slope of the expansion: $v = c/2$

4.3.3 Size of the ion source

In this high density regime close to n_c, we observed that the ions are in fact accelerated up to a level comparable to that at lower densities with few percent of n_c because of the smooth decrease observed with transonic/sonic nozzles (see figure 3.32). However, there is a clear increase in the size of the source at high density as illustrated in figure 4.16. At low density, the trace keeps the same thickness
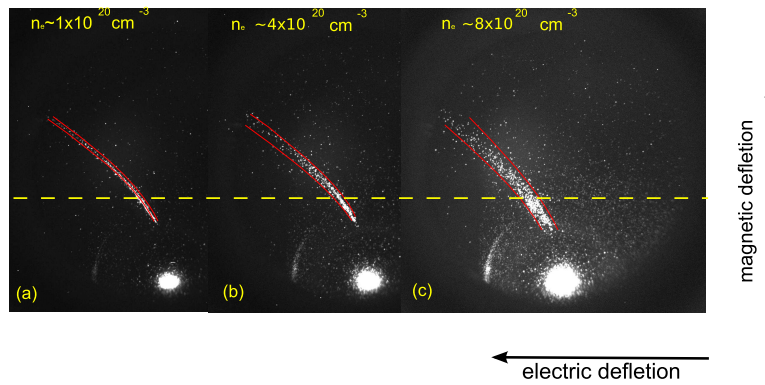
Figure 4.16: Ion source for three plasma densities. The horizontal dashed line corresponds to an energy of about 80 keV

at all energies (see panel (a)), while at high density, the thickness increases as the energy decreases (panel (b) and (c)). The thickness of the trace is in fact directly related to the size of the source as explained in the following. For a point-like and monoenergetic source, the thickness of the trace obtained on the MCP depends merely on the pinhole size and the magnification of the ion detector (see panel (a) in figure 4.17). In our case, this would give for a 100 μm-pinhole and a magnification $(A : B) = (2 : 1)$ a 150 μm-long segment (3 pixels on the CCD image). For an extended monoenergetic source, the same applies for each off-axis point of the source producing an off-axis segment on the MCP. Thus, the final trace is the overlapping of all segments, so all the thicker since the source is extended. For our case, a 700 μm source size will end up on the MCP as a 500 μm-long segment (10 pixels on the CCD image). For a non-mononergetic source, the segments are in addition shift on the MCP plane according to the dispersion of the Thomson parabola (see appendix B).

Comparisons between the thickness of the traces in figure 4.16 are done at two distinct energies of 40 and 80 keV, and reported in table 4.1. The trace is about 15 times thicker at $n_e \sim 8 \times 10^{20}$ than at $n_e \sim 1 \times 10^{20}$cm^{-3} at 40 keV for instance. Taking into account a point-like pinhole out of simplicity and a 2:1 magnification, the source in the gas jet plane is found to be about 1.3-1.4 mm at high density (hence, it would start about 600-700 μm before the nozzle edges). A simple reason can be the fact, that increasing the density scales up
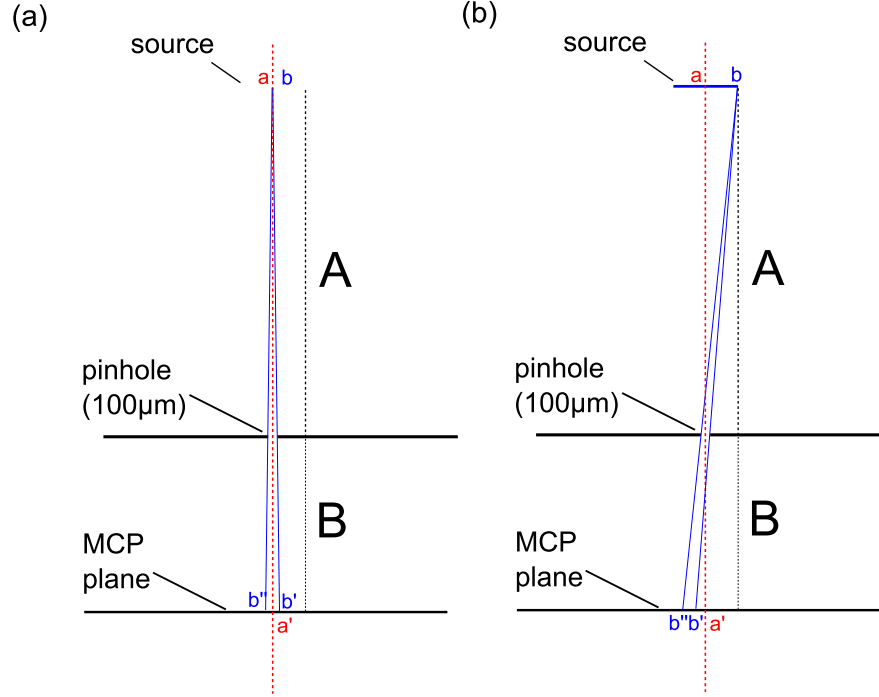
Figure 4.17: Pinhole imaging on the MCP. (a) Point-like source. (b) Extended source

Energy (keV)	$n_e \sim 1 \times 10^{20}$	$n_e \sim 4 \times 10^{20}$	$n_e \sim 8 \times 10^{20}$
40	0.16-0.18	1.4	2.6-2.8
80	0.16-0.18	0.7-1	1.8

Table 4.1: FWHM thickness of the MCP traces (in mm) at 40 and 80 keV for three different plasma densities (in cm^{-3})

the jet profile (without modifying the shape). This is coherent with the fact that I measured at high density a neutral source size on the MCP image of 2.6 mm against 1.5mm at low density (i.e 1.3 mm against 0.75 in the gas jet plane; this extension can be seen in figure 3.15 in chapter 3). Note, that the neutral source are due to different emissions from the plasma (Xrays, neutral, harmonics) and not to ions, so that the extension is somehow representative of the plasma size and not of the ion source size. In fact, the important point here is that at high density, the interaction with the laser could be efficient enough far from the nozzle to accelerate suprathermal ions. With a systematic report of thickness of the trace, an interesting spectral-resolved reconstruction of the source sizes in the high density case could be done if required.

4.4   Conclusion

From simulations in our conditions, the channel (filament and shell) and the sheath are the plasma structures supporting the ion acceleration that we recorded.

In this chapter, these structures have been observed (clearly for the shell and sheath and probably for the filament) and studied. The shell is seen to evolve into shocks that propagate radially as a cylindrical Taylor-Sedov blast wave in a fully hydrodynamic regime. Inside the channel, indications of an axial density hump could reveal the presence of a remnant filament pinched by the wakefield at the early instants of the interaction. When the laser depletion length is increased by tailoring *in situ* the plasma gradient scale length, bubble-like nonlinear coherent structures instead of a straight channel are observed to develop in the laser wake. We observed an anticorrelation between ion acceleration and the presence of these bubbles, and deduced that they are a laser-excited plasma mode in competition with the wakefield mode, with the consequence of hindering the acceleration by the wakefield. An original setup to study these bubbles was also presented. Finally, at a critical density, a preliminary study of the laser hole boring is presented. It reveals the formation of a large spherical structure expanding at a quasi-relativistic velocity (with on-going discussions on the very nature of this observation). A transverse ion acceleration to hundreds of keVs is also observed as in the lower density regime, but the ion source size is in general greater because of a longer gas jet profile from sonic nozzle used to reach this regime.

Chapter 5

Conclusion & perspectives

5.1 Synopsis of the results obtained in thesis

To tackle experimentally the topic of laser-underdense plasma for ion acceleration almost ten years after the publication of the latest major results was pretty challenging, and all the more since no clear evidence of such acceleration to a suprathermal level using an intense ultrashort pulses was ever reported. Though, within this long period, powerful instruments and techniques have been developed and successfully implemented to significantly improve the control of the interaction and the freedom of the experimentalist. In particular, (i) from the laser viewpoint, the XPW technique and deformable mirror enable enhancement of the pulse temporal contrast, clean the spectral and spatial phase fronts in order to reach diffraction-limited and quasi-gaussian pulses on targets; (ii) from the detection viewpoint, the use of flexible MCP assemblies with adjustable gain allows a single-shot data collection contrary to CR39 plates and thus makes it possible to do very significant statistics on the interaction for parametric studies; (iii) from the target viewpoint, with the advent of new types of fast-switching and highly resistant electro-valve, from which I took benefit to make innovative gas jets enabling to carry out experiments of laser-gas jet interaction in original as well as simplified conditions. Beyond the acceleration studies, the context provided to me a unique opportunity to proceed with an exploratory work on the physics of the interaction at relativistic intensities within the near-critical density range never entered in the laboratory beforehand.

5.1.1 Acceleration geometry

Thanks to that fruitful context, several novel results have been obtained during my thesis work. Ion acceleration directly from a gas jet with an ultrashort pulse was demonstrated for the first time and studied within a broad range of parameters. The geometry of the acceleration in our conditions was systematically controlled by means of a pair of identical sensitive ion detectors set along and transverse to the laser propagation direction. On the basis of the investigations that were carried

out in controlled and reproducible conditions at the LOA, we concluded that ions are accelerated transversely and not longitudinally, when the peak density from a nozzle of typically few hundreds of microns is scanned through three orders of magnitudes, from 0.001 to about 2 n_c, with $n_c \sim 10^{21}$ cm^{-3} for a Ti:Sapphire laser. In some other less stable conditions at near-critical density, longitudinal ion acceleration was observed but we did not explore further this point and left it to future investigations (see further part 5.2.3). Furthermore, on the basis of the experiments we carried at the Brookhaven National Laboratory with a CO_2-laser in well-controlled conditions (I did not report on this work in the present), no ion could be detected longitudinally from the interaction of an energetic and ps-long pulse with a jet, when the peak density is varied within a higher range, from ten to hundreds of n_c, with $n_c \sim 10^{19}$ cm^{-3} for CO_2-laser.

5.1.2   Wakefield effect

As for the transverse acceleration, the very good reproducibility of the interaction allowed to collect a large amount of reliable data in an "ion pulse response" regime, i.e. when the laser pulse duration is shorter than the inverse ion plasma frequency $\tau_L \omega_{pi} < 1$. In this regime, we showed that ions are accelerated to several hundreds of keVs, whereas the 35-fs laser pulse at a relativistic intensity would accelerate the ions to few keVs via the space-charge field due to the electron ponderomotive displacement. On the basis of several numerical studies with PIC codes in different geometries (axisymmetry, 2D and 3D) that were carried out within my Ph.D. period, this energy difference is seen to be gained from the strong electromagnetic field excited in the pulse wake. This wakefield that can last over few ω_{pi}^{-1} accelerates ions in the transverse direction with a much better momentum transfer than it would have been done by the ultrashort laser pulse. In experiments, when the plasma density was varied from about 1×10^{18} to 8×10^{19} cm^{-3}, an optimum in cutoff energy was precisely observed for $1 - 3 \times 10^{19}$ cm^{-3}, where the wakefield is expected to be resonant with the laser pulse and very nonlinear with large amplitude. For a given density within that optimal interval, we noticed that the cutoff energy dropped as the pulse duration was increased, what is in agreement with the fact that the wakefield amplitude is weakened and becomes non-resonant in these cases.

5.1.3   Plasma gradient and laser propagation effects

Interestingly in the long-pulse situations, even if $\tau_L \omega_{pi} > 1$, the cutoff energies are one order of magnitude smaller than predicted for a positive-channel Coulomb explosion, as I demonstrated it analytically in the chapter 2, and also as reported in previous experimental investigations. This fact emphasizes clearly the difference between the previous interaction regimes where a high power laser pulse of hundreds of femtoseconds deplete significantly the channel of electrons, so that, to a good approximation, the ion dynamics can be considered to be governed essentially

by the repulsive Coulomb field, and our regime where the electron dynamics in the channel and/or in the laser wake must be included in the description. As a corollary, the conditions of laser propagation in the underdense plasma play a crucial role in our case, since they determine the whole structure of the accelerating wakefield. This complex coupling was experimentally observed when we parametrically tested sonic, transonic or supersonic gas flows, each of them exhibiting a characteristic gradient scale length in which the pulse self-focuses differently. As a matter of fact, for a peak density at $n_e = 1 \times 10^{19}$ cm^{-3}, a sonic jet with a long gradient scale length produces no acceleration and a supersonic jet with a three times shorter gradient scale length, an acceleration up to 200-250 keV, while for $n_e = 1 - 3 \times 10^{20}$ cm^{-3}, it is the reverse situation.

5.1.4   Ion central filament

In the PIC simulations done by G. Sanchez-Arriaga and A. Lifschitz, the wakefield reshapes the channel bored by the ultrashort laser pulse into an annular structure composed of a shell and a central ion filament strongly pinched in the transverse direction. Eventually, this filament Coulomb explodes as the positive charge density cannot be screened by the electron population. This filament is interesting from the acceleration viewpoint, because it provides the ion population of highest radial momentum in the simulation box when it Coulomb explodes. I wrote a small particle code based on an electrostatic model which shows, that when the ion density distribution within the filament have a smooth transverse gradient, irrespective of its form, shocks are always created because inner ions, as they expand, eventually overtake the outer ones. The strength of the shock is determined by the steepness of the gradient. In fact, this observation is more general and applies whenever an electric field peaks *inside* a population of ions, so when gradients exist. Therefore, these shocks are also observed in the simulations to happen in the shell and also in the sheath between the plasma and the neutral gas.

Experimentally, we observed with the interferometric diagnostics with $n_e \sim 1 \times 10^{-19}$ cm^{-3} a density transverse modulation around the laser propagation axis that might be attributed to the presence of a central filament in the laser wake. Besides, sharp edges in the density maps are also observed to form at large radii and could be ascribed to hydrodynamic shocks occurring at late time after the laser has passed. These results are preliminary but reproducible over a set of several interferograms. Moreover, in 3D simulations with linearly-polarized laser pulse, the filament is elongated along the polarization direction, so that the explosion is about twice as more efficient in perpendicular direction. However, these ions are accelerated in very little fraction compared to those from the circularly-symmetric shell (about 100 times lower particle number). Experimentally, by rotating the polarization of a linearly-polarized pulse from horizontal to vertical and collecting data along the transverse direction in the horizontal plane, we did not observe any difference in the cutoff energy. This means that no anisotropy of acceleration

could be recorded, possibly because the ions coming from the filament are few and below the detector noise level.

5.1.5   Ion spectral modulations

In addition to a new regime of interaction, this thesis was the occasion to implement a new apparatus that allowed new observations in the laboratory. The use of gas jets of thickness comparable to the beam Rayleigh range made it possible to vary the number of acceleration foci distributed along the laser channel by varying the plasma density and to observe the influence of that number on the structure of the detected spectra. At a low density $n_e \sim 2 \times 10^{19}$ cm^{-3}, we recorded robust peaks in ion spectra, and deduced that few foci of acceleration within the detector solid angle were created, so that they could be distinguished. For the same detector solid angle, when the density is increased by a factor of 3, the spectra lose their modulations, and we concluded that this was due to the creation of a continuum of foci of acceleration that overlap in the portion of the phase space corresponding to the detector position and solid angle.

5.1.6   Link between ion acceleration and plasma structures

In the available experimental literature, there is no clearly established link between the acceleration of ions and the supporting plasma structures and fields, be it in underdense or overdense regime. In my thesis work, we endeavoured to put in relation these two aspects by implementing simultaneously high-sensitive specific spectrometers for ion detection and high-resolution interferometer and polarimeters for plasma field evolution in time and space.
At about $n_e = 10\%$ n_c, we managed to establish an anticorrelation between ion acceleration in the transverse direction and the observation of nonlinear coherent structures (soliton/vortex), remnant in the pulse wake. This systematic result was obtained by tailoring in situ the plasma gradient scale length. We interpreted that result by efficient laser depletion in these bubble-like structures when the laser depletion length is well within the plasma length, hindering the acceleration. In the reverse case, few isolated structures are generated and we took this opportunity to extract the polarimetric map, in order to confirm the electromagnetic nature of the structures under examination. As such, the clean observation of theses bubbles with optical diagnostics instead of proton radiography is an unprecedented achievement, as it gives a direct insight of plasma entities as fundamental for the interaction as the wakefield is.
At $n_e = 60 - 70\%$ n_c, i.e. in a laser hole boring regime, the transverse acceleration reaches about a hundred of keVs and is accompanied with the rapid growth in the plasma, at a quasi-relativistic velocity, of a spherical structure with a shell density higher than 4 n_c and opaque to probe beam. We noticed that in this case the MCP trace corresponding to the low energy part ~ 80 keV is thicker than at

lower density, indicating that the corresponding ion sources are larger by a factor of ten.

Because of the large amount of data collected during the last year of my Ph.D. work in the laboratory, every topic tackled during the experimental campaigns could not be reported in the present document. The experimental results I selected for this manuscript shed new light on an unexplored but rich regime of the interaction at relativistic intensities. Some papers resulting from my work are presented in the appendix D.

Some hypotheses have been expressed and qualitatively motivated without providing numerical demonstrations to back them up. The reason of this rests on the fact that simulations in our conditions require important numerical resources, since one needs to describe the plasma response with a sufficient spatial precision to resolve shocks for instance, with a large simulation box in the longitudinal direction to describe correctly the laser propagation and also in the transverse direction to include effects of the plasma sheath, and over a timescale of tens of picoseconds until all accelerating fields vanish. I now conclude by presenting some thrilling perspectives that could nourish future investigations.

5.2 Perspectives

The exploratory work I did during my Ph.D. opens up perspectives directly in line with the international scientific project bearing upon the understanding of laser-plasma interactions and with its vast societal applications. Its implications can be eventually attached to each of the three main sections constituting that project, namely the technological, fundamental and societal sections.

5.2.1 Innovative debris-free targetry

A significant part of my work was dedicated to develop compact gas jets for the interaction at a near-critical density and over a few hundreds of microns only. These versatile jets give an unprecedented control over a wide range of experimental parameters, enabling one to down-scale by a factor of 5 the longitudinal plasma dimension while keeping the same peak density and profile. When operated at critical densities, the microjets as such could be excellent candidates to be used with commercially available 100-TeraWatt-class lasers to generate energetic ion beams at much lower peak power than previously [56]. In a similar way, with argon or neon jets at such a density level, large clusters can be produced at the nozzle ouptut with the perspective of efficient Coulomb explosion [18] or powerful blast waves with radiative shell instabilities [183], and also with a deuteron jet, short thermonuclear fusion neutrons with yield orders of magnitude higher than reported [203] could be obtained (see also Ref. [48] for an interesting setup to control the explosion and the fusion with two laser beams). Importantly and

very promising, this target could be a suitable medium for compact and shape-preserving plasma self-compression of ultrashort laser pulses [173].

The next important step to be overcome is the development and characterization of very dense microjets with gradient scale lengths on the order of $20 - 50$ μm. These targets would make it possible to test interesting acceleration schemes depending on the plasma gradient that were recently proposed [204], and to optically probe the fields in the sheath at the sharp plasma-vacuum output interface. In case of ion beam generation in the longitudinal direction, this would allow measurements in particular with a good signal-to-noise ratio the azimuthal and quasi-static magnetic field responsible for ion collimation [51, 91], as a preliminary step towards an efficient plasma lens.

The great advantage of a thin jet of high peak density is to localize very precisely the interaction with an intense pulse. This would make possible the use of a microscope objective of large numerical aperture to wide-field image the plasma with a resolution in time of 5 to 30 fs, and in space of hundreds of nanometers.

5.2.2   Real-time optical characterization of the plasma

To draw in experiments the relation between the plasma structures, pulse propagation and particle acceleration is a crucial aspect in order to track the important steps of the interaction and unravel the underlying mechanisms, as would do output from a PIC code. In my thesis, the wakefield was proven to play an important role in accelerating radially the ions. However, no evidence of its existence was experimentally demonstrated in our conditions (in Refs. [182] and [170], the wakefield is observed within the laser-plasma electron acceleration context). Moreover, some modulations near the laser propagation axis were attributed to the formation of a central filament. A clear experimental description of this object is interesting to better understand the wakefield structure and control the subsequent transverse acceleration.

The issue of the dynamic structure of the wakefield moving on a timescale on the order of 30 fs at $n_e \sim 10^{19}$ cm^{-3}, so that transverse imaging with an illuminating 30-fs pulse appear blurred, can be sorted out by using a few-cycle laser to transversally probe the plasma as in Ref. [170]. However, the absorption contrast of the images of such small-scale and quasi-transparent object is quite poor. Alternative techniques inherited from the microscopy biology, like the strioscopy, or phase contrast microscopy, could provide significant improvements in the characterization of weak fronts in the plasma. As for density measurements of thin structures, the recent implementation of a wavefront-sensor imaging at large angle and large field-of-view, based on multilateral shearing interferometry, that gives immediate access to local dephasings in a plasma with a better signal-to-noise ratio, seems to be a very promising path to be explored [205].

For the nonlinear coherent structures that we observed, it will be interesting to determine optically the evolution in time of these small bubbles in a single-shot manner as previously done with proton radiography, and check the expansion model proposed in Ref. [193]. Taking benefit of the setup we proposed to control the excitation of a single bubble, chirped pulse shadowgraphy can be used at low-cost (without streak camera) to monitor in time with a single shot the radius of a localized quasi-circular bubble that expands on a timescale of tens of picoseconds.

The real-time optical characterization of the plasma will lead to a finer understanding of the mechanism of laser absorption, and consequently will bring an enhanced control over structures that accelerate the ions.

5.2.3 Energetic and controllable hadron bunches

In my Ph.D. time, we managed to accelerate reproducibly ions in the transverse direction. The cutoff energy of these ions can be controlled by adjusting the density, and for an optimal density range, well-defined peak in spectra can be observed. Thus, by filtering the emissions, bunches of ions of hundreds of keV can readily be obtained. If the jet is operated at higher repetition rate (up to 10 Hz with the developed model, up to hundreds of Hz with the next prototype), a compact source of fast particles for applications can be produced with a simple jet.

As mentioned in the content of the present document, energetic ions accelerated in the longitudinal direction were observed in conditions that were not reproducible. For a series of about 30 consecutive laser shots with a new sonic brass nozzle of 400 μm-long and delivering a near-critical density, alpha particles were accelerated forwardly and detected by our MCP system. A scan over the laser focus point was carried out. However, the signal continuously decreased during that scan. We noticed from the Side-View imaging ablation of the nozzle cone, and after inspection, damaging of the internal duct. As a consequence, the gas flow was unknown, and the exact conditions of the interaction not clarified. Thus, attention was paid to the controllable transverse acceleration, but this investigation is to be revisited in a systematic future study. The following figure 5.1 shows the type of ion spectrum we obtained in the longitudinal direction, with helium ions being accelerated up to 1 MeV.

The perspective of generating reliably these longitudinal beams from a debris-free targets [56], contrary to thin foil experiments, is particularly interesting. If successful in controlling the conditions, this effort will have tremendous aftermaths, as it will give a unique insight of the real processes involved, from the laser absorption to the particle acceleration, and above all, as it could give birth
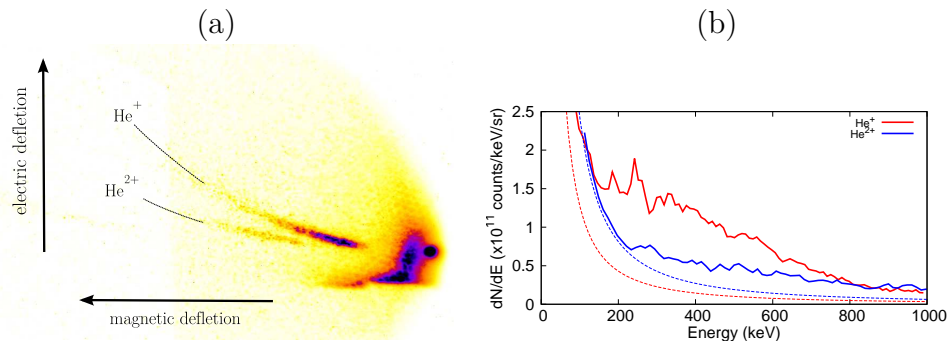
Figure 5.1: (a) Raw MCP picture along the laser propagation direction. The black dot on the right of the panel corresponds to the neutral axis of the Thomson parabola. Parameters: Sonic flow, $\tau_L = 35$ fs, $a_0 \sim 2$, plasma peak density $n_e = 0.6 - 0.7 \ n_c$. (b) Extracted ion spectra (solid lines) with relative counting. The dotted lines indicates the noise level

to energetic ions suitable for hadrontherapy at high repetition rate [26] or to laser-plasma-based fast ignition schemes [27, 206].

Appendix A

Over-critical submillimetric gas jet

Up to now, gas densities from jet used in laser-plasma interaction were limited to about 10^{20} cm^{-3}. For a fully ionized helium gas, the corresponding electron density was therefore limited to twice this value. The critical electronic density n_c of a plasma irradiated by a Ti:Sapphire laser beam of central wavelength $\lambda = 810$ nm is 1.68×10^{21} cm^{-3}, and sets the non-relativistic limit above which the electromagnetic wave cannot propagate. The maximum electron density was therefore limited to about 10 percent of the critical density, indicating that the range of densities for Ti:Sapphire solid-state lasers that one could explore so far was only underdense. The development I did during my thesis work led to a novel apparatus that allows to gain more than a factor of 10 in atomic density while reducing the length by a factor of 3, allowing to reach an unexplored range of densities from tens of percent of the critical density to overcritical density and over hundreds of microns only.

A.1 State of the art

Statement of the problem

The reduction in size of the jet to something submillimetric, coupled with the possibility of density variation over several order of magnitude, would give access to Rayleigh-range-long plasmas (even for tightly focussed laser) from low-density laser transparency to high-density laser opacity regimes. Such a perspective would make envisionable systematic investigations of laser-plasma interactions (e.g. parametric instabilities, laser filamentation, relativistic self-focussing and hole boring). It could also relax the constraints on laser power requirements for users of Terawatt-class lasers in studying energetic ion beam generation from gas jets, so far only reported with Petawatt-class laser facilities [56]. Importantly and very promising, this type of jet could be a suitable medium for compact and shape-preserving plasma self-compression of ultra- short laser pulse [172].

However, the broadly used solenoid valve systems which trigger the gas burst then close within typically tens of milliseconds timescale at working pressure ~ 100 bar "choke" when reducing the throat diameter to sub-millimeter. This property comes from the linear dependence of the mass flow rate in the 1DIFF model with that minimal cross-section in the duct (also called critical diameter). The increasing of the pressure to compensate the flow rarefaction prohibits subsequent opening of the magnetic-coil-driven poppet, shrinking further the downstreaming flow. This hinders the exploration of plasma density from microjets in the interval $10^{19} - 10^{21}$ cm^{-3}.

Simple analytical model: inviscid flow parameters

This section aims at illustrating qualitatively by using the 1DIFF model, how flow parameters relevant for laser-plasma experiments (density, radial gradient, mass flow) are expected to vary in steady state according to the nozzle geometry (or equivalently in that model, to the Mach number of the flow, noted M). As mentioned in [162], one observes an intrinsic competition between the two requirements (*i*) high peak density during the quasistatic gas expansion in vacuum out of the nozzle and (*ii*) steep-gradient radial profile with plateau. The position between these two limit cases is essentially quantified by the Mach number of the flow.

(*i*) The gas density at the nozzle exit is mainly determined by the exhaust gas velocity, i.e. by the conditions of expansion inside the nozzle and thus by the geometry of the nozzle. The 1DIFF model predicts for an ideal gas a simple system of equations linking the cross-sectional area A to the density ρ via the Mach number parameter.

$$\frac{\rho}{\rho_0} = \left[\frac{\gamma + 1}{2 + (\gamma - 1)M^2}\right]^{\frac{1}{\gamma - 1}} \quad (A.1)$$

$$\frac{A}{A_0} = \frac{1}{M}\left[\frac{2 + (\gamma - 1)M^2}{\gamma + 1}\right]^{\frac{\gamma + 1}{2(\gamma - 1)}} \quad (A.2)$$

with respectively A_0 and ρ_0 the cross-sectional area and the density at the throat,γ is the gas adiabatic constant ($\gamma_{He} \sim 1.6$). It is immediate from (A.1) that as M increases isentropically the density ρ decays. Considering a sonic flow ($M = 1$), with helium gas at $p = 300$ bar, then $\rho_0 \approx 4 \ n_c$ and $\rho \approx 2 \ n_c$. With the same pressure, for a supersonic flow as in our experiments ($M \simeq 4$), then $\rho \approx 0.2 \ n_c$.

(*ii*) Ideally, a related Prandtl-Meyer flow can model the fluid exiting the nozzle. This supposes that the pressure in the discharge chamber is much lower than the pressure delivered by the nozzle, so that the flow adapts via expansion waves. The convex nozzle corners rotate isentropically the outer layers giving birth to a

centred expansion fan through which the fluid is rarefied. The angle of rotation θ reads:

$$\theta = \nu(M_2) - \nu(M_1) \tag{A.3}$$

$$\nu(M_i) = \sqrt{\frac{\gamma+1}{\gamma-1}} \tan^{-1} \sqrt{\frac{\gamma-1}{\gamma+1}(M_i^2-1)} - \tan^{-1} \sqrt{M_i^2-1} \tag{A.4}$$

where $\nu(M_i)$ is the Prandtl-Meyer function, M_1 and M_2 the Mach numbers respectively up- and downstream the corner (see figure A.1 and also for upcoming implicit symbols).
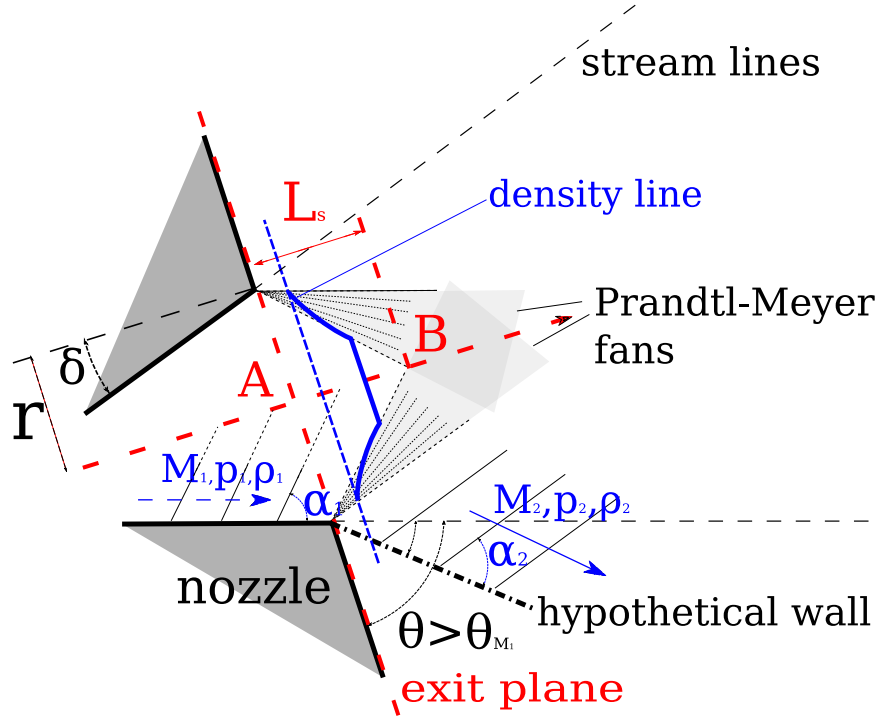
Figure A.1: Isentropic centred Prandtl-Meyer expansion outside a supersonic underexpanded nozzle (p_{exit} > ambient pressure p_a). Plateau density lines (blue line) develop in the inviscid triangle over the supersonic length L_s ($M_A \approx M_B$) delimited by weak density disturbances at Mach angle $\alpha_1 = \sin^{-1}\left(\frac{1}{M_1}\right)$

From (A.3) and (A.4), it follows the existence of a maximum total turn angle θ_{M_1} for a given M_1 above which $M_2 \to \infty$ and p_2 and ρ_2 vanish.

$$\theta_{M_1} = \frac{\pi}{2}\left[\sqrt{\frac{\gamma+1}{\gamma-1}}-1\right] - \nu(M_1) \tag{A.5}$$

With helium gas, for a sonic flow, $\nu(M_1) = 0$ and $\theta_{M_1} = 97.3°$. For a supersonic flow as in our experiments ($M_1 \simeq 4$), $\theta_{M_1} = 44.3°$. For all types of flow we produced experimentally, the nozzle corner angle reads $\theta = 70-90°$. This means

that in that model, a sonic flow for which $\theta < \theta_{M_1}$ spreads along the nozzle exit plane, so that the jet will exhibit quite a large radial gradient outside the nozzle. On the contrary, when using a supersonic flow, the convex corner extends over an angle $\theta > \theta_{M_1}$ and the expansion can smoothly develop to ambient pressure (typ. $p_a < 10^{-2}$ mbar). Thus, for the supersonic flow cases, the angular extension of the Prandtl-Meyer fan can be used to assess the radial gradient scale length l at a certain distance Z from the nozzle exit.

$$\frac{l}{Z} \sim (\sin^{-1}\left(\frac{1}{M_1}\right) + \theta_{M_1}) \tag{A.6}$$

For $M_1 \simeq 4$, the radial gradients of the jet at $Z = 200$ μm from the exit reads $l \approx 200$ μm. From (A.6), l/Z reduces, i.e. the jet profile steepens as M_1 increases.

For a supersonic flow, to trade off (*i*) and (*ii*) (steep profile along with plateau density), the laser-gas interaction should be operated not too far from the nozzle exit, at a distance $Z \leq L_s$ (see figure A.1 for the symbol definition).

$$\frac{L_s}{r} = \frac{1}{|\tan(\delta - \alpha_1)|} \tag{A.7}$$

with r the nozzle exit radius. When *cone-sonicity* matching is fulfilled i.e. $\delta = \sin^{-1}\left(\frac{1}{M_1}\right)$, the ideal supersonic length diverges. In practice, $\delta \neq \alpha_1$ and L_s/r is limited to few units. For $M_1 = 4$, i.e $\alpha_1 = 14°$ and our supersonic nozzles with $\delta = 20°$ and $r = 200$ μm, one obtains $L_s = 2$ mm.

The mass flow rate $\dot{m}$ for such a system in the 1DIFF model yields:

$$\dot{m} = \sqrt{\frac{\gamma}{R}} \frac{p^*}{T^*} \left(\frac{2}{\gamma+1}\right)^{\frac{\gamma+1}{2(\gamma-1)}} A_0 \tag{A.8}$$

with p^* and T^*, the stagnation pressure and temperature respectively, and R the specific gas constant.
This parameter shows that, for a given nozzle geometry selected according to the equations (A.1) and (A.2) to reach a certain sonicity, the mass flow rate and thus the achievable density at the exit is limited by the throat area A_0 (or any smaller area in the flow). Therefore, for designing a jet down-scaled to micrometric dimensions, a proportional increase of the backing pressure must be applied to compensate the rarefaction of the gas.

A.2   Experiments

Apparatus

The apparatus I used for the characterization was made of an interferometer and a complex gas system with a pressure booster.

Optical characterization

The jet characterization was carried out by using a similar set-up as the one presented in [162]. In our case, the Mach-Zehnder interferometer stands outside the vacuum chamber and the jet is illuminated by a HeNe 633nm-CW laser. An $f/3$-doublet images the central plane of the nozzle onto an 8-bit CCD camera. The spatial resolution is about 2 μm and the magnification around 12.
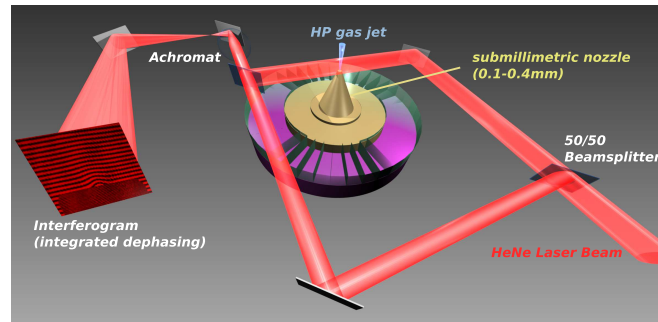

Figure A.2: Mach-Zehnder interferometer with typical interferogram obtained when the high pressure (HP) gas jet is fired

Though powerful, this setup has some important limitations which have to be taken into account when characterizing microjets.

- the intrinsic noise, assessed by extracting the phase from two consecutive reference images without firing the gas, corresponds to a level of about 10^{18} cm^{-3}. It is mainly due to parasitic vibrations of the interferometer components and therefore requires to shield out the thin beamsplitters from any airstream and to set the assembly on a stabilized optical table

- the thickness of the microjet is a ten-fold thinner than usual jets. Therefore the output density has to be at least ten-fold higher than in the millimetric case, in order to overshoot the noise level.

- jets produced by usual millimetric nozzles are often characterized using a high refractive index gas like argon, krypton..., that give similar profiles as helium, massively used for laser-gas jet interaction, but having a smaller index. However in the present case, when using any of these ersatz at such high pressures, the formation of molecular jets with large clusters corrupting the characterization is expected, as the empirical Hagena parameter $\Gamma^* \geq 10^5$, much greater than the admitted limit $\Gamma^* \sim 10^3$ for cluster formation [207–209] (see the section A.3).

Since the main goal was to produce very dense jets, these points could have been circumvented by using a pneumatic pressure booster ($\times 75$) delivering up to 400 bar of backing pressure. When low densities below 10^{20} cm^{-3} were produced (typ. with supersonic nozzles of Mach number > 4), peculiar care was employed to

stabilize the system. For cases lying below the noise level, fit functions of the experimental points were calculated.

Density extraction

The phase shift due to the gas is deduced from the interferogram fringe shift with a continuous wavelet transform technique [210]. A typical raw phase map and the corresponding density calculations at three heights above the nozzle are presented in figure. A.3. For the following, we define $n_{ca} = 1.68 \times 10^{21}$ atoms/cm^3 (referred to as atomic critical density). The good axial symmetry of the flow makes the density estimation using the Abel inversion technique very reliable (estimations with a generalized Abel-inversion assuming non-axisymmetric profiles [166] give the same results).

Innovative apparatus

The He pressure in the upstream reservoir could be in theory varied within the range $p = 50 - 450$ bar. In practice, the pressure was fixed around 300 bar. This corresponds to mass flow rates of an order of magnitude higher than rates with usual jets. However, in this range, the electro-valve I used can fully open and close according to the manufacturer within three milliseconds[1]. This fast switching is made possible by the implementation of the *bid* technology, which is a very recent invention consisting in a bid rotating in an asymmetric induced magnetic field to gate the gas flow out (see the drawing at the end of this appendix). This has the advantage to significantly reduce the inertia of the switch and increase the pressure limit by a factor of 10, as compared to translational plastic poppet driven by a spring in usual electro-valve.
The conjunction of the fast-switching electro-valve and the high mass flow rate makes the assembly capable of delivering overdense gas jet while being usable in the vacuum interaction chamber without endangering the vacuum pump assembly. The stability of the overall gave a very good shot-to-shot reproducibility in density over the tested pressure range (fluctuations of less than few percent RMS).

Operating mode

The method adopted in the following studies to vary the density differs from the one usually employed in laser-plasma interaction. Here, the gas pressure feeding the valve is kept constant at $p = 300$ bar because of the long transient regime of the pressure booster, and delays Δt between the gas and the laser pulse are varied. Equivalently, Δt can be fixed and the opening time of the valve varied. Thus, the interest of this method rests on the fact that the interaction regime is

---

[1]in practice, kinetic problems due to a not-optimized matching between the nozzle and the valve was observed, see the result part
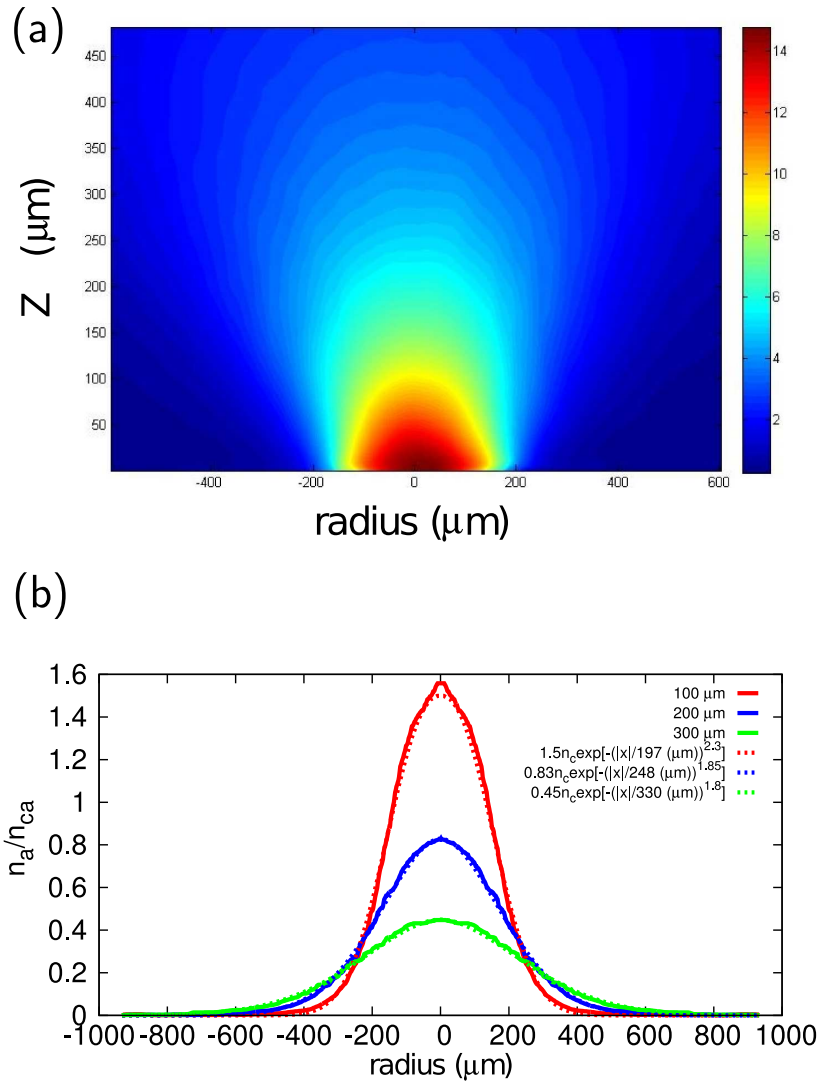
Figure A.3: Data extraction from interferograms obtained with a 400 μm-cylindrical nozzle pressurized at $p = 300$ bar. (a) Phase shift distribution (colormap in radian) from CWT. (b) Neutral He profiles n_a normalized to the the atomic critical density n_{ca} at 100 (red line), 200 (blue line) and 300 μm above a 400 μm sonic nozzle from Abel inversion. The dotted lines indicate the best exponential fits

determined by a time, which can be set experimentally much more conveniently than a pressure[2].

---

[2]at the precision of the jitter of a simple time-delay pulse generator within a nanosecond timescale

A.2.1   Results

Extensive spatial and temporal characterizations of diffent type of nozzle have been carried out. I present here in details only the results relative to studies of sonic and transonic nozzles and discuss their specific features. A good experimental review in the supersonic case at low density is presented in [162].

Flows

As expected from the 1DIFF model, the spatial profile of the jet depends upon the exit Mach number via the nozzle geometry (ratio of the exit to the critical diameter). This was experimentally verified as shown in figure A.4, where neutral densities normalized to the peak density at 200 μm for each nozzle type are plotted to underline the gradients in radial and vertical directions. From (A.8), one can
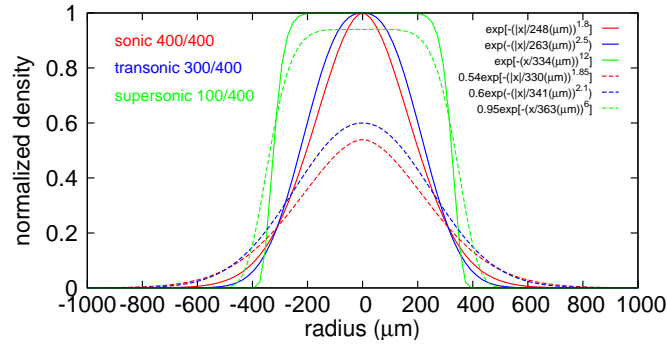

Figure A.4: Sonic (red), transonic (blue) and supersonic (green) flows (best fits) for three nozzles of throat diameters 400, 300 and 100 μm respectively (same exit diameters of 400 μm). The curves are normalized to the peak density at 200 μm. The solid and dashed lines correspond to profiles at 200 and 300 μm from the exit respectively. Both vertical and radial gradients become larger as the sonicity (Mach number) decreases

understand that the output mass flow rate will be lower in the supersonic case ($A_0 = (100\ \mu\text{m})^2$) than in transonic and sonic ones ($A_0 = (300)^2$ and $(400\ \mu\text{m})^2$ respectively), and so will be the density, for a given stagnation pressure p^*. In our conditions, only the sonic and transonic flows supply neutral densities over 10^{20} cm^{-3}.

Sonic nozzle

The time-resolved density at height $Z = 200\ \mu$m is depicted in figure A.5, where the peak densities are plotted against the delay between firing of the valve and the instant of the measurement (also instant at which the laser is fired when the interaction is carried out). A typical asymmetric bell shape trendline is obtained and near-critical atomic peak densities are measured at about 20 ms after the
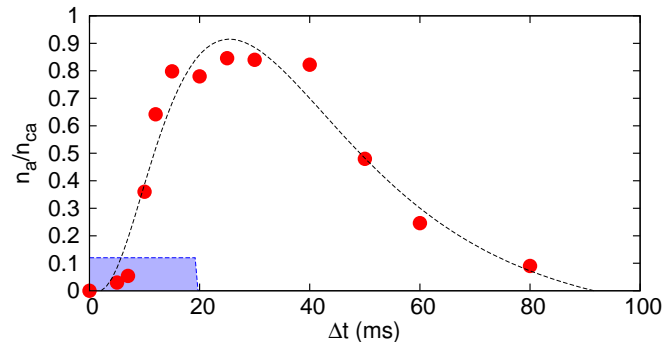
Figure A.5: Time-resolved neutral peak density n_a at 200 μm from the exit of a sonic nozzle (400 μm diameter). The blue region indicates the opening time of the valve. The interpolated dashed line is an indication to guide the reader

valve opening. Despite the fast-switching of the valve within 3 ms, the transient state lasts for about 15 ms. This delay is probably due to some kinetic issue in the bid motion that restricts the mass flow rate[3]. I did not carry out any optimization for this aspect which I considered not to be critical for our purposes, and proceeded with the sound characterization of the transient and steady-state regimes with the system as such.

For different delays, the figure A.6 presents the jet profiles at $Z = 200$ μm. From figure A.5, one notices that either side of the maximum peak densities at

Figure A.6: Profile evolution for different Δt using the same nozzle as in figure A.5. (Top) radial profiles normalized to the peak density at 25 ms. (Bottom) gradient calculated as the peak density over the gradient scale length (black empty dots), and gradient scale lengths from gaussian fits of the profiles (red dots). The blue region indicates the opening time of the valve

---

[3]causing the "displacement" of the duct critical diameter at the valve output orifice, the diameter of which evolving too slowly with time during the opening phase

(25 ms, 0.8 n_c), the same peak densities can be found out for different Δt. It is interesting to compare the jet shape for these two corresponding positions, as done in the bottom panel in figure A.6, where one see that the gradient scale length is almost constant over the timespan (red full dots). Thus, the two corresponding positions refer in fact to gas jet profiles at different instants of the expansion but still very similar in space. In this respect, for a sonic nozzle, it is possible to vary the gradient (black empty dots), i.e. the ratio of the peak density to the gradient scale length, without changing the gradient scale length. This is of utmost importance for carrying out controllable parametric studies on, for instance, laser self-focusing, filamentation instability or electron injection in a density ramp.

Transonic nozzle

Similar as in the sonic case, I present the temporal and spatial behaviours of a transonic flow at $Z = 200$ μm. The same type of curve shape is obtained,
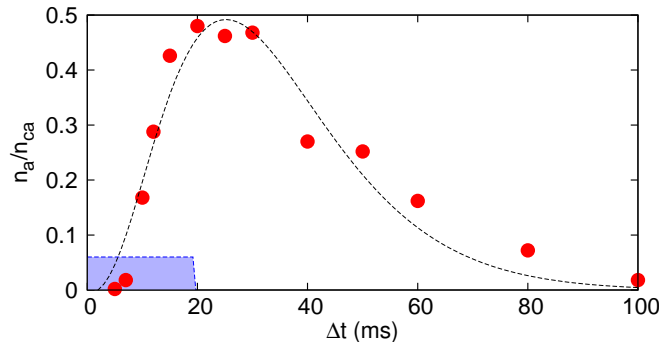
Figure A.7: Time-resolved neutral peak density n_a at 200 μm from the exit of a sonic nozzle (300 μm throat diameter and 400 μm exit diameter). The blue region indicates the opening time of the valve. The interpolated dashed line is an indication to guide the reader

but with a lower maximum peak density at 0.5 n_c, due to a smaller critical diameter (see (A.8)). The same remark about the non-optimized kinetics of the assembly can be here renewed. The figure A.7 depicts the spatial behaviours for that type of flow. In this case, as the time elapses, the gradient scale length is found to change significantly (bottom panel). For a couple of delays exhibiting similar peak densities (10 and 80 ms), different gradient scale length can be measured, thus entailing different gradients. This makes it possible to scan the gradients without changing the peak density (complementary to the sonic case). Thus, it opens up opportunities to study the interaction in different conditions of gradient scale length, as done in chapter 4, where nonlinear coherent structures like solitons/vortices are only excited when a density ramp is present for a given plasma peak density of about $n_e = 10^{20}$ cm^{-3}.
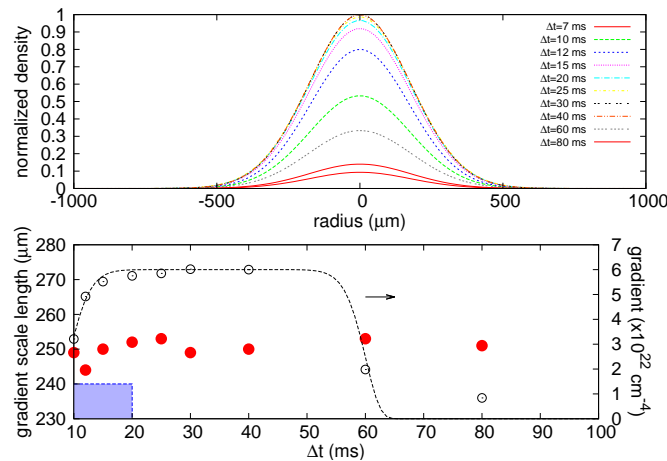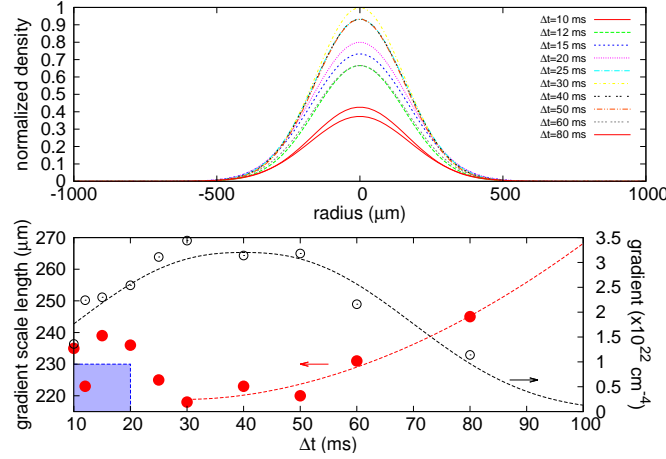
Figure A.8: Profile evolution for different Δt using the same nozzle as in figure A.7. (Top) radial profiles normalized to the peak density at 30 ms. (Bottom) gradient calculated as the peak density over the gradient scale length (black empty dots), and gradient scale lengths from gaussian fits of the profiles (red dots). The blue region indicates the opening time of the valve. The interpolated dashed line is an indication to guide the reader

A.3 Cluster formation

It is well known that gas jets operated in our conditions can lead to condensation of the fluid due to dominant Van der Waals attractive forces between atoms, entailing the formation of a biphasic mixture of gas with molecular clusters [207]. This type of molecular flow presents an interest as it can be suitable for efficient ion acceleration to several keV/nucleon from laser plasma interaction inducing Coulomb explosion [18, 209]. As far as nozzle characterization is concerned, strong cluster formation can be a drawback as it distorts the density measurement as well as introduces an additional level of complexity in the problem. I have not carried out specific measurements of the cluster size (by mass spectroscopy [207]), but computed instead the empirical reduced Hagena parameter Γ^* related to the average number of atoms n per cluster through the so-called original Hagena equations [208, 209].

$$\Gamma^* = 1000K\frac{(d/\tan\alpha)^{0.85}}{T_0^{2.29}}p_0 \qquad (A.9)$$

$$\text{and} \quad n = A(\Gamma^*/1000)^\gamma \qquad (A.10)$$

where d is the nozzle diameter in μm, α the nozzle cone half angle [4], p_0 the backing pressure in bar, T_0 the room temperature in Kelvin. K is a gas dependant constant (equal to 3.65 for He and 1650 for Ar, see [211] for other gases), A and γ take different values when $\Gamma^* < 1800$ and $\Gamma^* > 1800$ (termed small and large Γ^*

---

[4]this definition of the angle supposes a large ratio of the exit diameters to the critical one. In our sonic (400/400) and transonic (300/400) cases, I considered α to be close to 45°

respectively) such as:

$$\Gamma^* < 1800 \qquad n \; = 4.62 \times 10^{-4} (\Gamma^*)^{2.35} \qquad\qquad (A.11)$$

$$\Gamma^* > 1800 \qquad n \; = \exp[-12.83 + 3.51 (\ln \Gamma^*)^{0.8} \qquad (A.12)$$

The validity of (A.10) was experimentally verified with different gases for values of Γ^* ranging up to 10^5 [212] (and also reference therein), making Hagena theory perfectly applicable.

The figure A.9 plots the reduced Hagena parameters for the sonic and transonic nozzle I used with helium and argon. At room temperature, the use of He prevents
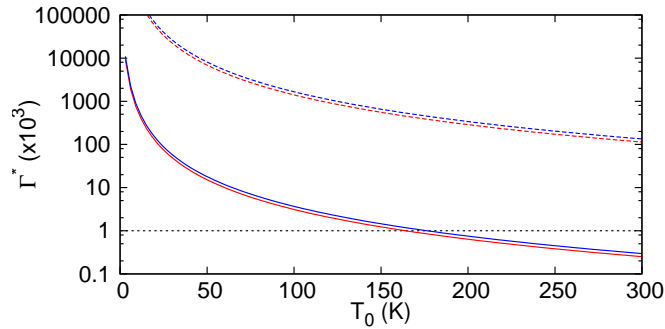
Figure A.9: Reduced Hagena parameter for sonic (red) and transonic (blue) nozzles with $p_0 = 300$ bar at $T = 300$K. The solid and dashed lines refer to He and Ar respectively. The horizontal dotted line indicates the experimental limit for clear large cluster formation

from the condensation of large cluster detrimental for the characterization. This is not the case for Ar and could explain the discrepancies observed when comparative density measurements have been carried out, the Ar density level lying always below that of th He. For the small calculated Γ^*, the average number of atom/cluster is given by (A.11) and reads for both nozzles $n < 6$.
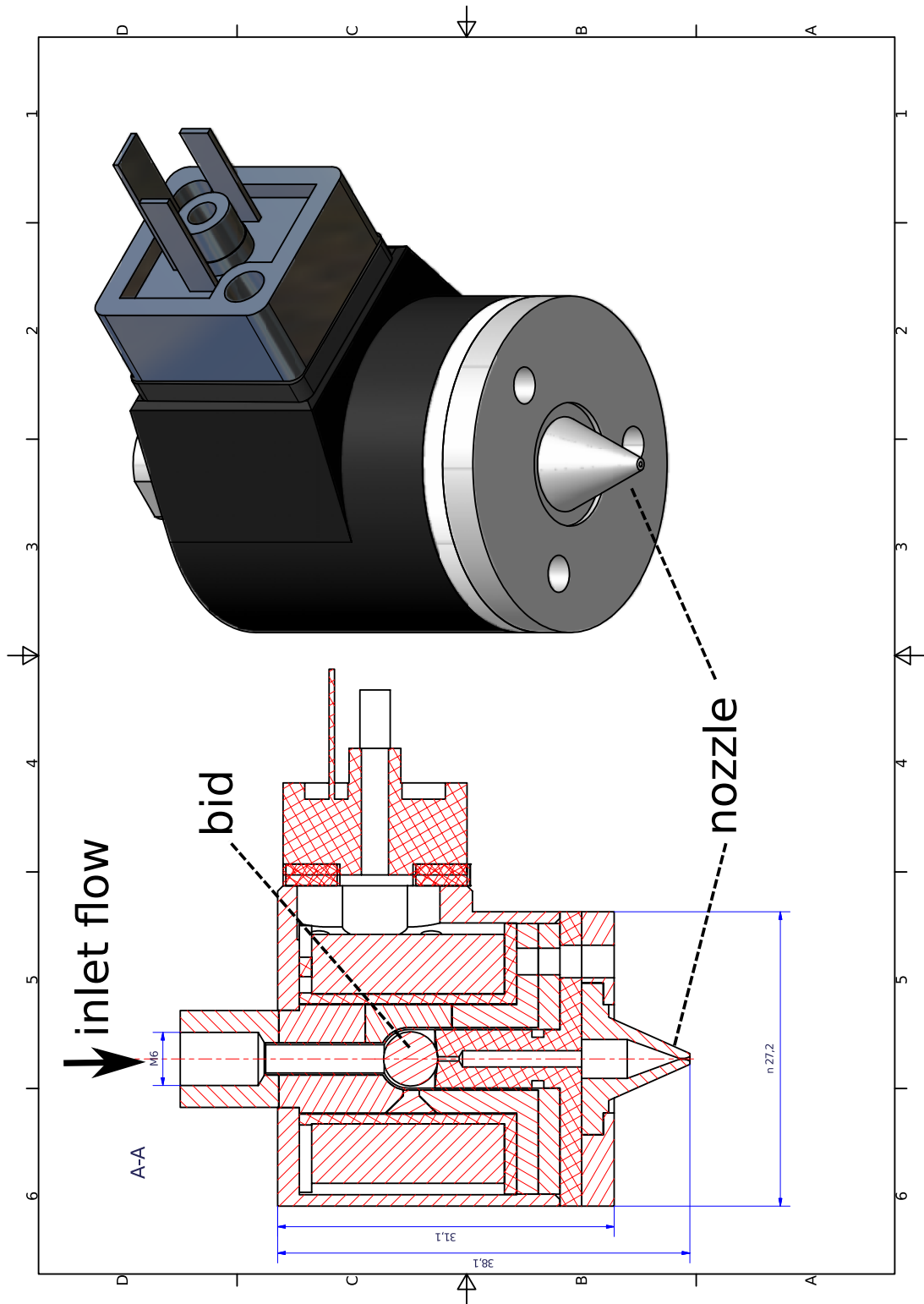
Figure A.10: Cross-section on the left and general outlook of the assembly electro-valve + nozzle on the right

Figure A.11: Photographs of the jet assembly (each square on the paper is 5 mm-wide)

Appendix B

Thomson Parabola

The Thomson parabola device enables one to separating of charged particles embedded in a beam for subsequent spectrum analysis. This separation is done with regards to charge-to-mass ratio q/m and incident velocity $\vec{v_i}$ by collinear constant electric and magnetic fields (usually decoupled in space). The figure B.1 gives an outlook of how such a device was implemented in the typical laser-gas jet experiments I carried out during my Ph.D. studies. The figure introduces the notations to be used in the following.

Figure B.1: Schematic of the ion acceleration from a gas jet along the transverse to the laser propagation direction, and specific ion detection with the Thomson parabola and MCP. Notations are used in the text. Note that the referential is not orthonormally oriented

Let a charged particle with mass m, charge q and incident velocity $\vec{v_i} = v_{iy} \cdot \vec{e_y}$ be. Let the constant electric and magnetic fields be respectively such that: $\vec{E} = E \cdot \vec{e_x}$ and $\vec{B} = B \cdot \vec{e_x}$.
By noting $\vec{v}_\parallel = v_x \cdot \vec{e_x}$ and $\vec{v}_\perp = v_y \cdot \vec{e_y} + v_z \cdot \vec{e_z}$, we can write for this particle the

following :

$$m\frac{d\vec{v}_\parallel}{dt} = q\vec{E}$$

$$m\frac{d\vec{v}_\perp}{dt} = q(\vec{v}_\perp \times \vec{B})$$

The previous yields to the common integration result:

$$v_x = \omega_c \frac{E}{B}t \tag{B.1a}$$

$$v_y = v_{iy}\cos(\omega_c t) \tag{B.1b}$$

$$v_z = v_{iy}\sin(\omega_c t) \tag{B.1c}$$

where: $\omega_c = qB/m$ is the cyclotron frequency.
The trajectory of the particle in the transverse (YZ) plane traces out a circle of equation:

$$Y^2 + \left(Z - \frac{v_{iy}}{\omega_c}\right)^2 = \left(\frac{v_{iy}}{\omega_c}\right)^2$$

Application: For $B \approx 0.45$ T, $q = 1.6 \cdot 10^{-19}$ C, and $m = 1836 \cdot 10^{-30}$ kg,then $\omega_c \approx 3.9 \cdot 10^7$ rad.s^{-1}.   For an average incident velocity $v_{iy} \approx 1.7 \cdot 10^7$ m.s^{-1} (i.e. a particle of energy 5 MeV), then the radius of the circle reads $\frac{v_{iy}}{\omega_c} \approx 0.42$ m.

Let now L be the length over which the particle feels the fields. In practice, the fields expand over few centimeters ($L \leq 4$ cm). Therefore:

$$\frac{L\omega_c}{v_{iy}} \ll 1 \tag{B.2}$$

This relation will be called further in the study. We continue the analytical development by assuming that the particle flies in field-region without bumping into the walls. This is equivalent to saying that its motion is limited along the $\vec{e}_y$-direction, i.e. by distance L. By integration of (B.1b), one calculates the time t_o needed to exit the magnet:

$$t_o = \frac{\arcsin\left(\frac{L\omega_c}{v_{iy}}\right)}{\omega_c} \tag{B.3}$$

We call v_{ox}, v_{oy} and v_{oz} the velocities reached by the particle at the magnet exit plane respectively in $\vec{e}_x, \vec{e}_y$ and $\vec{e}_z$-direction. We consider a detection screen being at distance D from the magnet exit in the (XZ) plane. The time t_D needed by the particle to reach the detector is given by the following[1]:

$$t_D = \frac{D}{v_{oy}} = \frac{D}{v_{iy}\cos(\omega_c t_o)} = \frac{D}{v_{iy}\sqrt{1 - \left(\frac{L\omega_c}{v_{iy}}\right)^2}} \tag{B.4}$$

---

[1]using: $\forall x \in [-1,1] \quad \cos(\arcsin(x)) = \sqrt{1-x^2}$

and thus the coordinates of the impact point on the detector yield:

$$x_D = v_{ox}t_D + x_o$$
$$z_D = v_{oz}t_D + z_o$$

where: x_o and z_o are the diversions in the $\vec{e}_x$ and $\vec{e}_z$-directions in the magnet exit plane.

It should be noticed that x_o and z_o depend upon the particle incident velocity v_{iy} in the following way:

$$x_o = \frac{1}{2\omega_c} \cdot \frac{E}{B} \cdot \arcsin^2\left(\frac{L\omega_c}{v_{iy}}\right) \tag{B.5a}$$

$$z_o = \frac{v_{iy}}{\omega_c} \cdot \left[1 - \sqrt{1 - \left(\frac{L\omega_c}{v_{iy}}\right)^2}\right] \tag{B.5b}$$

We consider the frame $(XZ)_D$ centered about the exit point $(x_o; z_o)$. In that frame, the particle impacts the detector in $(X; Z)$ with:

$$X = x_D - x_o = v_{ox}t_D \tag{B.6a}$$
$$Z = z_D - z_o = v_{oz}t_D \tag{B.6b}$$

It should be noticed that these formulae mean that the frame origin is *dependent* upon the particle charge-to-mass ratio along with the velocity. This point will be addressed later. Using (B.1a),(B.1c) and (B.3), the full derivation for X and Z follows:

$$X = \left(\omega_c \frac{E}{B} t_o\right) t_D$$

$$Z = v_{iy} \sin\left(\omega_c \cdot \frac{\arcsin\left(\frac{L\omega_c}{v_{iy}}\right)}{\omega_c}\right) t_D$$

and using (B.4):

$$X = \left(\frac{E}{B}\right) \arcsin\left(\frac{L\omega_c}{v_{iy}}\right) \cdot \frac{D}{v_{iy}\sqrt{1 - \left(\frac{L\omega_c}{v_{iy}}\right)^2}} \tag{B.7a}$$

$$Z = \left(\frac{L\omega_c}{v_{iy}}\right) \cdot \frac{D}{\sqrt{1 - \left(\frac{L\omega_c}{v_{iy}}\right)^2}} \tag{B.7b}$$

So far, all results proceed from exact analytical derivations. It should be emphasized that, analytically, the impact points of the bunch of particles embedded in the beam will not map out a parabola on the detector plane. To push things slightly forward, we start from this point onward to do approximations based

on the fact that in practice $\frac{L\omega_c}{v_{iy}} \ll 1$ (see (B.2)). Indeed, let us first do a Taylor expansion of $\arcsin\left(\frac{L\omega_c}{v_{iy}}\right)$ at third order when: $\left(\frac{L\omega_c}{v_{iy}}\right) \to 0$:

$$\arcsin\left(\frac{L\omega_c}{v_{iy}}\right) \overset{\to 0}{=} \frac{L\omega_c}{v_{iy}}\left[1 + \frac{1}{6}\left(\frac{L\omega_c}{v_{iy}}\right)^2 + o\left(\left(\frac{L\omega_c}{v_{iy}}\right)^2\right)\right]$$

Using (B.7) and neglecting terms of order bigger than three, we derive an equivalent of X:

$$X \overset{3^{\text{rd}}}{\sim} \left(\frac{E}{B}\right)\underbrace{\left(\frac{L\omega_c}{v_{iy}}\right)\cdot\frac{D}{\sqrt{1 - \left(\frac{L\omega_c}{v_iy}\right)^2}}}_{=Z}\cdot\underbrace{\frac{1}{v_{iy}}\cdot\left[1 + \frac{1}{6}\left(\frac{L\omega_c}{v_{iy}}\right)^2\right]}_{=\widetilde{Z}} \tag{B.8}$$

Likewise, let us do a Taylor expansion of $\left[1 - \left(\frac{L\omega_c}{v_iy}\right)^2\right]^{-1/2}$ at the third order when: $\left(\frac{L\omega_c}{v_{iy}}\right) \to 0$ and find an equivalent of Z:

$$\left[1 - \left(\frac{L\omega_c}{v_iy}\right)^2\right]^{-\frac{1}{2}} \overset{\to 0}{=} \left[1 + \frac{1}{2}\left(\frac{L\omega_c}{v_iy}\right)^2 + o\left(\left(\frac{L\omega_c}{v_{iy}}\right)^3\right)\right]$$

Hence, using (B.7) and neglecting terms of order bigger than three:

$$\frac{Z}{DL\omega_c} \overset{3^{\text{rd}}}{\sim} \frac{1}{v_{iy}}\cdot\left[1 + \frac{1}{2}\left(\frac{L\omega_c}{v_{iy}}\right)^2\right] \tag{B.9}$$

Looking at (B.9) and (B.8), $Z/DL\omega_c$ and $\widetilde{Z}$ are comparable at the first order.

$$\frac{Z}{DL\omega_c} \overset{1^{\text{st}}}{\sim} \widetilde{Z} \tag{B.10}$$

Recalling (B.8), we can write down the following equivalent valid at the first order when: $\left(\frac{L\omega_c}{v_{iy}}\right) \to 0$:

$$X \overset{1^{\text{st}}}{\sim} \left(\frac{E}{BDL\omega_c}\right)Z^2 \tag{B.11}$$

Having done these approximations, the parabolic form of the mapping out of the impact points arises, what is in agreement with experimental observation. However, several points should be emphasized to end up the study:

- the relation (B.5) show that particles with different charge-to-mass ratio *and* velocity come out of the magnet at different points of the exit plane $(XZ)_o$. This means that for each group of particle, the origin of the parabolic trace will be shifted from the ideal case (unique point source), which causes the parabola on detector to be distorted.

- yet, if we do a Taylor expansion of (B.5) at the first order when $\left(\frac{L\omega_c}{v_{iy}} \right) \to 0$, equivalents for x_o and z_o at second order are obtained:

$$x_o \overset{1^{\text{st}}}{\sim} \frac{1}{2\omega_c} \cdot \frac{E}{B} \cdot \left(\frac{L\omega_c}{v_{iy}} \right)^2$$

$$z_o \overset{1^{\text{st}}}{\sim} \frac{v_{iy}}{\omega_c} \cdot \left(\frac{L\omega_c}{v_{iy}} \right)^2$$

This means that, with regard to the approximations done in the frame $(XZ)_D$, the bunch of particle can be considered as emerging from a single point in the plane XZ_o.

- the discrepancy owing to series of approximations lead to an overall relative error of the order of $\left(\frac{L\omega_c}{v_{iy}} \right)$, which in practice equals $\approx 10\ \%$.

Appendix C

Complementary analytical derivations on Coulomb explosions in *simple cases*

The following completes the calculations I carried out on Coulomb explosion in *simple cases* and partially reported in chapter 2. The notations adopted are the same as in chapter 2. I examine first the case of a neutralizing electron shell at fixed radius r in cylindrical and spherical geometry (the time-dependent cases in these geometries are examined in chapter 2, section 2.1.2), and then both fixed-radius and time-dependent cases in the planar geometry.

C.1 Fixed radius r for cylindrical and spherical symmetries

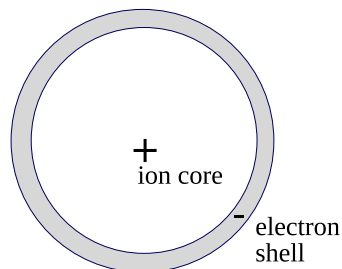The electrons shell is assumed to be fixed at r (see figure C.1)

Figure C.1: Positive ion core surrounded by a negative electron shell in the initial state

C.1.1   Fixed radius r for cylindrical and spherical symmetries

Effect of electron slowing down

I consider now the fact that cold electrons (not heated but just ponderomotively pushed outwards) and fast ions interact collisionally by Rutherford diffusion within the Debye sphere (unshielded electrostatic interactions) over the thickness l of the shell. Figure C.2 illustrates this point.
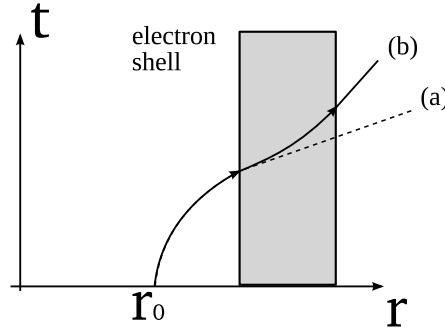

Figure C.2: Interaction between the electronic shell and one exploding ion. (a): trajectory without slowing down. (b) trajectory with slowing down

Owing to the large mass ratio between the populations of different velocities, the elastic collisions manifest themselves mainly by a slowing down of the ions without angular diffusion. The instantaneous slowing down can be quantified by a phenomenological model valid within the Debye sphere of radius λ_D and beyond the Landau or de Broglie spheres of radii λ_L and λ_B. This ensures that the charge stays unscreened (impact parameter $b < \lambda_D$) and avoids the divergence of the energy transfer when the impact parameter vanishes ($b > \lambda_L, \lambda_B$) [67]. The minimal contact distance (or cutoff distance) is noted $\lambda_C = \max(\lambda_L; \lambda_B)$. Then the model predicts the following energy loss rate:

$$\frac{\mathrm{d}\,E_c}{\mathrm{d}\,t} = -\frac{n_e Z^2 e^4}{4\pi\epsilon_0 m_e v} \ln\left[\frac{\lambda_D}{\lambda_C}\right] \tag{C.1}$$

with n_e and m_e, respectively, the electron density and mass, e the elementary charge, Z and v, the ion charge and velocity. The factor $\ln[\lambda_D/\lambda_C] = \Lambda$ is the Coulomb logarithm (see equation (1.39)). In practice, Λ varies little and $10 < \Lambda < 20$ for plasma of electronic temperature $T_e > 10$ eV (satisfied condition with an intense laser pulse). In the following, I consider Λ to be a constant. By introducing the electron plasma frequency ω_{pe} and the constant $K = Z^2 e^2 \Lambda/4\pi\epsilon_0$:

$$\frac{\mathrm{d}\,E_c}{\mathrm{d}\,t} = \frac{\mathrm{d}\,E_c}{\mathrm{d}\,r_{r0}} \underbrace{\frac{\mathrm{d}\,r_{r0}}{\mathrm{d}\,t}}_{=v} = -\frac{\omega_{pe}^2 K}{v} \tag{C.2}$$

hence, by variable separation:

$$\mathrm{d}\, E_c E_c = -\frac{\omega_{pe}^2 K m_i}{2}\, \mathrm{d}\, r_{r_0} \tag{C.3}$$

By integration over the thickness l of the shell:

$$E_c^2 = E_{c,i}^2 - \omega_{pe}^2 K m_i l \tag{C.4}$$

with $E_{c,i}^2$ the incident energy of the ion. I adopt now the following reduced notations:

$$\frac{E_c}{E_{c,\mathrm{max}}} \rightarrow \varepsilon$$

$$L = \frac{E_{c,\mathrm{max}}^2}{\omega_{pe}^2 K m_i}$$

$$\frac{l}{L} \rightarrow \mathrm{L}$$

L is the minimal shell thickness to stop the fastest ions with kinetic energy $E_{c,\mathrm{max}}$. Finally, the reduced equation from (C.4) takes the form:

$$\varepsilon^2 = \varepsilon_i^2 - \mathrm{L} \tag{C.5}$$

For a given L, there exists a single incident energy $\varepsilon_i = \epsilon$ in $\left[\sqrt{\mathrm{L}}, 1\right]$ giving a final energy ε in $\left[0, \sqrt{1 - \mathrm{L}}\right]$ (see figure C.3):

$$\epsilon = \sqrt{\varepsilon^2 + \mathrm{L}} \tag{C.6}$$

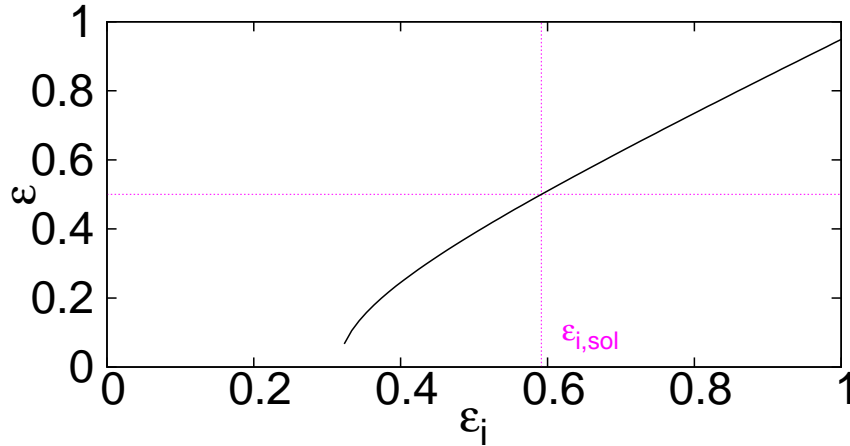Then, similarly to the expression (2.11), I can pose for the corresponding distri-

Figure C.3: Final energy ε versus initial incident energy ε_i for $\mathrm{L} = 0.1$. There exists a single solution $\varepsilon_{i,sol} \in \left[\sqrt{\mathrm{L}}, 1\right]$ to the equation (C.6)

bution function $\mathcal{F}_L$ for both symmetries:

$$\mathcal{F}_{\mathrm{L}}(\varepsilon) = \int\limits_0^1 \mathcal{F}_{2,3}(\varepsilon)\delta\left[\varepsilon - \sqrt{\varepsilon_i^2 - \mathrm{L}}\right] \tag{C.7}$$

As in equations (2.14) and (2.16), the integral can be made explicit by using the root ϵ.

$$
\begin{aligned}
\mathcal{F}_{\mathrm{L}}(\varepsilon) &= \frac{|\mathcal{F}_{2,3}(\varepsilon^2 + \mathrm{L})|}{\left|\dfrac{\varepsilon_i}{\sqrt{\varepsilon_i^2 - \mathrm{L}}}\right|_\epsilon} \\
&= \left|\frac{\varepsilon}{\sqrt{\varepsilon^2 + \mathrm{L}}}\mathcal{F}_{2,3}(\sqrt{\varepsilon^2 + \mathrm{L}})\right|
\end{aligned}
\tag{C.8}
$$

The reader can notice that by taking $\mathrm{L} = 0$, one obtains again the distributions (2.14) and (2.16). Besides, ε takes its value in $\left[0, \sqrt{1 - \mathrm{L}}\right]$; so, for $\mathrm{L} = 1$, ε vanishes and no ion can escape the shell. The figure C.4 summarizes the case.
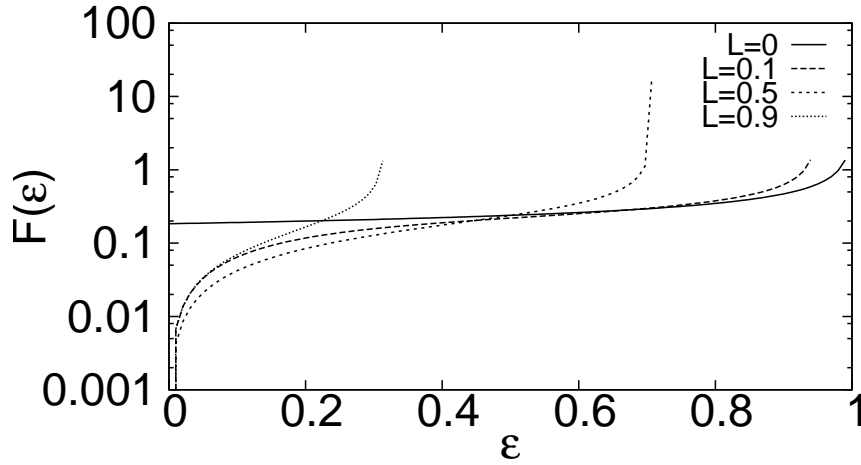

Figure C.4: Distribution functions $\mathcal{F}(\epsilon)$ after slowing down in the shell of reduced thickness L in cylindrical symmetry ($n = 2$) (the case $n = 3$ gives qualitatively similar results)

Neutral core and positive ring

To complete this study, let us consider the case illustrated in figure C.5. In practice, this situation would schematically be created by a laser ponderomotive effect acting on electrons not over the entire pulse area but on an annular fraction of it, leaving the central region in a quasineutral state. This hypothesis is reasonable in presence of a long laser pulse or with a moderate intensity so as to reduce the longitudinal intensity gradient responsible of the depletion of the centre. I
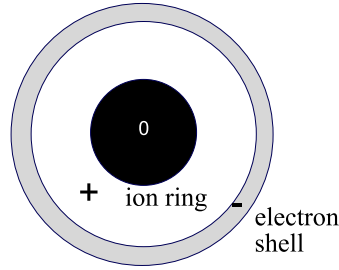
Figure C.5: Neutral core of radius R surrounded by a positively charged ring and a neutralizing negatively charged shell

compute the spectrum at the exit of the shell in the spherical symmetry (the cylindrical symmetry is similar). For a central quasi-neutral region of radius R, it follows from equation (2.3b):

$$E_c(r_0) = m_i \frac{\omega_{pi}^2}{3} r^2 \left[\left(\frac{r_0^2}{r^2} - \frac{R^3}{r_0 r^2} \right) - \frac{r_0^3 - R^3}{r^3} \right] \tag{C.9}$$

With $X = r_0/r$ and $a = R/r$, both in $[0, 1]$:

$$E_c(X) = m_i \frac{\omega_{pi}^2}{3} r^2 \left[\left(X^2 - \frac{a^3}{X} \right) - (X^3 - a^3) \right] \tag{C.10}$$

By deriving equation (C.10), one obtains the condition on X to reach a maximum in energy:

$$3X^4 - 2X^3 = a^3 \tag{C.11}$$

From figure C.6, there exists graphically a single positive solution $b_a \in \left[\frac{2}{3}, 1 \right]$ of (C.11) so that:

$$3b_a^4 - 2b_a^3 = a^3 \tag{C.12}$$

(note please the trivial solutions $b_{a=0} = 0$ or $b_{a=0} = \frac{2}{3}$).
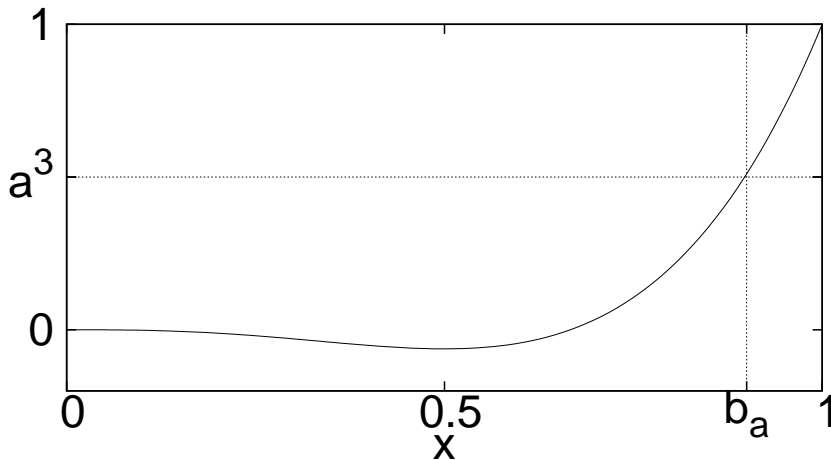

Figure C.6: single solution $b_a \in [2/3, 1]$ of the equation (C.11)

Then, the maximum energy reads:

$$E_{c,\max} = m_i \frac{\omega_{pi}^2}{3} r^2 \underbrace{\left[\left(b_a^2 - \frac{a^3}{b_a} \right) - (b_a^3 - a^3) \right]}_{= C_a} \tag{C.13}$$

(note that $C_{a=0} = \frac{4}{27}$, in agreement with the numerical factor in equation (2.5)). C_a decreases as a increases, so that the final energy drops accordingly as less charges push the ions outwards. By noting again $\varepsilon = E_c(r_0)/E_{c,\max}$ the reduced energy, one gets:

$$\varepsilon = \frac{\left[\left(X^2 - \frac{a^3}{X} \right) - (X^3 - a^3) \right]}{C_a} \tag{C.14}$$

Figure C.7 plots the reduced equation (C.14) for different value of a. Similarly

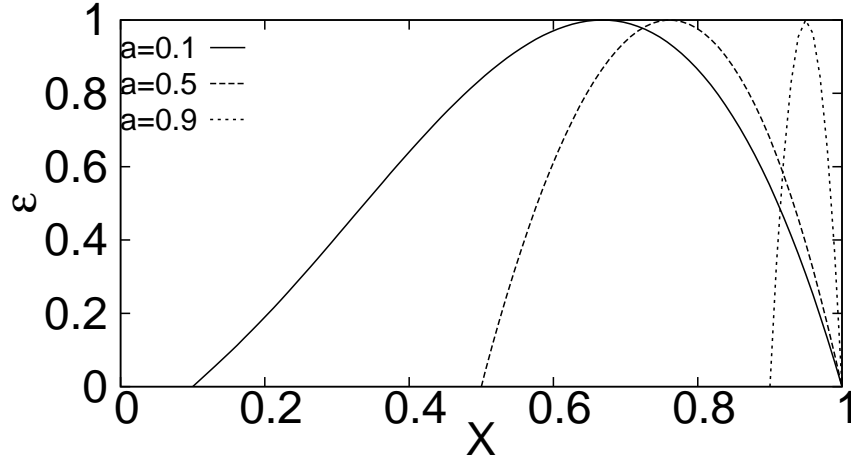Figure C.7: Final kinetic energy ε versus the initial position X for three values of the neutral core radius a (reduced notations)

to the above discussion, for a given core radius a, the function $X_a(\varepsilon)$ is bivalued with two solutions $X_{a,-}$ and $X_{a,+}$ on either side of the maximum b_a.

$$\frac{dN_i}{dE} = \frac{3N_i}{E_{c,\max}} \mathcal{F}_{3,a}(\varepsilon) \tag{C.15}$$

and,

$$\mathcal{F}_{3,a}(\varepsilon) = \frac{C_a X_{a,-}^2(\varepsilon)}{\left| 2X_{a,-} + \dfrac{a^3}{X_{a,-}^2} - 3X_{a,-}^2 \right|} + \frac{C_a X_{a,+}^2(\varepsilon)}{\left| 2X_{a,+} + \dfrac{a^3}{X_{a,+}^2} - 3X_{a,+}^2 \right|} \tag{C.16}$$

The figure C.8 shows the distribution profiles with the dependences upon the reduced radius a.
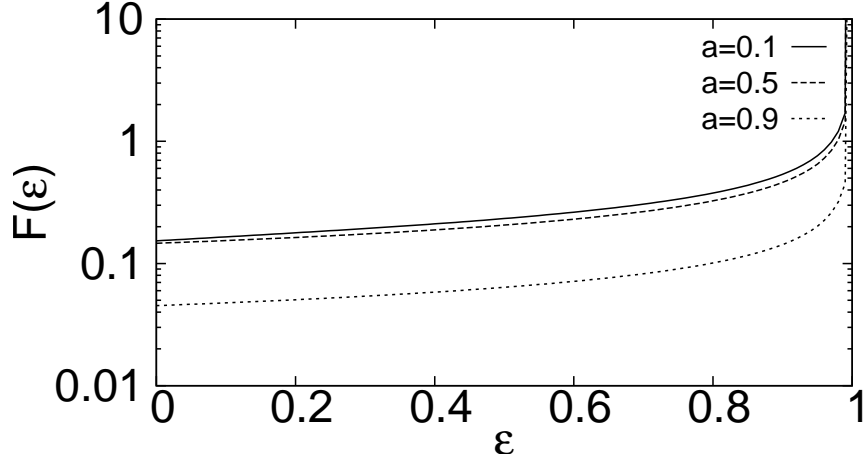
Figure C.8: Distribution function $\mathcal{F}_{3,a}$ with a neutral core of reduced radius a

C.2 Planar symmetry

To complete the overall view of CE, let us consider a charged slab subject to CE in the NCHA. The same lagrangian description is adopted with $r_{r_0} = r_0 + \xi(t)$. From the Maxwell-Gauss equation in this symmetry:

$$E(r_0 + \xi) \cdot (r_0 + \xi) = \frac{n_{i0}r_0}{\epsilon_0} \tag{C.17}$$

with E the electric field.

The kinetic energy is given through the same derivations as in the cylindrical and spherical symmetries (see equations (2.3)). Using the reduction $x_0 = \frac{r_0}{r_0 + \xi}$:

$$\frac{m_i}{2}\left(\frac{\partial \xi}{\partial t}\right)^2 = m_i \omega_{pi}^2 x_0 \xi(t) \tag{C.18}$$

As in the cylindrical symmetry, the kinetic energy diverges for $\xi \to \infty$ because of the presence of an infinite amount of charges in the slab. After integration of (C.18):

$$\xi(x_0, t) = \frac{\omega_{pi}^2}{2} x_0 t^2 \tag{C.19}$$

and, with $\mathrm{T} = \omega_{pi}t$,

$$\xi(x_0, \mathrm{T}) = \frac{x_0 \mathrm{T}^2}{2} \tag{C.20}$$

I consider now both cases of neutralization of the SCF from (*i*) the electron shell at a fixed position and (*ii*) the sudden electron backflow.

Fixed length $\mathbf{x_0} + \xi = \mathbf{x}$

From the energy equation (C.18):

$$E_c(x_0) = m_i \omega_{pi}^2 x_0(x - x_0) \tag{C.21}$$

Thus, the maximum obtained kinetic energy is $E_{c,\max} = \frac{m\omega_{pi}^2 x^2}{4}$. Using the notations $X = \frac{x_0}{x}$ and $\varepsilon = \frac{E_c}{E_{c,\max}}$, the reduced energy equation gives:

$$\varepsilon = 4X(1-X) \tag{C.22}$$

The figure C.9 plots the energy equation and shows the bivaluation of the function $X(\epsilon)$. For a given $\varepsilon \in [0,1]$, there exist in general two initial positions X_- and X_+ located either side of the position $X(1)$:
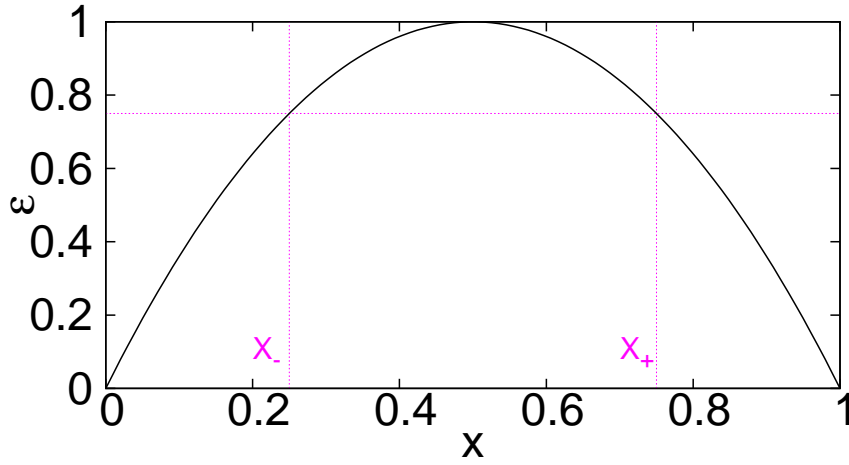

Figure C.9: Final kinetic energy ε versus the initial position X. For a given ε, there exists two solutions X_- and X_+, equally distant from X(1)=0.5

These solutions are given by:

$$X_\pm = \frac{1 \pm \sqrt{1-\varepsilon}}{2} \tag{C.23}$$

Similarly to the expressions (2.11),(2.14) and (2.16), the ion distribution function $\mathcal{F}_1$ can be obtained:

$$\mathcal{F}_1(\varepsilon) = \int_0^1 \delta(\varepsilon - 4X(1-X)) \tag{C.24}$$

Then, using the solutions (C.23),

$$
\begin{aligned}
\mathcal{F}_1(\varepsilon) &= \frac{1}{|X_-(\varepsilon) - 4|} + \frac{1}{|X_+(\varepsilon) - 4|} \\
&= \frac{1}{2\left|\sqrt{1-\varepsilon}\right|}
\end{aligned} \tag{C.25}
$$

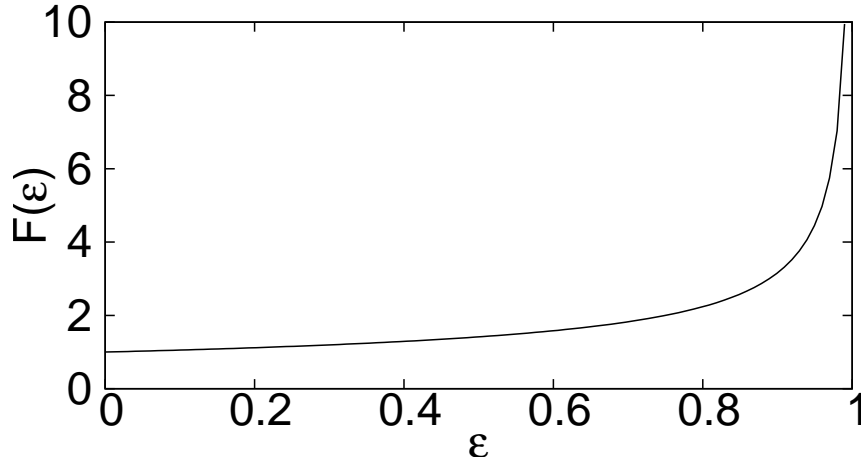The figure C.10 shows the distribution function for fixed shell position.

Figure C.10: Distribution function $\mathcal{F}_1$ for a charged ion slab with fixed electron shell position

Fixed time T

Let us inject (C.20) in (C.18).

$$E_c(x_0) = m\omega_{pi}^2 \frac{x_0^2 T^2}{2} \tag{C.26}$$

With a chosen characteristic length L of the problem (e.g. the radius of the laser), the following reductions are made:

$$\varepsilon = \frac{E_c(x_0)}{\dfrac{m\omega_{pi}^2 R^2}{2}}$$

$$X_0 = \frac{x_0}{R}$$

The equation (C.26) takes the form:

$$\varepsilon = X_0^2 T^2 \tag{C.27}$$

Thus, the simple solution $X_{s,1} = X_0(\varepsilon)$ giving the initial position for a given energy ε at T is:

$$X_{s,1} = \frac{\sqrt{\varepsilon}}{T} \tag{C.28}$$

Finally, the ion distribution $\mathcal{F}_{1,T}$ can be calculated:

$$
\begin{aligned}
\mathcal{F}_{1,T} &= \int_0^1 \delta(\varepsilon - X_0^2 T^2) \\
&= \frac{1}{2T^2 X_{s,1}} \\
&= \frac{1}{2T\sqrt{\varepsilon}} \tag{C.29}
\end{aligned}
$$

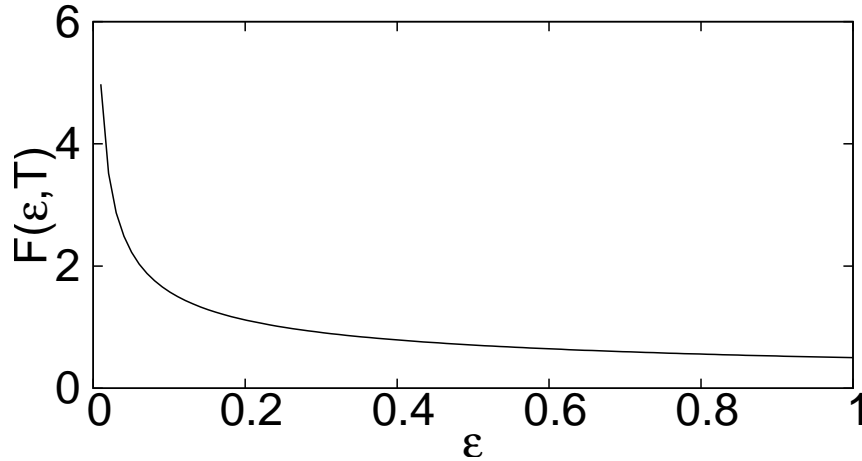The figure C.11 traces out the ion distribution function at a time T.

Figure C.11: Distribution function $\mathcal{F}_{1,\text{T}}$ for a charged ion slab at T=1

One can notice that in this peculiar geometry, the ion spectrum from CE does not present the same qualitative behaviour as one regards the problem from a fixed-positioned or from a fixed-timed viewpoint.

Appendix D

Publications

The following lists the papers related to laser-gas jets experiments written during my Ph.D. period:

- F. Sylla, A. Flacco, S. Kahaly, M. Veltcheva, G. Sanchez-Arriaga, E. Lefebvre, and V. Malka. Anticorrelation between Ion Acceleration and Nonlinear Coherent Structures from Laser-Underdense Plasma Interaction, *Phys. Rev. Lett 108, 115003 (2012)*

- F. Sylla, M. Veltcheva, S. Kahaly, A. Flacco and V. Malka. Development and characterization of very dense submillimetric gas jets for laser-plasma interaction, *Rev. Sci. Instr. 83, 033507 (2012)*

- F. Sylla, S. Kahaly, A. Flacco, M. Veltcheva, G. Sanchez-Arriaga, E. Lefebvre, and V. Malka. Observation of Ions Accelerated in the Wake of a Short Laser Pulse, *in submission*

- F. Sylla, S. Kahaly, A. Flacco, M. Veltcheva, E. d'Humières, V. Tikhonchuk, and V. Malka. Ultrafast Near-Critical Plasma Dynamics and Magnetic Dipole Excitation After Collapse of Short Intense Pulse, *in submission*

Also, two publications on laser-thin foil experiments have been published with my coauthorship:

- A. Flacco, F. Sylla, M. Veltcheva, M. Carrié, R. Nuter, E. Lefebvre, D. Batani, and V. Malka. Dependence on pulse duration and foil thickness in high-contrast-laser proton acceleration. *Phys. Rev. E 81, 036405 (2010)*

- A. Flacco, T. Ceccotti, H. George, P. Monot, Ph. Martin, F. Reau, O. Tcherbakoff, P. d'Oliveira , F. Sylla, M. Veltcheva, F. Burgy, A. Tafzi, V. Malka, D. Batani. Comparative study of laser ion acceleration with different contrast enhancement techniques. *Nuclear Instruments and Methods in Physics Research A 620 (2010) 18-22*

Finally, one patent on the overdense gas jet was submitted to the French and European Patent Offices and reveived a positive first assessment in the process of approval.

- Procédé et agencement pour engendrer un jet de fluide, procédé et système de transformation du jet en un plasma et applications de ce système, *Priorité n° FR110055056 du 09 Juin 2011*
  Inventors: F. Sylla, V. Malka, A. Flacco, M. Veltcheva, S. Kahaly

Anticorrelation between Ion Acceleration and Nonlinear Coherent Structures from Laser-Underdense Plasma Interaction

F. Sylla,[1] A. Flacco,[1] S. Kahaly,[1] M. Veltcheva,[1,2] A. Lifschitz,[1] G. Sanchez-Arriaga,[3] E. Lefebvre,[3] and V. Malka[1]

[1]*Laboratoire d'Optique Appliquée, ENSTA, CNRS, Ecole Polytechnique, UMR 7639, 91761 Palaiseau, France*
[2]*Dipartimento di Fisica "G. Occhialini," Università degli Studi di Milano-Biccoca, piazza della Scienza 3, 20126 Milan, Italy*
[3]*CEA, DAM, DIF, 91297 Arpajon, France*
(Received 22 July 2011; published 13 March 2012)

In laser-plasma experiments, we observed that ion acceleration from the Coulomb explosion of the plasma channel bored by the laser is prevented when multiple plasma instabilities, such as filamentation and hosing, and nonlinear coherent structures (vortices or postsolitons) appear in the wake of an ultrashort laser pulse. The tailoring of the longitudinal plasma density ramp allows us to control the onset of these instabilities. We deduced that the laser pulse is depleted into these structures in our conditions, when a plasma at about 10% of the critical density exhibits a gradient on the order of 250 μm (Gaussian fit), thus hindering the acceleration. A promising experimental setup with a long pulse is demonstrated enabling the excitation of an isolated coherent structure for polarimetric measurements and, in further perspectives, parametric studies of ion plasma acceleration efficiency.

Laser-underdense plasma acceleration rests on the interaction of an intense relativistic pulse ($I\lambda^2 > 10^{18}$ W cm^{-2} μm^2) with a plasma in a large range of electronic density ($n_e \in [10^{18}, 10^{20}]$ cm^{-3}) [1–4]. In particular, the Coulomb explosion of a positively charged channel, created by the laser as it propagates in the plasma, is an efficient way to radially accelerate ions [1,5]. However, this acceleration can be accompanied by the copious generation of nonlinear plasma structures that significantly deplete the pulse energy, theoretically up to 30%–40% of the laser energy [6–10]. These structures aroused the interest of numerous theoretical and experimental studies [6,8,11–15]. An underdense plasma with $n_e \sim$ tens of percent of n_c, n_c being the critical density, is particularly suitable for the excitation of coherent structures like electromagnetic solitons and electron vortices, as predicted in Refs. [6,8,10,11] and observed with proton radiography diagnostics in Refs. [12,13,16]. In Ref. [6], a 3D electromagnetic cavity structure in the wake of the pulse, termed a transverse magnetic soliton, is identified and slowly expands into a postsoliton, as ions within the cavity explode to energies of tens of keV. This example illustrated a novel ion acceleration scheme from underdense plasma, different from the channel Coulomb explosion [1], the target normal sheath accelerationlike process [3], or longitudinal magnetic vortex acceleration [17].

In this Letter, we present for the first time an "inverse correlation" (mutual exclusion) between the ion acceleration by radial Coulomb explosion and the generation of nonlinear coherent structures in the wake of the laser pulse. Our results tend to prove that the efficiency of the laser-ion acceleration directly from a gas jet is highly dependent upon the density gradient profile. In our case, though the density ramp should contribute to the increase of the laser

intensity by self-focusing of the pulse [18,19], it induces filamentation [19], hosing instabilities [20], and ultimately generation of nonlinear coherent structures, the overall turning out to be detrimental for the acceleration.

The experiment was conducted at the Laboratoire d'Optique Appliquée with the Ti:sapphire laser "Salle Jaune," which delivers an ultrashort (duration $\tau = 30$ fs), linearly polarized (along z; see Fig. 1) pulse with $E_L \sim 810$ mJ on target [21]. The pulse was focused with an $f/10$ off-axis parabolic mirror to a 25-μm ($1/e^2$) focal spot onto a 700-μm (FWHM) supersonic He jet at ~300 μm above the nozzle exit. The vacuum laser intensity is $I_0 \sim 1 \times 10^{19}$ W cm^{-2}. With $n_e = 1–10 \times 10^{19}$ cm^{-3}, it gives a ratio $P_L/P_c = 5.3–53$ (with P_L the laser power and $P_c = 16.2n_c/n_e$ GW the critical power for self-focusing). Before focusing, the beam was split and 10% of the energy sent to a beta barium borate crystal for second harmonic generation. The intensity and spatial quality of this collimated frequency-doubled beam were improved by passing through a 50-μm-pinhole-filtered beam reducer. It was finally incident on the jet normally to the main laser axis for illuminating and probing the interaction transversally (see Fig. 1). Measurements of ion emission and plasma probing (interferometry and polarimetry), both at 90° from the main laser propagation axis, were simultaneously done by means of a 45°-pierced mirror reflecting the probe beam onto the gas jet without cutting the ion beam (see Fig. 1).

The ion detector is composed of a 100-μm spatial filter (solid angle acceptance is 1.2×10^{-8} sr) with a Thomson parabola spectrometer coupled to 40-mm imaging microchannel plate chevron assembly [see Fig. 1(a)]. A linearized 16-bit CCD camera (1024×1024 pixels) enables single-shot recordings of scintillating traces and thus shot-to-shot statistical analyses of ion spectra.
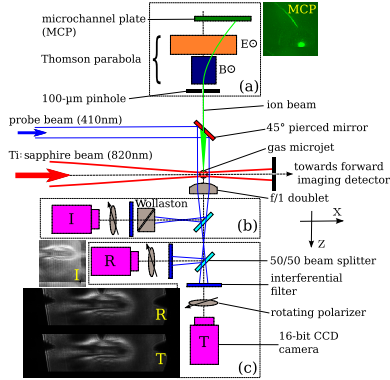
FIG. 1 (color online).   Experimental setup for the interaction of a microjet and a short Ti:sapphire pulse, illuminated by a linearly polarized frequency-doubled probe pulse. (a) Imaging ion spectrometer along the normal to the main beam with a Thomson parabola ($B = 0.3$ T) and chevron microchannel plate (MCP). A second ion spectrometer is also set on the laser axis. (b) Nomarski interferometer. (c) Polarimeter using the Faraday rotation effect. For polarigrams R and T, the polarizers are rotated by, respectively, $+10$ and $-10°$ from the extinction.

An $f/1$ achromatic doublet coupled with a 50/50 beam splitter enables us to record at the same time with spatial resolution ~ 1 μm, interferograms encoding the plasma density variations using a Nomarski interferometer [22] [see Fig. 1(b)], and polarigrams revealing the component of the magnetic field collinear to the probe beam direction [see Fig. 1(c)]. The interferometer contains a Wollaston biprism of 10×10 mm^2 with a 410-nm interferential filter to improve the temporal coherence of the interferences. The polarimeter is composed of two identical assemblies, each comprising, in particular, a Glan laser polarizer (extinction ratio better than 10^{-4}) and a 16-bit CCD camera. For each assembly, a scan of the rotating polarizer was carried out for probe beam transmission calibration (every 5° over the entire rotation). For the measurements, the polarizers were detuned by a common angle from each minimum of transmission [typical detunings $\theta_R = +10$ and $\theta_T = -10°$ for, respectively, the transmitted and reflected images from the beam splitter; see Fig. 1(c)].

The magnetic field detection rests on the measurement of the rotation, due to the Faraday effect, of the incident linear polarization of the probe beam electric field when it crosses the plasma [23,24]. The total rotation angle along a path l_z is given by $\phi_{rot}(x, y) = \frac{e}{2m_e c n_c} \int_{l_z} n_e(x, y, z) B_z dz$. Here B_z is the magnetic field component collinear to the probe beam direction, n_c the plasma critical density for the probe beam, e and m_e the mass and charge of the electron, respectively, and c the light velocity in vacuum. Taking the

intensity ratio from the two shadowgrams R and T obtained with opposite detuning angles [see Fig. 1(c)] prevents the extracted ϕ_{rot} map from being corrupted by probe beam shot-to-shot fluctuations in intensity and image shift from plasma refraction or vibrations. However, this requires a pixel-to-pixel correspondence of the pictures. We achieved a subpixel-accurate matching of the two pictures by tagging the field of view at three reference areas prior to the beam splitting and by running a numerical pattern-matching routine.

Figure 2 shows the MCP recordings at 90° from the laser axis for two plasma gradient conditions. In Fig. 2(a), the laser is shot on the gas jet at an early stage of its expansion in the vacuum chamber so that the plasma gradient is steep: ~ 150 μm (with a Gaussian fit). In Fig. 2(b), the interaction occurs at a late time of the expansion (80 ms after the closing of the valve), and the gradient is smooth: ~ 250 μm. For both conditions, the peak density in the jet has the same value: $n_e \sim 10^{20}$ cm^{-3}. We observe *systematically* radial ion acceleration from Coulomb explosion in case (a) and no trace in (b). In both cases, no ion was detected in the forward direction (see Fig. 1 for the geometry). When acceleration occurs, only He$^+$ are detected from 12 keV to cutoff energies of 250 keV. We attribute
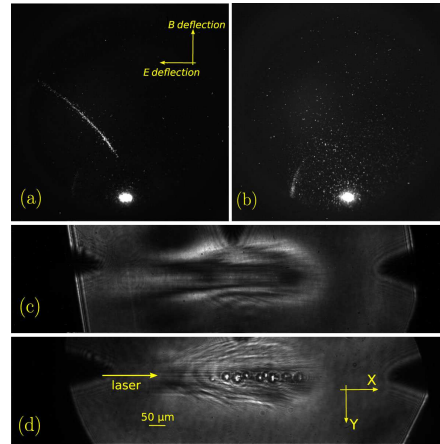

FIG. 2 (color online).   (a),(b) MCP recordings normally to the laser axis for $n_e \sim 10^{20}$ cm^{-3}. (a) Short-plasma gradient ~ 150 μm. He$^+$ trace with energy cutoff ~ 250 keV. (b) Long-plasma gradient ~ 250 μm. (c),(d) Shadowgram at 1 ps after the pulse enters the jet (resolution ~ 1 μm, magnification 8.2). (c) Short-plasma gradient. (d) Long-plasma gradient. The shadowgram shows a clear train of bubblelike structures in the laser wake. The laser polarization is normal to the picture (S polarized).

the absence of He^{2+}, though the laser peak intensity is 1000 times higher than the helium potential of full ionization, to efficient recombination of this species in the neutral corona starting at 100 μm from the laser axis. Indeed, the electron capture is the most probable channel of interaction (cross section $\sigma \sim 10^{16}$ cm^{-2}) for a He^{2+} projectile of 250 keV streaming in He gas [25]. In Fig. 2(d), one can see the typical shadowgram (revealing sharp electron density fronts) obtained in case (b). A train of zigzag ordered and well separated bubble structures with an average size of about 30 μm ($\gg \lambda_p = c/\omega_{pe}$, the plasma wavelength) can be clearly seen in the wake of the laser pulse. The bubbles have a bright spot in their centers that is not observable when the probe beam is turned off. This means that the emission is not of a self-emission nature and results from refractive effects of the probe light by these structures behaving like microlenses. An interesting point is the quasicircular shape of these structures, meaning that, during the transverse illumination of 30 fs, their centers are quasistatic in the picture plane. In the short-plasma scale length case, for which transverse ion acceleration is detected [Fig. 2(a)], no such isolated structure is ever observed in the gas jet [Fig. 2(c)].

To understand this inverse correlation, we investigated in time the interaction in the long gradient case. Figure 3 presents a sequence of five shadowgrams taken at different delays after the pulse enters the jet (t_0). Very early in the interaction ($t_0 + 540$ fs), sizable filaments develop next to the main laser channel [19] [see the arrows in Fig. 3(b)]. As the pulse propagates along, the filamentation becomes stronger and multiple circular structures appear about the
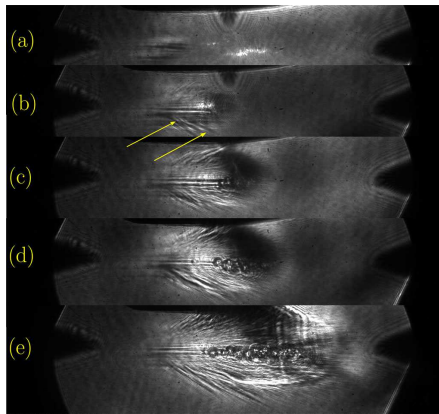
laser channel, near the center of the jet. In this time-resolved scan, we observe that the structures appear randomly in the laser path, and no correspondence could be drawn between the pulse and bubble positions. Moreover, even if this shadowgram diagnostic is not intrinsically time-resolved, contrary to the proton radiography technique [26], the stability of the interaction was sufficient to assess statistically the average size of the structure until the moment when the shadowgrams become blurred and unexploitable, at about 7 ps after the onset of the interaction. Over that time span, we observed that the structures have fairly the same size, irrespective of their positions to the laser front, and measured an average increase of less than 10 μm in size.

Besides being copiously generated by the interaction, the nonlinear structures distribute spatially into two remarkable patterns, identifiable by following the bright central blobs, which arose randomly in our experiment. Figure 4 illustrates both antisymmetric (zigzag about the laser axis) [panel (a)] and axial [panel (b)] distributions of the bubbles. In Ref. [27], the authors carried out a 2D particle-in-cell simulation with $a_0 = 3$, $\tau = 30$ fs, and about 1 mm of plasma at $n_e = 10^{19}$ cm^{-3}. They obtained for initially p- and s-polarized light (i.e., an electric field collinear and normal to the observation plane), respectively, antisymmetric and axial density map patterns resembling our experimental results (see Figs. 3 and 4 in Ref. [27]). In particular, the antisymmetric modulation is ascribed to the hosing instability (see also [9]). Although in our experiment the incident laser polarization is normal to the observation plane, corresponding to the s polarization of simulations [9,27], hosing instabilities have also been observed experimentally in similar conditions [28]. Therefore, following Refs. [9,27,28], we propose to ascribe our observations to the laser excitation of the hosing instability inducing the development of a von Kármán row of electron vortices (a) and to shadowgraphic traces left by postsolitons (b).

At that point, it is clear that the interaction in this operating regime ($n_e \sim 10^{20}$ cm^{-3}, long gradient ~ 250 μm) produces numerous instabilities (filamentation, hosing, vortex or soliton), known to seriously deplete the pulse energy [6,8,9] and prevent efficient plasma channel

FIG. 3 (color online). Time-resolved pulse penetration in the plasma gradient. (a) Reference instant t_0, (b) $t_0 + 540$ fs, (c) $t_0 + 940$ fs, (d) $t_0 + 1.54$ ps, and (e) $t_0 + 2.84$ ps. Arrows indicate the growth of prominent laser filaments.
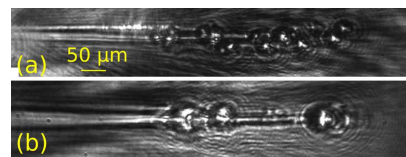

FIG. 4 (color online). Spatial distribution of the bubbles for two shots in the same conditions at $t_0 + 1.54$ ps showing (a) antisymmetric (zigzag) and (b) symmetric axial patterns about the main plasma channel.
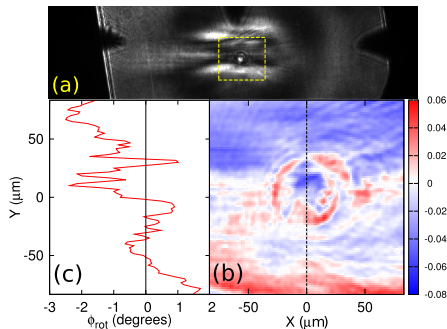
FIG. 5 (color online). (a) Shadowgram with one isolated structure in the laser wake at $t_0 + 940$ fs ($\tau = 350$ fs, 10^{19} cm^{-3}). (b) ϕ_{rot} map (in radians) of the yellow square dotted zone in (a). Detuning angle of the polarizers: $\pm 10°$. (c) Lineout along the black dotted line in (b).

charging for subsequent Coulomb explosion. Moreover, despite their expansions by ion core explosion [9,12,15], the bubbles do not provide a detectable acceleration, possibly because of a number of accelerated ions below the detector noise level. Therefore, we were unable to verify the postsoliton acceleration scenario predicted in Refs. [6,15].

To confirm the electromagnetic nature of the coherent structures, we carried out some polametric measurements. To simplify these measurements, we have identified a regime where few structures are generated at each laser shot, near the center of the jet (statistically close to 1). For that, we used a stretched laser pulse $\tau = 250$ fs carrying the same energy ($a_0 = 0.8$) and a small sonic nozzle of 200-μm diameter delivering a jet of peak density of a few 10^{19} cm^{-3} which we let expand in vacuum to increase the gradient before the interaction. This setup enables (i) a well-localized interaction, (ii) smoother interferograms and polarigrams without filaments and bubble overlapping, and (iii) efficient energy transfer to the structures [9].

Figure 5(a) shows a shadowgram with one single spherical structure of 57-μm diameter in a clean area. In that simplified case, we were able to extract a ϕ_{rot} map around the structure [Fig. 5(b)]. From Figs. 5(b) and 5(c), we can deduce that the structure in this condition has an almost axisymmetric polarimetric imprint about the laser polarization direction. The density in the bubble shell is found to be $\sim 7 \times 10^{19}$ cm^{-3}, 5 times that of the surrounding plasma. Though the polarimetric information is the convolution of B_z by the density along the integrated probe beam path in the plasma, we will assume for the remainder that the main contribution comes from the structure and not from the surrounding plasma, as the major part of the bubble seems to be lying in a weakly magnetized area

(white region). Doing so, we thus calculate the maximum magnetic field extractable from our data. For $n_e = 7 \times 10^{19}$ cm^{-3}, an average path l_z in the shell of 25 μm [from Fig. 5(c)], $n_c = 4 \times 1.67 \times 10^{21}$ cm^{-3}, and a Faraday rotation of 0.04 rad, we find $B_z \leq \phi_{rot}(\frac{2 m_e c n_c}{n_e l e}) = 570$ T. Though lower, this value is of the same order of magnitude as in the numerical computations in similar conditions [6,8] and is consistent with the fact that the fields dissipate as the structure expands. The extraction of the space-resolved magnetic field map and a refined magnetic description of the nonlinear structures will be the subject of another publication.

In conclusion, our reproducible observations of bubbles identified as nonlinear coherent structures (vortex or postsoliton) made it possible to demonstrate their detrimental effect on the efficiency of laser-ion acceleration. These structures appear abundantly in the laser wake when the plasma has a long gradient profile in which the laser self-focuses, filaments, and develops hosing. When using a small nozzle with lower density, simple conditions with one structure per laser shot can be statistically obtained. We think this all-optical setup represents a powerful method that opens up a new opportunity of in-depth investigation of fundamental nonlinear plasma instabilities and also particle acceleration for users of well-spread terawatt-class lasers.

[1] K. Krushelnick *et al.*, Phys. Rev. Lett. **83**, 737 (1999).
[2] V. Malka *et al.*, Nature Phys. **4**, 447 (2008).
[3] L. Willingale *et al.*, Phys. Rev. Lett. **96**, 245002 (2006).
[4] M. S. Wei *et al.*, Phys. Rev. Lett. **93**, 155003 (2004).
[5] G. S. Sarkisov *et al.*, Phys. Rev. E **59**, 7042 (1999).
[6] T. Esirkepov *et al.*, Phys. Rev. Lett. **89**, 275002 (2002).
[7] T. Z. Esirkepov, Y. Kato, and S. V. Bulanov, Phys. Rev. Lett. **101**, 265001 (2008).
[8] S. V. Bulanov *et al.*, Phys. Rev. Lett. **82**, 3440 (1999).
[9] N. M. Naumova *et al.*, Phys. Plasmas **8**, 4149 (2001).
[10] Y. Sentoku *et al.*, Phys. Rev. Lett. **83**, 3434 (1999).
[11] S. V. Bulanov *et al.*, Phys. Rev. Lett. **76**, 3562 (1996).
[12] M. Borghesi *et al.*, Phys. Rev. Lett. **88**, 135002 (2002).
[13] L. Romagnani *et al.*, Phys. Rev. Lett. **105**, 175002 (2010).
[14] G. Sánchez-Arriaga and E. Lefebvre, Phys. Rev. E **84**, 036403 (2011).
[15] G. Sánchez-Arriaga and E. Lefebvre, Phys. Rev. E **84**, 036404 (2011).

[16] G. Sarri *et al.*, Phys. Rev. Lett. **105**, 175007 (2010).
[17] A. Kuznetsov *et al.*, Plasma Phys. Rep. **27**, 211 (2001).
[18] G. Sun *et al.*, Phys. Fluids **30**, 526 (1987).
[19] W. B. Mori *et al.*, Phys. Rev. Lett. **60**, 1298 (1988).
[20] P. Sprangle, J. Krall, and E. Esarey, Phys. Rev. Lett. **73**, 3544 (1994).
[21] A. Flacco *et al.*, Nucl. Instrum. Methods Phys. Res., Sect. A **620**, 18 (2010).
[22] R. Benattar *et al.*, Rev. Sci. Instrum. **50**, 1583 (1979).
[23] J. A. Stamper and B. H. Ripin, Phys. Rev. Lett. **34**, 138 (1975).
[24] M. C. Kaluza *et al.*, Phys. Rev. Lett. **105**, 115002 (2010).
[25] M. B. Shah and H. B. Gilbody, J. Phys. B **18**, 899 (1985).
[26] L. Romagnani *et al.*, Phys. Rev. Lett. **95**, 195001 (2005).
[27] L. M. Chen *et al.*, Phys. Plasmas **14**, 040703 (2007).
[28] M. C. Kaluza *et al.*, Phys. Rev. Lett. **105**, 095003 (2010).

Development and characterization of very dense submillimetric gas jets for laser-plasma interaction

F. Sylla,[1,a)] M. Veltcheva,[1,2] S. Kahaly,[1,b)] A. Flacco,[1] and V. Malka[1]

[1]*Laboratoire d'Optique Appliquée, ENSTA-ParisTech, CNRS, Ecole Polytechnique, UMR 7639, 91761 Palaiseau, France*
[2]*Dipartimento di Fisica "G. Occhialini," Università degli Studi di Milano-Biccoca, piazza della Scienza 3, 20126 Milan, Italy*

We report on the characterization of recently developed submillimetric He gas jets with peak density higher than 10^{21} atoms/cm^3 from cylindrical and slightly conical nozzles of throat diameter of less than 400 μm. Helium gas at pressure $300-400$ bar has been developed for this purpose to compensate the nozzle throat diameter reduction that affects the output mass flow rate. The fast-switching electro-valve enables to operate the jet safely for multi-stage vacuum pump assembly. Such gaseous thin targets are particularly suitable for laser-plasma interaction studies in the unexplored near-critical regime. © *2012 American Institute of Physics*. [http://dx.doi.org/10.1063/1.3697859]

I. INTRODUCTION

The use of gas jet targets to generate a suitably dense, reliable, and reproducible interaction medium is particularly important in the broad field of laser-plasma interactions, where they are copiously employed for relativistic laser-plasma interaction for electron acceleration (LPA)[1–5] or ion acceleration,[6,7] parametric instabilities studies,[8–11] atomic physics,[12] investigations of inertial confinement fusion,[13] X-ray lasers,[14] and high harmonic generation.[15]

The control of the gas flow is essential in order to provide the desired interaction density. For example, the use of a sonic or a supersonic gas flow provides a gaussian-like or plateau neutral density profile. By changing the gas pressure, one can change the initial neutral density and by using a combination of gases, one can obtain plasmas with multiple ions species, which is needed to localize electrons injection for innovative laser-plasma accelerator schemes.[16,17] Also, changing the nozzle diameter changes the plasma length, which for LPA schemes allows to control the electron energy and for parametric instabilities studies allows a fine measurement of the corresponding growth rates.

Compared to the thin-foil-explosion techniques, the use of a gas jet presents some interesting advantages. In the previous case, the laser beam impinges on the target, which explodes symmetrically, with a density decreasing rapidly from the solid density to the sub-critical desired density, giving a parabolic longitudinal density profile, for which density and length are interdependent. In contrast, homogeneous plasmas with independent adjustable lengths and density can be produced with pre-ionized gas jets, with a much better reproducibility.[18,19] In addition gas jet targets

can be used with a high repetition rate lasers[2] at a reasonable cost and without any requirement for beam realignment and/or mechanical target movement between two consecutive shots.

Up till now, maximum gas densities were limited to about 10^{20} cm^{-3} over few millimeters. For a fully ionized helium gas, the corresponding electron density was therefore limited to twice this value. The critical electronic density n_c of a plasma irradiated by a Ti:Sapphire laser beam of central wavelength $\lambda = 810$ nm is 1.68×10^{21} cm^{-3}, and sets in the non-relativistic case the density limit above which the electromagnetic wave cannot propagate. The maximum electron density was therefore limited to about tens of percent of the critical density, indicating that the range of densities for Ti:Sapphire solid-state lasers that one could explore so far was only underdense. We present in this article a novel apparatus that allows to gain more than a factor of 10 in atomic density, allowing to reach an unexplored range of densities from tens of percent of the critical density to overcritical density and over hundreds of microns only. For this apparatus, we experimented successfully an alternative method of varying the density by probing it during the transient regime, rather than changing the backing pressure. This switches from a pressure to a time adjustment of greater accuracy and ease of implementation.

II. STATEMENT OF THE PROBLEM

Stationary gaseous supersonic jets produced by axisymmetric nozzles have been specifically studied[20] and extensively used[21] over the past decade for laser-plasma interaction experiments. They provide suitable support for plasmas of tunable electronic density n_e, length L, and gradient scale length l (typically $n_e \sim$ few 10^{19} cm^{-3}, $L \sim 1$ mm, and $l \sim 100$s of μm). The tuning is achieved by optimizing the nozzle geometry (throat and exit diameters) and by varying the back pressure feeding the nozzle. A stationary quasi one-dimensional isentropic compressible fluid flow

---

model (1DIFF)[22] gives reliable rule-of-thumbs for millimeter-range nozzles for quickly selecting the nozzle geometry in an ideal situation.

The reduction in size of the jet to the submillimetric range, coupled with the possibility of density variation over several order of magnitude, would give access to laser-Rayleigh-range-long plasmas (even for tightly focussed lasers) from low-density laser transparency to high-density laser opacity regimes. Such an implementation would have tremendous positive impact on systematic investigations of laser-plasma interactions (e.g., parametric instabilites, laser filamentation, relativistic self-focusing, and hole boring). It could also relax the constraints on laser power requirements for users of terawatt-class lasers in studying energetic ion beam generation from gas jets, so far only reported with petawatt-class laser facilities.[7] Importantly and very promising, this type of jet could be a suitable medium for compact and shape-preserving plasma self-compression of ultrashort laser pulse.[23]

However, the broadly used solenoid valve systems which trigger the gas burst then close within typically tens of milliseconds timescale at working pressure ∼100 bar "choke" when reducing the throat diameter to sub-millimeter. This property comes from the linear dependence of the mass flow rate in the 1DIFF model with that minimal cross-section in the duct (also called critical diameter). Increasing the pressure to compensate the flow stagnation prohibits subsequent opening of the magnetic-coil-driven poppet, locking increasingly the downstreaming flow. This hinders the exploration of plasma density from microjets in the interval $10^{19} - 10^{21}$ cm^{-3}.

In this paper, we report on the production and the characterization of He gas jet of few hundreds of microns thick with atomic peak densities up to 2.7×10^{21} atoms/cm^3, which corresponds to $1.6\ n_c$ for a singly ionized gas, and drivable at 10 Hz rep rate. This is achieved by using a pressure pneumatic device that allows to boost up the backing pressure up to 400 bar starting from usual gas cylinders (delivering 200 bar at maximum), and a special fast electro-valve with a rise and fall time within 3 ms. This unique association meets the requirements for very dense and thin gas jets compatible with a delicate vacuum pump system.

We smoothly covered experimentally from sonic (Mach number $M \sim 1$) to supersonic ($M > 1$) flow expansions by testing different nozzle geometries from cylindrical to conical ones. With our apparatus, neutral densities $\geq 0.5 n_c$ were only obtained, at exploitable distances from nozzle exit (from few hundreds of microns upwards), with cylindrical of slightly conical nozzles, referring to sonic and transonic flows. This article presents in details only the corresponding experimental results but a sound study of supersonic flows can be found in Ref. 20. Additionally, the real system was characterized with full multiple dimensions computational fluid dynamics simulations in the transient regime. Good agreements with the experimental data are obtained but the simulations underline the sensitivity of the thin flow profile to the precision in the nozzle production. These results will be reported in a future detailed publication elsewhere.

III. SIMPLE ANALYTICAL MODEL: INVISCID FLOW PARAMETERS

This section aims at illustrating qualitatively by using the 1DIFF model, how flow parameters relevant for laser-plasma experiments (density, radial gradient, and mass flow) are expected to vary in steady state according to the nozzle geometry (or equivalently in that model, to the Mach number of the flow, noted M). As mentioned in Ref. 20, one observes an intrinsic competition between the two requirements (i) high peak density during the quasistatic gas expansion in vacuum out of the nozzle and (ii) steep-gradient radial profile with plateau. The position between these two limit cases is essentially quantified by the sonicity, i.e., M. In the following of this document, we will be referring to sonic, transonic, and supersonic flows to describe flows with Mach number, respectively, equal to one ($M = 1$), close to one but larger than one ($M \simeq 1$ and $M > 1$), and equal to several units ($M > 1$). By means of the 1DIFF model, we now explain qualitatively the intrinsic competition between points (i) and (ii) when $M \geq 1$.

(i) The gas density at the nozzle exit is mainly determined by the exhaust gas velocity, i.e., by the conditions of expansion inside the nozzle and thus by the geometry of the nozzle. The 1DIFF model predicts for an ideal gas a simple system of equations linking the cross-sectional area A to the density ρ via the Mach number parameter

$$\frac{\rho}{\rho_0} = \left[\frac{\gamma + 1}{2 + (\gamma - 1)M^2} \right]^{\frac{1}{\gamma - 1}}, \tag{1}$$

$$\frac{A}{A_0} = \frac{1}{M} \left[\frac{2 + (\gamma - 1)M^2}{\gamma + 1} \right]^{\frac{\gamma + 1}{2(\gamma - 1)}}, \tag{2}$$

with A_0 and ρ_0 the cross-sectional area and the density at the throat, respectively, γ is the gas adiabatic constant ($\gamma \sim 1.6$ for helium). It is immediate from (1) that as M increases isentropically the density ρ drops. Considering a sonic flow ($M = 1$), with helium gas at $p = 300$ bar, then $\rho_0 \approx 4 n_c$ and $\rho \approx 2 n_c$. With the same pressure, for a supersonic flow as in our experiments ($M \simeq 4$), then $\rho \approx 0.2 n_c$.

(ii) Ideally, a related Prandtl-Meyer flow can model the expanding fluid that exits the nozzle. This supposes that the pressure in the discharge chamber is way lower than the pressure delivered by the nozzle (underexpanded nozzle), so that the flow adapts via expansion waves. The convex nozzle corners, as defined in Fig. 1 by the angle θ, rotate isentropically the outer layers giving birth to a centered expansion fan through which the fluid is rarefied. The angle of rotation θ_r reads

$$\theta_r = \nu(M_2) - \nu(M_1), \tag{3}$$

$$\nu(M_i) = \sqrt{\frac{\gamma + 1}{\gamma - 1}} \tan^{-1} \sqrt{\frac{\gamma - 1}{\gamma + 1}(M_i^2 - 1)} - \tan^{-1} \sqrt{M_i^2 - 1}, \tag{4}$$

where $\nu(M_i)$ is the Prandtl-Meyer function, M_1 and M_2 the Mach numbers, respectively, up- and downstream the corner (see Fig. 1 and also for coming implicit symbols). From
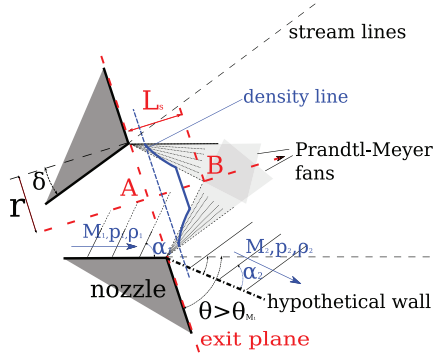
FIG. 1. Isentropic centered Prandtl-Meyer expansion outside a supersonic and underexpanded nozzle (p_{exit} > ambient pressure, p_a). Plateau density radial lines develop over the supersonic length L_s in the inviscid triangle, region between A and B with $M_A \approx M_B$ and delimited by weak density disturbances at Mach angle $\alpha_1 = \sin^{-1}(\frac{1}{M_1})$.

(3) and (4), it follows the existence of a maximum total turn angle θ_{M_1} for a given M_1 above which $M_2 \to \infty$ and p_2 and ρ_2 vanish,

$$\theta_{M_1} = \frac{\pi}{2}\left[\sqrt{\frac{\gamma+1}{\gamma-1}} - 1\right] - \nu(M_1). \quad (5)$$

With helium gas, for a sonic flow, $\nu(M_1) = 0$ and $\theta_{M_1} = 97.3°$. For a supersonic flow as in our experiments ($M_1 \simeq 4$), θ_{M_1} = 44.3°. For all types of flow we produced experimentally, the nozzle corner angle reads $\theta = 70°-90°$. This means that in that model, a sonic flow for which $\theta < \theta_{M_1}$ spreads along the nozzle exit plane, so that the jet will exhibit quite a large radial gradient outside the nozzle. On the contrary, when using a supersonic flow, the convex corner extends over an angle $\theta > \theta_{M_1}$ and the expansion can smoothly develop to ambient pressure (typ. $p_a < 10^{-2}$ mbar). Thus, for the supersonic flow cases, the angular extension of the Prandtl-Meyer fan can be used to assess the radial gradient scale length l at a certain distance Z from the nozzle exit,

$$\frac{l}{Z} \sim \left(\sin^{-1}\frac{1}{M_1} + \theta_{M_1}\right). \quad (6)$$

For $M_1 \simeq 4$, the radial gradients of the jet at $Z = 200$ μm from the exit reads $l \approx 200$ μm. From (6), l/Z reduces, i.e., the jet profile steepens as M_1 increases.

For a supersonic flow, to trade off (i) and (ii) (steep profile along with plateau density), the laser-gas interaction should be operated not too far from the nozzle exit, at a distance $Z \leq L_s$ (see Fig. 1 for the symbol definition),

$$\frac{L_s}{r} = \frac{1}{|\tan(\delta - \alpha_1)|} \quad (7)$$

with r the nozzle exit radius. When cone-sonicity matching is fulfilled, i.e., $\delta = \sin^{-1}(\frac{1}{M_1})$, the ideal supersonic length diverges. In practice, $\delta \neq \alpha_1$ and L_s/r is limited to few units.

For $M_1 = 4$, i.e, $\alpha_1 = 14°$ and our supersonic nozzles with $\delta = 20°$ and $r = 200$ μm, one obtains $L_s = 2$ mm.

The mass flow rate $\dot{m}$ for such a system in the 1DIFF model yields

$$\dot{m} = \sqrt{\frac{\gamma}{R}}\frac{p^*}{T^*}\left(\frac{2}{\gamma+1}\right)^{\frac{\gamma+1}{2(\gamma-1)}} A_0 \quad (8)$$

with p^* and T^*, the stagnation pressure and temperature, respectively, (cylinder inlet pressure and room temperature), and R the specific gas constant.

This parameter shows that, for a given nozzle geometry selected according to the Eqs. (1) and (2) to reach a certain sonicity, the mass flow rate and thus the achievable density at the exit is limited by the throat area A_0 (or any smaller area in the flow). Therefore, for designing a jet down-scaled to micrometric dimensions, a proportional increase of the backing pressure must be applied to compensate the rarefaction of the gas. This was done in practice by operating with a backing pressure from ~200 to 400 bar.

IV. EXPERIMENTS

A. Interferometry

The jet characterization was carried out by using a similar setup as the one presented in Ref. 20. In our case, the Mach-Zehnder interferometer stands outside the vacuum chamber and the jet is illuminated by a HeNe 633 nm-CW laser. An *f*/3-doublet images the central plane of the nozzle onto an 8 bit CCD camera. The spatial resolution is about 2 μm and the magnification around 12 (see Fig. 2). Though powerful, this setup has some important limitations which have to be taken into account when characterizing microjets:

- The error (intrinsic noise), assessed by extracting the phase from two consecutive reference images without firing the gas, corresponds to a level of about 10^{18} cm^{-3}. It is mainly due to parasitic vibrations of the interferometer components and therefore requires to shield out the thin beamsplitters from any airstream and to set the assembly on a stabilized optical table.
- The thickness of the microjet is tenfold thinner than usual jets. Therefore the output density has to be at least tenfold higher than in the millimetric case, in order to overshoot the noise level.
- Jets produced by usual millimetric nozzles are often characterized using high refractive index gases such as argon, krypton, ..., that give similar profiles as helium, massively used for laser-gas jet interaction, but having a smaller optical index. However, in the present case, when using any of these ersatz at such high pressures, the corruption of the characterization is expected due to the formation of molecular jets with large clusters, as the empirical Hagena parameter $\Gamma^* \geq 10^5$ is much greater than the admitted limit $\Gamma^* \sim 10^3$ for cluster formation.[24–26]

Since the main goal was to produce very dense jets, these points could have been circumvented by using a pneumatic
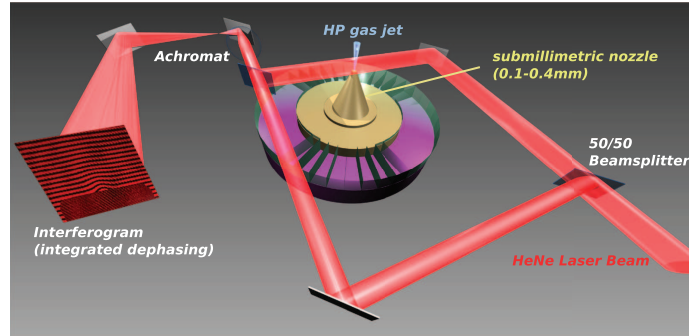
FIG. 2. Mach-Zehnder interferometer with typical interferogram (see Ref. 20) obtained when the high pressure (HP) gas jet is fired.

pressure booster ($\times 75$) delivering up to 400 bar of backing pressure.

The phase shift due to the gas is deduced from the interferogram fringe shift with a continuous wavelet transform technique (CWT).[27] A typical raw phase map and the corresponding density calculations at three heights above the nozzle are presented in Figure 3. For the following, we define

FIG. 3. Data extraction from interferograms obtained with a 400 μm-cylindrical nozzle pressurized at $p = 300$ bar. (a) Phase shift distribution (colormap in radian) from CWT. (b) Neutral He profiles n_a normalized to the atomic critical density n_{ca} at 100 (red line), 200 (blue line), and 300 μm above a 400 μm sonic nozzle from Abel-inversion. The dotted lines indicate the best exponential fits.

$n_{ca} = 1.68 \times 10^{21}$ atoms/cm^3 (referred to as atomic critical density). The good axial symmetry of the flow makes the density estimation using the Abel-inversion technique very reliable (estimations with a generalized Abel-inversion assuming non-axisymmetric profiles[28] give the same results).

B. Innovative apparatus

The He pressure in the upstream reservoir could be in theory varied within the range $p = 50 - 450$ bar. In practice, the pressure was fixed between 300 and 400 bar. This corresponds to mass flow rates of an order of magnitude higher than rates with usual jets used in laser-plasma interaction experiments. However, in this range, the electro-valve we used can fully open and close according to the manufacturer within 3 ms. This fast-switching is made possible by the implementation of the *bid* technology, a recent invention consisting in a bid rotating in an asymmetric induced magnetic field to gate the gas flow out (see Figure 4). This has the advantage to significantly reduce the inertia of the switch and increase the pressure limit by a factor of 10, as compared to translational plastic poppet driven by a spring in usual electro-valve. The conjunction of the fast-switching electro-valve and the high mass flow rate makes the assembly capable of delivering overdense gas jet (see Figure 3), while being usable in the vacuum interaction chamber without endangering the vacuum pump assembly. The stability of the overall system gave a very good shot-to-shot reproducibility in density over the tested pressure range (fluctuations of less than few percent rms).

The method we adopted to vary the density differs from the one usually employed in laser-plasma interaction. Here, the gas pressure feeding the valve is kept constant at $p = 300$ bar because of the long transient regime of the pressure booster, and delays Δt between the gas and the probing laser are varied. Equivalently, Δt can be fixed and the opening time of the valve varied (but this would also result in gas throughput change and hence caution should be practised regarding vacuum pumps). Thus, the interest of this method rests on the fact that the jet profile is determined by
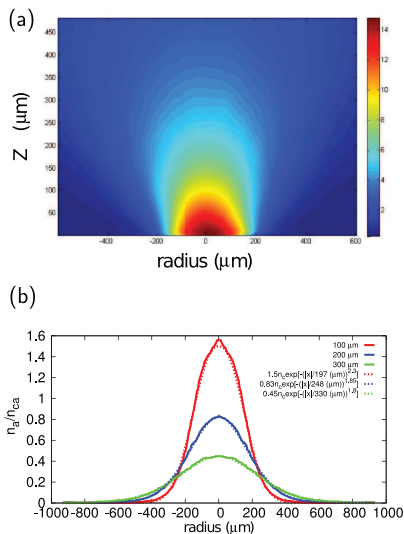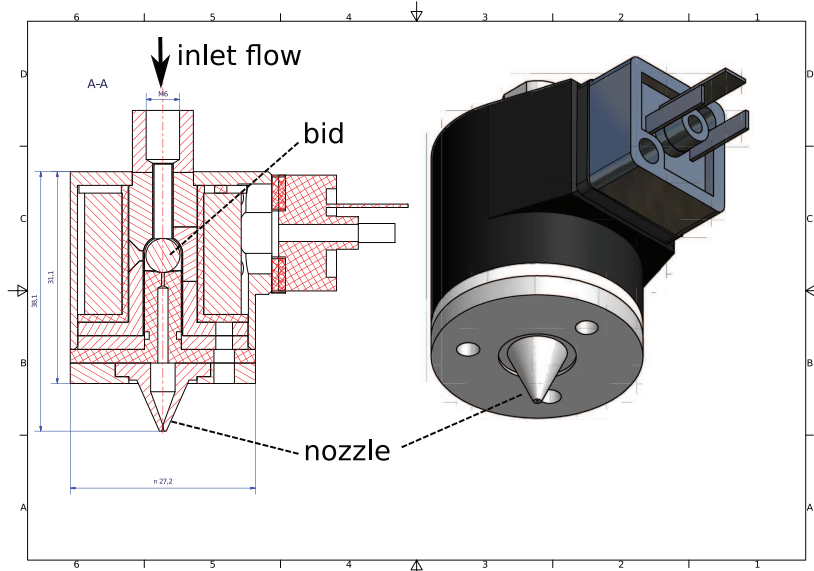
FIG. 4. (Left) Cross-section of the assembly electro-valve + nozzle. The rotating stainless steel bid in the center of the assembly replaces the translational plastic poppet in standard valves. (Right) General outlook of the assembly.

a time, which can be set experimentally much more conveniently than a pressure, and at the precision of the jitter of a simple time-delay pulse generator (with a nanosecond precision).

C. Results

As expected from the 1DIFF model, the spatial profile of the jet depends upon the exit Mach number via the nozzle geometry (ratio of the exit to the critical diameter). This was experimentally verified as shown in Figure 5, where neutral densities normalized to the peak density at 200 μm for each nozzle type are plotted to underline the gradients in radial and vertical directions.

From Eq. (8), the output mass flow rate will be lower in the supersonic case ($A_0 = (100 \ \mu\text{m})^2$) than in transonic and sonic ones ($A_0 = (300)^2$ and $(400 \ \mu\text{m})^2$, respectively), and so will be the density, for a given stagnation pressure p^*. In our conditions, only the sonic and transonic flows supply neutral densities over 10^{20} cm^{-3}. For the sonic flow the peak density reaches 10^{21} cm^{-3} at 200 μm from the nozzle exit and the flow spreads over 500 μm FWHM. Theses specs make it particularly interesting for an efficient coupling with an ultrashort Ti:Sapphire laser pulse. We describe specifically that high-density flow in the following.

1. Time dependence

The time-resolved density at height $Z = 200 \ \mu$m is depicted in Figure 6, where the peak densities are plotted against the delay between firing of the valve and the instant of the measurement (instant at which the laser is fired when the interaction is carried out). A typical asymmetric bell shape trendline is obtained and near-critical atomic peak densities are measured at about 20 ms after the valve opening. Despite
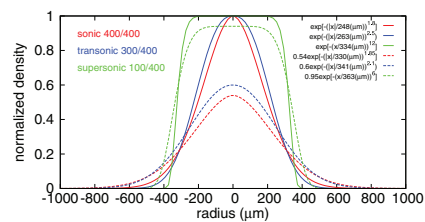
FIG. 5. Sonic (red), transonic (blue), and supersonic (green) flows (best fits) for three nozzles of throat diameters 400, 300, and 100 μm respectively (same exit diameters of 400 μm). The curves are normalized to the peak density at 200 μm. The solid and dashed lines correspond to profiles at 200 and 300 μm from the exit, respectively. Both vertical and radial gradients become larger as the sonicity (Mach number) decreases.
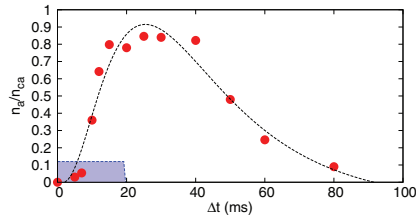
FIG. 6. Time-resolved neutral peak density n_a at 200 μm from the exit of a sonic nozzle (400 μm diameter). The blue region indicates the opening time of the valve. The interpolated dashed line is an indication to guide the reading.

the fast-switching of the valve within 3 ms, the transient state lasts for about 15 ms. This delay is probably due to some kinetic issue in the bid motion that restricts the mass flow rate and causes the "displacement" of the duct smallest area from the nozzle critical diameter down to the valve output orifice, the diameter of which evolving consequently too slowly with time during the opening phase. Optimization of this aspect by changing for instance the bid size and/or the valve housing dimensions will be subject to future developments.

2. Space dependence

It is interesting to compare the jet shape at different Δt. Figure 7 presents the jet profiles at $Z = 200$ μm at different delays in the top panel, and the corresponding gradient (ratio of the peak density to the gradient scale length), and gradient scale length in the bottom panel. It appears that the gradient scale length is almost constant over the investigated timespan (red full dots) even if the peak density and thus the gradient vary greatly. Thus, for a sonic nozzle, it is possible to vary the gradient without changing the gradient scale length. This is
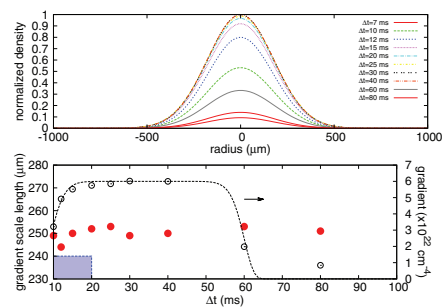

FIG. 7. Profile evolution for different Δt using the same nozzle as in Figure 6. (Top) radial profiles normalized to the peak density at 25 ms. (Bottom) gradient calculated as the peak density over the gradient scale length (black empty dots), and gradient scale lengths from gaussian fits of the profiles (red dots). The blue region indicates the opening time of the valve. The interpolated dashed line is an indication to guide the reading.

of utmost importance for carrying out controllable parametric studies on, for instance, laser self-focusing, filamentation instability or electron injection in a density ramp.[29,30]

V. CONCLUSION

Very dense compact gas jets have been developed for accessing experimentally the critical density limit for Ti:Sapphire laser-plasma interactions at $n_c = 1.68 \times 10^{21}$ cm^{-3}. These new tools enable to safely work in a standard interaction turbo-pumped environment by implementing bid-based electro-valve. The tunability of the jet characteristics (peak density and gradient scale length) from time-delay adjustments opens up opportunities to carry out systematic and exploratory studies of the interaction.

[1]A. Modena, A. Dangor, Z. Najmudin, C. Clayton, K. Marsh, C. Joshi, V. Malka, C. Darrow, D. Neely, and F. Walsh, Nature **377**, 606 (1995).
[2]V. Malka, S. Fritzler, E. Lefebvre, M.-M. Aléonard, F. Burgy, J.-P. Chambaret, J.-F. Chemin, K. Krushelnick, G. Malka, S. P. D. Mangles *et al.*, Science **298**, 1596 (2002).
[3]S. P. D. Mangles, C. D. Murphy, Z. Najmudin, A. G. R. Thomas, J. L. Collier, A. E. Dangor, E. J. Divall, P. S. Foster, J. G. Gallacher, C. J. Hooker *et al.*, Nature **431**, 535 (2004).
[4]C. G. R. Geddes, C. Tóth, J. van Tilborg, E. Esarey, C. B. Schroeder, D. Bruhwiler, C. Nieter, J. Cary, and W. P. Leemans, Nature **431**, 538 (2004).
[5]J. Faure, Y. Glinec, A. Pukhov, S. Kiselev, S. Gordienko, E. Lefebvre, J.-P. Rousseau, F. Burgy, and V. Malka, Nature **431**, 541 (2004).
[6]K. Krushelnick, E. L. Clark, Z. Najmudin, M. Salvati, M. I.K. Santala, M. Tatarakis, A. E. Dangor, V. Malka, D. Neely, R. Allott *et al.*, Phys. Rev. Lett. **83**, 737 (1999).
[7]L. Willingale, S. P. D. Mangles, P. M. Nilson, R. J. Clarke, A. E. Dangor, M. C. Kaluza, S. Karsch, K. L. Lancaster, W. B. Mori, Z. Najmudin *et al.*, Phys. Rev. Lett. **96**, 245002 (2006).
[8]F. Amiranoff, S. D. Baton, S. Huller, V. Malka, A. Modena, P. Mounaix, N. R. Galloudec, C. Rousseaux, and M. Salvati, Phys. Rev. E **61**, 1949 (2000).
[9]V. Malka, J. Faure, S. Hüller, V. T. Tikhonchuk, S. Weber, and F. Amiranoff, Phys. Rev. Lett. **90**, 075002 (2003).
[10]V. Malka, C. Coulaud, J. P. Geindre, V. Lopez, Z. Najmudin, D. Neely, and F. Amiranoff, Rev. Sci. Instrum. **71**, 6 (2000).
[11]S. D. Baton, F. Amiranoff, V. Malka, A. Modena, M. Salvati, C. Coulaud, C. Rousseaux, N. Renard, P. Mounaix, and C. Stenz, Phys. Rev. E **57**, R4895 (1998).
[12]C. Chenais-Popovics, V. Malka, J.-C. Gauthier, S. Gary, O. Peyrusse, M. R.-L. Gloahec, I. Matsushima, C. Bauche-Arnoult, A. Bachelier, and J. Bauche, Phys. Rev. E: Stat. Nonlin. Soft Matter Phys. **65**, 046418 (2002).
[13]J. Denavit and D. W. Phillion, Phys. Plasmas **1**, 1971 (1994).
[14]H. Fiedorowicz, A. Bartnik, Z. Patron, and P. Parys, Appl. Phys. Lett. **62**, 2778 (1993).
[15]E. Fill, S. Borgström, J. Larsson, T. Starczewski, C. Wahlström, and S. Svanberg, Phys. Rev. E **51**, 6016 (1995).

Observation of Ions Accelerated in the Wake of a Short Laser Pulse

F. Sylla,[1] S. Kahaly,[1] A. Flacco,[1] M. Veltcheva,[1,2] A. Lifschitz,[1] G. Sanchez-Arriaga,[3] E. Lefebvre,[3] and V. Malka[1]

[1]Laboratoire d'Optique Appliquée, ENSTA, CNRS,
Ecole Polytechnique, UMR 7639, 91761 Palaiseau, France
[2]Dipartimento di Fisica "G. Occhialini", Università degli Studi di Milano-Biccoca, piazza della Scienza 3, 20126 Milan, Italy
[3]CEA, DAM, DIF, 91297 Arpajon, France

We report on ion acceleration mechanisms that occur during the interaction of an intense and ultrashort laser pulse ($I\lambda^2 > 10^{18}$ Wcm$^{-2}\mu$m^2) with an underdense helium plasma produced from an ionized gas jet target at $\sim 10^{19}$ cm^{-3}. In this unexplored regime, where the laser pulse duration τ is smaller than the inverse of the ion plasma frequency ω_{pi}, non-thermal ion bunches have been measured in the radial direction. The two He ion charge states that are detected present pronounced modulations in their energy distributions with 200 keV cutoff energies. Fully electromagnetic PIC simulations explain the experimental behaviors and indicate the role of the various ion acceleration mechanisms, such as acceleration from filament structure, from the laser wakefield and from radial plasma sheath that are involved depending on the timescale and on the initial ion radial position.

Important studies [1–5] over the past decade have demonstrated the potential of ultraintense ($I\lambda^2 > 10^{18}$ Wcm$^{-2}\mu$m^2) lasers as compact ion accelerators from laser-plasma relativistic interaction. The interest in such a field stems not only from potential applications (fast ignition [6], ion therapy [7]) thanks to characteristics of the accelerated bunches (low-emittance [8], quasimonoenergetic spectra [9]), but also from possible fundamental investigations of the interaction and plasma properties through electron and ion spectral analyses [10–13].

Reported acceleration experiments using underdense plasmas ($n_e < n_c$, resp. electron and critical plasma densities) with relativistic pulse were all done with laser pulse durations ten times larger or more than in the present paper, i.e. in a regime where the pulse duration was larger than the inverse ion plasma frequency [1, 14]. In this regime, the fastest ions gain their radial momenta from Coulomb explosion, when the laser field is still present and bores a channel by expelling plasma electrons. They continue to drift undisturbed due to their inertia when the quasineutrality is restored as the electrons come back to their rest positions after the pulse is gone. Depending on the plasma density and laser power, ion maxwellian distribution (with $n_e \sim 10^{19}$ cm^{-3}[1]) and plateau-like spectra (with $n_e > 10^{20}$ cm^{-3} and power larger than 250 TW [14]) were obtained.

When the pulse duration becomes shorter than the inverse ion plasma frequency, the ions gain their radial momenta essentially after the pulse, since a laser wakefield of particular spatio-temporal profile [15] acts within the ion response timescale to form an annular radial ion density profile (see Eq. (8) in [16]). A recent theoretical study in this regime shows that, at higher densities and laser intensities, the electrostatic effects of trapped electrons in the laser wake compress axially ions that lately Coulomb explode [17]. Later on, when fast inner ions outrun slow outer ions a collisionless shock can form in the phase space with significant modification of the final energy distribution (see also reference 15 in Ref. 17).

In this Letter, radial acceleration from underdense He plasma ($n_e \sim 10^{19}$ cm^{-3}) in the sub-ion-response-timescale regime $\omega_{pi}\tau \ll 1$ is demonstrated for the first time. Observations with single-shot diagnostics of spectral patterns close to quasimonoenergetic helium ion bunches (cutoff $E_0 \sim 200$ keV) are presented and discussed. Owing to the ultrashort laser pulse and to the relativistic laser intensities used for interaction, direct laser-induced Coulomb explosion of a uniform positively-charged core from laser channeling is likely to be an incomplete picture for depicting the momentum transfer on the ion response timescale.

An ultrashort (duration $\tau = 35$ fs) linearly-polarized pulse from the LOA Ti:Sapphire Salle Jaune laser [18] carrying $E_L = 800$ mJ was focused with a $f/10$ off-axis parabolic mirror to a 20-μm ($1/e^2$) focal spot giving a laser intensity $I_0 = 1.3 \times 10^{19}$ Wcm^{-2}. The supersonic He jet density was varied from 0.8 to 4.8×10^{19}cm^{-3} and had a 700 μm diameter. The ratio between the laser power P_L and the critical power P_c for relativistic self-focusing ($P_c = 16.2$ n_c/n_e GW) was comprised between 2.4 to 40 (plasma and Rayleigh lengths values were comparable).

The interaction was spatially adjusted above the nozzle by mean of plasma emission imaging (10 μm spatial resolution). The Topview and Sideview imagings allow positionning the beam respectively along a diameter of the jet and at a chosen height from the nozzle (see figure 1). Measurements of ion emission were carried out at 85° from laser propagation axis through a 100 μm-diameter pinhole (solid acceptance is 1.2×10^{-8} sr) with a Thomson parabola spectrometer coupled to 40-mm imaging microchannel plate chevron assembly (two MCPs + Phosphor screen). This very narrow angle of collection filters out efficiently ions accelerated at different directions from the laser axis normal. A linearized TE-cooled 16-bit CCD camera (1024×1024 px) enables single-shot recordings of scintillating traces and thus shot-to-shot statistical analyses of ion spectra. The electric gains of the MCP assembly were set to preserve the full dynamics
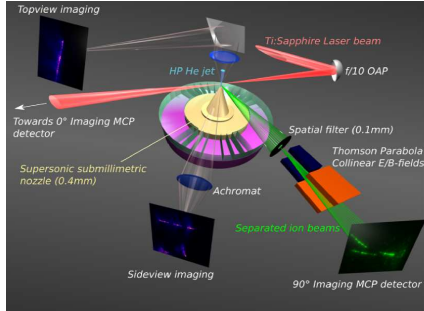
FIG. 1: Experimental setup with characteristic plasma emission images (Topview and Sideview with stretched pulse of 300-fs) and ion emission spectral recordings (with compressed pulse of 30-fs).

of 16-bit pictures from saturation and keep the signal-to-noise ratio better than 50:1. With a 2:1 magnification, the system gives a 500-μm pinhole-image of the jet on the first MCP plane (10 pixels on the CCD image), which allows to regard the source as point-like and the ion emission as laminar.

A raw picture from a single laser shot is presented in figure 2 and shows striking gaps in spectral traces and presence of both species He^+ and He^{2+}. However, the ratio $I_0/I_{sb}(He^{2+}) > 100$, ensures full ionization of gas in the focal volume (with $I_{sb}(He^{2+})$ the threshold intensity for suppression of the potential barrier). Calculations with $I_0/I_{sb}(He^{2+}) = 100$, using sequential field ionization of neutral gas by a gaussian laser pulse, show fully-ionized plasma over a radius of $\sim 200~\mu$m. Within the energy range $[20-200]$ keV, elastic collisions of He^{2+} projectiles with He atoms are largely dominated by a one-electron capture process with a typical capture cross section $\sigma_c \sim 10^{-16}$cm^2 [19]. Thus, He^+ ions are very likely to stem from single electron capture of radially streaming He^{2+} in outer layers of the jet (hence the importance of the gas profile in detecting both species). Moreover, the He^+ spectrum presents an upper branch above point a and a lower branch below point b ($\Delta E_{ab} \sim 27$ keV, see figure 2). In this gap region the signal falls below the noise level (see inset in figure 2). An energy gap is also observed between the least energetic detected alpha ~ 60 keV and the lower limit of detection in He^{2+} spectrum ~ 48 keV. Both upper branches (above gaps) lie precisely within the range $[60-200]$ keV, supporting the electron capture hypothesis. The corresponding spectra with multi-humps of relative energy spread $\Delta E/E < 20\%$ and energy cutoff at 200 keV have been obtained in density range from 1 to 3×10^{19} cm^{-3}. Changing the laser polarization direction does not affect the spectra and no ion was detected in the forward direction (see figure 1).
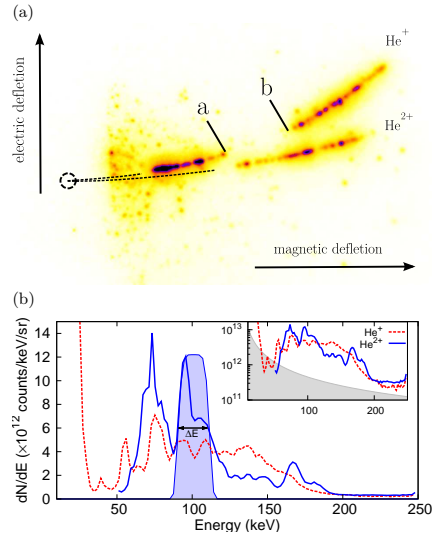

FIG. 2: (a) Raw picture from single shot at 85° for $n_e = 2.8 \times 10^{19}$cm^{-3} with $I = 1.3 \times 10^{19}$ Wcm^{-2}. The neutral blob (dashed circle) is filtered out and the dotted lines indicate the fit dispersion traces for each species. The dispersive magnetic field reads B=0.25 T. The points a and b are located at 55 and 28 keV in He$^+$ spectrum. (b) Extracted spectra (relative counting, bin width $dE = 2$ keV) show multi-peak structures with $\Delta E = 20.6$ keV. Inset (logscale): cutoff ~ 200 keV, signal-to-noise ratio 50 : 1 (shaded below dark noise level).

To get an insight about the mechanism of ion acceleration, we carried out a numerical study of the interaction process via Particle-in-Cell simulations, performed using the fully electromagnetic PIC code Calder-Circ [20]. In this code, Maxwell equations are solved by projecting over a basis of Fourier modes. Few modes are enough to accurately describe the laser evolution and the wakefield, resulting in simulations needing much less computational resources than fully 3D simulations. Simulations performed here include 2 Fourier modes.

Parameters of the simulations correspond to those used in the experiments: a laser wavelength $\lambda_0 = 0.8~\mu$m, and a laser pulse duration of 30 fs full width half maximum (FWHM). The laser spot waist is 20 μm, the laser intensity is $I = 1.2 \times 10^{19}$ W/cm^2 (normalized vector potential $a_0 = 2.4$). The cell size in the longitudinal direction is $\Delta x = 0.628~k_0^{-1}$ and in the radial direction $\Delta r = 1.5~k_0^{-1}$. The plasma is fully ionized (composed by He^{2+} and electrons), with an hypergaussian density longitudinal profile given by $n_e = 0.015~n_c~\exp(-(r(\mu m)/363)^6)$. The simulation box is
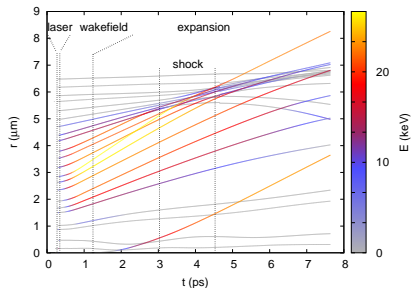
FIG. 3: Ion trajectories for ions initially at $x = 300$ μm. The colors along their trajectories correspond to their energies according to the color table.
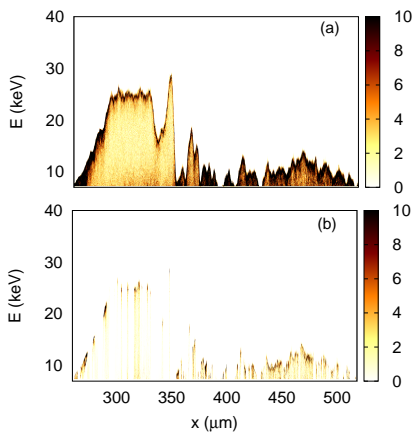

FIG. 4: Ion density distribution in phase space (x, E) at 2 ps, collecting all ions (a) and for ions emitted at 90° from the laser propagation axis (b).

composed by 11000(longitudinal) $\times$ 600(radial) cells.

The laser pulse becomes relativistically self-focused as it propagates through the plasma, reaching a maximum normalized amplitude of $a_0 \sim 5$ at $x \sim 300$ μm. The pulse excites a strongly non-linear wakefield, able to self-inject and to accelerate electrons to few hundreds MeV. The wakefield lasts up to the arisement of wave-breaking, that roughly corresponds to $t = 1.1$ ps on the rear side of the jet and to $t = 2.5$ ps on the foward side.

The radial ion dynamics under the decaying wakefield and for later times is visible in figure 3, showing the radial trajectories of selected ions at the plane $x = 300$ μm. Colorscale indicates the ion energy. Three stages can be distinguished in the radial acceleration process. The first

one corresponds to the passage of the laser pulse. As can be seen in figure 3, the ponderomotive force associated with the 30 fs laser pulse has little effect over the energy of the ions.

The second phase of the process corresponds to the wakefield lifespan, up to $t \sim 1.2$ ps in this region of the jet ($x = 300$ μm). The radial electric field of the decaying wakefield oscillates at a frequency close to ω_p. For a linear wakefield, the time averaged radial field at a given position vanishes. In this case, the acceleration relies on ponderomotive effects [16]. For a non-linear wakefield, on the other hand, the mean radial field takes a finite value, and the acceleration is mainly not ponderomotive. Close to the axis ($r < 0.5$ μm) the time averaged radial field is negative. The presence of electron bunches self-injected in the wakefield enhances the radially inward field close to the axis [17], although the average field is negative even if there are not trapped electrons. For $r > 0.5$ μm the average field is positive, reaching its maximum for $r \sim 5$ μm. For radii larger than $r \sim 7$ μm the radial electric field is negligibly. During the wakefield decay, ions with $r < 0.5$ μm are pushed towards the axis, whereas ions between $r = 0.5$ μm and 7 μm are pushed radially outwards. The result is the formation of a channel with low ion density with a central filament. Most of the energy gained by the ions comes from the decaying wakefield. At this time, the ion energy spectrum is similar to that produced by a Coulomb explosion, peaking at the cutoff energy. The cutoff energy depends strongly on the longitudinal position, with a maximum close to 30 keV in the region where the laser pulse reaches its maximum amplitude.

After wavebreaking, the electron screening of the ionic positive space charge becomes efficient, and therefore the channel and the filament will radially expand roughly ballistically. As the most energetic ions, initially around $r = 5$ μm, overcome less energetic ions from outer shells of the channel, the edge of the channel becomes sharp. Electrons are then no longer able to efficiently screen the sharp edge peaking in the ion spatial density distribution, and thus a large radial electric field arise over the channel outer shell [21]. This electrostatic shock results in the acceleration of ions of the outer shell and the deceleration of more inner ions. For longer times (several tens of μs), ions will eventually reach the electrostatic radial sheath created at the boundary between the plasma and the neutral gas, where they will gain extra energy. The continuation of the simulation up to these times would require very large computational resources. Moreover, the energy gain in the sheath is strongly dependent on the radial profile of the plasma, and thus a realistic simulation requires reliable information on this profile.

Comparison of the experimental spectra of He$^+$ and He^{2+} allows us to make a rough estimation of the energy gained in the sheath. He$^+$ ions, not present in the channel because of the large laser amplitude, are accel-

erated in the sheath. As can be clearly seen in the raw image from the Thomson parabola (2.a), the He^+ spectrum presents two branches. The high energy branch is in the same energy range than He^{2+} ions, and arguably corresponds to He^{2+} ions capturing an electron after the wave-breaking. Thus, the low energy branch should correspond to He^+ accelerated in the plasma sheath. The energy cut-off of this branch, i.e. the maximum energy gained in the sheath, is $E \sim 40$ keV. An He^{2+} ion accelerated in the channel could then gain up to 80 keV in the sheath and get a final energy of about 120 keV, close to the experimental values. The estimation of the energy gained in the sheath constitutes actually a superior bound because the potential drop within the sheath will decay with time.

In order to explain now the multi-humps observed in the ion spectra, we investigate the effect of the angular angle collection. Ion spectra are inspected before the shock, because the radial resolution needed to accurately resolve it should be much higher that the used here ($\Delta r \sim 0.2\,\mu$m). Small-scale simulations that we performed with sufficient radial resolution showed that the main features of the ion spectra remain after the shock. Ion density in the phase space (x, E) before the shock (at 2 ps) is shown in figure 4. As can be seen, for a given value of x the spectrum peaks at the high energy cutoff, like a Coulomb explosion spectrum. The cutoff strongly varies as the laser propagates along x, and the peaks are not clearly resolved when integrating over x (similar conclusions as in Ref. [22]). In the experiment, only ions inside a small emission cone are actually detected. The phase space corresponding to ions emitted at a $(90 \pm 0.1)°$ is shown in figure 4.b. The density vanishes for most of x-values. When the density is integrated over x, the individual peaks corresponding the different emission regions become visible. The obtained spectrum (figure 5) presents several peaks corresponding to different regions of emission along the gas jet. The strongly modulated spectra experimentally observed would therefore come from the finite acceptance of the ion detector, that would allow to resolve the spectrum of ions coming from given regions of the gas jet.

In conclusion, novel aspects of laser ion acceleration have been revealed in a regime where τ is smaller than the inverse of the ion plasma frequency ω_{pi}. It has been shown from the experimental data that ions are accelerated radially in this regime. On the basis of PIC simulations, the ion are accelerated by radial electric fields that arise in laser wakefield from the filament and from the plasma channel, and that additional acceleration could be due to the sheath at the plasma-gas boundary. The multiple humps that are present in the ion spectra have been for the first time identified thanks to the high resolution angle collection.
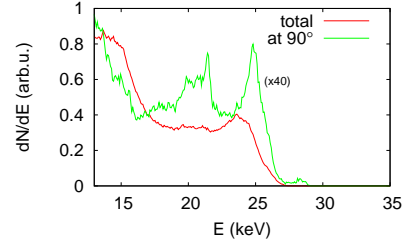
FIG. 5: Energy spectrum of ions emitted at $90°$ in the case of high (green curve) and low angle (blue curve) resolution.

[1] K. Krushelnick et al., Phys. Rev. Lett. **83**, 737 (1999).
[2] E. L. Clark et al., Phys. Rev. Lett. **85**, 1654 (2000).
[3] P. McKenna et al., Phys. Rev. E **70**, 036405 (2004).
[4] J. Fuchs et al., Phys. Rev. Lett. **99**, 015002 (2007).
[5] A. Henig et al., Phys. Rev. Lett. **103**, 245003 (2009).
[6] M. Roth et al., Phys. Rev. Lett. **86**, 436 (2001).
[7] S. V. Bulanov and V. S. Khoroshkov, Plasma Physics Reports **28**, 453 (2002).
[8] T. E. Cowan et al., Phys. Rev. Lett. **92**, 204801 (2004).
[9] S. Ter-Avetisyan et al., Phys. Rev. Lett. **96**, 145006 (2006).
[10] L. M. Wickens et al., Phys. Rev. Lett. **41**, 243 (1978).
[11] S. Ter-Avetisyan et al., Phys. Rev. Lett. **93**, 155006 (2004).
[12] M. Allen et al., Physics of Plasmas **10**, 3283 (2003).
[13] P. Mora and T. Grismayer, Phys. Rev. Lett. **102**, 145001 (2009).
[14] M. S. Wei et al., Phys. Rev. Lett. **93**, 155003 (2004).
[15] N. E. Andreev et al., Physics of Plasmas **4**, 1145 (1997).
[16] L. M. Gorbunov et al., Phys. Rev. Lett. **86**, 3332 (2001).
[17] K. I. Popov et al., Phys. Rev. Lett. **105**, 195002 (2010).
[18] A. Flacco et al., Nuclear Instruments and Methods in Physics Research Section A: Accelerators, Spectrometers, Detectors and Associated Equipment **620**, 18 (2010).
[19] M. B. Shah and H. B. Gilbody, Journal of Physics B: Atomic and Molecular Physics **18**, 899 (1985).
[20] A. F. Lifschitz et al., Journal of Computational Physics **228**, 1803 (2009).
[21] A. Macchi et al., Plasma Physics and Controlled Fusion **51**, 024005 (2009).
[22] G. S. Sarkisov et al., Phys. Rev. E **59**, 7042 (1999).

Ultrafast Near-Critical Plasma Dynamics and Magnetic Dipole Excitation After Collapse of Short Intense Pulse

F. Sylla, A. Flacco, S. Kahaly, M. Veltcheva, A. Lifschitz, and V. Malka
Laboratoire d'Optique Appliquée, ENSTA, CNRS,
Ecole Polytechnique, UMR 7639, 91761 Palaiseau, France

E. d'Humières and V. Tikhonchuk
University Bordeaux - CNRS - CEA, Centre Lasers Intenses et Applications, UMR 5107, 33405 Talence, France
(Dated: June 16, 2012)

It is observed that interaction of an intense ultra-short laser pulse with an overdense gas jet results in the pulse collapse and the deposition of a significant part of energy in a small and well localized volume in the rising part of the gas jet, where the electrons are efficiently accelerated and heated. The subsequent plasma expansion at a sub-relativistic velocity ($\sim c/3$) has been optically monitored in time and space, and attributed to the quasistatic field ionization of the gas associated to the hot electron current. A first experimental evidence of a magnetic azimuthal structure around the collapse region is also presented. Numerical simulations suggest the acceleration of hot electrons along with the excitation of a sizeable magnetic dipole in the collapse region.

An efficient coupling between an intense laser pulse and a plasma takes place near the critical density, n_c, where the laser frequency equals to the local plasma frequency. This interaction regime has been theoretically investigated for two decades [1–7], and a great variety of nonlinear phenomena has been unraveled: an efficient pulse absorption [1], electron and ion acceleration [2], magnetic self-channeling [3], plasma instabilities and nonlinear coherent structures [4–6].

Recent experimental data have shown the interest of such an interaction regime for forward ion acceleration using a CO_2 laser [8, 9]. In particular, the generation of quasi-monoenergetic proton beams have been ascribed in these studies to the formation of an accelerating collisionless shock [9]. However, with visible or near-infrared (IR) lasers, very few experimental studies have been reported so far in this regime, owing essentially to the technical difficulties of creation of controllable and reproducible plasmas with near critical densities at these laser wavelengths. The known methods in this case consist in either exploding a thin solid foil in vacuum [10, 11] or in using foam targets [12, 13]. The exploding foil technique requires energetic laser pulses, that are difficult to control, and hydrodynamic simulations to predict the plasma density profile. A foam is a micro-structured material that is difficult to prepare, handle and simulate. Both methods suffer from a low repetition rate and shot-to-shot irreproducibility due to the fluctuations of laser and target parameters.

Here, we report on novel observations of ultrafast plasma dynamics using a compact 10 Hz near-IR laser and a reproducible high density helium gas jet target [14]. With that latter device, one can create a plasma with the electron density up to $(3-5) \times 10^{21}$ cm^{-3} within a spatial size of less than 1 mm. The pump-probe diagnostics with a high spatial and temporal resolution reveal a laser energy deposition in a small plasma volume and subse-

quent hot and dense electron cloud expansion forming an ultrafast ionizing shock front. The expansion velocity at the early moments is about one-third of the light velocity, $c/3$, which was never measured before in gas jets. Our observations differ from the experiment with a foil-gas-foil package [17] where the laser energy was deposited in the foil with no given experimental detail on that process, and the subsequent ionizing shock in a gas caused by hot electrons had a velocity lower by an order of magnitude. In fact, the expansion velocity is in our case comparable to the plasma expansion rates measured in solid dielectric targets a decade ago [15, 16]. In difference to the solid targets, the ionizing shock front in our experiment is formed on a collisionless timescale of less than 1 ps, so that our observations cover smoothly for this ultrafast front the transition from a collisionless to a collisional regime.

The experiment was carried out at the Laboratoire d'Optique Appliquée, using an ultrashort Ti:Sapphire laser "Salle Jaune" with the pulse duration ~ 35 fs and the energy on target 810 mJ. The laser was focused on a submillimetric supersonic helium jet to the focal spot of 20 μm full width at half maximum (FWHM). The normalized laser vector potential was $a_0 = 2.7$. The experimental setup shown in Fig. 1 enables a simultaneous detection of ion acceleration (along and transverse to the laser axis), the electron plasma density and the azimuthal magnetic field with respect to the laser propagation axis. The plasma optical probing is achieved with a spatial resolution of the order of 1 μm and with a temporal resolution equal to the duration of the frequency-doubled probe beam (~ 40 fs). The gas jet density distribution shown in Fig. 2 was measured with a Mach-Zehnder interferometer. The peak density in the jet exponentially decreases along the vertical direction with the characteristic scale length of $\sim 170 \,\mu$m, as the nozzle produces an expanding flow with a Mach number 1.5. The radial
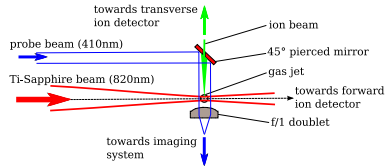
FIG. 1. Scheme of the experimental setup with pump (red) and probe (blue) beam traces. See the details in Ref. 18.

density profile at the distance of 200 μm from the nozzle exit is fit by: $n_e = 0.95 \ n_c \exp[-(r/r_0)^{2.5}]$, where $r_0 = 263 \, \mu$m is the jet radius, see Fig. 2(b). Though the
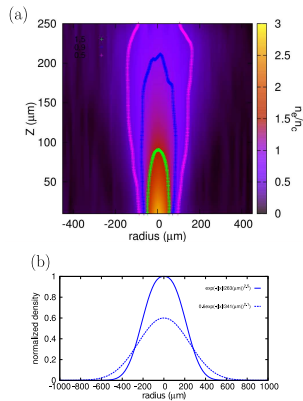

FIG. 2. (a) Electron density n_e map above the nozzle assuming double ionization of He gas (twice the atomic density interferometrically measured). Color contours are corresponding to $n_e = 0.5$ (pink), 0.9 (blue) and 1.5 (green) n_c. (b) Density profiles at $z = 200$ (solid) and 300 μm (dashed) from the nozzle exit (normalized to the peak level at $z = 200 \ \mu$m equal to $n_{e0} = 0.95 \ n_c$).

peak density in the jet is above the critical level close to the nozzle, the laser pulse may propagate through due to the effect of relativistic transparency [19].

The temporal evolution of the plasma is presented in Fig. 3 with a series of interferograms (showing plasma gradients and encoding the electron density) recorded at different pump-probe delays for the same plasma conditions. The laser propagates along the y-axis and it is linearly polarized along x-axis. All panels in Fig. 3 are in the y-z plane. On the left side of Fig. 3(a), 200 fs after the onset of the interaction, the plasma channel radius is much smaller than the laser beam width due

to self-focusing. The laser beam penetration terminates with a collapse [20, 21] well before the beam reaches the critical density. The on-axis bright spots, from plasma self-emission integrated with the CCD camera, are likely to indicate the longitudinal position where the laser pulse collapses. At this location, the laser breaks up into several filaments as can be seen later in panel (b), at 1.2 ps delay. Here, a striking circular plasma structure with sharp edges has grown asymmetrically about the laser, with its center located near the middle of the jet. This structure appears opaque to the probe beam, probably due to the strong refraction and absorption of that beam. Formation of such a structure results from the ionization of the dense gas by the expanding cloud of hot electrons [15–17], efficiently heated in the small volume where the pulse has collapsed. Multiple thin bright filaments can be seen on the left side of the opaque structure. These filaments are longer in the upper part of the picture (lower density) than in the lower part (higher density close to the nozzle exit) because of the light refraction on the vertical density gradient previously described (see Fig. 2(b)).

In panel (c), at 3.3 ps delay, the walls of the channel (on the left side of the figure) have started to expand and thicken. The lower edge of the structure have reached the limit of the field of view close to the nozzle exit. The asymmetric expansion either side of the laser axis (red line) can be particularly appreciated in that picture. The structure appears now elliptical and elongated along the laser propagation direction, with a forward burgeoning bubble developing ahead of the structure in the falling part of the jet, and separated from the main structure by a vertical bright edge. This secondary structure might be analogous to the dense plasma blocks ("light bullets") observed in the collisional regime near the critical density and moving along a decreasing density gradient [22]. We did not investigate further that unclear point which will be clarified in a future study.

Until the collapse point in the ramp of the jet, the laser pulse propagates straight in the plasma, although the gas jet presents a strong gradient in the vertical direction that would deflect a low intensity light upwards. This suppression of the beam deflection is explained by the ponderomotive force of the intense pulse that expels radially most of the plasma electrons. Nevertheless, the beam propagation may be affected by small-scale perturbations created by the hosing and filamentation instabilities [21, 23, 24], but diagnostics were unsufficiently resolved to evidence such fluctuations. Refraction can be observed for the thin bright and long filaments oriented towards the top of the picture, panels (b) and (c) in Fig. 3. These are scattered parts of the laser light with a moderate intensity that escaped the collapse region and are propagating deeper in plasma where no plasma channel is supposed to form.

The effect of laser beam self-focusing and formation of a channel before the collapse is confirmed by the de-

3

FIG. 3. Electron density interferograms for the peak density $n_e \approx 0.95 n_c$ at the probe delays at: (a) $t_0 + 0.2$ ps, (b) $t_0 + 1.2$ ps and (c) $t_0 + 3.3$ ps, where t_0 corresponds to our reference time (onset of the interaction). The blue dotted line in (a) maps out the eletron density profile at the laser axis height (blue scale in unit of n_c). The yellow scale is in microns. The small red arrows indicate the position of the laser pulse assuming the laser group velocity equal to c. From $\sim t_0 + 0.4$ ps, the spherical structure is opaque to the probe beam.

tection of energetic ions in the direction transverse to the laser beam axis, as numerical simulations show that transverse acceleration takes place in the channel formed prior to the collapse. For each shot, we consistently measured He$^+$ ions with energies up to 250 keV. Although the laser intensity is thousand times higher than the threshold for full helium ionization, no He^{2+} ions have been recorded. We attribute that fact to the electron capture process where the accelerated He^{2+} ions stream out radially through the neutral helium gas. The charge exchange cross section $\sigma_{cex} \gtrsim 10^{-16}$ cm^2 [25] is sufficiently high, so the capture free mean path for $n_e \sim 0.1$ n_c is of the order of 1 μm, which is much smaller than the jet radius. No forward ion acceleration has been detected. The acceleration geometry in our experiments differs from that reported in Ref. 13, where ions from a foam target where recorded along the laser axis.

The laser beam collapse is followed by the fast radial expansion of the opaque structure within the first picosecond of interaction. In order to measure precisely the expansion rate, we chose an axial coordinate where filaments do not significantly perturb the structure outer edges: a vertical yellow line at $x = 465$ μm from the left boundary in Fig. 4(a). The time dependence of the opaque zone size along the yellow line is presented in panel (b). Each cutoff (see inset) maps out the transverse plasma density gradients, so the peak intensity reveals a sharp density edge. Each column in the map represents an average profile obtained from at least two shots in the same conditions.

The structure expands asymmetrically, as can be observed from the inset in panel (a) and the contours in panel (b), the expansion being faster towards the nozzle (negative coordinates and increasing densities). The opaque structure is clearly visible from about $t_0 + 400$ fs and we measured, over a timespan of 1 ps, average radial velocities in both downward and upward directions $c/2$ and $c/3$, respectively (see oblique red lines in panel (b)). These radial expansion velocities of electron fronts are higher by an order of magnitude than other reported measurements at lower plasma densities [26]. The measurements in the upper part panel (b) are affected by a
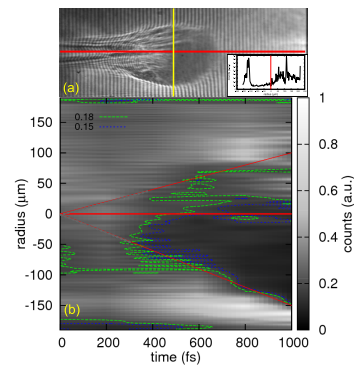
FIG. 4. Asymmetric ultrafast radial expansion: (a) interferogram at $t_0 + 1$ ps. Inset: cutoff along the yellow line. (b) Cutoffs along the yellow line in panel (a) versus time. Each cutoff is averaged over at least two shots. The cutoff intensity is normalized to the unity at the last time moment. Horizontal solid red line shows the laser axis. Isolines at the levels 0.15 (dashed blue) and 0.18 (dashed green) show the opaque structure formation. Oblique solid red lines indicate the expansion velocity $c/3$ upstream and $c/2$ downstream (red dotted lines to guide the reader).

noise due to the presence of several filaments, but the front stays trackable. The similar analysis leads to an expansion velocity of $c/2$ in the laser propagation direction. However, this fast cloud expansion slows down after the first picosecond and the further plasma evolution proceeds much slower.

The laser beam collapse in the gas and fast ionization were simulated with the particle-in-cell code PICLS [27]. This is fully electromagnetic 2D×3V kinetic code that accounts for the electron-electron and electron-ion collisions and the atom field ionization. The laser and plasma parameters correspond closely to the experimental ones. A laser pulse of the dimensionless amplitude $a_0 = 2.2$, of wavelength 0.8 μm, of duration 29 fs FWHM

and of transversal size 24 μm FWHM was injected horizontally in a helium gas, with a linear density profile with a scale length of 200 μm along the vertical direction, and a parabolic density profile with the same scale length along the laser propagation axis. The maximum electron density at the top of the plasma profile was $0.91\,n_c$ assuming the complete ionization. Analysis of the simulation results shows that the laser pulse undergoes strong self-focusing that ends up with a beam collapse in the plasma ramp at density $n_e \sim 0.2\,n_c$, close to the experimental value $\sim 0.27\,n_c$. As mentioned before, the numerical simulations show ion acceleration in the transverse direction from the channel before the collapse zone. The ion energies are in the range of a few hundred keV in good agreement with the observations. In the collapse region, a significant part of the laser pulse energy of a few tenths of joule is released in a volume with the characteristic size of less than 20 μm. Correspondingly, the electrons acquire in there energies up to a few MeV and stream away from the collapse zone with relativistic velocities. An extremely high electric current associated with these electrons leads to strong magnetic fields forming a dipole structure similar to the one described in Ref. 7. The magnetic field intensity is of the order of 10 MG, and the magnetic field energy in the collapse zone is comparable to the hot electron kinetic energy.

The hot electron cloud creates a strong electrostatic field at its edge that ionizes as it expands the ambient gas and creates a return current of plasma electrons. Consequently, the hot electron expansion creates a plasma far away from the laser axis of propagation. This process of plasma ionization by a beam of energetic electrons has been theoretically described in Refs. 28 and 29 in an 1D geometry. The velocity of the corresponding ionization front $\sim 0.7\,c$ observed in simulations is slower than the fast electron velocity as an accumulation of the electron density is necessary to generate a sufficiently strong electric field, comparable to the atomic field. This front velocity is higher than that of the experiments ($\sim 0.5\,c$), since our 2D simulation model overestimates the ionization front velocity because of slower electron cloud divergence as in the real 3D experiment. Fast electron propagation and plasma ionization obtained in the numerical simulation 900 fs after the laser pulse collapse are shown in Fig. 5. The collapse point is located at $x = 210\,\lambda_0$ and $y = 60\,\lambda_0$. This point is the origin of the electron cloud propagating radially. Panel a) shows three groups of electrons with the energies below 100 keV (red), between 0.1-1 MeV (green) and above 1 MeV (green). The width of the electron cloud is about 80 μm, which is much wider than the laser pulse in vacuum. This width depends on the magnetic dipole lifetime created in the collapse zone and sustaining the electron heating. The outer boundary of the electron cloud outlines the plasma edge, meaning that the electron cloud is responsible of the ionization of the gas. This can be seen in panels b) and c) showing

the electron plasma density and the electric field averaged over the laser period. The electric field amplitude at the cloud edge $\sim 0.1\,m_e c \omega_0/e$ is of the order of the atomic field $eE_{at}/m_e \omega_0 c \simeq 0.13$. That is sufficient for double ionization of helium within a characteristic time of a few femtoseconds. Also, as this time is comparable to the electron plasma period, the ionization is accompanied with large amplitude plasma oscillations seen in the electric field distribution in panels c) and d).

Similarly to the experimental data the plasma shape is anisotropic in the longitudinal and transverse directions. Longitudinally, there are almost no energetic electron behind the collapse point ($x < 210\,\lambda_0$) as the plasma density is too low to supply the return current. Transversally, the maximum of the electron density in panel b) is shifted down from the laser propagation axis in the direction of the density gradient, although the effect is weaker in simulations than in experiments because of a smoother vertical gradient. The shift would create the impression that the fast electrons are also deviating along the density gradient, as more refraction and absorption would be noticed. However, this is not seen in the fast electron distribution in panel a). As time goes on, the fast electrons that are propagating through the gas and ionizing it, lose their energy in the self-consistent electric field. The stopping power is a of few tens of keV/μm, therefore, in one picosecond time scale the fast electrons are reducing their energy to a few keV thus transforming a free streaming into a collisional diffusion.

The characteristics of the plasma cloud after the end of free streaming phase can be estimated by considering the electron density of the order of n_c and the size of the ionized zone of $\sim 200\,\mu$m. Assuming the deposited energy of about a few tenths of joule, the total number of ionized atoms would be $\sim 10^{15}$ with the average energy of $200-300$ eV per atom that is used for ionization and electron heating. Such a plasma blob may live for a relatively long time of a few nanosecond as the recombination is relatively slow as well as the expansion velocity, which is then of the order of 100 μm/ns.

In conclusion, our experiment demonstrates intense laser pulse channeling in a low density gas or plasma, terminated with a violent collapse as soon as the gas density exceeds a few tens of percent of the electron critical density. A very efficient absorption of the laser pulse energy in the collapse zone leads to acceleration of hot electrons accompanied with the creation of a long-lasting magnetic dipole structure that further accelerate electrons. The current of fast electrons originating from the collapse point sustains an ionization front propagating in the gas. The front is collisionless during the first picosecond, propagates with the velocity comparable but less than the light velocity, and unveils a plasma that appear transversally anisotropic due to the gas vertical gradient. Our results shed new light on fundamental aspects of the interaction in near-critical regime, paving the way for in-
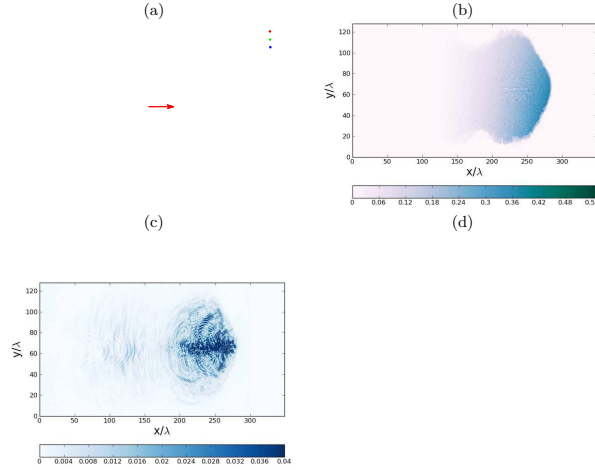
5

FIG. 5. Distribution of energetic electrons at $t = t_0 + 0.9$ ps (a), the plasma density n_e/n_c (b) and the modulus of electric field averaged over the laser period $e|E|/m_e\omega_0 c$ (c) near the zone of the beam collapse. The lengths are measured in the laser wavelengths, the plasma density in the collapse point is $0.2\,n_c$, the laser field dimensionless amplitude $a_0 = 1.0$. Other parameters are given in the text. The collapse point is marked by an arrow. Panel d) shows the cut of panel c) along the laser propagation axis $y = 60\,\mu$m.

stance towards controllable giant magnetic dipole [2] of great interest for efficient ion acceleration.

[1] S. C. Wilks *et al.*, Phys. Rev. Lett. **69**, 1383 (1992).
[2] T. Nakamura *et al.*, Phys. Rev. Lett. **105**, 135002 (2010).
[3] A. Pukhov and J. Meyer-ter-Vehn, Phys. Rev. Lett. **76**, 3975 (1996).
[4] S. V. Bulanov *et al.*, Phys. Rev. Lett. **76**, 3562 (1996).
[5] S. V. Bulanov *et al.*, Phys. Rev. Lett. **82**, 3440 (1999).
[6] T. Esirkepov *et al.*, Phys. Rev. Lett. **89**, 275002 (2002).
[7] T. Nakamura and K. Mima, Phys. Rev. Lett. **100**, 205006 (2008).
[8] C. A. J. Palmer *et al.*, Phys. Rev. Lett. **106**, 014801 (2011)
[9] D. Haberberger *et al.*, Nat. Phys. **8**, 95-99 (2011)
[10] M. Borghesi *et al.*, Phys. Rev. Lett. **78**, 879 (1997).
[11] A. Yogo *et al.*, Phys. Rev. E **77**, 016401 (2008).
[12] L. Willingale *et al.*, Phys. Rev. Lett. **102**, 125002 (2009).
[13] S. Okihara *et al.*, Phys. Rev. E **69**, 026401 (2004).
[14] F. Sylla *et al.*, Rev. Sci. Instrum. 83, 033507 (2012)
[15] M. Borghesi *et al.*, Phys. Rev. Lett. **83**, 4309 (1999).
[16] L. Gremillet *et al.*, Phys. Rev. Lett. **83**, 5015 (1999).
[17] D. Batani *et al.*, Phys. Rev. Lett. **94**, 055004 (2005).
[18] F. Sylla *et al.*, Phys. Rev. Lett. 108, 115003 (2012).
[19] E. Lefebvre and G. Bonnaud, Phys. Rev. Lett. **74**, 2002 (1995).
[20] W. B. Mori *et al.*, Phys. Rev. Lett. **60**, 1298 (1988).
[21] G. Li *et al.*, Phys. Rev. Lett. **100**, 125002 (2008).
[22] N. I. Vogel *et al.*, Phys. Rev. Lett. **86**, 232 (2001).
[23] N. M. Naumova *et al.*, Phys. Plasmas **8**, 4149 (2001).
[24] Z. Najmudin *et al.*, Phys. Plasmas **10**, 438 (2003).
[25] cross section of the charge exchange
[26] P. M. Nilson *et al.*, Phys. Rev. Lett. **103**, 255001 (2009).
[27] Y. Sentoku and A. Kemp, J. Comput. Phys. **227**, 6846 (2008).
[28] S. I. Krasheninnikov *et al.*, Phys. Plasmas **12**, 073105 (2005).
[29] A. Debayle and V. T. Tikhonchuk, Phys. Plasmas **14**, 073104 (2008).

Dependence on pulse duration and foil thickness in high-contrast-laser proton acceleration

A. Flacco,[1] F. Sylla,[1] M. Veltcheva,[1,2] M. Carrié,[3] R. Nuter,[3] E. Lefebvre,[3] D. Batani,[2] and V. Malka[1]

[1]*Laboratoire d'Optique Appliquée, ENSTA–ParisTech, École Polytechnique-ParisTech, CNRS UMR 7639, Chemin de la Huniére, 91761 Palaiseau Cedex, France*
[2]*Dipartimento di Fisica "G. Occhialini," Università degli Studi di Milano-Bicocca, Piazza della Scienza 3, 20126 Milano, Italy*
[3]*CEA, DAM, DIF, 91297 Arpajon, France*
(Received 23 March 2009; revised manuscript received 9 December 2009; published 11 March 2010)

Experimental measurements of proton acceleration with high intensity and high-contrast short laser pulses have been carried out over an order of magnitude range in target thickness and laser pulse duration. The dependence of the maximum proton energy with these parameters is qualitatively supported by two-dimensional particle-in-cell simulations. They evidence that two regimes of proton acceleration can take place, depending on the ratio between the density gradient and the hot electron Debye length at the rear target surface. As this ratio can be affected by the target thickness, a complex interplay between pulse duration and target thickness is observed. Measurements and simulations support unexpected variations in the laser absorption and hot electron temperature with the pulse duration and laser intensity, for which density profile modification at the target front surface is the controlling parameter.

Energetic proton and ion beams, resulting from the interaction of laser pulses at relativistic intensities ($I > 10^{18}$ W/cm^2) with thin foil targets, have been reported in many studies [1–3]. Laser-accelerated proton beams show a half divergence of $\approx 10°$, decreasing for higher energies, and a good laminarity [4,5].

During the interaction, the laser energy is primarily transferred to electrons in the target, accelerated to relativistic energies. The extraction and acceleration of ions is a consequence of the charge separation that is set between this hot electron component and the cold ions at the plasma/vacuum interface. This mechanism (TNSA [6,7], Target Normal Sheath Acceleration) has been extensively studied and is the source of the most energetic protons produced in the process [8,9]. The study of the accelerated protons also gives an insight on the interaction of relativistic intensity laser pulses with solid targets.

In experiments, the laser prepulse or Amplified Spontaneous Emission (ASE) pedestal affects the target surface and therefore the absorption of laser energy, the distribution of hot electrons and, in some cases, the conditions at the target rear surface. The pedestal interacts with the target on a nanosecond time scale before the ultrahigh intensity peak; its energy ionizes the illuminated surface and a density gradient is produced. This preplasma is known to affect the various mechanisms involved in the energy deposition process [10–12]; in previous studies it has been shown that a plasma density gradient can be beneficial to laser energy absorption [13,14]. On the other hand, a shock wave launched by the prepulse into the target can trigger the early expansion of the nonilluminated surface, where the TNSA process takes place: the evolution of a density gradient on the back surface has been proven to be detrimental to the acceleration process, decreasing the maximum proton energy [15–17]. Higher proton energies are usually reached with thinner targets, for hot electrons are less dispersed while drifting to the accelerating surface, thus resulting in a higher charge density. Nevertheless, thinner targets are also more easily destroyed by shock effects associated to the interaction with the pedestal. The

two competing phenomena are responsible for the existence of an optimal target thickness [18,19] for given laser parameters.

The dependence of the acceleration process on the laser pulse duration has been addressed in several works, both through fluid [20,21] and analytical [22] models, kinetic simulations [23], and experimental results [24,25]. For instance, it has been suggested [18,26,27] that the time over which the protons are accelerated is related to the laser pulse duration, since during this time the hot electron temperature T_{hot} is kept constant by the sustaining action of the laser field. If $L_{target}/c < \tau_L$, L_{target} being the target thickness and τ_L the laser pulse duration, it has been also suggested [24] that the hot electron density is enhanced by multiple round trips through the target during the laser action.

The measurement of the correlation between the laser pulse duration and proton acceleration is made difficult by the presence of the laser pedestal. The last developments in laser technology enable the production of contrast ratios as high as $I_0/I_{ASE} > 10^9$: this allows the use of thinner targets, thus increasing the maximum proton energy. High-contrast laser sources provide the user with cleaner and more controllable interaction conditions. The use of high-contrast laser pulses in ion acceleration experiments showed unprecedented results [19,28], deepening the insight on the acceleration mechanisms and underlining the importance of a precise control of the interaction parameters.

In this paper, we investigate the effect of the laser pulse duration on the proton acceleration process for different target thicknesses, using a high-contrast laser beam. In previous studies, the dependence of laser absorption and electron temperature with pulse duration and intensity were derived from past measurements under poor contrast conditions. The present work, associating experimental measurements and detailed simulation analysis, clearly demonstrates that new scalings must be accounted for under conditions of high laser contrast.

The experiments have been performed on the *Salle Jaune* multiterawatt laser facility at the *Laboratoire d'Optique Ap-*
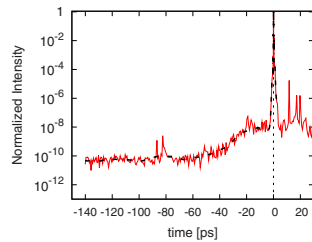
FIG. 1. (Color online) Cross-correlation (3ω) plot of the compressed laser beam from the *Salle Jaune* laser system, where a two crystal XPW is used to enhance the temporal contrast. The dashed plot represents the filtered curve with replicas removed.
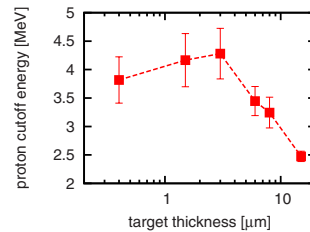

FIG. 2. (Color online) Proton cut-off energy for different target thicknesses with the fully compressed beam ($\tau_L = 30$ fs). The optimum is observed between 1.5 and 3 μm. (Dashed lines are added to help visualization.)

pliquée. The laser pulse has a central wavelength of $\lambda = 800$ nm and a duration, at the maximum compression, of $\tau_L = 30$ fs. The temporal contrast of the pulse is improved by a two-crystal Crossed Polarized Wave generation system [29] (XPW), which is inserted between the front-end of the Chirped Pulse Amplification (CPA) chain and the first amplification stage. The contrast of the output pulse, measured by 3ω autocorrelator before injection in the amplification chain, is as high as $I_0/I_{ASE} = 10^{10}$; a small pedestal is observed starting from $t = -50$ ps before the pulse and rising to $I_0/10^8$ (Fig. 1). During the experiment shots, the contrast of the fully amplified beam is kept under control by a fast photomultiplier tube and a 7 GHz oscilloscope. No pedestal was ever observed above the measurable limits of 10^{-9} in dynamic and $t = -400$ ps in time. The phase front is corrected after compression by a deformable mirror and the beam focused down to a waist of 2.3 μm by an $f/3$ off-axis parabola. A total of 250 mJ (about 70% of the total on-target energy) is contained in the $1/e^2$ focal spot (measured) which results in a peak intensity, at maximum compression, of $I_0 = 4 \times 10^{19}$ W/cm^2. The p-polarized beam impinges at 45° on thin aluminum targets. The different ion species accelerated from the target are collected and separated by a Thomson Parabola, and their spectra obtained from a Micro-Channel Plate (MCP) detector, imaged by a 16bit CCD camera. A 200 μm lead pinhole, 40 cm far from the interaction point, is used to collimate the analyzed beam. The diagnostic system has been validated with CR39 detectors. The use of a real-time proton diagnostic allows a statistical treatment of the data: each experimental point below is the averaged value of at least four different shots; error bars corresponds to the standard deviation of the set.

The proton cutoff energy is shown in Fig. 2 for different target thicknesses and a constant laser pulse duration of $\tau_L = 30$ fs. The proton signal is stable and reproducible for targets as thin as 0.4 μm; the highest energy is obtained for 3 μm thick targets.

The detailed behavior for different laser pulse durations is studied on thin, $D_{thin} = 1.5$ μm, and thick, $D_{Thick} = 15$ μm, targets. The pulse duration is varied between $\tau_{min} = 30$ fs and $\tau_{max} = 700$ fs by changing the separation between the gratings in the compressor. The measurements are repeated for

both positive and negative chirp; the obtained pulse duration is calculated by numerical interpolation of the experimental calibration curve of the compressor. Figure 3 shows the proton cutoff energies obtained for the two targets. For D_{thin}, the proton cut-off energy decreases monotonically as the peak intensity is lowered by stretching the pulse. The behavior for D_{Thick} is qualitatively different. At the maximum compression the observed proton energy is lower than what is observed for D_{thin}. As the pulse is stretched, a slight increase in proton energy results in the occurrence of a weak maximum, indicating that a pulse in the range $150 \div 250$ fs is more efficient than shorter ones. For $\tau_L > 150$ fs, the proton beam from D_{Thick} is more energetic than the one from D_{thin}.

A preliminar set of simulations is performed with the hydrodynamic code ESTHER [30] on Aluminum targets of the two thicknesses, in order to verify the effect of the small residual pedestal (see Fig. 1) on the target conditions. The simulations show the formation of a small preplasma, which reaches a density scalelength of $L \sim 90$ nm on the illuminated surface, at the arrival of the main intensity peak. However in no case is any ionization or early expansion of the back surface observed, which confirms that no correlation between the target thickness and the interaction conditions is added by the presence of the residual pedestal.

In order to explain the experimental results, we have performed a set of simulations with the two-dimensional (2D) particle-in-cell (PIC) code CALDER [31]. A $\lambda = 800$ nm laser
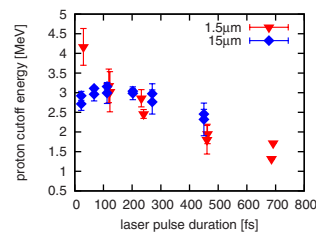

FIG. 3. (Color online) Proton cut-off energy for different laser pulse durations (at constant energy) on Aluminum targets of 1.5 and 15 μm.
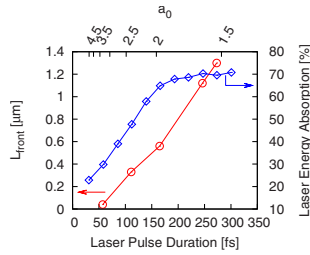
FIG. 4. (Color online) Simulated (2D PIC) values for the density gradient length on the illuminated surface *(circles)* and for the fraction of absorbed energy *(diamonds)* obtained with different pulse durations on the D_{Thick} target. The gradient length is measured by fitting the density profile with an exponential when the intensity peak arrives on the surface.

FIG. 5. (Color online) Hot electron temperature (simulation) for the 3 and 0.9 μm targets and different pulse durations. The ponderomotive temperature [32] is added for comparison (dashed line).

pulse, with spatial and temporal Gaussian profiles, is focused to a 5 μm spot. The total energy of the pulse is E_L =250 mJ in the $1/e^2$ spot and it impinges under p polarization at 45° on an homogeneous slab of fully ionized Hydrogen, at the density of $n_e = 50 n_c$ and at the initial temperature of 1 eV. The preplasma calculated with the hydro code is so small that we chose to ignore it in the PIC simulation setup. The intensity peak enters the simulation box at $t = 1.83\tau_L$, τ_L being the full width at half maximum duration of the laser pulse. In this way, the interaction of the rising front of the pulse is fully taken in account. The laser pulse duration is varied from 30 fs to 300 fs. The simulations have been run for the two thicknesses of 3 and 0.9 μm.

The PIC simulations show that the pulse duration plays a major role in laser absorption at the illuminated surface, as it impacts on both the hot electron temperature T_{hot} and the total absorbed energy. Figure 4 shows (blue diamonds) that the ratio of absorbed energy rises from ~20% to ~60% and then saturates to values of the order of ~70%. The leading edge of the longer pulses starts earlier to heat the surface, which results in the expansion of a preplasma; the gradient length that is present when the intensity peak interacts with the surface (red circles on the same figure) increases as the pulse is stretched. This behavior is qualitatively the same for D_{thin} and D_{Thick}.

For the shortest pulse ($\tau_L = 30$ fs, $a_0 = eA/mc = 4.6$), a hot electron temperature $T_{\mathrm{hot}} = 0.24$ MeV is observed (Fig. 5); the electron temperature increases as the pulse gets longer, illustrating that the lower laser field amplitude is compensated by an improved coupling with the plasma. The maximum temperature is reached for pulse durations between 100 and 150 fs. After the maximum is reached, the temperature decreases, as the normalized field amplitude approaches to $a_0 = 1$ (relativistic limit). Figure 5 shows that the heating process is similar for the two target thicknesses, and does not exhibit any effect of electron recirculation on electron temperature for the thinner target.

The dependence of the acceleration conditions on target thickness is made evident by the hot electron density on the rear (accelerating) surface. As laser intensity during the lead-
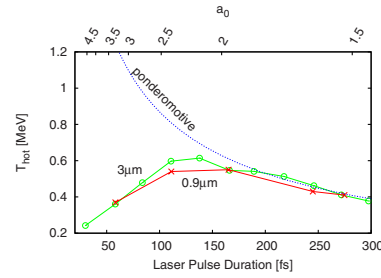
ing edge of the pulse increases over ~10^{17} W/cm^2, important electron heating starts. Fast electrons generated on the front surface travel to the back side and start driving the expansion, resulting in the formation of a density gradient. Simulations show that the gradient length L_{back} of the plasma on the rear surface (see circles in Fig. 6) is similar in the two cases, consistent with the similar temperatures measured in Fig. 5. By looking at the hot electron density (crosses on the same plot) it is evident that the thinner target reaches a higher density of hot electrons than the thicker one. This is in agreement with the picture of hot electrons experiencing less dilution in thinner targets than in thicker ones [33].

According to [15], two separate regimes of proton acceleration are recognized during the expansion of the plasma. In the first regime, for $\lambda_D > L_{\mathrm{back}}$, the TNSA accelerating field scales as $\propto \sqrt{n_{\mathrm{hot}} T_{\mathrm{hot}}}$, λ_D being the hot electron Debye length and n_{hot} the hot electron density on the rear surface. From Figs. 5 and 6, for $t < 100$ fs ($a_0 > 2.2$), an increase in pulse duration increases both the hot electron number and temperature, which corresponds, in the $\sqrt{n_{\mathrm{hot}} T_{\mathrm{hot}}}$ regime, to an increase in the proton energy. As the maximum T_{hot} is reached, the proton energy is expected to decrease: in fact the electron temperature falls down, whereas the energy absorption (Fig. 4) saturates. When the inequality changes, $\lambda_D \ll L_{\mathrm{back}}$ the ac-
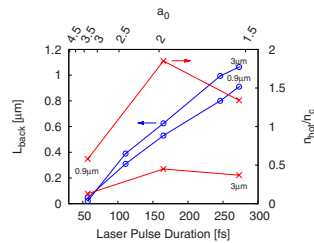

FIG. 6. (Color online) Density scale length on the back (nonilluminated) surface *(circles)*. Hot electron density at the back surface *(crosses)*. Values are measured when the intensity peak arrives on the front surface.
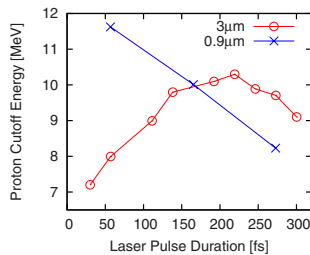
FIG. 7. (Color online) Comparison between the maximum simulated proton energy for thin (0.9 μm) and thick (3 μm) targets.

celerating field scales as $\propto T_{hot}/L_{back}$. This change in dependence adds a correlation between the conditions of acceleration and the thickness of the target. In fact (Fig. 6), while the evolution of L_{back} with the pulse duration is comparable for the two thicknesses, the hot electron density is larger for thinner target and the hot electron Debye length of the thicker target is therefore larger. Starting from a $\lambda_D > L_{back}$ regime at short pulse durations, the thinner target will more rapidly evolve to a gradient-dominated expansion. Indeed, the simulations show that for D_{Thick} the second regime is reached at $\tau_L \sim 200$ fs, and that the same should happen for D_{thin} at $\tau_L < 30$ fs. Once the $\lambda_D \ll L_{back}$ regime is reached, the proton energy is governed by the density gradient on the rear surface, which worsens the acceleration condition as τ_L keeps increasing. Figure 7 shows the simulated proton energy, which clarify the overall effect. On D_{Thick} the energy increase is slowed down for τ_L between 130 and 220 fs, and starts decreasing for longer durations. For the thinner target, the accelerating field is instead completely governed by the expansion of the rear surface, in the $\lambda_D \ll L_{back}$ regime. The behavior observed in the simulations qualitatively reproduces the experimental data presented in Fig. 3. In particular, the simulations show that for a laser pulse duration τ_L

> 150 fs, the protons accelerated from the thicker target are more energetic than those from the thinner one, in agreement with the experiment (Fig. 3). To understand why a quantitative agreement is not observed, it is important to underline that the simulation target (material, thickness, density) is notably different from what was used in the experiments. This is particularly important when considering that the transition between the two regimes is regulated by the local electron density on the rear surface, thus depending on the electron transport through the target.

In conclusion we reported the behavior of a laser proton accelerator for different pulse durations in conjunction with two different target thicknesses. For constant laser energy, the proton cutoff depends on the balance between the increased efficiency of the laser-plasma coupling and the maximum obtainable electron temperature. The ratio between the rear density gradient and the Debye length sets the proton acceleration regime, with an accelerating field scaling either as T_{hot}/L_{back} for $\lambda_D \ll L_{back}$ or as $\sqrt{n_{hot}T_{hot}}$ for $\lambda_D > L_{back}$. We believe that our experimental measurements shed light on a correlation among the interaction parameters (duration of the pulse and thickness of the target) that was not completely clarified before. Our observations are also supported by PIC simulations, evidencing unexpected variations in absorption and temperature with intensity. It is important to underline that these effects can be observed only on laser systems where the lack of pedestal provides sufficiently clean interaction conditions with dense targets. Under these conditions, absorption and temperature are found to be decreasing functions of intensity, at constant laser energy. This experimental work suggests that for an optimal acceleration of ions, the experimental parameters should fall within the $\sqrt{n_e T_e}$ regime, where a pre-existent preplasma could be used to enhance the energy absorption on a thicker target and increase the proton cut-off energy [14,34].

[1] E. L. Clark *et al.*, Phys. Rev. Lett. **84**, 670 (2000).
[2] R. A. Snavely *et al.*, Phys. Rev. Lett. **85**, 2945 (2000).
[3] S. P. Hatchett *et al.*, Phys. Plasmas **7**, 2076 (2000).
[4] M. Borghesi, A. J. Mackinnon, D. H. Campbell, D. G. Hicks, S. Kar, P. K. Patel, D. Price, L. Romagnani, A. Schiavi, and O. Willi, Phys. Rev. Lett. **92**, 055003 (2004).
[5] T. E. Cowan *et al.*, Phys. Rev. Lett. **92**, 204801 (2004).
[6] A. Gurevich, D. Anderson, and H. Wilhelmsson, Phys. Rev. Lett. **42**, 769 (1979).
[7] M. A. True, J. R. Albritton, and E. A. Williams, Phys. Fluids **24**, 1885 (1981).
[8] A. Pukhov, Phys. Rev. Lett. **86**, 3562 (2001).
[9] J. Fuchs *et al.*, Phys. Rev. Lett. **94**, 045004 (2005).
[10] F. Brunel, Phys. Rev. Lett. **59**, 52 (1987).
[11] W. L. Kruer and K. Estabrook, Phys. Fluids **28**, 430 (1985).
[12] J. P. Freidberg, R. W. Mitchell, R. L. Morse, and L. I. Rudsin-

ski, Phys. Rev. Lett. **28**, 795 (1972).
[13] A. A. Andreev, R. Sonobe, S. Kawata, S. Miyazaki, K. Sakai, K. Miyauchi, T. Kikuchi, K. Platonov, and K. Nemoto, Plasma Phys. Controlled Fusion **48**, 1605 (2006).
[14] R. Nuter, L. Gremillet, P. Combis, M. Drouin, E. Lefebvre, A. Flacco, and V. Malka, J. Appl. Phys. **104**, 103307 (2008).
[15] T. Grismayer and P. Mora, Phys. Plasmas **13**, 032103 (2006).
[16] A. J. Mackinnon, M. Borghesi, S. Hatchett, M. H. Key, P. K. Patel, H. Campbell, A. Schiavi, R. Snavely, S. C. Wilks, and O. Willi, Phys. Rev. Lett. **86**, 1769 (2001).
[17] J. Fuchs *et al.*, Phys. Rev. Lett. **99**, 015002 (2007).
[18] M. Kaluza, J. Schreiber, M. I. K. Santala, G. D. Tsakiris, K. Eidmann, J. Meyer-ter-Vehn, and K. J. Witte, Phys. Rev. Lett. **93**, 045003 (2004).
[19] T. Ceccotti, A. Lévy, H. Popescu, F. Réau, P. D'Oliveira, P. Monot, J. P. Geindre, E. Lefebvre, and P. Martin, Phys. Rev.

Lett. **99**, 185002 (2007).

[20] P. Mora, Phys. Rev. Lett. **90**, 185002 (2003).

[21] P. Mora, Phys. Rev. E **72**, 056401 (2005).

[22] J. Schreiber, F. Bell, F. Grüner, U. Schramm, M. Geissler, M. Schnurer, S. Ter-Avetisyan, B. M. Hegelich, J. Cobble, E. Brambrink, J. Fuchs, P. Audebert, and D. Habs, Phys. Rev. Lett. **97**, 045005 (2006).

[23] M. Carrié, E. Lefebvre, A. Flacco, and V. Malka, Phys. Plasmas **16**, 053105 (2009).

[24] A. J. Mackinnon, Y. Sentoku, P. K. Patel, D. W. Price, S. Hatchett, M. H. Key, C. Andersen, R. Snavely, and R. R. Freeman, Phys. Rev. Lett. **88**, 215006 (2002).

[25] Y. Oishi, T. Nayuki, T. Fujii, Y. Takizawa, and X. Wang, Phys. Plasmas **12**, 073102 (2005).

[26] L. Robson *et al.*, Nat. Phys. **3**, 58 (2007).

[27] J. Fuchs *et al.*, Nat. Phys. **2**, 48 (2006).

[28] D. Neely, P. Foster, A. Robinson, F. Lindau, O. Lundh, A. Persson, C. G. Wahlström, and P. McKenna, Appl. Phys. Lett. **89**, 021502 (2006).

[29] A. Jullien, O. Albert, G. Chériaux, J. Etchepare, S. Kourtev, N. Minkovsky, and S. M. Saltiel, Opt. Express **14**, 2760 (2006).

[30] S. Jacquemot, L. Bonnet, and A. Decoster, Laser Interaction with Matter Institute of Physics Conference Series, 1995 (unpublished), Vol. 140, p. 193.

[31] E. Lefebvre *et al.*, Nucl. Fusion **43**, 629 (2003).

[32] S. C. Wilks, W. L. Kruer, M. Tabak, and A. B. Langdon, Phys. Rev. Lett. **69**, 1383 (1992).

[33] J. J. Santos, A. Debayle, P. Nicolaï, V. Tikhonchuk, M. Manclossi, D. Batani, A. Guemnie-Tafo, J. Faure, V. Malka, and J. J. Honrubia, Phys. Plasmas **14**, 103107 (2007).

[34] A. Flacco, A. Guemnie-Tafo, R. Nuter, M. Veltcheva, D. Batani, E. Lefebvre, and V. Malka, J. Appl. Phys. **104**, 103304 (2008).

Bibliography

[1] Herwig Kogelnik. On the propagation of gaussian beams of light through lenslike media including those with a loss or gain variation. *Appl. Opt.*, 4(12):1562–1569, December 1965. 6

[2] Melvin Lax, William H. Louisell, and William B. McKnight. From maxwell to paraxial wave optics. *Phys. Rev. A*, 11(4):1365–, April 1975. 6

[3] C. E. Max, J. Arons, and A. B. Langdon. Self-modulation and self-focusing of electromagnetic waves in plasmas. *Phys. Rev. Lett.*, 33(4):209, 1974. 6

[4] P. Monot, T. Auguste, P. Gibbon, F. Jakober, G. Mainfray, A. Dulieu, M. Louis-Jacquet, G. Malka, and J. L. Miquel. Experimental demonstration of relativistic self-channeling of a multiterawatt laser pulse in an underdense plasma. *Phys. Rev. Lett.*, 74(15):2953–2956, 1995. 6, 93

[5] L. V. Keldysh. Ionisation in the field of a strong electromagnetic wave. *Sov. Phys. JETP*, 20:1307, 1965. 7

[6] Lewi Tonks and Irving Langmuir. Oscillations in ionized gases. *Phys. Rev.*, 33(2):195–210, Feb 1929. 8, 11

[7] D. V. Romanov, V. Yu. Bychenkov, W. Rozmus, C. E. Capjack, and R. Fedosejevs. Self-organization of a plasma due to 3D evolution of the weibel instability. *Phys. Rev. Lett.*, 93(21):215004, 2004. 8

[8] D. Pesme, G. Laval, and R. Pellat. Parametric instabilities in bounded plasmas. *Phys. Rev. Lett.*, 31(4):203, 1973. 8

[9] Kent Estabrook, W. L. Kruer, and B. F. Lasinski. Heating by raman backscatter and forward scatter. *Phys. Rev. Lett.*, 45(17):1399, 1980. 8

[10] E. S. Weibel. Spontaneous growing transverse waves in a plasma due to an anisotropic velocity distribution. *Phys. Rev. Lett.*, 2(3):83, 1959. 8, 111

[11] Hannes Alfvén. Existence of electromagnetic-hydrodynamic waves. *Nature*, 150:405–406, 1942. 10

[12] E. Lefebvre and G. Bonnaud. Transparency/opacity of a solid target illuminated by an ultrahigh-intensity laser pulse. *Phys. Rev. Lett.*, 74(11):2002–2005, 1995. 12, 20

[13] W.I. Linlor. Ion energies produced by laser giant pulse. *Appl. Phys. Letters*, 3, 1963. 13

[14] R. Carlson, J. Carpenter, D. Casperson, R. Gibson, R. Godwin, R. Haglund, J. Hanlon, E. Jolly, and T. Stratton. Helios: A 15 tw carbon dioxide laser-fusion facility. *Quantum Electronics, IEEE Journal of*, 17(9):1662–1678, 1981. 13

[15] S. J. Gitomer, R. D. Jones, F. Begay, A. W. Ehler, J. F. Kephart, and R. Kristal. Fast ions and hot electrons in the laser–plasma interaction. *Physics of Fluids*, 29(8):2679–2688, 1986. 13

[16] D. Strickland and G. Mourou. Compression of amplified chirped optical pulses. *Opt. Comm.*, 56:219–221, 1985. 13, 59

[17] K. Krushelnick, E. L. Clark, Z. Najmudin, M. Salvati, M. I. K. Santala, M. Tatarakis, A. E. Dangor, V. Malka, D. Neely, R. Allott, and C. Danson. Multi-MeV ion production from high-intensity laser interactions with underdense plasmas. *Phys. Rev. Lett.*, 83(4):737–740, 1999. 13, 14, 15, 23, 25, 29, 63, 79, 98, 99, 100, 103

[18] T. Ditmire, J. W. G. Tisch, E. Springate, M. B. Mason, N. Hay, R. A. Smith, J. Marangos, and M. H. R. Hutchinson. High-energy ions produced in explosions of superheated atomic clusters. *Nature*, 386(6620):54–56, 1997. 13, 14, 25, 131, 145

[19] A. P. Fews, P. A. Norreys, F. N. Beg, A. E. dangor, C. N. Danson, P. Lee, and S. J. Rose. Plasma ion emission fron high-intensity picosecond laser-pulse interactions with solid targets. *Phys. Rev. Lett.*, 73(13):1801–1804, 1994. 13

[20] E. L. Clark, K. Krushelnick, J. R. Davies, M. Zepf, M. Tatarakis, F. N. Beg, A. Machacek, P. A. Norreys, M. I. K. Santala, I. Watts, and A. E. Dangor. Measurements of energetic proton transport through magnetized lasma from intense laser interactions with solids. *Phys. Rev. Lett.*, 84(4):670–673, 2000. 13

[21] WL Brown, LJ Lanzerotti, and RE Johnson. Fast ion bombardment of ices and its astrophysical implications. *Science*, 218(4572):525, 1982. 13

[22] P. K. Patel, A. J. Mackinnon, M. H. Key, T. E. Cowan, M. E. Foord, M. Allen, D. F. Price, H. Ruhl, P. T. Springer, and R. Stephens. Isochoric heating of solid-density matter with an ultrafast proton beam. *Phys. Rev. Lett.*, 91(12):125004–, September 2003. 13, 14

[23] G. M. Dyer, A. C. Bernstein, B. I. Cho, J. Osterholz, W. Grigsby, A. Dalton, R. Shepherd, Y. Ping, H. Chen, K. Widmann, and T. Ditmire. Equation-of-state measurement of dense plasmas heated with fast protons. *Phys. Rev. Lett.*, 101(1):015002, 2008. 13

[24] V. Malka, J. Faure, Y. A. Gauduel, E. Lefebvre, A. Rousse, and K. Ta Phuoc. Principles and applications of compact laser-plasma accelerators. *Nature Physics*, 44:447–453, 2008. 13

[25] V. Malka, S. Fritzler, E. Lefebvre, R. Ferrand, G. Grillon, C. Albaret, S. Meyroneinc, J.P. Chambaret, A. Antonetti, and D. Hulin. Practicability of protontherapy using compact laser systems. *Medical physics*, 31:1587, 2004. 13

[26] S. V. Bulanov and V. S. Khoroshkov. Feasibility of using laser ion accelerators in proton therapy. *Plasma Physics Reports*, 28(5):453–456, 2002. 13, 134

[27] M. Roth, T. E. Cowan, M. H. Key, S. P. Hatchett, C. Brown, W. Fountain, J. Johnson, D. M. Pennington, R. A. Snavely, S. C. Wilks, K. Yasuike, H. Ruhl, F. Pegoraro, S. V. Bulanov, E. M. Campbell, M. D. Perry, and H. Powell. Fast ignition by intense laser-accelerated proton beams. *Phys. Rev. Lett.*, 86(3):436–439, 2001. 13, 134

[28] S. P. Hatchett, C. G. Brown, T. E. Cowan, E. A. Henry, J. S. Johnson, M. H. Key, J. A. Koch, B. F. Lasinski A. B. Langdon, R. W. lee, A. J. Mackinnon, M. D. Perry D. M. Pennington, T. W. Phillips, M. Roth, T. C. Sangster, M. S. Singh, R. A. Snavely, M. A. Stoyer, S. C. Wilks, and K. Yasuike. Electron, photon, and ion beams from the relativistic interaction of Petawatt laser pulses with solid targets. *Phys. Plasmas*, 7(5):2076–2082, 2000. 13, 16

[29] R. A. Snavely *et al.* Intense high-energy proton beams from petawatt-laser irradiation of solids. *Phys. Rev. Lett.*, 85:2945, 2000. 13, 16, 17

[30] A. Maksimchuk, S. Gu, K. Flippo, D. Umstadter, and V.Y. Bychenkov. Forward ion acceleration in thin films driven by a high-intensity laser. *Physical Review Letters*, 84(18):4108–4111, 2000. 13, 18

[31] M. Hegelich, S. Karsch, G. Pretzler, D. Habs, K. Witte, W. Guenther, M. Allen, A. Blazevic, J. Fuchs, J. C. Gauthier, M. Geissel, P. Audebert, T. Cowan, and M. Roth. Mev ion jets from short-pulse-laser interaction with thin foils. *Phys. Rev. Lett.*, 89(8):085002, 2002. 13, 17

[32] A. J. Mackinnon, Y. Sentoku, P. K. Patel, D. W. Price, S. Hatchett, M. H. Key, C. Andersen, R. Snavely, and R. R. Freeman. Enhancement of proton acceleration by hot-electron recirculation in thin foils irradiated by ultraintense laser pulses. *Phys. Rev. Lett.*, 88(21):215006, 2002. 13, 14

[33] S. Fritzler, V. Malka, G. Grillon, JP Rousseau, F. Burgy, E. Lefebvre, P. McKenna, and KWD Ledingham. Proton beams generated with high-intensity lasers: Applications to medical isotope production. *Applied physics letters*, 83:3039, 2003. 13, 14

[34] T. E. Cowan, J. Fuchs, H. Ruhl, A. Kemp, P. Audebert, M. Roth, R. Stephens, I. Barton, A. Blazevic, E. Brambrink, J. Cobble, J. Fernández, J.-C. Gauthier, M. Geissel, M. Hegelich, J. Kaae, S. Karsch, G. P. Le Sage, S. Letzring, M. Manclossi, S. Meyroneinc, A. Newkirk, H. Pépin, and N. Renard-LeGalloudec. Ultralow emittance, multi-mev proton beams from a laser virtual-cathode plasma accelerator. *Phys. Rev. Lett.*, 92(20):204801, 2004. 13, 14, 18

[35] P. McKenna, K. W. D. Ledingham, J. M. Yang, L. Robson, T. McCanny, S. Shimizu, R. J. Clarke, D. Neely, K. Spohr, R. Chapman, R. P. Singhal, K. Krushelnick, M. S. Wei, and P. A. Norreys. Characterization of proton and heavier ion acceleration in ultrahigh-intensity laser interactions with heated target foils. *Phys. Rev. E*, 70(3):036405, Sep 2004. 13

[36] M. Kaluza, J. Schreiber, M. I. K. Santala, G. D. Tsakiris, K. Eidmann, J. Meyer-ter Vehn, and K. J. Witte. Influence of the laser prepulse on proton acceleration in thin-foil experiments. *Phys. Rev. Lett.*, 93(4):045003, 2004. 13, 14, 61

[37] F. Lindau, O. Lundh, A. Persson, P. McKenna, K. Osvay, D. Batani, and C.-G. Wahlström. Laser-accelerated protons with energy-dependent beam direction. *Physical Review Letters*, 95(17):175002, 2005. 13

[38] L. Romagnani, J. Fuchs, M. Borghesi, P. Antici, P. Audebert, F. Ceccherini, T. Cowan, T. Grismayer, S. Kar, A. Macchi, P. Mora, G. Pretzler, A. Schiavi, T. Toncian, and O. Willi. Dynamics of electric fields driving the laser acceleration of multi-mev protons. *Phys. Rev. Lett.*, 95(19):195001, 2005. 14, 111, 113

[39] J. Fuchs, P. Antici, E. D'humières, E. Lefebvre, M. Borghesi, E. Brambrink, CA Cecchetti, M. Kaluza, V. Malka, M. Manclossi, et al. Laser-driven proton scaling laws and new paths towards energy increase. *Nature Physics*, 2:48–54, 2005. 14, 18, 19

[40] S. Ter-Avetisyan, M. Schnürer, P. V. Nickles, M. Kalashnikov, E. Risse, T. Sokollik, W. Sandner, A. Andreev, and V. Tikhonchuk. Quasimonoen-ergetic deuteron bursts produced by ultraintense laser pulses. *Phys. Rev. Lett.*, 96(14):145006, 2006. 14, 21

[41] H.C. Kapteyn, M.M. Murnane, A. Szoke, and R.W. Falcone. Prepulse energy suppression for high-energy ultrashort pulses using self-induced plasma shuttering. *Optics letters*, 16(7):490–492, 1991. 14

[42] T. Ceccotti, A. Lévy, H. Popescu, F. Réau, P. D'Oliveira, P. Monot, J. P. Geindre, E. Lefebvre, and Ph. Martin. Proton acceleration with high-intensity ultrahigh-contrast laser pulses. *Physical Review Letters*, 99(18):185002, 2007. 14

[43] K. Zeil, SD Kraft, S. Bock, M. Bussmann, TE Cowan, T. Kluge, J. Metzkes, T. Richter, R. Sauerbrey, and U. Schramm. The scaling of proton energies in ultrashort pulse laser plasma acceleration. *New Journal of Physics*, 12:045015, 2010. 14

[44] S. Ter-Avetisyan, B. Ramakrishna, D. Doria, G. Sarri, M. Zepf, M. Borghesi, L. Ehrentraut, H. Stiel, S. Steinke, G. Priebe, et al. Complementary ion and extreme ultra-violet spectrometer for laser-plasma diagnosis. *Review of Scientific Instruments*, 80:103302, 2009. 14

[45] S. Ter-Avetisyan, M. Schnürer, PV Nickles, W. Sandner, T. Nakamura, and K. Mima. Correlation of spectral, spatial, and angular characteristics of an ultrashort laser driven proton source. *Physics of Plasmas*, 16:043108, 2009. 14

[46] S. Ter-Avetisyan, M. Schnürer, and P. V. Nickles. *Characterisation and Manipulation of Proton Beams Accelerated by Ultra-Short and High-Contrast Laser Pulses, Coherence and Ultrashort Pulse Laser Emission,*, pages 404–434. Coherence and Ultrashort Pulse Laser Emission, 2010. 14

[47] G. S. Sarkisov, V. Yu. Bychenkov, V. N. Novikov, V. T. Tikhonchuk, A. Maksimchuk, S. Y. Chen, R. Wagner, G. Mourou, and D. Umstadter. Self-focusing, channel formation, and high-energy ion generation in the interaction of an intense short laser pulse with a he gas jet. *Phys. Rev. E*, 59(6):7042, 1999. 14, 25, 98, 99, 100, 103, 108

[48] F. Peano, RA Fonseca, and LO Silva. Dynamics and control of shock shells in the coulomb explosion of very large deuterium clusters. *Physical review letters*, 94(3):33401, 2005. 14, 50, 131

[49] SS Bulanov, A. Brantov, V.Y. Bychenkov, V. Chvykov, G. Kalinchenko, T. Matsuoka, P. Rousseau, S. Reed, V. Yanovsky, DW Litzenberg, et al. Accelerating monoenergetic protons from ultrathin foils by flat-top laser pulses in the directed-coulomb-explosion regime. *Physical Review E*, 78(2):026412, 2008. 14

[50] Andrea Macchi, Francesco Ceccherini, Fulvio Cornolti, Satyabrata Kar, and Marco Borghesi. Electric field dynamics and ion acceleration in the self-channeling of a superintense laser pulse. *Plasma Physics and Controlled Fusion*, 51(2):024005, 2009. 14, 15, 25, 29, 39, 84

[51] K. I. Popov, W. Rozmus, V. Yu. Bychenkov, N. Naseri, C. E. Capjack, and A. V. Brantov. Ion response to relativistic electron bunches in the blowout regime of laser-plasma accelerators. *Phys. Rev. Lett.*, 105(19):195002, 2010. 14, 23, 25, 47, 132

[52] D.A. Gurnett. Sheath effects and related charged-particle acceleration by jupiter's satellite io. *The Astrophysical Journal*, 175:525, 1972. 15

[53] SD Shawhan, RF Hubbard, G. Joyce, and DA Gurnett. Sheath acceleration of photoelectrons by jupiter's satellite io. In *Photon and Particle Interactions with Surfaces in Space*, volume 37, page 405, 1973. 15

[54] V. K. Tripathi, T. Taguchi, and C. S. Liu. Plasma channel charging by an intense short pulse laser and ion coulomb explosion. *Physics of Plasmas*, 12(4):043106, 2005. 15, 25

[55] G. Sun, E. Ott, Y. C. Lee, and P. Guzdar. Self-focusing of short intense pulses in plasmas. *Phys. Fluids*, 30(2):526–532, 1987. 16, 39, 70, 93

[56] L. Willingale, S. P. D. Mangles, P. M. Nilson, R. J. Clarke, A. E. Dangor, M. C. Kaluza, S. Karsch, K. L. Lancaster, W. B. Mori, Z. Najmudin, J. Schreiber, A. G. R. Thomas, M. S. Wei, and K. Krushelnick. Collimated multi-mev ion beams from high-intensity laser interactions with underdense plasma. *Phys. Rev. Lett.*, 96(24):245002, 2006. 16, 19, 23, 131, 133, 135

[57] B. Bezzerides, SJ Gitomer, and DW Forslund. Randomness, maxwellian distributions, and resonance absorption. *Physical Review Letters*, 44(10):651–654, 1980. 17

[58] J. P. Freidberg, R. W. Mitchell, R. L. Morse, and L. I. Rudsinski. Resonant absorption of laser light by plasma targets. *Phys. Rev. Lett.*, 28:795, 1972. 17

[59] F. Brunel. Not-so-resonant, resonant absorption. *Phys. Rev. Lett.*, 59:52–55, 1987. 17

[60] HM Milchberg and R.R. Freeman. Light absorption in ultrashort scale length plasmas. *JOSA B*, 6(7):1351–1355, 1989. 17

[61] W. L. Kruer. Ponderomotive and thermal filamentation of laser light. *Comments Plasma Phys. Controlled Fusion*, 9(2):63–72, 1985. 17, 19

[62] G. Malka and J. L. Miquel. Experimental confirmation of ponderomotive-force electrons produced by an ultrarelativistic laser pulse on a solid target. *Phys. Rev. Lett.*, 77(1):75–78, 1996. 17

[63] JS Green, VM Ovchinnikov, RG Evans, KU Akli, H. Azechi, FN Beg, C. Bellei, RR Freeman, H. Habara, R. Heathcote, et al. Effect of laser

intensity on fast-electron-beam divergence in solid-density plasmas. *Physical review letters*, 100(1):15003, 2008. 17

[64] L. Grémillet, F. Amiranoff, S. D. Baton, J.-C. Gauthier, M. Koenig, E. Martinolli, F. Pisani, G. Bonnaud, C. Lebourg, C. Rousseaux, C. Toupin, A. Antonicci, D. Batani, A. Bernardinello, T. Hall, D. Scott, P. Norreys, H. Bandulet, and H. Pépin. Time-resolved observation of ultrahigh intensity laser-produced electron jets propagating through transparent solid targets. *Phys. Rev. Lett.*, 83:5015–5018, 1999. 17, 118

[65] J. J. Santos, F. Amiranoff, S. D. Baton, L. Gremillet, M. Koenig, E. Martinolli, M. Rabec Le Gloahec, C. Rousseaux, D. Batani, A. Bernardinello, G. Greison, and T. Hall. Fast electron transport in ultraintense laser pulse interaction with solid targets by rear-side self-radiation diagnostics. *Phys. Rev. Lett.*, 89:025001, 2002. 17

[66] J. M. Rax. *Physique des plasmas*, chapter 6, pages 205–207. Dunod, 2005. 17

[67] J. M. Rax. *Physique des plasmas*, chapter 4, pages 115–118. Dunod, 2005. 17, 18, 156

[68] P. Mora and T. Grismayer. Rarefaction acceleration and kinetic effects in thin-foil expansion into a vacuum. *Phys. Rev. Lett.*, 102(14):145001, 2009. 17

[69] K. Riemann. The Bohm criterion and sheath formation. *Journal of Physics D: Applied Physics*, 24:493, 1991. 18

[70] RN Franklin. The plasma–sheath boundary region. *Journal of Physics D: Applied Physics*, 36:R309, 2003. 18

[71] L. Oksuz and N. Hershkowitz. First experimental measurements of the plasma potential throughout the presheath and sheath at a boundary in a weakly collisional plasma. *Phys. Rev. Lett.*, 89(14):145001, 2002. 18

[72] L. Oksuz and N. Hershkowitz. Plasma, presheath, collisional sheath and collisionless sheath potential profiles in weakly ionized, weakly collisional plasma. *Plasma Sources Science and Technology*, 14:201, 2005. 18

[73] K.U. Riemann. Plasma-sheath transition in the kinetic Tonks-Langmuir model. *Physics of plasmas*, 13:063508, 2006. 18

[74] RN Franklin. Plasmas with more than one species of positive ion and the bohm criterion. *Journal of Physics D: Applied Physics*, 33:3186, 2000. 18

[75] N. Hershkowitz. Sheaths: More complicated than you think. *Physics of plasmas*, 12:055502, 2005. 18

[76] L. M. Wickens, J. E. Allen, and P. T. Rumsby. Ion emission from laser-produced plasmas with two electron temperatures. *Phys. Rev. Lett.*, 41(4):243–246, 1978. 18

[77] LM Wickens and JE Allen. Free expansion of a plasma with two electron temperatures. *Journal of Plasma Physics*, 22:167–185, 1979. 18

[78] Y. Kishimoto, K. Mima, T. Watanabe, and K. Nishikawa. Analysis of fast-ion velocity distributions in laser plasmas with a truncated maxwellian velocity distribution of hot electrons. *Physics of Fluids*, 26:2308, 1983. 18

[79] P. Mora. Plasma expansion into a vacuum. *Phys. Rev. Lett.*, 90(18):185002, 2003. 18

[80] P. Mora. Thin-foil expansion into a vacuum. *Physical Review E (Statistical, Nonlinear, and Soft Matter Physics)*, 72(5):056401, 2005. 18

[81] T. Grismayer and P. Mora. Influence of a finite initial ion density gradient on plasma expansion into a vacuum. *Physics of Plasmas*, 13(3):032103, 2006. 18, 19, 49

[82] M. Passoni and M. Lontano. Theory of light-ion acceleration driven by a strong charge separation. *Phys. Rev. Lett.*, 101(11):115001–, September 2008. 18

[83] S. Ter-Avetisyan, M. Schnürer, S. Busch, E. Risse, P. V. Nickles, and W. Sandner. Spectral dips in ion emission emerging from ultrashort laser-driven plasmas. *Phys. Rev. Lett.*, 93(15):155006, 2004. 18

[84] Y. Oishi, T. Nayuki, T. Fujii, Y. Takizawa, X. Wang, T. Yamazaki, K. Nemoto, T. Kayoiji, T. Sekiya, K. Horioka, et al. Dependence on laser intensity and pulse duration in proton acceleration by irradiation of ultrashort laser pulses on a cu foil target. *Physics of plasmas*, 12:073102, 2005. 18

[85] J. Fuchs, C. A. Cecchetti, M. Borghesi, T. Grismayer, E. d'Humières, P. Antici, S. Atzeni, P. Mora, A. Pipahl, L. Romagnani, A. Schiavi, Y. Sentoku, T. Toncian, P. Audebert, and O. Willi. Laser-foil acceleration of high-energy protons in small-scale plasma gradients. *Phys. Rev. Lett.*, 99(1):015002, 2007. 18, 19

[86] S. C. Wilks, W. L. Kruer, M. Tabak, and A. B. Langdon. Absorption of ultra-intense laser pulses. *Phys. Rev. Lett.*, 69(9):1383–1386, 1992. 19

[87] M. Carrié. *Accélération de protons par laser à ultra-haute intensité: étude et application au chauffage isochore*. PhD thesis, Université Paris XI, http://tel.archives-ouvertes.fr/tel-00608050, 2011. 19

[88] AV Brantov, VT Tikhonchuk, O. Klimo, DV Romanov, S. Ter-Avetisyan, M. Schnürer, T. Sokollik, and PV Nickles. Quasi-mono-energetic ion acceleration from a homogeneous composite target by an intense laser pulse. *Physics of plasmas*, 13:122705, 2006. 19, 21

[89] A. Lévy, R. Nuter, T. Ceccotti, P. Combis, M. Drouin, L. Gremillet, P. Monot, H. Popescu, F. Réau, E. Lefebvre, et al. Effect of a nanometer scale plasma on laser-accelerated ion beams. *New Journal of Physics*, 11:093036, 2009. 19, 49

[90] AV Kuznetsov, T.Z. Esirkepov, FF Kamenets, and SV Bulanov. Efficiency of ion acceleration by a relativistically strong laser pulse in an underdense plasma. *Plasma Physics Reports*, 27(3):211–220, 2001. 19, 22, 23

[91] S. V. Bulanov and T. Zh. Esirkepov. Comment on "collimated multi-mev ion beams from high-intensity laser interactions with underdense plasma". *Phys. Rev. Lett.*, 98(4):049503, 2007. 19, 23, 132

[92] V. Chvykov, P. Rousseau, S. Reed, G. Kalinchenko, and V. Yanovsky. Generation of 10^{11} contrast 50 TW laser pulses. *Optics letters*, 31(10):1456–1458, 2006. 20

[93] A. Pukhov. Topical review: Strong field interaction of laser radiation. *Reports on Progress in Physics*, 66:47, 2003. 20

[94] T. Esirkepov, M. Borghesi, S. V. Bulanov, G. Mourou, and T. Tajima. Highly efficient relativistic-ion generation in the laser-piston regime. *Phys. Rev. Lett.*, 92(17):175003, 2004. 20

[95] Luís O. Silva, Michael Marti, Jonathan R. Davies, Ricardo A. Fonseca, Chuang Ren, Frank S. Tsung, and Warren B. Mori. Proton shock acceleration in laser-plasma interactions. *Phys. Rev. Lett.*, 92(1):015002, 2004. 20

[96] Andrea Macchi, Federica Cattani, Tatiana V. Liseykina, and Fulvio Cornolti. Laser acceleration of ion bunches at the front surface of overdense plasmas. *Physical Review Letters*, 94(16):165003, 2005. 20, 21, 49, 88

[97] L. Yin, BJ Albright, BM Hegelich, and JC Fernandez. Gev laser ion acceleration from ultrathin targets: The laser break-out afterburner. *Laser and Particle Beams*, 24(02):291–298, 2006. 20

[98] APL Robinson, M. Zepf, S. Kar, RG Evans, and C. Bellei. Radiation pressure acceleration of thin foils with circularly polarized laser pulses. *New Journal of Physics*, 10:013021, 2008. 20, 21

[99] SV Bulanov, E.Y. Echkina, T.Z. Esirkepov, IN Inovenkov, M. Kando, F. Pegoraro, and G. Korn. Unlimited ion acceleration by radiation pressure. *Physical review letters*, 104(13):135003, 2010. 20

[100] Tatsufumi Nakamura, Sergei V. Bulanov, Timur Zh. Esirkepov, and Masaki Kando. High-energy ions from near-critical density plasmas via magnetic vortex acceleration. *Phys. Rev. Lett.*, 105(13):135002, 2010. 20, 118, 120

[101] D. W. Forslund and C. R. Shonk. Formation and structure of electrostatic collisionless shocks. *Phys. Rev. Lett.*, 25(25):1699–1702, Dec 1970. 20

[102] M. S. Wei, S. P. D. Mangles, Z. Najmudin, B. Walton, A. Gopal, M. Tatarakis, A. E. Dangor, E. L. Clark, R. G. Evans, S. Fritzler, R. J. Clarke, C. Hernandez-Gomez, D. Neely, W. Mori, M. Tzoufras, and K. Krushelnick. Ion acceleration by collisionless shocks in high-intensity-laser–underdense-plasma interaction. *Phys. Rev. Lett.*, 93(15):155003, 2004. 20, 23, 25, 29, 63, 89

[103] A. Henig, D. Kiefer, M. Geissler, S. G. Rykovanov, R. Ramis, R. Hörlein, J. Osterhoff, Zs. Major, L. Veisz, S. Karsch, F. Krausz, D. Habs, and J. Schreiber. Laser-driven shock acceleration of ion beams from spherical mass-limited targets. *Phys. Rev. Lett.*, 102(9):095002, 2009. 20

[104] A. Zhidkov, M. Uesaka, A. Sasaki, and H. Daido. Ion acceleration in a solitary wave by an intense picosecond laser pulse. *Physical review letters*, 89(21):215002, 2002. 20

[105] BM Hegelich, D. Jung, BJ Albright, JC Fernandez, DC Gautier, C. Huang, TJ Kwan, S. Letzring, S. Palaniyappan, RC Shah, et al. Experimental demonstration of particle energy, conversion efficiency and spectral shape required for ion-based fast ignition. *Nuclear Fusion*, 51:083011, 2011. 20

[106] S.G. Rykovanov, J. Schreiber, J. Meyer-ter Vehn, C. Bellei, A. Henig, HC Wu, and M. Geissler. Ion acceleration with ultra-thin foils using elliptically polarized laser pulses. *New Journal of Physics*, 10:113005, 2008. 21

[107] B. Quesnel, P. Mora, J. C. Adam, S. Guérin, A. Héron, and G. Laval. Electron parametric instabilities of ultraintense short laser pulses propagating in plasmas. *Phys. Rev. Lett.*, 78(11):2132–2135, 1997. 21, 93, 96

[108] A. Henig, S. Steinke, M. Schnürer, T. Sokollik, R. Hörlein, D. Kiefer, D. Jung, J. Schreiber, B. M. Hegelich, X. Q. Yan, J. Meyer-ter Vehn, T. Tajima, P. V. Nickles, W. Sandner, and D. Habs. Radiation-pressure acceleration of ion beams driven by circularly polarized laser pulses. *Phys. Rev. Lett.*, 103(24):245003, 2009. 21

[109] Charlotte A. J. Palmer, N. P. Dover, I. Pogorelsky, M. Babzien, G. I. Dudnikova, M. Ispiriyan, M. N. Polyanskiy, J. Schreiber, P. Shkolnikov, V. Yakimenko, and Z. Najmudin. Monoenergetic proton beams accelerated by a radiation pressure driven shock. *Phys. Rev. Lett.*, 106(1):014801, 2011. 21

[110] F. Dollar, T. Matsuoka, GM Petrov, AGR Thomas, SS Bulanov, V. Chvykov, J. Davis, G. Kalinchenko, C. McGuffey, L. Willingale, et al. Control of energy spread and dark current in proton and ion beams generated in high-contrast laser solid interactions. *Physical Review Letters*, 107(6):065003, 2011. 21

[111] Aurélie Jullien, Olivier Albert, Frédéric Burgy, Guy Hamoniaux, Jean-Philippe Rousseau, Jean-Paul Chambaret, Frédérika Augé-Rochereau, Gilles Chériaux, Jean Etchepare, Nikolay Minkovski, and Solomon M. Saltiel. 10^{-10} temporal contrast for femtosecond ultraintense lasers by cross-polarized wave generation. *Opt. Lett.*, 30(8):920–922, 2005. 21, 60

[112] G. Doumy, F. Quéré, O. Gobert, M. Perdrix, P. Martin, P. Audebert, JC Gauthier, J.P. Geindre, and T. Wittmann. Complete characterization of a plasma mirror for the production of high-contrast ultraintense laser pulses. *Physical Review E*, 69(2):026402, 2004. 21

[113] Y. Kitagawa, H. Fujita, R. Kodama, H. Yoshida, S. Matsuo, T. Jitsuno, T. Kawasaki, H. Kitamura, T. Kanabe, S. Sakabe, et al. Prepulse-free petawatt laser for a fast ignitor. *Quantum Electronics, IEEE Journal of*, 40(3):281–293, 2004. 21

[114] F. Druon, G. Chériaux, J. Faure, J. Nees, M. Nantel, A. Maksimchuk, G. Mourou, J.C. Chanteloup, and G. Vdovin. Wave-front correction of femtosecond terawatt lasers by deformable mirrors. *Optics letters*, 23(13):1043–1045, 1998. 21

[115] A.J. Verhoef, J. Seres, K. Schmid, Y. Nomura, G. Tempea, L. Veisz, and F. Krausz. Compression of the pulses of a Ti: Sapphire laser system to 5 femtoseconds at 0.2 terawatt level. *Applied Physics B: Lasers and Optics*, 82(4):513–517, 2006. 21

[116] C. G. R. Geddes, Cs. Tóth, J. van Tilborg, E. Esarey, C. B. Schroeder, D. Bruhwiler, C. Nieter, J. Cary, and W. P. Leemans. High quality electron beams from a laser wakefield accelerator using plasma-channel guiding. *Nature*, 431:538–541, 2004. 22

[117] S. P. D. Mangles, C. D. Murphy, Z. Najmudin, A. G. R. Thomas, J. L. Collier, A. E. Dangor, E. J. Divall, P. S. Foster, J. G. Gallacher, C. J. Hooker, D. A. Jaroszynski, A. J. Langley, W. B. Mori, P. A. Norreys, F. S. Tsung, B. R. Walton, and K. Krushelnick. Monoenergetic beams of relativistic electrons from intense laser-plasma interactions. *Nature*, 431:535–538, 2004. 22

[118] J. Faure, Y. Glinec, A. Pukhov, S. Kiselev, S. Gordienko, E. Lefebvre, J.-P. Rousseau, F. Burgy, and V. Malka. A laser-plasma accelerator producing monoenergetic electron beams. *Nature*, 431:541–544, 2004. 22

[119] L.M. Gorbunov and A.A. Frolov. Collision of two short laser pulses in plasma and the generation of short lived Bragg mirrors. *Sov. Phys. JETP*, 93:510–518, 2001. 22, 23, 40, 42, 79

[120] Emmanuel D'humières. *Accélération de protons par interaction laser-plasma et applications.* Partie C: Accélération de protons avec une cible sous-dense, Université Paris 6, 2006. 22

[121] E. Lefebvre, N. Cochet, S. Fritzler, V. Malka, M.-M. Aléonard, J.-F. Chemin, S. Darbon, L. Disdier, J. Faure, A. Fedotoff, O. Landoas, G. Malka, V. Méot, P. Morel, M. Rabec Le Gloahec, A. Rouyer, Ch. Rubbelynck, V. Tikhonchuk, R. Wrobel, P. Audebert, and C. Rousseaux. Electron and photon production from relativistic laser-plasma interactions. *Nucl. Fusion*, 43:629–633, 2003. 22, 40

[122] L. Willingale, SPD Mangles, PM Nilson, RJ Clarke, AE Dangor, MC Kaluza, S. Karsch, KL Lancaster, WB Mori, Z. Najmudin, J. Schreiber, A. G. R. Thomas, M. S. Wei, and K. Krushelnick. Willingale et al. reply. *Physical Review Letters*, 98(4):49504, 2007. 23

[123] M. C. Kaluza, H.-P. Schlenvoigt, S. P. D. Mangles, A. G. R. Thomas, A. E. Dangor, H. Schwoerer, W. B. Mori, Z. Najmudin, and K. M. Krushelnick. Measurement of magnetic-field structures in a laser-wakefield accelerator. *Phys. Rev. Lett.*, 105(11):115002, 2010. 23, 76, 77

[124] S. V. Bulanov, T. Zh. Esirkepov, N. M. Naumova, F. Pegoraro, and V. A. Vshivkov. Solitonlike electromagnetic waves behind a superintense laser pulse in a plasma. *Phys. Rev. Lett.*, 82(17):3440–3443, 1999. 23, 111, 114, 116

[125] Timur Esirkepov, Katsunobu Nishihara, Sergei V. Bulanov, and Francesco Pegoraro. Three-dimensional relativistic electromagnetic subcycle solitons. *Phys. Rev. Lett.*, 89(27):275002, 2002. 23, 111, 114, 116

[126] G. Both, EP Kanter, Z. Vager, BJ Zabransky, and D. Zajfman. Ultrathin foils for coulomb-explosion experiments. *Review of scientific instruments*, 58(3):424–427, 1987. 25

[127] R. Stoian, D. Ashkenasi, A. Rosenfeld, and EEB Campbell. Coulomb explosion in ultrashort pulsed laser ablation of Al2O3. *Physical Review B*, 62(19):13167, 2000. 25

[128] M. D. Perry, J. A. Sefcik, S. Hatchett T. Cowan, A. Hunt, M. Mora, D. Pennington, R. Snavely, and S. C. Wilks. Hard X-ray production from high-intensity laser solid interactions. *Rev. Sci. Instrum.*, 70(1):265–269, 1999. 25

[129] N. E. Andreev, L. M. Gorbunov, V. I. Kirsanov, K. Nakajima, and A. Ogata. Structure of the wake field in plasma channels. *Phys. Plasmas*, 4(4):1145–1153, 1997. 25, 42, 43

[130] L. M. Gorbunov, P. Mora, and A. A. Solodov. Plasma ions dynamics in the wake of a short laser pulse. *Phys. Rev. Lett.*, 86(15):3332–3335, 2001. 25

[131] F. Peano, JL Martins, RA Fonseca, LO Silva, G. Coppa, F. Peinetti, and R. Mulas. Dynamics and control of the expansion of finite-size plasmas produced in ultraintense laser-matter interactions. *Physics of plasmas*, 14:056704, 2007. 39, 50

[132] P. Mora and T. M. Antonsen, Jr. Electron cavitation and acceleration in the wake of an ultra-intense, self-focused laser pulse. *Phys. Rev. E*, 53(3):2068–2071, 1996. 40

[133] T. Tajima and J. M. Dawson. Laser electron accelerator. *Phys. Rev. Lett.*, 43(4):267, 1979. 40

[134] A. Modena, A.E. Dangor, Z. Najmudin, C.E. Clayton, K. Marsh, C. Joshi, V. Malka, C.B. Darrow, D. Neely, and F.N. Walsh. Electron acceleration from the breaking of electron plasma waves. *Nature*, 377:606–608, 1995. 40, 63, 111

[135] M. N. Rosenbluth and C. S. Liu. Excitation of plasma waves by two laser beams. *Phys. Rev. Lett.*, 29(11):701–705, 1972. 40

[136] J. B. Rosenzweig. Trapping, thermal effects, and wave breaking in the nonlinear plasma wake-field accelerator. *Phys. Rev. A*, 38(7):3634, 1988. 40

[137] J. M. Dawson. Nonlinear electron oscillations in a cold plasma. *Phys. Rev.*, 113:383–387, 1959. 40

[138] A. I. Akhiezer and R. V. Polovin. Theory of wave motion of an electron plasma. *Sov. Phys. JETP*, 3(5):696–705, 1956. 40

[139] L. M. Gorbunov and V. I. Kirsanov. Excitation of plasma waves by an electromagnetic wave packet. *Sov. Phys. JETP*, 66:290–294, 1987. 40, 41

[140] P. Mora. Physique des plasmas chauds en régime ultra-rapide. Cours donné à l'École de printemps des Houches « Lasers haute intensité, physique et applications », 5-7 mai 1997, 1997. 40

[141] S. V. Bulanov, F. Pegoraro, and A. M. Pukhov. Two-dimensional regimes of self-focusing, wake field generation, and induced focusing of a short intense laser pulse in an underdense plasma. *Phys. Rev. Lett.*, 74(5):710–713, 1995. 40, 42, 43

[142] S. V. Bulanov, F. Pegoraro, A. M. Pukhov, and A. S. Sakharov. Transverse-wake wave breaking. *Phys. Rev. Lett.*, 78(22):4205–4208, 1997. 40, 43, 91

[143] E. Esarey, P. Sprangle, J. Krall, and A. Ting. Overview of plasma-based accelerator concepts. *IEEE Trans. Plasma Sci.*, 24(2):252–288, 1996. 41

[144] E. Esarey, CB Schroeder, and WP Leemans. Physics of laser-driven plasma-based electron accelerators. *Reviews of Modern Physics*, 81(3):1229, 2009. 43, 44, 85

[145] VI Berezhiani and IG Murusidze. Relativistic wake-field generation by an intense laser pulse in a plasma. *Phys. Lett. A*, 148:338–340, 1990. 44

[146] P. Sprangle, E. Esarey, and A. Ting. Nonlinear theory of intense laser-plasma interactions. *Phys. Rev. Lett.*, 64(17):2011–2014, 1990. 44

[147] R. Sadighi-Bonabi, M. Habibi, and E. Yazdani. Improving the relativistic self-focusing of intense laser beam in plasma using density transition. *Physics of Plasmas*, 16(8):3105, 2009. 46

[148] A. E. Kaplan, B. Y. Dubetsky, and P. L. Shkolnikov. Shock shells in coulomb explosions of nanoclusters. *Phys. Rev. Lett.*, 91(14):143401, 2003. 48, 50

[149] VF Kovalev, KI Popov, V.Y. Bychenkov, and W. Rozmus. Laser triggered coulomb explosion of nanoscale symmetric targets. *Physics of plasmas*, 14:053103, 2007. 50

[150] AF Lifschitz, X. Davoine, E. Lefebvre, J. Faure, C. Rechatin, and V. Malka. Particle-in-Cell modelling of laser-plasma interaction using Fourier decomposition. *Journal of Computational Physics*, 2008. 51

[151] A. Flacco, F. Sylla, M. Veltcheva, M. Carrié, R. Nuter, E. Lefebvre, D. Batani, and V. Malka. Dependence on pulse duration and foil thickness in high-contrast-laser proton acceleration. *Physical Review E*, 81(3):036405, 2010. 61

[152] A. Flacco, T. Ceccotti, H. George, P. Monot, Ph. Martin, F. Réau, O. Tcherbakoff, P. d'Oliveira, F. Sylla, M. Veltcheva, F. Burgy, A. Tafzi, V. Malka, and D. Batani. Comparative study of laser ion acceleration with different contrast enhancement techniques. *Nuclear Instruments and Methods in Physics Research Section A: Accelerators, Spectrometers, Detectors and Associated Equipment*, 620:18–22, 2010. 61

[153] J.P. Colombier, P. Combis, F. Bonneau, R. Le Harzic, and E. Audouard. Hydrodynamic simulations of metal ablation by femtosecond laser irradiation. *Physical Review B*, 71(16):165406, 2005. 61, 62

[154] M. Carrié, E. Lefebvre, A. Flacco, and V. Malka. Influence of subpicosecond laser pulse duration on proton acceleration. *Physics of Plasmas*, 16:053105, 2009. 63

[155] GR Plateau, NH Matlis, O. Albert, C. Tóth, CGR Geddes, CB Schroeder, J. van Tilborg, E. Esarey, and WP Leemans. Optimization of THz radiation generation from a laser wakefield accelerator. In *Advanced Accelerator Concepts(AIP Conference Proceedings)*, volume 1086, pages 707–712, 2009. 63

[156] V. Malka, S. Fritzler, E. Lefebvre, M.-M. Aléonard, F. Burgy, J.-P. Chambaret, J.-F. Chemin, K. Krushelnick, G. Malka, S. P. D. Mangles, Z. Najmudin, M. Pittman, J.-P. Rousseau, J.-N. Scheurer, B. Walton, and A. E. Dangor. Electron acceleration by a wake field forced by an intense ultrashort laser pulse. *Science*, 298:1596–1600, 2002. 63

[157] J. Faure, C. Rechatin, A. Norlin, A. Lifschitz, Y. Glinec, and V. Malka. Controlled injection and acceleration of electrons in plasma wakefields by colliding laser pulses. *Nature*, 444:737–739, 2006. 63

[158] C. Rechatin, J. Faure, A. Lifschitz, X. Davoine, E. Lefebvre, and V. Malka. Quasi-monoenergetic electron beams produced by colliding cross-polarized laser pulses in underdense plasmas. *New Jour. Phys.*, 11(1):013011, 2009. 63

[159] JS Liu, CQ Xia, WT Wang, HY Lu, C. Wang, AH Deng, WT Li, H. Zhang, XY Liang, YX Leng, et al. All-optical cascaded laser wakefield accelerator using ionization-induced injection. *Physical Review Letters*, 107(3):35001, 2011. 63

[160] BB Pollock, CE Clayton, JE Ralph, F. Albert, A. Davidson, L. Divol, C. Filip, SH Glenzer, K. Herpoldt, W. Lu, et al. Demonstration of a narrow energy spread, 0.5 GeV electron beam from a two-stage laser wakefield accelerator. *Physical Review Letters*, 107(4):45001, 2011. 63

[161] J. Osterhoff, A. Popp, Zs. Major, B. Marx, T. P. Rowlands-Rees, M. Fuchs, M. Geissler, R. Hörlein, B. Hidding, S. Becker, E. A. Peralta, U. Schramm, F. Grüner, D. Habs, F. Krausz, S. M. Hooker, and S. Karsch. Generation of stable, low-divergence electron beams by laser-wakefield acceleration in a steady-state-flow gas cell. *Phys. Rev. Lett.*, 101(8):085002, 2008. 63

[162] S. Semushin and V. Malka. High density gas jet nozzle design for laser target production. *Rev. Sci. Instrum.*, 72:2961–2965, 2001. 64, 136, 139, 142

[163] P. Sprangle, E. Esarey, J. Krall, and G. Joyce. Propagation and guiding of intense laser pulses in plasmas. *Phys. Rev. Lett.*, 69:2200, 1992. 70

[164] T. Matsuoka, C. McGuffey, P. G. Cummings, Y. Horovitz, F. Dollar, V. Chvykov, G. Kalintchenko, P. Rousseau, V. Yanovsky, S. S. Bulanov, A. G. R. Thomas, A. Maksimchuk, and K. Krushelnick. Stimulated raman side scattering in laser wakefield acceleration. *Phys. Rev. Lett.*, 105(3):034801–, July 2010. 72

[165] R. Benattar, C. Popovics, and R. Sigel. Polarized light interferometer for laser fusion studies. *Review of Scientific Instruments*, 50(12):1583–1586, 1979. 75

[166] P. Tomassini and A. Giulietti. A generalization of Abel inversion to non-axisymmetric density distribution. *Optics Communications*, 199(1-4):143 – 148, 2001. 76, 140

[167] B. Landgraf, M. Schnell, A. Sävert, M.C. Kaluza, and C. Spielmann. High resolution 3d gas-jet characterization. *Review of Scientific Instruments*, 82:083106, 2011. 75

[168] J. A. Stamper and B. H. Ripin. Faraday-rotation measurements of megagauss magnetic fields in laser-produced plasmas. *Phys. Rev. Lett.*, 34(3):138–141, 1975. 76

[169] M. Centurion, Y. Pu, and D. Psaltis. Holographic capture of femtosecond pulse propagation. *Journal of applied physics*, 100:063104, 2006. 76

[170] Alexander Buck, Maria Nicolai, Karl Schmid, Chris M. S. Sears, Alexander Savert, Julia M. Mikhailova, Ferenc Krausz, Malte C. Kaluza, and Laszlo Veisz. Real-time observation of laser-driven electron acceleration. *Nat Phys*, 7(7):543–548, 2011. 77, 132

[171] C. Ren, B. J. Duda, R. G. Hemker, W. B. Mori, T. Katsouleas, T. M. Antonsen, Jr., and P. Mora. Compressing and focusing of a short laser pulse by a thin plasma lens. *Phys. Rev. E*, 63(2):26411, 2001. 80

[172] O. Shorokhov, A. Pukhov, and I. Kostyukov. Self-compression of laser pulses in plasma. *Phys. Rev. Lett.*, 91(26):265002, 2003. 80, 135

[173] J. Faure, Y. Glinec, J. J. Santos, F. Ewald, J.-P. Rousseau, S. Kiselev, A. Pukhov, T. Hosokai, and V. Malka. Observation of laser pulse shortening in nonlinear plasma waves. *Phys. Rev. Lett.*, 95:205003, 2005. 80, 91, 132

[174] W. B. Mori, C. Joshi, J. M. Dawson, D. W. Forslund, and J. M. Kindel. Evolution of self-focusing of intense electromagnetic waves in plasma. *Phys. Rev. Lett.*, 60(13):1298–1301, 1988. 85, 93, 96, 113, 118

[175] S. Wilks, P. E. Young, J. Hammer, M. Tabak, and W. L. Kruer. Spreading of intense laser beams due to filamentation. *Phys. Rev. Lett.*, 73:2994–2997, 1994. 85, 93, 96

[176] N. M. Naumova, S. V. Bulanov, K. Nishihara, T. Zh. Esirkepov, and F. Pe-
      goraro. Polarization effects and anisotropy in three-dimensional relativistic
      self-focusing. *Phys. Rev. E*, 65(4):045402, 2002. 85

[177] J. Meyer-ter Vehn and Z.M. Sheng. On electron acceleration by intense
      laser pulses in the presence of a stochastic field. *Physics of Plasmas*, 6:641,
      1999. 88

[178] T. M. Antonsen, Jr. and P. Mora. Self-focusing and Raman scattering of
      laser pulses in tenuous plasmas. *Phys. Rev. Lett.*, 69(15):2204–2207, 1992.
      88

[179] E. Esarey, P. Sprangle, J. Krall, and A. Ting. Self-focusing and guiding of
      short laser pulses in ionizing gazes and plasmas. *IEEE J. Quant. Electron.*,
      33(11):1879–1914, 1997. 93, 99

[180] C.F. Barnett, H.T. Hunter, M.I. Fitzpatrick, I. Alvarez, C. Cisneros, and
      R.A. Phaneuf. Atomic data for fusion. volume 1: Collisions of h, h2, he and
      li atoms and ions with atoms and molecules. *NASA STI/Recon Technical
      Report N*, 91:13238, 1990. 94

[181] J. Faure, V. Malka, J.-R. Marquès, P.-G. David, F. Amiranoff, K. Ta Phuoc,
      and A. Rousse. Effects of pulse duration on self-focusing of ultra-short lasers
      in underdense plasmas. *Phys. Plasmas*, 9(3):756–759, 2002. 99

[182] N. H. Matlis, S. Reed, S. S. Bulanov, V. Chvykov, G. Kalintchenko, T. Mat-
      suoka, P. Rousseau, V. Yanovsky, A. Maksimchuk, S. Kalmykov, G. Shvets,
      and M. C. Downer. Snapshots of laser wakefields. *Nat Phys*, 2(11):749–753,
      2006. 105, 132

[183] M. J. Edwards, A. J. MacKinnon, J. Zweiback, K. Shigemori, D. Ryutov,
      A. M. Rubenchik, K. A. Keilty, E. Liang, B. A. Remington, and T. Ditmire.
      Investigation of ultrafast laser-driven radiative blast waves. *Phys. Rev. Lett.*,
      87(8):085004, 2001. 106, 108, 131

[184] Y. B. Zel'dovich and Y. P. Raizer. *Physics of shock waves and high temper-
      ature hydrodynamic phenomena.* Academic, New York, 1967. 108

[185] J. Grun, J. Stamper, C. Manka, J. Resnick, R. Burris, J. Crawford, and
      BH Ripin. Instability of taylor-sedov blast waves propagating through a
      uniform gas. *Physical review letters*, 66(21):2738–2741, 1991. 108

[186] S. V. Bulanov, I. N. Inovenkov, V. I. Kirsanov, N. M. Naumova, and A. S.
      Sakharov. Nonlinear depletion of ultrashort and relativistically strong laser
      pulses in an underdense plasma. *Phys. Fluids*, 4:1935, 1992. 111, 116, 117

[187] N. M. Naumova, J. Koga, K. Nakajima, T. Tajima, T. Zh. Esirkepov, S. V.
      Bulanov, and F. Pegoraro. Polarization, hosing and long time evolution of

relativistic laser pulses. *Physics of Plasmas*, 8(9):4149–4155, 2001. 111, 114, 115

[188] M. Borghesi, S. Bulanov, D. H. Campbell, R. J. Clarke, T. Zh. Esirkepov, M. Galimberti, L. A. Gizzi, A. J. MacKinnon, N. M. Naumova, F. Pegoraro, H. Ruhl, A. Schiavi, and O. Willi. Macroscopic evidence of soliton formation in multiterawatt laser-plasma interaction. *Phys. Rev. Lett.*, 88(13):135002, 2002. 111, 114, 116

[189] L. Romagnani, A. Bigongiari, S. Kar, S. V. Bulanov, C. A. Cecchetti, T. Zh. Esirkepov, M. Galimberti, R. Jung, T. V. Liseykina, A. Macchi, J. Osterholz, F. Pegoraro, O. Willi, and M. Borghesi. Observation of magnetized soliton remnants in the wake of intense laser pulse propagation through plasmas. *Phys. Rev. Lett.*, 105(17):175002, 2010. 111, 112

[190] L. Gorbunov, P. Mora, and T. M. Antonsen, Jr. Magnetic field of a plasma wake driven by a laser pulse. *Phys. Rev. Lett.*, 76:2495, 1996. 111

[191] S. V. Bulanov, M. Lontano, T. Zh. Esirkepov, F. Pegoraro, and A. M. Pukhov. Electron vortices produced by ultraintense laser pulses. *Phys. Rev. Lett.*, 76(19):3562–3565, 1996. 111

[192] EC Harding, JF Hansen, OA Hurricane, RP Drake, HF Robey, CC Kuranz, BA Remington, MJ Bono, MJ Grosskopf, and RS Gillespie. Observation of a kelvin-helmholtz instability in a high-energy-density plasma on the omega laser. *Physical review letters*, 103(4):45005, 2009. 111

[193] G. Sarri, D. K. Singh, J. R. Davies, F. Fiuza, K. L. Lancaster, E. L. Clark, S. Hassan, J. Jiang, N. Kageiwa, N. Lopes, A. Rehman, C. Russo, R. H. H. Scott, T. Tanimoto, Z. Najmudin, K. A. Tanaka, M. Tatarakis, M. Borghesi, and P. A. Norreys. Observation of postsoliton expansion following laser propagation through an underdense plasma. *Phys. Rev. Lett.*, 105(17):175007, 2010. 111, 133

[194] A. Macchi, A. Bigongiari, F. Ceccherini, F. Cornolti, T.V. Liseikina, M. Borghesi, S. Kar, and L. Romagnani. Ion dynamics and coherent structure formation following laser pulse self-channeling. *Plasma Physics and Controlled Fusion*, 49:B71, 2007. 112

[195] L. M. Chen, H. Kotaki, K. Nakajima, J. Koga, S. V. Bulanov, T. Tajima, Y. Q. Gu, H. S. Peng, X. X. Wang, T. S. Wen, H. J. Liu, C. Y. Jiao, C. G. Zhang, X. J. Huang, Y. Guo, K. N. Zhou, J. F. Hua, W. M. An, C. X. Tang, and Y. Z. Lin. Self-guiding of 100 tw femtosecond laser pulses in centimeter-scale underdense plasma. *Physics of Plasmas*, 14(4):040703, 2007. 114

[196] M. C. Kaluza, S. P. D. Mangles, A. G. R. Thomas, Z. Najmudin, A. E. Dangor, C. D. Murphy, J. L. Collier, E. J. Divall, P. S. Foster, C. J. Hooker, A. J. Langley, J. Smith, and K. Krushelnick. Observation of a long-wavelength hosing modulation of a high-intensity laser pulse in underdense plasma. *Phys. Rev. Lett.*, 105(9):095003, 2010. 114

[197] G. Sarri, S. Kar, L. Romagnani, SV Bulanov, CA Cecchetti, M. Galimberti, LA Gizzi, R. Heathcote, R. Jung, I. Kourakis, et al. Observation of plasma density dependence of electromagnetic soliton excitation by an intense laser pulse. *Physics of Plasmas*, 18:080704, 2011. 117

[198] M. Borghesi, A.J. Mackinnon, A. R. Bell, G. Malka, C. Wickers, O. Willi, J. R. Davies, A. Pukhov, and J. Meyer ter Vehn. Observations of collimated ionization channels in aluminum-coated glass targets irradiated by ultraintense laser pulses. *Phys. Rev. Lett.*, 83:4309–4312, 1999. 118

[199] D. Batani, SD Baton, M. Manclossi, JJ Santos, F. Amiranoff, M. Koenig, E. Martinolli, A. Antonicci, C. Rousseaux, M.R. Le Gloahec, et al. Ultraintense laser-produced fast-electron propagation in gas jets. *Physical review letters*, 94(5):55004, 2005. 118

[200] N.I. Vogel and N. Kochan. Experimental investigation of stochastic pulsation and formation of light bullets with megagauss magnetic fields by an intense laser pulse propagating in a preionized plasma. *Physical Review Letters*, 86(2):232–235, 2001. 119

[201] T. Nakamura and K. Mima. Magnetic-dipole vortex generation by propagation of ultraintense and ultrashort laser pulses in moderate-density plasmas. *Phys. Rev. Lett*, 100(20):205006, 2008. 120

[202] P. M. Nilson, S. P. D. Mangles, L. Willingale, M. C. Kaluza, A. G. R. Thomas, M. Tatarakis, Z. Najmudin, R. J. Clarke, K. L. Lancaster, S. Karsch, J. Schreiber, R. G. Evans, A. E. Dangor, and K. Krushelnick. Generation of ultrahigh-velocity ionizing shocks with petawatt-class laser pulses. *Phys. Rev. Lett.*, 103(25):255001, 2009. 120

[203] S. Fritzler, Z. Najmudin, V. Malka, K. Krushelnick, C. Marle, B. Walton, M. S. Wei, R. J. Clarke, and A. E. Dangor. Ion heating and thermonuclear neutron production from high-intensity subpicosecond laser pulses interacting with underdense plasmas. *Phys. Rev. Lett.*, 89(16):165004, 2002. 131

[204] E. D'Humières, JL Feugeas, P. Nicolaï, S. Gaillard, T. Cowan, Y. Sentoku, and V. Tikhonchuk. Investigation of high intensity laser proton acceleration with underdense targets. In *Journal of Physics: Conference Series*, volume 244, page 042023. IOP Publishing, 2010. 132

[205] GR Plateau, NH Matlis, CGR Geddes, AJ Gonsalves, S. Shiraishi, C. Lin, RA van Mourik, and WP Leemans. Wavefront-sensor-based electron density measurements for laser-plasma accelerators. *Review of Scientific Instruments*, 81(3):033108–033108, 2010. 132

[206] V.T. Tikhonchuk, T. Schlegel, C. Regan, M. Temporal, J.-L. Feugeas, Ph. Nicolaï, and X. Ribeyre. Fast ion ignition with ultra-intense laser pulses. *Nuclear Fusion*, 50(4):045003, 2010. 134

[207] OF Hagena and W. Obert. Cluster formation in expanding supersonic jets: effect of pressure, temperature, nozzle size, and test gas. *The Journal of Chemical Physics*, 56:1793, 1972. 139, 145

[208] O.F. Hagena. Nucleation and growth of clusters in expanding nozzle flows. *Surface Science*, 106(1-3):101–116, 1981. 139, 145

[209] O.F. Hagena. Cluster ion sources. *Review of scientific instruments*, 63(4):2374–2379, 1992. 139, 145

[210] C.E. Heil and D.F. Walnut. Continuous and discrete wavelet transforms. *Siam Review*, 31:628–666, 1989. 140

[211] RA Smith, T. Ditmire, and JWG Tisch. Characterization of a cryogenically cooled high-pressure gas jet for laser/cluster interaction experiments. *Review of scientific instruments*, 69:3798, 1998. 145

[212] OG Danylchenko, SI Kovalenko, and VN Samovarov. Experimental verification of the hagena relation for large clusters formed in a conical nozzle. *Technical Physics Letters*, 34(12):1037–1040, 2008. 146

Accélération d'ions par interaction laser-plasma du régime sous-dense au régime proche sur-dense : effets de sillage et structures plasma associées

Ce travail s'est attaché à démontrer théoriquement et expérimentalement l'intérêt d'une analyse spectrale de l'émission ionique radiale, croisée à l'observation quantitative des structures plasma excitées, pour cerner plus clairement les phénomènes en jeu au cours de l'interaction d'un laser avec un plasma. Le réglage fin des paramètres laser et plasma ont permis une étude paramétrique détaillée de l'interaction sur une large gamme de densité plasma. Lorsque l'on fait varier la densité plasma pic de très sous-dense à quasi-surdense, les distributions ioniques passent de piquées à maxwelliennes, et présentent de fortes modulations quand la durée de l'impulsion laser est proche de la demi-période plasma, i.e. proche de la résonance du sillage laser. Dans ce cas, le mécanisme d'accélération est différent de celui de l'explosion Coulombienne par l'intervention des effets du champ de sillage laser et du champ de la gaine plasma au bord du canal creusé par le laser. Par ailleurs, pour une densité plasma pic donnée et plus élevée que celle de la résonance, lorsque la longueur du gradient plasma est augmentée, l'accélération ionique est supprimée au profit de structures électromagnétiques fondamentales (soliton/vortex) clairement identifiées optiquement pour la première fois. Grâce à un protocole expérimental innovant, l'étude optique des champs magnétiques au sein de ces structures est à présent rendue possible. Enfin, proche de la densité critique, l'autofocalisation efficace du laser conduit à un dépôt très localisé de l'énergie laser, donnant naissance à une expansion électronique ultra-rapide (moins d'une picoseconde) et à la naissance d'un dipôle magnétique intense qui participe au chauffage des électrons.

Pour ces études, des techniques et diagnostics ont été développés et testés simultanément avec succès. Il s'agit, d'une part, de jets de gaz submillimétriques à haute densité permettant une exploration localisée, stable et reproductible sur une large gamme de densités et de profils plasma, et d'autre part, d'interféromètre et polarimètre à hautes résolutions spatiales et temporelles afin d'observer la propagation laser et l'évolution des densités et champs au sein du plasma.

Ion acceleration from laser-plasma interaction in underdense to near-critical regime : wakefield effects and associated plasma structures

This work endeavoured to demonstrate theoretically and experimentally the interest of a spectral analysis of the radial ion emission, coupled to the quantitative observation of the excited plasma structures, to grasp more clearly the phenomena occurring when a laser interacts with a plasma. The fine tuning of the laser and plasma parameters made it possible to parametrically study in details the interaction. When the plasma peak density is varied from under- to quasi-overdense, the ion distributions change from a peak-like to a maxwellian-like shape, and exhibit strong modulations close to the laser wakefield resonance. This resonance is obtained when the pulse duration is close to half the plasma period. In this case, the accelerating mechanism is different from Coulomb explosion due to laser wakefield effects and influence of the plasma sheath at the edge of the laser-bored channel. Besides, for a given peak density, when the gradient scale length is increased, ion acceleration is suppressed and fundamental electromagnetic structures (soliton/vortex) appear and they were optically identified for the first time. Finally, close to the critical density, the efficient laser self-focusing leads to a very localized energy deposit, that entails an ultrafast electron expansion (within one picosecond) and the growth of an intense magnetic dipole heating further the electrons.

Thanks to an innovative experimental setup, optical studies of magnetic fields within these structures are from now on possible. For these studies, technical means and diagnostics have been developed and simultaneously tested with success. They consist, on the one hand, in submillimetric very dense gas jets for a localized, stable and reproducible investigation within a wide range of plasma densities and profiles, and, on the other hand, in interferometer and polarimeter with high spatial and temporal resolutions, to inspect the laser propagation, along with densities and fields evolution inside the plasma.